Biomolecular design elements

cortical microtubules and DNA-coated colloids

Simon Tindemans

Biomolecular design elements

cortical microtubules and DNA-coated colloids

Simon Harrie Tindemans

Abstract

The research described in this thesis deals with the self-organizing properties of systems of biomolecules. Biomolecules exhibit two properties that guarantee a large 'design space' for creating order through interactions. First, they often consist of a large number of subunits that can be connected many different ways. In the case of DNA this is the nucleotide base-pair sequence, in proteins the sequence of amino acids and in filamentous protein aggregates, like microtubules, the varying number of subunits and the dynamical state of the aggregate. Second, biomolecular interactions often have a high degree of specificity, allowing selective engineering of molecular contacts and the targeted modulation of properties. In this thesis we explore these possibilities, using two concrete examples.

The first system under study is the microtubule cytoskeleton of the interphase plant cell, which is organized into the highly ordered transverse cortical array. Microtubules are long, dynamical protein aggregates that form a major component of all eukaryotic cells. Each individual microtubule is a dynamical system that stochastically switches between periods of growth and shrinkage, with frequencies that can be modulated by other biomolecular interactions. The cortical microtubules in plant cells are thought to be rigidly attached to the inside of the cell membrane, thereby effectively forming a two-dimensional system in which their intrinsic dynamics are modulated by motion through treadmilling and direct collisions. Recent experiments have suggested that simple collision rules with three possible outcomes - cross-over, induced catastrophe and re-alignment - underlie the observed self-organization. These observations naturally lead to a stochastic many-parameter model that has been studied using both analytical and simulation methods. The theoretical approach has led to the identification of control parameters for the alignment of the cortical array, and to predictions regarding the alignment that agree qualitatively, and in some cases quantitatively, with the simulation results. The combined approach has made it possible to isolate the alignment potential that results from the various interaction mechanisms. Furthermore, the simulations have been extended to three-dimensional cell shapes and spatially varying parameters to investigate the orientation mechanism of the cortical array.

The second system under consideration is the man-made model system of DNA-coated colloids, for which the interactions can be tuned by a suitable choice of the DNA-linkers between individual beads. These systems promise the creation of designer colloidal crystals in which specific local arrangements of distinct particles can be extended over macroscopic distances. Here we address the fundamental question of what patterns are designable given isotropic pair-wise interactions. We investigate this question for two-dimensional finite range interactions on lattices of a given symmetry. It is shown that a periodic ground state of arbitrary size can be designed if the interaction range satisfies a minimum criterion, depending on the lattice type. In addition, a recipe is presented that guarantees the existence of such a unique ground state. The recipe is extended to periodic patterns with non-trivial unit cells and illustrated using simulation results.

Contents

Introduction

Looking at the world around us, we find ourselves surrounded by complex structures on all scales: machines, buildings, social groups, and on a smaller level organisms, cells and proteins. The inquisitive mind naturally wonders how all of this is being produced. For man-made objects, this process often involves the gathering of materials, assembly and verification of the result. Needless to say, all of this is done by a person – or factory robot – overseeing the production process.

It immediately becomes clear that this picture of assembly cannot apply to all objects. There is no building plan for organizations and societies, nor are cells assembled piece by piece by an outside constructor. Even the basic crystal of kitchen salt is not constructed by careful placement of each individual ion. Rather, these and many other structures emerge from the collective interactions of their constituents: they are self-organizing systems.

Through the cooperative behavior of their constituents, such systems eliminate the need for an external constructor. Such a non-hierarchial organization can be very efficient, especially as the systems get larger. Most importantly, even though there is no central control, it is not necessary for the individual components to 'know' what the completed design should look like, but only the (small) part they should be playing. In this way, complicated behavior or structures can emerge from simple components.

This thesis is concerned with two particular self-organizing systems that consist of biomolecules. In the first chapters, we take a look at how cortical microtubules in plant cells align spontaneously to form the ordered structure that is known as the cortical array, a question that is of basic importance in the understanding of plant morphology. Later, in chapter 6, we turn to the possible application of self-organizing principles to man-made materials, specifically systems consisting of DNA-coated colloids. For this model system we address the fundamental question how much knowledge individual particles should have about the final product for them to

assemble it from scratch. Our approach to these questions starts from a detailed understanding of the components that make up these self-organizing systems.

1.1 A quantitative approach to biology

Over the past decades, many techniques and technologies have been developed that allow us to study the inner workings of the cell with an ever increasing resolution. The discovery, cloning and fusion of green fluorescent protein (GFP) has triggered a revolution through its ability to tag specific proteins in live cells, so that they can be observed directly through the microscope (Tsien, 1998). Also, the development of the optical tweezers (Ashkin, 1970) has opened up a new world of micro-manipulation. Taken together, these types of innovations have produced large amounts of detailed and quantitative data on the inner workings of the cell. This has made intracellular processes amenable to the types of quantitative questions that are often asked by physicists: how much, how fast and to what extent? In recent years, this has caused a rapid expansion of the field of biophysics.

The work that is described in this thesis involves mathematical models and simulations. The common aspect of these two methods is that they both make use of an explicit *quantitative model*. To write down a set of equations or to run a simulation you not only need to specify which interactions take place, but you also need to provide an exact description of the strength of these interactions. This is in stark contrast to more *qualitative models* that usually only specify the existence and the generic type of interactions. These qualitative models form an essential initial step in the understanding of a system, especially when detailed experimental data are hard to obtain. As such, many models of biological systems are primarily qualitative. However, now that experimental observations with sufficient accuracy are within reach, these qualitative models can, and should, be further specified to yield testable quantitative models.

In the following sections we will introduce a number of basic properties of the self-organizing systems that will be studied in the context of this thesis: cortical microtubules and DNA-coated colloids.

1.2 Microtubules

Every eukaryotic cell has an internal network of filaments know as the cytoskeleton, consisting of microtubules, actin and (in some species) intermediate filaments (Alberts et al., 2002). Microtubules, the stiffest of the three structural elements, are the topic of much of the work in this thesis. The basic building block of a microtubule is a heterodimer consisting of two subunits, α- and β-tubulin. These heterodimers assemble head to tail to form long protofilaments that, in turn, associate laterally to create the hollow tube that is the microtubule. *In vivo*, a microtubule usually consists of 13 protofilaments (Desai and Mitchison, 1997). Due to its fairly large diameter

(25nm), microtubules are extremely rigid on a cellular scale, with a persistence length between 0.08 and 8 mm (Van den Heuvel et al., 2008).

DYNAMIC INSTABILITY

Microtubules extend by polymerization, the incorporation of new tubulin dimers into the microtubule lattice at either one of the ends. Each of the α and β subunits need to bind to GTP molecule before they can become part of the microtubule. The β-tubulin-associated GTP is hydrolyzed to GDP soon after the polymerization step and remains in that state as long as it is part of the microtubule (Desai and Mitchison, 1997). The polymerization process thus leads to the maintenance of a GTP-tubulin ring (cap) on a polymerizing microtubule end.

Microtubules have been observed to switch spontaneously from periods of relatively steady polymerization to periods of rapid depolymerization. This so-called 'catastrophe' is thought to be caused by fluctuations that cause the GTP-tubulin cap to disappear. The switch from the polymerizing to a depolymerizing state and the persistence of this state is likely to be enhanced by the intrinsic curvature of the protofilaments, especially in the GDP state (Desai and Mitchison, 1997). After a period of rapid depolymerization, microtubules can switch back to the growing state in a process called a 'rescue' event. The existence of alternating periods of growth and shrinkage has been dubbed *dynamic instability* (Mitchison and Kirschner, 1984).

The asymmetry of the microtubule building blocks, the tubulin dimers, means that the microtubules themselves are also polar molecules. This asymmetry is exploited by various motor proteins that are able to walk along the microtubules unidirectionally. In addition, the asymmetry results in differences in dynamics at each microtubule end. The direction in which the β-tubulin subunits are pointed is called the *plus end* and is the most dynamic of the two. The dynamics of the opposite *minus end* are much less well studied. (Desai and Mitchison, 1997). Although the minus end is capable of showing dynamic instability in *in vitro* conditions, it seems to be more regulated inside the cell. In many cases, the minus end remains attached to a nucleation site (Burk et al., 2007), or is found to undergo (relatively) steady depolymerization (Shaw et al., 2003). The combination of net addition of dimers at and a net removal at the minus end leads to an effective transport of dimers from the plus to the minus end, and an apparent forward motion of the microtubule in a process called *treadmilling* (Rodionov and Borisy, 1997).

On a mesoscopic level, the dynamics of the plus end has been described by a model in which the plus end of a microtubule is in either a growing or a shrinking state, with associated effective growth and shrinkage speeds. The switching between these two states occurs stochastically, according to two independent switching rates (Mitchison and Kirschner, 1984; Hill, 1984; Dogterom and Leibler, 1993). This model works surprisingly well (Verde et al., 1992) and the necessary parameters have been measured in many systems, including plant cells (Vos et al., 2004; Ishida et al., 2007).

Over the years, many models have been introduced that describe the dynamics of microtubules starting in a more detailed fashion, such as the GTP cap models by

Flyvbjerg et al. (1994) and Antal et al. (2007) and explicit elasticity models by Jánosi et al. (2002) and VanBuren et al. (2005). However, in the context of this thesis we will make use of the mesoscopic two-state model of microtubule dynamics, both because of its simplicity and because it allows for better comparisons with experimental observations on the cellular scale.

NUCLEATION

At cellular tubulin concentrations, there exists a prohibitive barrier for the spontaneous self-assembly of microtubules. This barrier is overcome with the help of the γ-tubulin protein that is the main component of the γ-tubulin ring complex (γ-TuRC) (Zheng et al., 1995). These ring-shaped complexes are thought to provide a 'mould' for the initial polymerization of tubulin dimers. In addition, they serve to stabilize and hold the microtubule minus end. The controlled release of minus ends from the γ-TuRCs is thought to have biological relevance (Desai and Mitchison, 1997).

SEVERING

It was noted by Vale (1991) that apparently stable microtubules could be severed in mitotic extracts of Xenopus eggs. This activity was traced back to a protein that is able to use ATP hydrolysis to sever microtubules. The protein was identified only later and given the name katanin after the *katana*, the Japanese Samurai sword (McNally and Vale, 1993). Katanin is a heterodimer, consisting of the p60 and p80 subunits. The p80 subunit is thought to be responsible for the targeting of the protein, whereas p60 is involved in the actual severing as part of a hexameric ring (Hartman and Vale, 1999). The hexameric form of katanin appears to remove individual dimers from the microtubule lattice, thereby compromising the structural integrity of the microtubule. It is not currently clear whether katanin acts uniformly along the microtubule, or whether it is attracted by pre-existing lattice defects (Davis et al., 2002).

Katanin homologs have since been discovered across the animal and plant kingdoms (Burk et al., 2007). Also, another severing protein by the name of spastin has been identified. Like katanin, it also assembles in a hexameric ring, suggesting a severing mechanism similar to that of katanin (Roll-Mecak and Vale, 2008). Severing proteins can be used by the cell to assist in the regulation of the cytoskeleton, for example in the mitotic and meiotic spindles (McNally et al., 2006). Generally, the activity of severing proteins leads to a decrease in the average microtubule length, but an *increase* in their number (Roll-Mecak and Vale, 2006). Surprisingly, this increase in number can sometimes more than offset the loss of microtubule length due to the average length decrease (Srayko et al., 2006).

Earlier theoretical studies have assessed the effect of severing on actin filament length distributions (Edelstein-Keshet and Ermentrout, 1998; Roland et al., 2008). In chapter 2 we investigate the length distribution of microtubules in the presence of severing proteins by extending the dynamic instability model for microtubule dynamics.

Nucleation
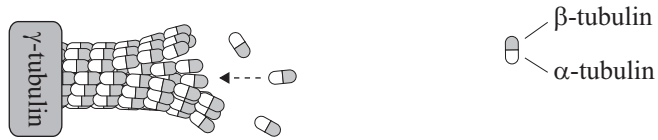
Dynamic instability
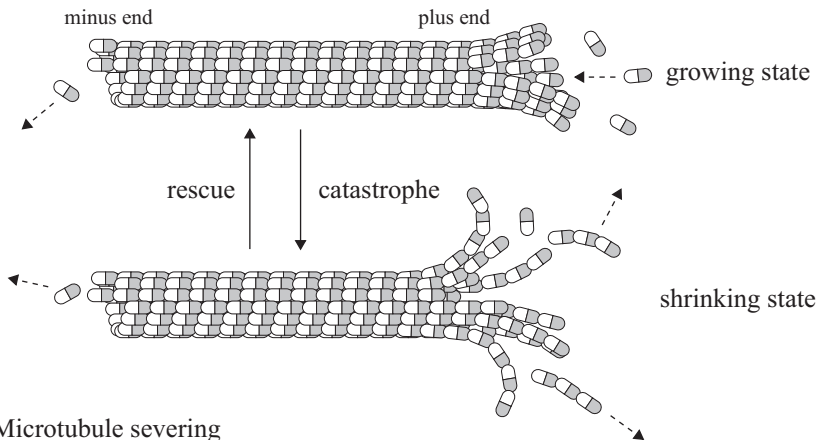
Microtubule severing
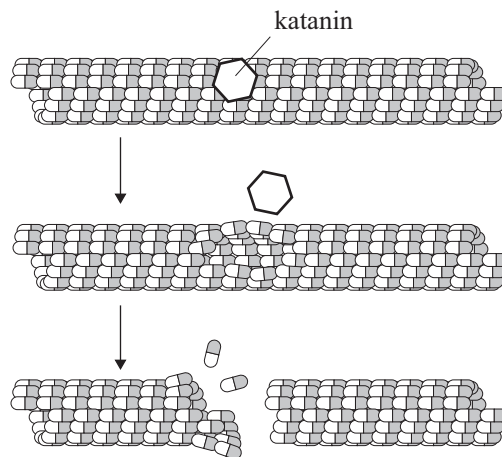
Figure 1.1: Schematic overview of microtubule nucleation, dynamic instability and severing, indicating the tubulin dimers and their α- and β-subunits.

1.3   The plant cell cortical array

Plant cells have a basic organization that is different from many other eukaryotic cells. Because the individual cells must contribute to the structural integrity of the plant as a whole, they have rigid cell walls and contain large pressure-regulating vacuoles that keep the cell under constant tension (Wasteneys, 2002).
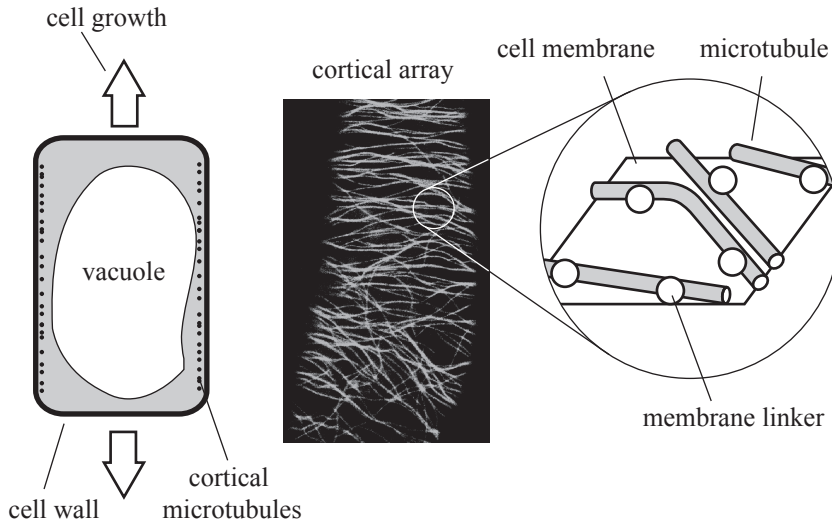
Figure 1.2: Schematic picture of a plant cell (left) alongside an image of an interphase BY-2 cell with fluorescently labelled tubulin (center; courtesy of Jan Vos, Wageningen University). The enlargement illustrates the connections of aligned microtubules with the plasma membrane.

This configuration presents the plant cell with a unique morphological problem. To construct the plant's body plan, cells need to expand and divide in well-defined directions. How can this be coordinated with the deposition and maintenance of the cell wall? The answer is linked to the cellulose microfibrils inside the cell wall. These are deposited in regular arrays that wrap the cell in more or less parallel orientations. The cell wall therefore responds anisotropically to stress. Effectively, the microfibrils form a *corset* that guides the expansion of the cell in the direction transverse to their orientation (Lucas and Shaw, 2008).

The existence of ordered microfibrils begs the question of how they are laid down. Interestingly, the parallel organization of microfibrils – on the outside of the cellular membrane – has been found to mimic that of the microtubule cytoskeleton (Paradez et al., 2006). During interphase, most microtubules in plant cells are found at the cell cortex where they form the cortical array, a structure that is also oriented

transversely to the direction of cell growth. It has long been speculated that the cortical microtubules serve as rails for the deposition of the cellulose microfibrils, an interpretation that has been strengthened by the experimental observations of Paredez et al. (2006). However, recent experiments have suggested that the causality may not be so clear-cut (Paredez et al., 2008).

The question of cellular growth in plants therefore leads to the basic question how the cortical microtubules form the cortical array, and how its orientation is established. In contrast to animal cells, in which most microtubule arrays are radially attached to a centrosome, there is no obvious microtubule organizing center in plant cells (Pastuglia and Bouchez, 2007). Instead, the cortical array is a self-organizing structure that emerges from the interactions between the constituent microtubules, mediated by microtubule-associated proteins. The intriguing question how the cortical array is established forms the basis of the majority of the work in this thesis: chapters 3–5.

1.3.1   Microtubule-associated proteins

Microtubule-associated proteins (MAPs) perform a large variety of functions related to the cytoskeleton, and a number of these have been identified to play a role in the regulation of the plant cytoskeleton, and the formation of the cortical array in particular (Lloyd and Hussey, 2001; Sedbrook and Kaloriti, 2008). In the theoretical and simulation work in this thesis, we restrict ourselves to three particular types of MAP activity: nucleation (γ-tubulin), severing (katanin) and cell membrane anchoring. Each of these is discussed in more detail below. The arguably important class of plus end associated proteins (+TIPS) will not be discussed in detail, because their activity can likely be absorbed into the four parameters of the dynamic instability model of the plus end.

CELL MEMBRANE ADHESION

Electron microscopy images first hinted at the existence of a link between the cortical microtubules and the plasma membrane (Hardham and Gunning, 1978; Barton et al., 2008). The resulting idea that cortical microtubules are stably anchored to the plasma membrane (and perhaps the cell wall) has been reinforced by subsequent observations. Tracking of GFP-labelled microtubules has clearly demonstrated that the cortical microtubules do not move laterally, and any axial motion is only due to treadmilling (Shaw et al., 2003; Vos et al., 2004). Finally, although the polymerizing plus end is moving because of the cytoplasmic streaming, the body of the microtubule remains firmly in place (Sainsbury et al., 2008). Although the adhesion of microtubules to the plasma membrane is now widely accepted, its nature remains unclear. Phospholipase D is thought to be involved in this connection, and has been observed to aggregate in a punctate pattern along microtubules (Gardiner et al., 2001). A similar pattern occurs in the distribution of CLASP, a plus end binding protein (Kirik

et al., 2007). The evidence points to the existence of more or less regularly spaced attachment points that involve more than a single protein.

Despite the uncertainty regarding the mechanism of attachment, the qualitative observation that cortical microtubules are anchored to the membrane has important consequences. Firstly, it implies that there is no rotational or translational movement of existing microtubules. The dynamics of the system are therefore a product of the movement of the microtubule plus and minus ends. Secondly, the anchoring combines with the stiffness of the microtubules to confine the system to a quasi two-dimensional space: all interactions occur in the close vicinity of the plasma membrane.

γ-TUBULIN

Also in plant cells, the nucleation of new microtubules involves γ-tubulin. However, unlike most other eukaryotes, the γ-tubulin is not part of a microtubule organizing center like a centrosome. Rather, it is mostly found adhered to existing microtubules, nucleating new microtubules that 'branch off' at an angle of approximately 40° (Murata et al., 2005). Nucleation along the direction of existing microtubules (especially in bundles) has also been reported (Ehrhardt, 2008).

Although these microtubule-associated nucleation mechanisms are thought to be the dominant modes of nucleation once the cortical array has been established, another type of nucleation is necessary to explain the initial creation of microtubules after cell division. Just after cytokinesis, microtubules grow towards the cortex from the nuclear periphery (Bartolini and Gundersen, 2006). Also, microtubules are seen to nucleate at random positions and in random directions during interphase (Chan et al., 2003; Shaw et al., 2003). These mechanism are likely to lead to a random orientation of nucleated microtubules, but recent experiments[1] suggest a transient preference for diagonal orientations of these early microtubules.

KATANIN

Studies of the microtubule severing protein katanin[2] in plant cells have indicated that it colocalizes with the cortical microtubules (Burk et al., 2007). Mutations in the *Arabidopsis* katanin gene have been shown to cause a breakdown or decrease of the alignment of the cortical microtubules (Bichet et al., 2001; Burk et al., 2001). The disordered cortical array in these mutants is reflected by the aberrant orientations of the cellulose microfibrils in the cell wall, resulting in reduced cell elongation and an overall decrease in size of the organism (Burk et al., 2007). On the other hand, overexpression of katanin in *Arabidopsis* and the resulting increase in severing events initially leads to the formation of bundles (Stoppin-Mellet et al., 2006). The

---

[1]Lindeboom *et al.*, in preparation

[2]Homologs of the microtubule severing protein katanin have been discovered in plant cells under many different names (Burk et al., 2007), but for reasons of clarity we will use the common name katanin in the context of this thesis.

mechanism behind this is likely twofold. First, severing creates shorter microtubule fragments that are free to move by treadmilling, so that they can align with other fragments through the zippering process that is explained in the next section. Second, if both fragments of a single severed microtubule start growing, they effectively form a bundle. The same authors have reported that a further increase in the severing rate leads to a disorganized array of very short microtubules, as is to be expected.

Where on the microtubule does the severing take place? Three different scenarios have been reported in the literature. Firstly, katanin is thought to be responsible for the release of microtubules from their nucleation sites and therefore enables tread-milling (Wasteneys, 2002). Secondly, it is unclear whether any significant amount of severing takes place along the length of the microtubules. In katanin-overexpression experiments by Burk et al. (2007) no fragmentation of microtubules was observed. However, in the study by Stoppin-Mellet et al. (2006), severing along the length of microtubules was observed. The factors influencing unbiased microtubule fragmen-tation and their relevance are still largely unknown. Finally, Wightman and Turner (2007) have observed in *Arabidopsis* cotyledons that severing events in ordered arrays occurred almost exclusively at the locations where two microtubules cross. This suppression of intersections can be a powerful ordering agent by itself, as we will see in section 4.4.2.

1.3.2   Microtubule collisions

The effective confinement of the cortical microtubules to a two-dimensional surface leads to a unique property of the plant cell's cortical array: frequent collisions of polymerizing microtubule plus ends with existing microtubules. Such a collision leads to one of three outcomes (sometimes after a short pause): (1) *zippering*, the bending of the microtubule plus end and its continued polymerization in the direc-tion of the encountered microtubule; (2) *induced catastrophe*, a collision-induced switch to the depolymerizing state; (3) *cross-over*, the continued polymerization in the original growth direction (Shaw et al., 2003; Dixit and Cyr, 2004; Wightman and Turner, 2007; Barton et al., 2008). The probability of each outcome is highly depen-dent on the angle of incidence between the two microtubules. Generally, zippering is likely to occur for small incidence angles, and is not observed at all for angles larger than approximately 40° (tobacco BY-2) or 30° (*Tradescantia virginiana*) (Dixit and Cyr, 2004; Barton et al., 2008). Conversely, the probability for an induced catastro-phe increases with the angle. For experimental observations of the probabilities of zippering, induced catastrophe and cross-over in tobacco BY-2 cells, see figure 3.2. Measurements on *Arabidopsis* indicate a similar propensity for zippering, but a less frequent occurrence of induced catastrophes, resulting in more cross-over events (Wightman and Turner, 2007).
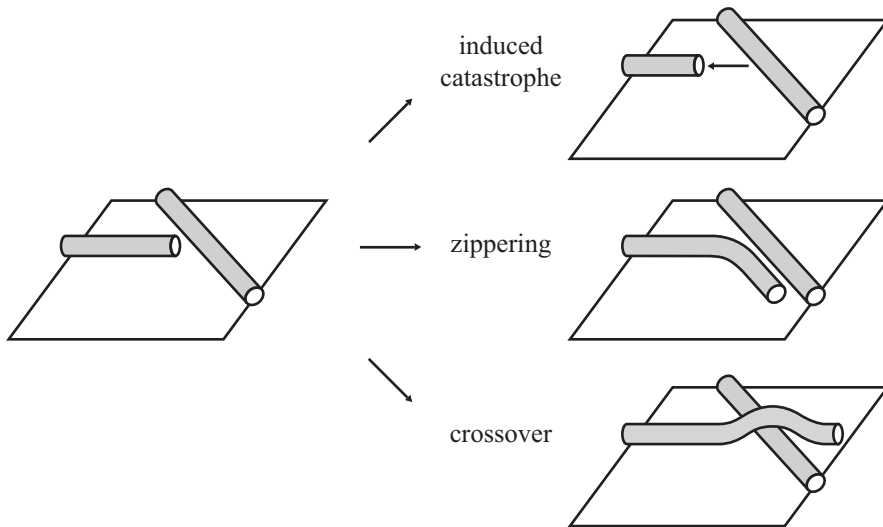
Figure 1.3: The possible outcomes of a microtubule collision event.

1.3.3   Array dynamics

When the first microtubules appear at the cell cortex, shortly after cell division, they are short and disorganized. In a period of approximately one hour they grow, interact and align to form the cortical array. In the final state, the microtubules have a length of approximately 1/8 the cell circumference (Hardham and Gunning, 1978; Barton et al., 2008), corresponding to approximately 10 μm and the mean distance between microtubules (equivalent to the inverse density) is approximately 1 μm (Ambrose et al., 2007)[3]. The degree of order is best expressed in terms of the order parameter S_2 (see equation (3.72)), which attains values in the range 0.6-0.8 (out of a range [0,1]) (Tanase, 2004). It has been reported that the array as a whole has a net polarity (Dixit et al., 2006), but due to the low number of microtubules that has been measured per cell, the effect may not be very significant. Chapters 3 and 4 address, both theoretically and using simulations, the question how such an ordered system can emerge from the interactions between microtubules.

In interphase growing cells, the cortical array is oriented transversely to the growth direction. As cells mature and growth slows, the cortical array reorients towards the long axis or becomes less organized. Cells have also been observed to reorient the cortical array in response to light (Paredez et al., 2006) or cell wall stress (Hamant et al., 2008). Finally, there are reports of cells in which the microtubules are not aligned globally, but have ordered domains that are continuously evolving (Chan et al., 2007). Not much is known about the physical or biological mechanisms

---

[3]Also observed in Lindeboom *et al.*, in preparation.

determining the orientation and reorientation of the cortical array, but it has been suggested that biochemical signals can locally change the microtubule dynamics, thereby creating a preferred direction (Ehrhardt and Shaw, 2006). This possibility, and the potential effect of geometry, is addressed in chapter 5.

1.4 Harnessing DNA for self-assembly

The sections above have highlighted a selection of the many processes in plant cells that have evolved over the course of millions of years to allow for the reliable creation of the microtubule cortical array. In this section we switch to the area of man-made self-assembling materials, the design elements of which are up to us to decide on. There are many promising applications of complex materials with features on the micrometer scale, such as photonic crystals, micro-arrays and electric circuits. Unfortunately, the direct production of such materials, especially in three dimensions, is often difficult, requiring an assembly process that is accurate over several orders of magnitude, from the smallest scale of the pattern to the size of the final product. Therefore it is an attractive option to look into alternative production methods, such as the use of smaller components that can self-assemble into larger structures. This way, the sampling power of thermodynamics can be harnessed to allow the components to 'search' for their target position in the final material.

This leads us to the question of how these self-assembling components and their interactions should be designed. Biomolecules are obvious candidates for the design of interactions, due to their large variety and the specificity of their interactions. One of the most promising approaches to the design of interactions between components has been the use of DNA hybridization. Each single DNA strand consist of a series of bases, commonly denoted by the letters A, T, C and G. Because there is a strong preferential binding between A and T, and between C and G, every strand has a unique complementary strand to which it can bind with maximum affinity. The range of possible binding sequences provided by DNA's four-letter alphabet combined with the specificity of base pair binding means that the binding affinity can be precisely manipulated, and this can not only be done for a single pair of DNA strands, but orthogonal interactions can be defined simultaneously for a large number of strands in the same solution. These properties of DNA make it an ideal candidate for the biochemical 'glue' of designed interactions, and it has been successfully used to create many intriguing structures, such as rigid tetrahedrons (Goodman et al., 2005), functionalized 2D lattices (Zheng et al., 2006) and nearly arbitrary 2D objects, such as smiley faces (Rothemund, 2006).

1.4.1 DNA-coated colloids

In chapter 6, we focus on a specific case of a DNA-mediated self-assembling system that was first proposed by Mirkin et al. (1996). In this system, the DNA is grafted onto micrometer-sized beads. The two strands forming the DNA are of slightly different
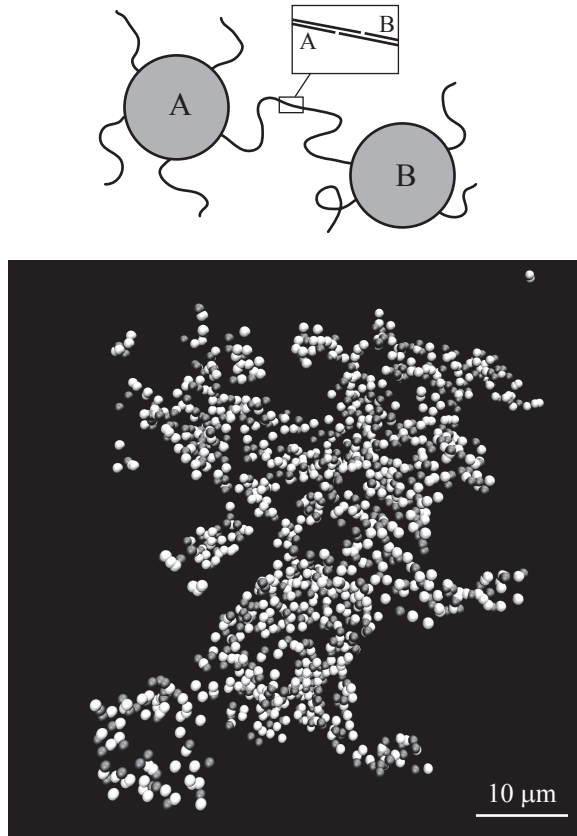
Figure 1.4: Depiction of a DNA-mediated specific connection between two bead types, indicated by A and B. The bottom image is a reconstructed image based on experiments with a similar system (Geerts et al., 2008, reproduced with permission).

lengths, so that a short stretch of single stranded DNA is exposed at the far end of the strand. This creates what is called a 'sticky' end, to which another single DNA strand can bind through hybridization of the DNA strands, provided the binding affinity is high enough. The sticky ends of two different beads can either bind directly (see figure 1.4), or mediated by a piece of linker DNA, that has preferential affinities for the sticky ends of both types of beads. The latter provides more flexible control over the possible interactions in the system, especially when many beads with different sticky ends are involved. In principle, it is therefore possible to create a system with many different types of beads, each of which has tunable interactions with every

other type of bead. The holy grail of the research on DNA-coated colloids is to design colloidal materials that will, in the proper circumstances, self-assemble from their constituents (the DNA-coated beads).

In spite of the theoretical possibilities, it has proven difficult to experimentally create the predicted self-assembling crystals, due in part to the sensitivity of the system to the strength of binding and the length of the DNA strands (Schmatko et al., 2007; Geerts et al., 2008). Furthermore, in those cases where macroscopic crystal structures have been created, this has been done for a single bead species (Biancaniello et al., 2005; Hill et al., 2008) or two species of beads (Nykypanchuk et al., 2008; Park et al., 2008). However, theoretical work suggests that more complicated patterns are worth investigating (Tkachenko, 2002; Licata and Tkachenko, 2006; Lukatsky et al., 2006).

1.5   Outline

Following this introduction, the research presented in this thesis starts with two theoretical chapters. In chapter 2, we construct a model for the severing of non-interacting microtubules by severing proteins and how this affects the length distribution of microtubules. Following this, in chapter 3 we formulate a model for the alignment of microtubules in the cortical array, taking into account their dynamic instability and collisions between microtubules.

The theory proposed in chapter 3 is constructed as a coarse-grained model derived from an underlying microscopic picture. This abstraction is put to the test in chapter 4, which describes an efficient simulation method to explicitly evaluate the dynamics of the underlying microscopic models. Furthermore, these simulations are used to probe parameter regimes that were not accessible to the theory. Taken together, the theory and simulations provide insight into the mechanisms leading to microtubule alignment. Chapter 5 addresses the poignant question what determines the direction in which the microtubules align, focusing on geometry and protein activity as possible orientational cues.

Switching from the naturally evolved structure in plants, chapter 6 explores the limits of man-made self-organizing materials. Using the model system of DNA-coated colloids as a paradigm for self-assembly, a simple 2D lattice model for self-assembling materials is introduced. For this model, a minimal recipe is derived for the required particle-particle interactions that are needed for the system to assemble into a predetermined ground state.

The most relevant result of preceding chapters are collected in chapter 7 and placed into their biological and physical context. In addition, interesting avenues for future research are indicated.

The effect of severing on microtubule length

Many different cell types have been shown to exhibit severing of microtubules by the ATPases katanin and spastin (Roll-Mecak and Vale, 2006) and mutation experiments suggest that this severing process plays an important, and sometimes crucial, role in the regulation of the cytoskeleton (McNally et al., 2006; Burk et al., 2001). Generally, the activity of severing proteins has been linked to a decrease in the average length of the microtubules, accompanied by an increase in their number (Roll-Mecak and Vale, 2006).

Three distinct types of severing by katanin have been reported. Firstly, in plant cells it is thought to be responsible for the release of microtubules from their nucleation sites, thereby enabling treadmilling motion (Wasteneys, 2002). Secondly, in *Arabidopsis* cotyledons, Wightman and Turner (2007) have observed severing specifically at the intersections of cortical microtubules. Finally, both katanin and spastin are capable of severing microtubules at seemingly random locations (Roll-Mecak and Vale, 2006).

In this chapter, we investigate theoretically how the occurrence of microtubule severing affects the average length distribution and the total number of microtubules. Previous studies have assessed the effect of severing on actin filaments (Edelstein-Keshet and Ermentrout, 1998; Roland et al., 2008). However, whereas actin dynamics can be described well by a single growth mode with constant polymerization and depolymerization rates, microtubules have a plus end that switches between prolonged periods of growth (polymerization) and shrinkage (depolymerization).

2.1 Model

In modelling this problem, we start from the basic dynamic instability model that was introduced by Dogterom and Leibler (1993). In this model, microtubules exist in either the growing or the shrinking state, and switch between these states with

fixed 'catastrophe' and 'rescue' rates r_c and r_r. In the growing state, the microtubule extends with an effective speed v^+, and in the shrinking state it recedes with an effective speed v^-. New microtubules are being nucleated with a steady nucleation rate r_n. This set of constraints gives rise to an ensemble length distribution that evolves over time.

Microtubule severing is modelled by a constant severing rate per unit length. This is a valid approximation if we assume that microtubule severing occurs on a time scale that is much shorter than the time in which a microtubule grows significantly ($t_{sev} \ll l/v^+$, where l is the average microtubule length). By taking a constant severing rate, we also implicitly assume that severing is limited by the availability of microtubules, i.e. severing protein is available in abundance. However, because we focus on steady-state results, where the total amount of microtubules is constant, the possible invalidity of this assumption will not qualitatively affect the results.
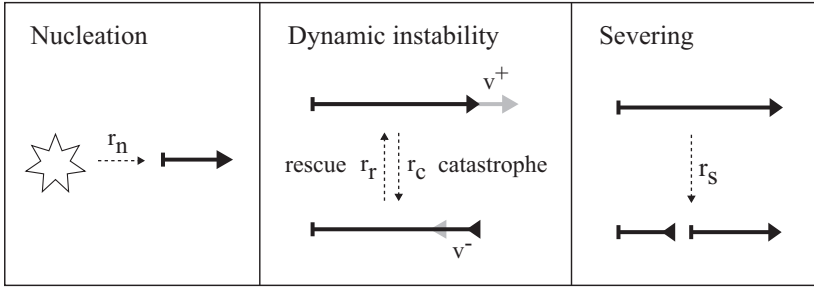
Figure 2.1: Schematic representation of the elements of the model. A list of parameters is given in table 2.1.

Following the approach by Dogterom and Leibler (1993), we construct a set of master equations for the length distributions of growing and shrinking microtubules. Denoting the growing and shrinking microtubule length distributions by $m^+(l, t)$ and $m^-(l, t)$, respectively, the equations can be written as

$$\partial_t m^+(l, t) = -\Phi_{catastrophe} + \Phi_{rescue} + \Phi_{growth} + \Phi^+_{severing} \tag{2.1a}$$

$$\partial_t m^-(l, t) = +\Phi_{catastrophe} - \Phi_{rescue} + \Phi_{shrinkage} + \Phi^-_{severing}, \tag{2.1b}$$

where each term stands for the contribution from a specific process, the explicit form of which is explained below. These equations are supplemented by the boundary conditions

$$m^+(0, t) = \frac{r_n}{v^+}, \tag{2.2}$$

specifying the nucleation of new microtubules with rate r_n, and

$$\lim_{l \to \infty} m^+(l, t) = 0 \tag{2.3}$$

$$\lim_{l \to \infty} m^-(l, t) = 0. \tag{2.4}$$

Parameters	
v^+	growth speed
v^-	shrinkage speed
r_c	catastrophe rate
r_r	rescue rate
r_n	nucleation rate
r_s	severing rate
Dependent variables	
$m^+(l)$	length distribution of growing microtubules
$m^-(l)$	length distribution of shrinking microtubules

Table 2.1: Overview of all parameters and variables in natural dimensions

The latter two represent the physically motivated constraint that there are no infinitely long microtubules.

2.1.1 Dynamic instability

Φ_{growth} in equation (2.1a) corresponds to the length increase of the growing segments. For segment growth in isolation, the length increase in a small time interval δt is given by $v^+ \delta t$, where v^+ is the growth velocity, and we have $m^+(l + v^+ \delta t, \theta, t + \delta t) = m^+(l, \theta, t)$. By expanding the left hand term to first order in δt, we find

$$\partial_t m_i^+(l, t) = -v^+ \partial_l m_i^+(l, t) \equiv \Phi_{growth} \tag{2.5}$$

A similar derivation yields that

$$\partial_t m_i^-(l, t) = v^- \partial_l m_i^-(l, t) \equiv \Phi_{shrink} \tag{2.6}$$

where v^- is the shrinking velocity.

Φ_{rescue} and $\Phi_{catastrophe}$ in equations (2.1) correspond to the fluxes due to the spontaneous rescues and catastrophe events. These events occur with a constant rate r_r and r_c per microtubule, leading to

$$\Phi_{rescue} = r_r m_i^-(l_i, \theta_i, t) \tag{2.7}$$

$$\Phi_{spont.\ cat.} = r_c m_i^+(l_i, \theta_i, t) \tag{2.8}$$

The contributions that have been discussed up to this point (the first three terms of equations (2.1)) together constitute the dynamic instability model that was introduced by Dogterom and Leibler (1993). These equations have been studied in great detail by Bicout (1997) (see also Bicout and Rubin, 1999).

2.1.2 Microtubule severing

Extending the basic dynamic instability model, we proceed to add the effect of microtubule severing. A similar contribution was derived by Edelstein-Keshet and

Ermentrout (1998) as the continuous limit of a discrete monomer addition and severing model for actin filaments.

The inclusion of severing events leads to two specific contributions to the length distributions: the *disappearance* flux $\phi_{\text{out}}(l, t)$ of microtubules of a certain length l and the *appearance* flux $\phi_{\text{in}}(l', t)$ of two new microtubules with a total length that is equal to l. In addition, the newly created microtubules can be created from microtubules that were initially growing (+) or shrinking (-). Symbolically, we write

$$\Phi^+_{\text{severing}} = -\phi^+_{\text{out}}(l, t) + \phi^+_{\text{in},+}(l, t) + \phi^+_{\text{in},-}(l, t) \tag{2.9}$$

$$\Phi^-_{\text{severing}} = -\phi^-_{\text{out}}(l, t) + \phi^-_{\text{in},+}(l, t) + \phi^-_{\text{in},-}(l, t) \tag{2.10}$$

These contributions will be discussed individually below.

The process of severing is controlled by the severing rate r_s that is given as a rate per unit of length. Thus we find that the fluxes of disappearing microtubules $\phi^+_{\text{out}}(l, t)$ (growing) and $\phi^-_{\text{out}}(l, t)$ (shrinking) are given by

$$\phi^+_{\text{out}}(l, t) = r_s l m^+(l, t) \tag{2.11}$$

$$\phi^-_{\text{out}}(l, t) = r_s l m^-(l, t) \tag{2.12}$$

Moving on to the influx terms $\phi^\pm_{\text{in},\pm}$, it is necessary to specify the process of severing in more detail. We will assume that the action of the severing protein is local, thus having no effect on the remote plus and minus ends of the microtubule it severs. This implies that the plus end fragment of a severed microtubule remains in the same state. However, we must make an explicit assumption regarding the state of the newly created plus end. In line with biological observations (Quarmby, 2000), we assume that the plus end starts out in the shrinking state. If necessary, the model can easily be extended to handle (a fraction of) severing-created plus ends that start out in the growing state.

Defining $P(l|l') = 1/l'$, $l \in [0, l']$ as the uniform probability distribution of selecting a severing location l on a microtubule of length l' we can then derive the influx $\phi^+_{\text{in},+}(l, t)$ of growing microtubules of length l that results from the severing of growing microtubules.

$$\phi^+_{\text{in},+}(l, t) = \int_0^\infty \phi^+_{\text{out}}(l', t) P(l' - l|l') \mathrm{d}l' \tag{2.13}$$

$$= r_s \int_0^\infty l' m^+(l') \theta(l' - l) \frac{1}{l'} \mathrm{d}l' \tag{2.14}$$

$$= r_s \int_l^\infty m^+(l') \mathrm{d}l', \tag{2.15}$$

where $\theta(x)$ is the Heaviside step function. In a similar way, and taking account the

fact that the minus end fragment is always in a shrinking state, we also derive

$$\phi_{in,-}^{+}(l,t) = 0 \tag{2.16}$$

$$\phi_{in,+}^{-}(l,t) = r_s \int_{l}^{\infty} m^{+}(l')\mathrm{d}l' \tag{2.17}$$

$$\phi_{in,-}^{-}(l,t) = 2r_s \int_{l}^{\infty} m^{-}(l')\mathrm{d}l'. \tag{2.18}$$

By taking the appropriate integrals, it can be shown that these terms conserve the total microtubule length, and that a new microtubule is created by each severing event. Furthermore, note that we do not need to keep track of the correlations between the lengths of the *individual* microtubules that are created from a single cutting event, because we are looking only at ensemble-averaged length distributions.

2.1.3   Reducing the complexity of the equations

We are now in the position to combine all the elements of the master equations (2.1), yielding

$$\partial_t m^{+}(l,t) = - r_c m^{+}(l,t) + r_r m^{-}(l,t) - v^{+}\partial_l m^{+}(l,t)$$
$$- r_s l m^{+}(l,t) + r_s \int_{l}^{\infty} m^{+}(l',t)\mathrm{d}l' \tag{2.19}$$

$$\partial_t m^{-}(l,t) = + r_c m^{+}(l,t) - r_r m^{-}(l,t) + v^{-}\partial_l m^{-}(l,t)$$
$$- r_s l m^{-}(l) + r_s \int_{l}^{\infty} [m^{+}(l') + 2m^{-}(l')]\mathrm{d}l'. \tag{2.20}$$

We can further simplify these equations by introducing common length and time scales in order to reduce the number of free parameters. As a length scale we will use the free run length $l_0 = v^{+}/r_c$ and as a time scale the associated catastrophe time $t_c = 1/r_c$. This leads to the definition of the dimensionless units

$$x = \frac{r_c}{v^{+}}l, \tag{2.21}$$

$$\tau = r_c t. \tag{2.22}$$

Furthermore, we rescale the distributions to absorb the nucleation rate and we drop the explicit time dependence of the variables in anticipation of our steady state analysis. Explicitly, we define

$$f^{+}(x) \equiv \frac{v^{+}}{r_n} m^{+}(l(x), t(\tau)) \tag{2.23}$$

$$f^{-}(x) \equiv \frac{v^{+}}{r_n} m^{-}(l(x), t(\tau)) \tag{2.24}$$

$$v \equiv v^{+}/v^{-} \tag{2.25}$$

$$r \equiv r_r/r_c \tag{2.26}$$

$$s \equiv r_s v^{+}/r_c^{2}, \tag{2.27}$$

producing the set of dimensionless equations

$$\partial_\tau f^+(x) = -f^+(x) + rf^-(x) - \partial_x f^+(x) - sxf^+(x) + s\int_x^\infty f^+(x')\mathrm{d}x' \qquad (2.28)$$

$$\partial_\tau f^-(x) = +f^+(x) - rf^-(x) + \frac{1}{v}\partial_x f^-(x) - sxf^-(x) + s\int_x^\infty [f^+(x') + 2f^-(x')]\mathrm{d}x', \qquad (2.29)$$

with the boundary conditions

$$f^+(0) = 1 \qquad (2.30)$$

$$\lim_{x\to\infty} f^+(x) = 0 \qquad (2.31)$$

$$\lim_{x\to\infty} f^-(x) = 0. \qquad (2.32)$$

Looking at the structure of these equations, we see that they constitute a coupled set of transport equations, with boundary conditions on the 'entry points' (0 for the growing microtubules, ∞ for the shrinking ones). The constraint on the growing microtubules at ∞ is not a strictly independent constraint, but we will include it for clarity's sake. In the steady state, the time derivatives vanish and we arrive at the final set of equations.

$$\partial_x f^+(x) = -f^+(x) + rf^-(x) - sxf^+(x) + s\int_x^\infty f^+(x')\mathrm{d}x' \qquad (2.33a)$$

$$\frac{1}{v}\partial_x f^-(x) = -f^+(x) + rf^-(x) + sxf^-(x) - s\int_x^\infty [f^+(x') + 2f^-(x')]\mathrm{d}x', \qquad (2.33b)$$

with the boundary conditions

$$f^+(0) = 1 \quad ; \quad \lim_{x\to\infty} f^+(x) = 0 \quad ; \quad \lim_{x\to\infty} f^-(x) = 0. \qquad (2.33c)$$

2.2 Results

We will proceed to analyze the steady state equations (2.33) in a number of steps. Initially, we determine a number of global properties of the length distributions. Subsequently, we obtain explicit expressions for the microtubule length distributions in two special cases: very small amounts of severing ($s \ll (1-rv)^2$) and in the absence of rescues ($r = 0$). We conclude with a numerical method with which the distribution can be calculated for arbitrary parameter values.

2.2.1 Integral relations

Let us define the nth moment of the functions $f^+(x)$, $f^-(x)$ as

$$M^{\pm(n)} \equiv \int_0^\infty x^n f^\pm(x)\mathrm{d}x. \qquad (2.34)$$

To obtain the relations between the moments, we multiply equations (2.33a) and (2.33b) by x^n and integrate from 0 to ∞. This yields the relations

$$-nM^{+(n-1)} = -M^{+(n)} + rM^{-(n)} + \delta_{n0} - s\frac{n}{n+1}M^{+(n+1)} \tag{2.35}$$

$$-n\frac{1}{v}M^{-(n-1)} = -M^{+(n)} + rM^{-(n)} + \delta_{n0}\frac{f^-(0)}{v} - s\frac{1}{n+1}M^{+(n+1)} + s\frac{n-1}{n+1}M^{-(n+1)}. \tag{2.36}$$

Subtracting equation (2.36) from (2.35) and evaluating the result for $n = 1$ gives

$$vM^{+(0)} = M^{-(0)}, \tag{2.37}$$

and for $n = 0$ we get

$$M^{+(1)} + M^{-(1)} = \frac{1}{s}\left(\frac{f^-(0)}{v} - 1\right). \tag{2.38}$$

This expression gives us the integrated microtubule *length* present in the system. The quantity $f^-(0)/v$ is the ratio of the microtubule flux *out of* the system by total catastrophes and the nucleation rate. Each severing event creates a new microtubule, so in the steady state this number will be larger than one.

If we use (2.37) to simplify the equation (2.35) for $n = 0$, we obtain expressions for the total *number* of growing and shrinking microtubules.

$$M^{+(0)} = \int_0^\infty f^+(x)\mathrm{d}x = \frac{1}{1-rv} \tag{2.39a}$$

$$M^{-(0)} = \int_0^\infty f^-(x)\mathrm{d}x = \frac{v}{1-rv}. \tag{2.39b}$$

This leads to the surprising result that the total number of microtubules in the system does *not* depend on the rate of microtubule severing.

2.2.2 Small severing rates

The results of the model in the absence of severing are exponential functions with the length scale $(1 - rv)^{-1}$. To investigate the changes that occur for very limited severing activity s, we introduce the perturbation

$$f^+(x) = e^{-(1-rv)x}(1 + s\hat{f}^+(x)) + O(s^2) \tag{2.40}$$

$$f^-(x) = ve^{-(1-rv)x}(1 + s\hat{f}^-(x)) + O(s^2). \tag{2.41}$$

Inserting these expressions into equations (2.33) and dropping all higher order terms gives a set of equations that can be solved to yield

$$f^+(x) = e^{-(1-rv)x}\left(1 + s\left[\frac{1+rv^2}{(1-rv)^2}x - \frac{1+rv^2}{2(1-rv)}x^2\right]\right) + O(s^2) \tag{2.42}$$

$$f^-(x) = ve^{-(1-rv)x}\left(1 + s\left[\frac{1+v}{(1-rv)^2} + \frac{-v+rv+2rv^2}{(1-rv)^2}x - \frac{1+rv^2}{2(1-rv)}x^2\right]\right) + O(s^2). \tag{2.43}$$

Both solutions will become negative for large values of x. However, even though this is decidedly unphysical, we expect the effect on measurable parameters such as the average microtubule length to be small, because of the rapid decay of $|f^+(x)|$ and $|f^-(x)|$. The properties of the resulting distributions, such as the average length, will therefore still remain valid.

The first-order distributions in s satisfy the total microtubule number constraint $\int_0^\infty [f^+(x) + f^-(x)] \mathrm{d}x = (1+v)/(1-rv) + O(s^2)$, consistent with the general result (2.39). For the average length we obtain (to first order in s)

$$< x > = \frac{1}{1-rv} - s\frac{1+v}{(1-rv)^4} + O(s^2).\qquad(2.44)$$

For $r = 0$, this result is consistent with the exact result that is derived below (section 2.2.3). Finally, we also determine the variation

$$\sigma_x^2 = <(x-<x>)^2> = \frac{1}{(1-rv)^2} - k\frac{2(2+v+rv^2)}{(1-rv)^5} + O(s^2)\qquad(2.45)$$

and, from that, the coefficient of variation ($\sigma_x/<x>$)

$$\sigma_x/<x> = 1 - k\frac{1+rv^2}{(1-rv)^3} + O(s^2).\qquad(2.46)$$

This number provides a measure for the relative width of the distribution. From the results (2.44) and (2.46) we conclude that severing decreases both the width and the relative width of the length distribution.

RANGE OF VALIDITY

The results above have been obtained under the assumption that s is very small. To make an *a priori* estimate for the validity range of s, we estimate the relative importance of the terms on the right-hand side in equations (2.33a) and (2.33b). Using the results in the absence of severing as a benchmark, the terms *not* involving s give contributions of the order $(1-rv)e^{-(1-rv)x}$. Comparing the integral term (evaluated for the $s = 0$ situation) with this term gives $s \ll (1-rv)^2$. The term that is proportional to sx will dominate the other terms for large x, but this does not significantly affect the results if it only occurs for lengths that are much longer than the average length. Evaluating the terms at $x = n/(1-rv)$, where n is the number of average lengths, we obtain the constraint $s \ll (1-rv)^2/n$. Because n is of the order 1, we simply state that the approximation is accurate for

$$s \ll (1-rv)^2.\qquad(2.47)$$

2.2.3   In the absence of rescues

In the limit $r = 0$ (no rescues), equation (2.33a) for $f^+(x)$ decouples from (2.33b) and can be solved analytically. This solution can then be used to obtain an expression for

$f^-(x)$. We introduce the primitive functions $F^\pm(x) = -\int_x^\infty f^\pm(x')\mathrm{d}x'$, allowing us to rewrite equations (2.33) as

$$\partial_x(\partial_x F^+(x) + (1 + sx)F^+(x)) = 0 \tag{2.48}$$

$$\frac{\partial_x^2 F^-(x)}{v} = -\partial_x F^+(x) + sx\partial_x F^-(x) + sF^+(x) + 2sF^-(x). \tag{2.49}$$

Using the boundary conditions $F^+(0) = -1$ (from (2.39a)) and $\partial_x F^+(0) = f^+(0) = 1$ we can solve the first of these equations and obtain the solution

$$F^+(x) = -\exp\left(-x - \frac{1}{2}sx^2\right). \tag{2.50}$$

Inserting this solution into equation (2.49), it can be solved using the boundary conditions $F^-(0) = -v$ (from (2.39b)) and $\lim_{x\to\infty} F^-(0) = 0$ to give

$$F^-(x) = -v\exp\left(-x - \frac{1}{2}sv^2\right) \times$$
$$\left[1 - \sqrt{\frac{\pi}{2}}\sqrt{s(1+v)}x\exp\left(\frac{(1+s(1+v)x)^2}{2s(1+v)}\right)\left(1 - \mathrm{erf}\left(\frac{1+s(1+v)x}{\sqrt{2s(1+v)}}\right)\right)\right], \tag{2.51}$$

where $\mathrm{erf}(z)$ is the error function

$$\mathrm{erf}(z) = \frac{2}{\sqrt{\pi}}\int_0^z \mathrm{e}^{-t^2}\mathrm{d}t. \tag{2.52}$$

The expressions for $f^+(x)$ and $f^-(x)$ follow by differentiation of (2.51). The resulting distribution for $v = 1/2$ and various values of s is shown in figure 2.2.

Looking at the derivative of the combined distribution $f^+(x) + f^-(x)$, we find that for $x = 0$

$$\partial_x(f^+(x) + f^-(x))|_{x=0} = -(1+v)(1 - s(1 - 2v)). \tag{2.53}$$

The perhaps surprising implication is that if $v < 1/2$, sufficiently high severing rates can lead to a positive slope of the distribution at $x = 0$. In other words, in that case the length distribution no longer decreases monotonically with length. Finally, we compute the average microtubule length as

$$<x> = \frac{\int_0^\infty x(f^+(x) + f^-(x))\mathrm{d}x}{\int_0^\infty (f^+(x) + f^-(x))\mathrm{d}x} \tag{2.54}$$

$$= -\frac{1}{1+v}\int_0^\infty \left(F^+(x) + F^-(x)\right)\mathrm{d}x \tag{2.55}$$

$$= \frac{\sqrt{\pi}}{z}\mathrm{e}^{1/z^2}\left(1 - \mathrm{erf}\left(\frac{1}{z}\right)\right), \qquad \text{with } z = s(1+v). \tag{2.56}$$

As expected, the average length decreases with increasing severing activity. Also, this result matches with the small-s expansion (2.44).
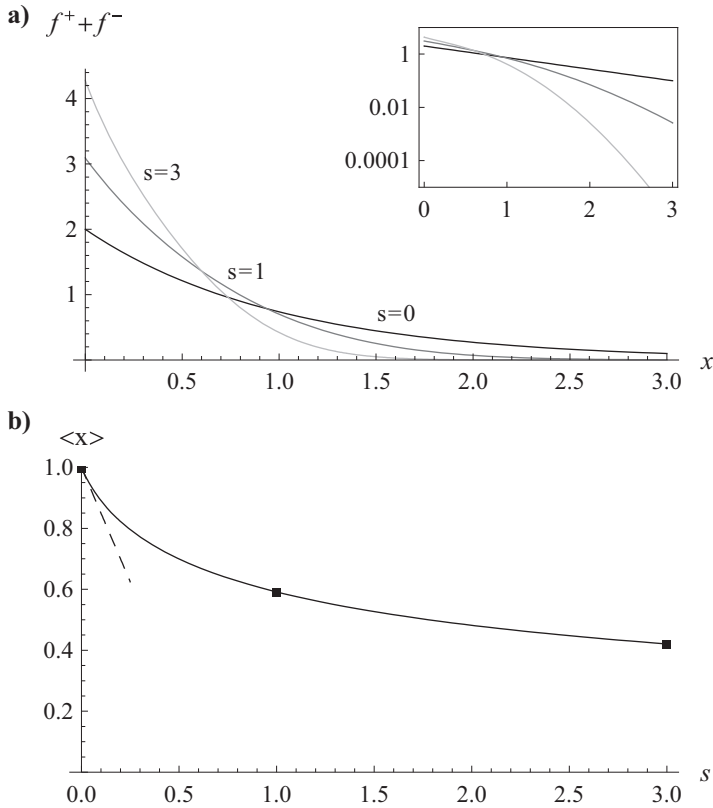
Figure 2.2: Results in the absence of rescues ($v = 1/2$, $r = 0$). **a)** Length distributions for three different values of the severing rate: $s = 0$ (black), $s = 1$ (dark gray) and $s = 3$ (light gray). The inset shows the same distributions on a logarithmic scale. **b)** Average length as a function of the severing parameter s. The squares indicate the parameter values of the distributions in (a). The dashed line is the small-s approximation (2.44). Based on the *in-vivo* measurements reported by Vos et al. (2004, interphase cells), an indicative value of $v = 1/2$ has been used for all calculations. Length distributions have been calculated from (2.50) and (2.51); the average length from (2.56).
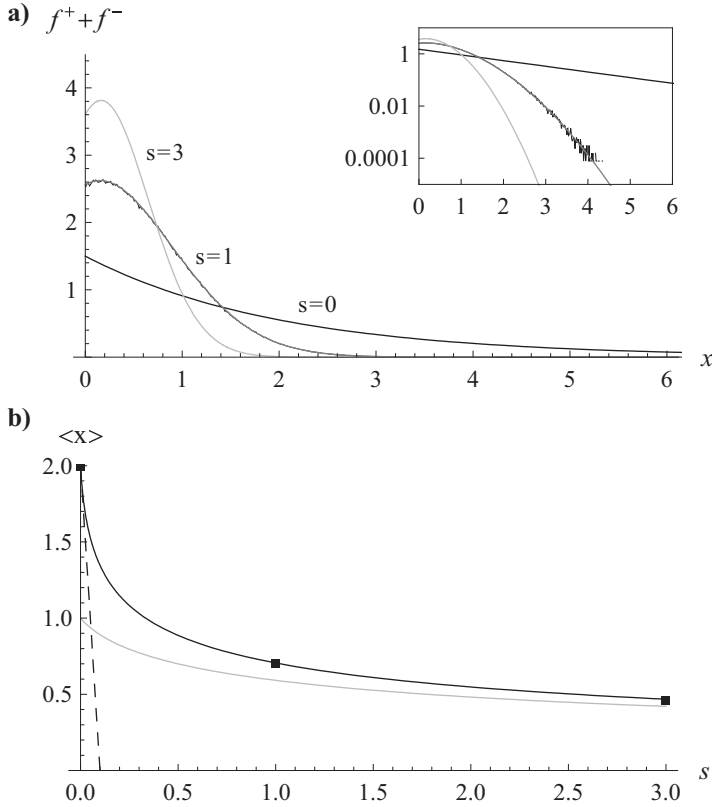
Figure 2.3: Numerically computed length distributions ($v = 1/2$, $r = 1$) and comparison with simulation data. **a)** Length distributions for three different values of the severing rate: $s = 0$ (black), $s = 1$ (dark gray) and $s = 3$ (light gray). The inset shows the same distributions on a logarithmic scale. Also shown is simulation data (see chapter 4) for $s = 1$, matching the predicted distribution. Simulation parameters were [$v^+ = 0.1\,\mu\text{m s}^{-1}$, $v^- = 0.2\,\mu\text{m s}^{-1}$, $r_c = 0.01\,\text{s}^{-1}$, $r_r = 0.01\,\text{s}^{-1}$, $r_n = 10\,\text{s}^{-1}$, $r_s = 0.001\,\mu\text{m}^{-1}\text{s}^{-1}$]. Length data was distributed into 500 bins and sampled 1000 times at 50 second intervals after an initial equilibration period of 50,000 seconds. **b)** Average length as a function of the severing parameter s. The squares indicate the parameter values of the distributions in (a). The dashed line is the small-s approximation (2.44) The light gray curve, which converges for large s, is the result for $r = 0$ (figure 2.2). Based on the *in-vivo* measurements reported by Vos et al. (2004, interphase cells), an approximate value of $v = v^+/v^- = 1/2$ has been used for all graphs. Length distributions have been calculated from (2.63).

2.2.4   Numerical evaluation of the length distribution

In order to numerically solve the distributions for arbitrary parameters, we introduce
a different parametrization. Inspired by the results (2.37) and (2.39) we define

$$p(x) \;=\; f^+(x) + f^-(x) \tag{2.57}$$
$$q(x) \;=\; v f^+(x) - f^-(x). \tag{2.58}$$

Hence, $p(x)$ is a (dimensionless) measure of the total microtubule density and $q(x)$
is proportional to the imbalance between polymerization and depolymerization of
the microtubules with a given length x. In the steady state, such an imbalance can
be produced only by severing (otherwise, $q(x) = 0$), causing microtubules to 'jump'
from one location in the distribution to another, and $q(x)$ must satisfy $\int_0^\infty q(x) = 0$.
In terms of $p(x)$ and $q(x)$, the steady state equations (2.33) are written as

$$\partial_x q(x) \;=\; sv\left[-x p(x) + 2\int_x^\infty p(x')\mathrm{d}x' \right] \tag{2.59}$$
$$\partial_x p(x) \;=\; -(1 - rv)p(x) - (1 + r)q(x) - s(1 - v)x p(x) - sx q(x) +$$
$$s\int_x^\infty \left[q(x') + (1 - 2v)p(x') \right]\mathrm{d}x' \tag{2.60}$$

Equation (2.59) can be formally solved to give

$$q(x) = sv\int_x^\infty \left[x' p(x') - 2\int_{x'}^\infty p(x'')\mathrm{d}x'' \right]\mathrm{d}x' \tag{2.61}$$
$$= sv\int_x^\infty \left[(2x - x')p(x') \right]\mathrm{d}x'. \tag{2.62}$$

By inserting this equation in equation (2.60), we transform the problem into a single
integral equation. We can subsequently remove the integrals by differentiating three
times and obtain the linear fourth-order ODE

$$p^{(4)}(x) = (-1 + rv - s(1 - v)x)p^{(3)}(x) + s(-4 + v(5 + x(1 + r + sx)))p^{(2)}(x) +$$
$$4sv(1 + r + 2sx)p^{(1)}(x) + 12vs^2 p(x), \tag{2.63}$$

where $p^{(n)}(x)$ stands for $(\mathrm{d}/\mathrm{d}x)^n p(x)$. To derive the boundary conditions for this
problem we will make use of (2.39) and (2.30), from which we can derive

$$\int_0^\infty p(x)\mathrm{d}x = \frac{1 + v}{1 - rv}, \tag{2.64}$$

$$\int_0^\infty q(x)\mathrm{d}x = 0, \tag{2.65}$$

$$q(0) = -p(0) + 1 + v. \tag{2.66}$$

By repeated application of these equalities and differentiation of equations (2.59) and (2.60) we obtain the boundary conditions

$$p^{(1)}(0) = (1+v)r\,p(0) - (1+v)(1+r) + s(1+v)\left(\frac{1-2v}{1-rv}\right) \tag{2.67}$$

$$p^{(2)}(0) = [-r(1+v)(1-rv) + 3sv]\,p(0) + (1+v)\left[(1+r)(1-rv) - s\left(\frac{3-rv+2rv^2}{1-rv}\right)\right] \tag{2.68}$$

$$p^{(3)}(0) = r(1+v)\left[(1-rv)^2 + sr(-3+7v)\right]p(0) - (1+v)(1+r)(1-rv)^2 +$$
$$s(1+v)\left[6+3r-4v-5rv+2rv^2\right] - s^2\left(\frac{1+v}{1-rv}\right)(3-4v+8v^2) \tag{2.69}$$

We note that these boundary equations are of the form

$$\begin{pmatrix} p(0) \\ p^{(1)}(0) \\ p^{(2)}(0) \\ p^{(3)}(0) \end{pmatrix} = \mathbf{P_1}\,p(0) + \mathbf{P_2} \tag{2.70}$$

with a single undetermined parameter $p(0)$. Because equation (2.63) is a homogeneous linear ODE, we can evaluate it independently using either $\mathbf{P_1}$ or $\mathbf{P_2}$ as a boundary condition. We generally find that both solutions diverge, with opposite signs. The value of $p(0)$ can be determined from the constraint $\lim_{x\to\infty} p(x) = 0$.

To this end, both solutions should be evaluated over a range that is as high as possible, whilst maintaining a very high numerical accuracy, because the final result is obtained by subtracting the two diverging functions. In our calculations, we have evaluated the differential equation with sufficient precision to achieve an accuracy of 13 significant digits and the integration range was limited to a range of 10 decay lengths ($x = 10(1-rv)^{-1}$) or to the point at which the first solution exceeded the value 10^8.

Figure 2.3 shows the numerically computed distributions for $v = 1/2$, $r = 1$ and various values of s. It is interesting to note the total distribution is no longer monotonically decreasing for $s = 1$ and higher. Figure 2.4 shows that this is solely due to the contribution from the growing microtubules. We also note that the average length decreases rapidly for relatively small severing rates. As the severing rate increases, the average length converges to that of the system without rescue events ($r = 0$). In other words, if severing events occur very frequently, rescue events are no longer significant, presumably because the microtubule become so short that they disappear before they can be rescued. This statement is summarized by the condition $1/r_r \gg \langle l \rangle / v^-$, where $\langle l \rangle$ is the average length of the microtubules, or in dimensionless units $rv\langle x \rangle \ll 1$.
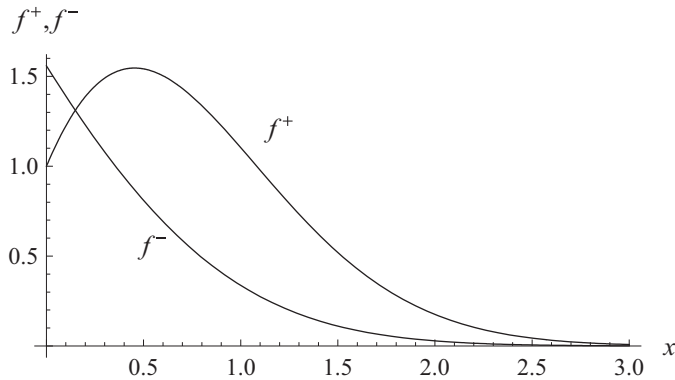
Figure 2.4: Length distributions for growing and shrinking microtubules separately ($v = 1/2$, $r = 1$, $s = 1$). The total distribution function $p(x) = f^+(x) + f^-(x)$ has been computed numerically using (2.63); $f^+(x)$ and $f^-(x)$ have been computed using (2.62) and (2.58).

2.3   Discussion

In this chapter we have constructed a model that describes the dynamic instability of microtubules in combination with their severing. This model takes the form of two coupled integro-differential equations that are a function of three parameters: v, the ratio of polymerization and depolymerization speeds, r, the ratio of the rescue and catastrophe rates, and the dimensionless severing rate s. We have analyzed these equations, searching for steady state solutions and their properties: notably the number of microtubules and their average length. For the special cases of small severing rates ($s \ll (1 - rv)^2$) and the case without rescues ($r = 0$), we have presented analytical solutions. The generic case has been addressed by transforming the coupled integro-differential equations into a single fourth order differential equation that can be solved numerically. The resulting microtubule length distributions have a number of interesting properties.

COMPACT LENGTH DISTRIBUTION

As was to be expected, an increase in the severing rate always leads to a shortening of the average length of the microtubules. In addition, we have found that the distributions became more compact, meaning that the microtubules become more similar in length. This can be appreciated from the fact that the rate of severing is proportional to the length of each microtubule, so the number of long microtubules is strongly reduced. Furthermore, in contrast to the dynamic instability model without severing, the length distributions are no longer always monotonically decreasing with increasing length. A 'bump' can sometimes be created in the length distribution of

growing microtubules, originating in the steady supply of short growing microtubules that are created by severing events. If these microtubules do not rapidly undergo a catastrophe, the continuous 'nucleation' profile can lead to an increasing number density as a function of x.

CONSERVATION OF MICROTUBULE NUMBER

Finally, we have shown that the total number of microtubules does not depend on the severing rate, even though the average length of each microtubule decreases. For a system without severing in the steady state, the following relation holds: population size = nucleation rate × average lifetime. Obviously, the shorter microtubules that are created through severing have a shorter expected lifetime, however, this effect is apparently compensated *exactly* by the fact that every severing event 'nucleates' an extra microtubule. For this cancelation to occur, the sum of the two fragments of a severed microtubule should equal the expected lifetime of the microtubule if severing had not occurred.
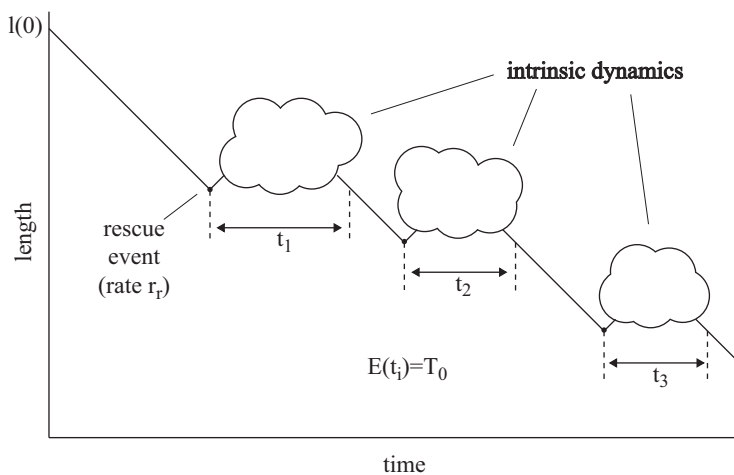
Figure 2.5: Schematic depiction of the life history of a shrinking microtubule with an initial length $l(0)$.

That this is indeed the case can be shown using a simple argument. First, we know that the dynamics of the microtubule tip are independent of its length. This implies that the average time it takes for a growing microtubule of length l to return to the same length in the form of a shrinking microtubule is independent of the value of l, and therefore equal to the average microtubule lifetime T_0 (obtained by starting from $l = 0$). The remaining contribution to the lifetime is given by the time it takes for the shrinking microtubule of length l to disappear. In the absence of rescue events, this takes a time l/v^-. However, each rescue event switches the microtubule back

to the growing state, extending the microtubule's expected lifetime by T_0 before it returns to the same position in the shrinking state. The expected number of such rescue events is therefore equal to $r_r l / v^-$. This argument is illustrated in figure 2.5. Putting the pieces together, we obtain the following expression for the microtubule lifetime $T(l, \sigma)$ of a microtubule of length l and state $\sigma \in -, +$:

$$T(l, \sigma) = T_0 \delta_{\sigma, +} + \frac{l}{v^-} (1 + r_r T_0).$$ (2.71)

The same relation, including an expression for T_0, has been derived analytically by Bicout (1997). This expression for the microtubule lifetime proves that the severing of a microtubule into two fragments with the same total length therefore indeed leaves the sum of the lifetimes intact, assuming that the 'trailing' fragment immediately undergoes a catastrophe.

It is important to note that this argument holds regardless of the frequency and location of severing events. This implies that any distribution of severing events – provided they lead to a catastrophe of the trailing end – conserves the total number of microtubules. Specifically, this also applies to severing at the position where microtubules of different orientations cross (Wightman and Turner, 2007). In chapter 4 we will investigate the effects of both random severing and severing at intersections on the ability of the cortical microtubules to align.

The conservation of microtubule number in the presence of severing is in apparent contradiction with the experimentally reported increase in microtubule numbers (Roll-Mecak and Vale, 2006). However, this is readily explained by the fact that our result is based on constant parameter values. In a living cell, the decrease in average microtubule length that is the result of severing will lead to an increased availability of free tubulin dimers. In turn, this is likely to increase the polymerization rate (growth speed) and nucleation rate, both of which indeed cause an increase in the number of microtubules.

TREADMILLING

The model as described in this chapter has not explicitly taken into account the depolymerization of microtubules at their minus ends that leads to treadmilling. However, this case is easily addressed through a renormalization of the growth and shrinkage speeds. Denoting the shrinkage speed at the minus end by v^{tm}, this is achieved by the substitutions $v^+ \to v^+ - v^{tm}$ and $v^- \to v^- + v^{tm}$. Qualitatively, none of the results in this chapter are affected by this change.

Unfortunately, a quantitative comparison of the results from this chapter with experimental observations is not possible, as we are not aware of experiments in which the required parameters have been observed. However, using known values for the dynamic instability parameters we can estimate which values of the severing rate are significant. From the data summarized by Vos et al. (2004), we find that $s = 1$ corresponds to dimensional values in the range $r_s = r_c^2 / v^+ = 3 \cdot 10^{-4} \mu m^{-1} s^{-1}$ to $3 \cdot 10^{-2} \mu m^{-1} s^{-1}$.

3

A model for the alignment of cortical microtubules

In the previous chapter, we treated the microtubules in isolation, investigating the effects of severing in combination with the intrinsic microtubule dynamics. However, in the plant cell cortex, the microtubules also interact with one another. Their non-trivial interactions are thought to be essential for the alignment of the microtubules within the cortical array (Dixit and Cyr, 2004). In this chapter we will model the collective dynamics of cortical microtubules in order to gain a deeper understanding of the factors responsible for microtubule alignment.

In vivo imaging of microtubules labelled with fluorescent proteins in plant cells by several groups has shown how the cortical array is established both following cell division and after microtubule depolymerizing drug (oryzalin) treatment (Wasteneys and Williamson, 1989; Kumagai et al., 2001; Shaw et al., 2003; Vos et al., 2003; Paradez et al., 2006; Ehrhardt and Shaw, 2006). In these studies microtubules are seen to nucleate at the cortex and then develop from an initially disorganized state into the transverse ordered array over a time period on the order of one hour. The nature of the self-organization process by which the specific spatial and orientational patterning of this cytoskeletal structure is achieved is as yet only partially understood and forms the subject of this chapter.

An important aspect of the problem is the nature of localization of the micro-tubules to the cortical region. Fluorescence recovery after photo-bleaching (FRAP) experiments by Shaw et al. (2003) showed that the microtubules are fixed in space, so any apparent mobility of microtubules is due to 'treadmilling', the process of simulta-neous polymerization at one end and depolymerization at the other end. Therefore, cortical microtubules do not translate or rotate as a whole. The same authors also did not detect detachment or (re)attachment of microtubules to the cell cortex, apart from some growing ends of single microtubules moving out of focus and found no evidence for motors working in the cortical array. These experiments indicate that the microtubules in the cortical array are fixed to the inside of the cell membrane.

Electron microscopy has also shown cross-bridges between cortical microtubules and the membrane (Hardham and Gunning, 1978; Barton et al., 2008). It is therefore widely assumed that there exist linker proteins that anchor the microtubules through the plasma membrane to the rigid cell wall, although their molecular identity is under debate (Dhonukshe and Gadella, 2003; Gardiner et al., 2001; Hashimoto and Kato, 2006; Hamada, 2007; Kirik et al., 2007). Since the cortical microtubules are thus effectively confined to a 2D surface, they can interact through 'collisions' that occur when the polymerizing tip of a growing microtubule encounters an pre-existing microtubule. The resulting dynamical interaction events were first characterized by Dixit and Cyr (2004) in tobacco Bright Yellow-2 (BY-2) cells. They observed three different possible outcomes: (i) *zippering*: a growing microtubule bending towards the direction of the microtubule encountered, which occurs only when the angle of incidence is relatively small ($\lesssim 40°$) (ii) *induced catastrophe*: an initially growing microtubule switching to a shrinking state and retracting after the collision, an effect predominant at larger angles of incidence and (iii) *cross-over*: a growing microtubule 'slipping over' the other and continuing to grow in its original direction.

There are clearly many coupled mechanisms at work, contributing to the assembly and maintenance of this microtubule cortical array structure. We are interested in understanding what are the main contributing factors and how their interplay leads to the observed orientational ordering. With this aim we develop a coarse-grained model, incorporating all the effects discussed above. Our emphasis on the plant-specific biological mechanism of the ordering in the cortical array distinguishes our approach from earlier work.

Over the years, various models for self-organization of cytoskeletal filaments (and polar rods in general) have been proposed (Geigant et al., 1998; Kruse et al., 2005; Aranson and Tsimring, 2006; Rühle et al., 2008), and the model by Zumdieck et al. (2005) was applied to the plant cortex. However, in each of these models the filaments are assumed to have rotational and, in most cases, translational freedom. This is inconsistent with the experimental finding that the plant cortical microtubules are stably anchored. Inspired by the experimental results of Dixit and Cyr (2004), Baulin et al. (2007) were the first to report on a two dimensional dynamical system of treadmilling and colliding microtubules. Their focus was on establishing the minimal interactions needed to generate dynamical alignment. Using stochastic simulations they showed that a pausing mechanism, whereby a growing microtubule stalls against another microtubule until the latter moves away, can indeed lead to ordering. Stalling, however, is not often observed in the cortical array. Moreover their model lacks dynamic instabilities, i.e. catastrophes, both spontaneous and induced, and rescues, and employs a form of deterministic microtubule motion, which is arguably unrealistic in view of the observed dynamics.

The outline of the chapter is as follows. In the following section we formulate our course-grained model starting from a description of the dynamics of individual microtubules. We then construct the continuity equations that couple the densities of growing, shrinking and inactive microtubule segments due to the intrinsic and collisional dynamics. In the steady state we can reduce the initial set of equations to

four coupled non-linear integral relations. We then perform a dimensional analysis to identify the relevant control parameter of the system. We also discuss the collisional interactions in the light of the experimental data. In section 3.2 we present the results of our model. We first solve the model analytically in the isotropic stationary state. Using a bifurcation analysis we then determine the critical values of the control parameter at which the system develops ordered solutions. We interpret these results in terms of the physical parameters of microtubule segment length and mesh size. Finally, we formulate a minimal model with realistic interaction parameters that we can solve numerically to obtain all stationary ordered solutions. In addition, we investigate the potential stabilizing effect of a finite amount of tubulin. The results and their consequences are summarized in the discussion section.

3.1 Model

3.1.1 Description of individual microtubules

As described in the introduction we confine the configuration of the microtubules to a 2D plane. Since collision-induced zippering events can cause microtubules to bend along the direction of pre-existing ones, we divide each microtubule into distinct segments with a fixed orientation. We treat these segments as straight rigid rods. This is justifiable since the persistence length l_p of microtubules is long ($\sim$ mm) compared to the average length of a microtubule ($\sim 10\mu$m) and, as mentioned above, adhesion to the plasma membrane further inhibits thermal motion.

Microtubules are known to be dynamic in that they are continually growing or shrinking by (de)polymerization. We use the standard two-state dynamic instability model of Dogterom and Leibler (1993), which assumes that every microtubule has a 'plus' end, located on the final segment of each microtubule, which is either growing (labelled by +) with speed v^+ or shrinking (labelled by −) with speed v^-. This plus end can switch stochastically from growing to shrinking (a so-called 'catastrophe') with rate r_c, or from shrinking to growing (a so-called 'rescue') with rate r_r in a process known as dynamic instability.

We model the creation of new microtubules with a constant, homogeneous, isotropic nucleation rate r_n in the plane of the 2D model. *In vivo* nucleation appears to occur at the cortex and has been observed to occur in random orientations unattached to pre-existing microtubules (Shaw et al., 2003). Although microtubules have also been observed to also nucleate from γ-tubulin complexes binding to pre-existing microtubules (Murata et al., 2005; Murata and Hasebe, 2007; Ehrhardt and Shaw, 2006) we ignore this possibility for simplicity's sake. By the same token we disregard the possibility of the shrinking of microtubules at their less active 'minus' end, leading to motion through the 'treadmilling' mechanism (Margolis and Wilson, 1998). The initial segment of each microtubule therefore remains attached to the nucleation point in our model.

We call the final segment of a microtubule, which contains the growing or shrink-
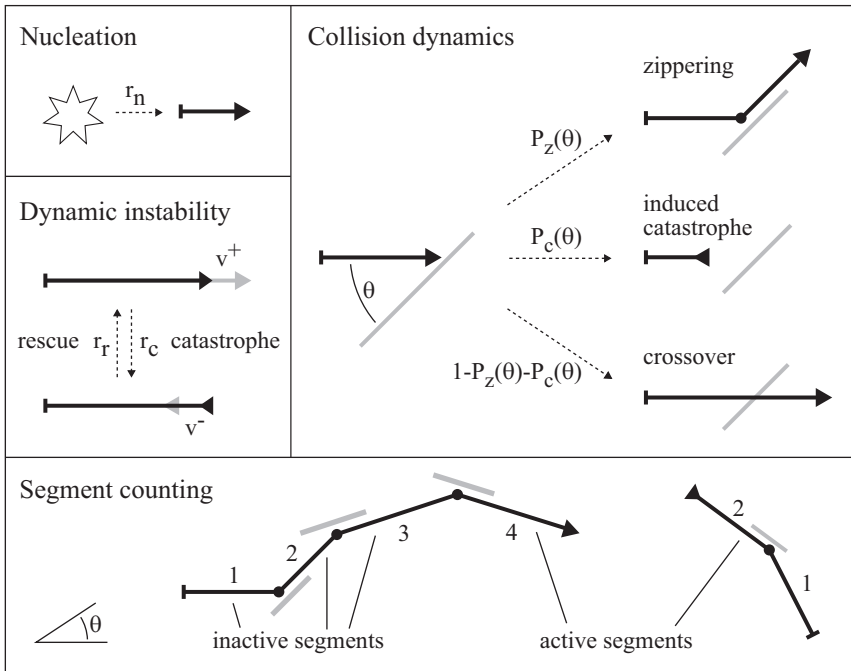
Figure 3.1: Schematic representation of the model interaction. The microtubule of interest is drawn in black and other microtubules that it encounters are in grey. The active segments of the black microtubule have an arrow head indicating growth or shrinkage whereas inactive segments end in the junction with the following segment depicted by a dot. See also the description of the parameters in table 3.1.

ing tip *active* and all the remaining ones, that do not change their length, *inactive* (labelled by 0). A cartoon of an individual microtubule according to these definitions is depicted in figure 3.1. When a microtubule collides with another microtubule and experiences a zippering event, its active segment is converted into an inactive segment, and a new active segment is created alongside the encountered microtubule. The inverse can also occur: if the active segment shrinks to zero length, a previously inactive segment in another direction can be reactivated. An induced catastrophe event simply causes the growing active segment to become a shrinking one, as is the case for spontaneous catastrophes. Finally, a crossover results in the growing active segment continuing to grow unperturbed.

In figure 3.2 we present the relative probabilities for zippering, induced catastrophes and crossovers as a result of collisions between microtubules, based on the data provided by Dixit and Cyr (2004). We assume that there are no microtubule

polarity effects, as they were not reported. The probabilities $P_z(\theta - \theta')$, $P_x(\theta - \theta')$ and $P_c(\theta - \theta')$ for zippering, cross-overs and induced catastrophes respectively are therefore even functions of the angle difference $\theta - \theta'$ defined by their values on the interval $[0, \frac{\pi}{2}]$. In this article we will use only the following minimal set of properties, which are qualitatively supported by the data. Firstly, zippering becomes less likely for increasing angle of incidence, and is effectively zero at $\theta - \theta' = \frac{\pi}{2}$, which is reasonable as the energy associated with bending the microtubule increases with angle. Secondly, the probability for induced catastrophes monotonically increases with increasing angle of incidence, reaching a maximum at $\theta - \theta' = \frac{\pi}{2}$, consistent with observations that indicate that a microtubule which is hindered in its growth will undergo a catastrophe at a rate that depends inversely on its growth speed (Janson et al., 2003).

3.1.2   Continuum model

Since there are many ($\approx 10^2$ - 10^3) microtubules, each of which can have multiple segments, in the cortical array of a typical interphase plant cell we treat the system using a coarse-grained description. In this approach, instead of individual microtubules, we consider local densities of microtubule segments. This approximation is reasonable as long as the length scale of an individual microtubule segment is small compared to the linear dimensions of the cell. From the outset we assume that the system is (and remains) spatially homogeneous. In order to deal with the memory effect caused by the isotropic nucleation, followed by subsequent reorienting zippering events, we need to keep track of the segment number i, which starts at 1 for the segments connected to their nucleation site and increases by unity at each zippering event. Our fundamental variables are thus the areal number densities $m_i^\sigma(l, \theta, t)$ of segments in state $\sigma \in \{0, -, +\}$ with segment number i having length l and orientation θ (measured from the long axis of the cell) at time t. These densities obey a set of evolution equations that can symbolically be written as

$$\partial_t m_i^+(l_i, \theta_i, t) = \Phi_{growth} + \Phi_{rescue} - \Phi_{spont.\ cat.} - \Phi_{induced\ cat.} - \Phi_{zipper} \tag{3.1a}$$

$$\partial_t m_i^-(l_i, \theta_i, t) = \Phi_{shrinkage} - \Phi_{rescue} + \Phi_{spont.\ cat.} + \Phi_{induced\ cat.} + \Phi_{reactivation} \tag{3.1b}$$

$$\partial_t m_i^0(l_i, \theta_i, t) = \Phi_{zipper} - \Phi_{reactivation} \tag{3.1c}$$

The flux terms Φ_{event} couple the equations for the growing, shrinking and inactive segments and between different values of i. Equations (3.1) must be supplemented by a set of boundary conditions for the growing segments at $l = 0$. For the initial segment ($i = 1$) this reflects the isotropic nucleation of new microtubules, given by

$$v^+ m_1^+(l_1 = 0, \theta, t) = \frac{r_n}{2\pi}, \tag{3.2}$$

where r_n is nucleation rate. For the subsequent segments $i > 1$, this 'nucleation' of growing segments is the result of the zippering of segments with index $i - 1$. Defining $\varphi_{zipper}(\theta_{i-1} \to \theta_i, l_{i-1}, t)$ as the flux of i-segments with angle θ_i and length

l_i zippering into angle θ_{i+1} at time t (this will be made explicit in equation (3.13)), we obtain the boundary condition

$$v^+ m^+_{i \geq 2}(l_i = 0, \theta_i, t) = \int \mathrm{d}l_{i-1} \int \mathrm{d}\theta_{i-1}\, \varphi_{\text{zipper}}(\theta_{i-1} \to \theta_i, l_{i-1}, t)\,. \qquad (3.3)$$

Generally, this leads to a qualitatively different boundary condition for every value of i. The model therefore consists of an infinite set of coupled equations, three for every value of i. However, in section 3.1.3 we will show that in the steady state, this can be reduced to a finite set by summing over all segment indices i. In the following, we derive explicit expressions for each of the flux terms Φ_{event}.

GROWTH AND SHRINKAGE TERMS: $\Phi_{\text{GROWTH}}, \Phi_{\text{SHRINKAGE}}$

Φ_{growth} in Equation (3.1a) corresponds to the length increase of the growing segments. For segment growth in isolation, the length increase in a small time interval δt is given by $v^+ \delta t$, where v^+ is the growth velocity, and we have $m^+(l + v^+ \delta t, \theta, t + \delta t) = m^+(l, \theta, t)$. By expanding the left hand term to first order in δt, we find

$$\partial_t m^+_i(l, \theta, t) = -v^+ \partial_l m^+_i(l, \theta, t) \equiv \Phi_{growth} \qquad (3.4)$$

A similar derivation yields that

$$\partial_t m^-_i(l, \theta, t) = v^- \partial_l m^-_i(l, \theta, t) \equiv \Phi_{shrink} \qquad (3.5)$$

where v^- is the shrinking velocity.

DYNAMIC INSTABILITY TERMS: $\Phi_{\text{RESCUE}}, \Phi_{\text{SPONT. CAT.}}$

Φ_{rescue} and $\Phi_{spont. cat.}$ in equations (3.1a) and (3.1b) correspond to the fluxes due to the spontaneous rescues and spontaneous catastrophe, respectively, and are simply given by

$$\Phi_{rescue} = r_r m^-_i(l_i, \theta_i, t) \qquad (3.6)$$
$$\Phi_{spont.\ cat.} = r_c m^+_i(l_i, \theta_i, t) \qquad (3.7)$$

where r_r is the spontaneous rescue rate and r_c is the spontaneous catastrophe rate.

So far, we have described the first three terms of equations (3.1a) and (3.1b) (growth, shrinkage and dynamic instability terms). Together, these fully describe a system of non-interacting microtubules, in which also the boundary condition (3.3) vanishes due to the absence of zippering. In this special case we recover the well-known equations introduced by Dogterom and Leibler (1993) (for $i = 1$).

INTERACTION TERMS: $\Phi_{\text{INDUCED CAT.}}, \Phi_{\text{ZIPPER}}$

An interaction can occur when a growing active microtubule segment collides with another segment, irrespective of the latter's state and length. This prompts the

definition of the total length density $k(\theta, t)$ of all microtubule segments in direction θ at time t, given by:

$$k(\theta, t) = \sum_i \int dl_i \, l_i \, (m_i^+(l_i, \theta, t) + m_i^-(l_i, \theta, t) + m_i^0(l_i, \theta, t)). \tag{3.8}$$

The density of collisions of a microtubule segment growing in direction θ with other segments in direction θ' is determined by the geometrical projection

$$\left|\sin\left(\theta - \theta'\right)\right| k(\theta', t), \tag{3.9}$$

where the presence of the $\sin\left(\theta - \theta'\right)$ factor ensures the correct geometrical weighting reflecting the fact that parallel segments do not collide. When a collision occurs, one of the three possible events, induced catastrophe (c), zippering (z) or crossover (x) occurs, with probabilities $P_c\left(\theta - \theta'\right)$, $P_z\left(\theta - \theta'\right)$ and $P_x\left(\theta - \theta'\right)$ respectively. These probabilities can (and *in-vivo* do, see figure 3.2) depend on the relative angle $\theta - \theta'$ between the incoming segment and the 'scatterer'. For convenience sake we will absorb the geometrical factor $\left|\sin\left(\theta - \theta'\right)\right|$ into the probabilities, by defining $f\left(\theta - \theta'\right) = \left|\sin\left(\theta - \theta'\right)\right| P_f\left(\theta - \theta'\right)$ for all events $f \in \{c, z, x\}$. The incoming flux of growing microtubule segments with given segment number, length and orientation is given by $v^+ m_i^+(l, \theta, t)$. With these definitions we can write the interaction terms as

$$\Phi_{\text{induced cat.}} = v^+ m_i^+(l_i, \theta_i, t) \int d\theta' \, c(\theta_i - \theta') k(\theta', t) \tag{3.10}$$

$$\Phi_{\text{zipper}} = v^+ m_i^+(l_i, \theta_i, t) \int d\theta' \, z(\theta_i - \theta') k(\theta', t) \tag{3.11}$$

The analogous term for crossovers is not used, because the occurrence of a crossover event has no effect on the growth of a microtubule.

REACTIVATION TERM: $\Phi_{\text{REACTIVATION}}$

The reactivation term $\Phi_{\text{reactivation}}$ corresponds to the flux of active microtubule segments, with segment number $i + 1$, that, by shrinking to length zero, reactivate a previously inactive segment, effectively undoing a past zippering event and so create a new, shrinking, active segment with segment number i. The incoming flux of such segments coming from a given direction θ_{i+1} is given by $v^- m_{i+1}^-(l_{i+1} = 0, \theta_{i+1}, t)$. The reactivation flux is given by

$$\Phi_{\text{reactivation}} = \int d\theta_{i+1} \, v^- m_{i+1}^-(l_{i+1} = 0, \theta_{i+1}, t) \, p_{\text{unzip}}(\theta_i, l_i | \theta_{i+1}, t), \tag{3.12}$$

where the 'unzippering' distribution $p_{\text{unzip}}(\theta_i, l_i | \theta_{i+1}, t)$ gives the probability that the shrinking microtubule reactivates an inactive segment with orientation θ_i and length l_i. This distribution will be determined below.

A microtubule that has zippered will take a certain amount of time τ to undergo a catastrophe and return to the zippering location, where τ is a stochastic variable.
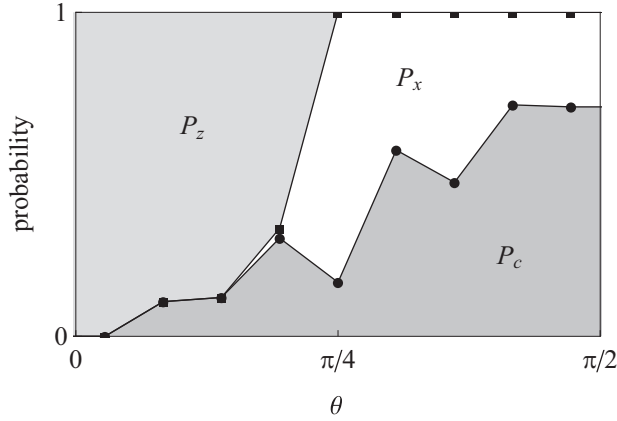
Figure 3.2: *In vivo* microtubule collision data from Dixit and Cyr (2004) (combined data from MBD-DsRed and YFP-TUA6 labelling), where $P_c(\theta)$, $P_z(\theta)$ and $P_x(\theta)$ are plotted on a cumulative scale. Every data point is located at the center of the corresponding bin, and the shaded regions have been extended to the boundaries using horizontal lines. The corresponding Fourier coefficients of the interaction functions are: $\hat{c}_0 = 0.59$, $\hat{c}_2 = -0.36$, $\hat{z}_0 = 0.24$ (computed using numerical integration of the product of $|\sin(\theta)|$ and a piecewise linear interpolation of the data).

The unzipppering flux from direction θ_{i+1} at time t consists of microtubules that had zippered at a range of times $t - \tau$ and have now returned to the zippering location. This implicitly defines an *originating time* distribution $p_{\text{origin}}(t - \tau | \theta_{i+1}, t)$ for the returning microtubules. Furthermore, because the evolution of a microtubule between the zippering event and its return to the same location does not depend on the previous segments, the segment that is re-activated by a microtubule returning to the zippering position after a time τ should be selected proportional to the 'forward' zippering flux at time $t - \tau$. The forward flux $\varphi_{\text{zipper}}(\theta_i \to \theta_{i+1}, l_i, t)$ of microtubules with length l_i and angle θ_i zippering into angle θ_{i+1} is defined in accordance with equation (3.11) as

$$\varphi_{\text{zipper}}(\theta_i \to \theta_{i+1}, l_i, t) = v^+ m_i^+(l_i, \theta_i, t) z(\theta_i - \theta_{i+1}) k(\theta_{i+1}, t). \qquad (3.13)$$

At each of the originating times $t - \tau$, the distribution of microtubules that zipper into the direction θ_{i+1} with length l_i and orientation θ_i is given by

$$p_{\text{zip}}(\theta_i, l_i | \theta_{i+1}, t - \tau) = \frac{\varphi_{\text{zipper}}(\theta_i \to \theta_{i+1}, l_i, t - \tau)}{\int \mathrm{d}l' \mathrm{d}\theta' \, \varphi_{\text{zipper}}(\theta' \to \theta_{i+1}, l', t - \tau)}. \qquad (3.14)$$

The probability distributions $p_{\text{origin}}(t - \tau | \theta_{i+1}, t)$ and $p_{\text{zip}}(\theta_i, l_i | \theta_{i+1}, t - \tau)$ can be

Parameters	
v^+	growth speed
v^-	shrinkage speed
r_c	catastrophe rate
r_r	rescue rate
r_n	nucleation rate
$P_c(\theta)$	probability of induced catastrophe upon collision
$P_z(\theta)$	probability of zippering upon collision
Synthetic parameters	
$g = \frac{r_r}{v^-} - \frac{r_c}{v^+}$	growth parameter
$u = 1 + \frac{v^+}{v^-}$	speed ratio
$c(\theta) = \sin(|\theta|) \, P_c(\theta) \longleftrightarrow \{\hat{c}_n\}$	effective catastrophic collision probability
$z(\theta) = \sin(|\theta|) \, P_z(\theta) \longleftrightarrow \{\hat{z}_n\}$	effective zippering probability
Dependent variables	
$k(\theta)$	microtubule length density
$l(\theta)$	average microtubule segment length
$\{m_i^+(l,\theta), m_i^-(l,\theta), m_i^0(l,\theta)\}$	density of growing/shrinking/inactive segments with length l and direction θ

Table 3.1: Overview of all parameters and variables in natural dimensions

combined to determine the unzippering distribution

$$p_{\text{unzip}}(\theta_i, l_i | \theta_{i+1}, t) = \int_0^t \mathrm{d}\tau \, p_{\text{origin}}(t - \tau | \theta_{i+1}, t) \times \frac{\varphi_{\text{zipper}}(\theta_i \to \theta_{i+1}, l_i, t - \tau)}{\int \mathrm{d}l' \mathrm{d}\theta' \, \varphi_{\text{zipper}}(\theta' \to \theta_{i+1}, l', t - \tau)},$$
(3.15)

where we assume the system evolved from an initial condition at $t_0 = 0$ in which no microtubules were present. Clearly all the complicated history dependence of the system is hidden in the originating time distribution. However, in the steady state situation we consider below, the time-dependence drops out and the details of this distribution become irrelevant.

3.1.3 The steady state

We now consider the steady state of the system of equations we have formulated. Setting the time derivatives to zero, the sum of equations (3.1a) to (3.1c) yields $\Phi_{growth} + \Phi_{shrinkage} = 0$, which together with equation (3.4) and (3.5) implies

$$\partial_{l_i}\left(v^+ m_i^+(l_i, \theta_i) - v^- m_i^-(l_i, \theta_i)\right) = 0.$$
(3.16)

Because physically acceptable solutions should be bounded as $l_i \to \infty$, we obtain the length flux balance equation

$$v^+ m_i^+(l_i, \theta_i) = v^- m_i^-(l_i, \theta_i)$$
(3.17)

showing that the growing and shrinking segments have, up to a constant amplitude, the same orientational and length distribution. This allows us to eliminate $m_i^-(l_i, \theta_i)$ from equation (3.1a) to obtain

$$\partial_{l_i} m_i^+(l_i, \theta_i) = m_i^+(l_i, \theta_i)\left(g - \int d\theta'\, k(\theta')(c(\theta_i - \theta') + z(\theta_i - \theta'))\right) \qquad (3.18)$$

where the *growth parameter*

$$g = \frac{r_r}{v^-} - \frac{r_c}{v^+}. \qquad (3.19)$$

characterizes the behavior of the bare, non-interacting, system in which microtubules remain bounded in length for $g < 0$ and become unbounded for $g \geq 0$. As the bracketed factor on the right hand side of equation (3.18) does not depend on the segment length nor on the segment number, we immediately obtain that $m_i^+(l_i, \theta_i)$ has an exponential length distribution

$$m_i^+(l_i, \theta_i) = m_i^+(\theta_i) e^{-l_i/l(\theta_i)} \qquad (3.20)$$

where the average segment length $l(\theta_i)$ in the direction θ_i is given by

$$\frac{1}{l(\theta)} = -g + \int d\theta'\, (c(\theta - \theta') + z(\theta - \theta'))k(\theta'). \qquad (3.21)$$

The nucleation boundary conditions (3.2) and (3.3) are now transformed into the following nucleation equations, expressed in terms of the amplitudes $m_i^+(\theta_i)$

$$v^+ m_1^+(\theta) = \frac{r_n}{2\pi}, \qquad (3.22)$$

$$m_{i\geq 2}^+(\theta) = k(\theta)\int d\theta'\, z(\theta' - \theta)l(\theta')m_{i-1}^+(\theta'). \qquad (3.23)$$

We now note that under these conditions equation (3.1c) is already satisfied, as can be explicitly checked by considering $\Phi_{\text{reactivation}}$ (3.12) and using that in the steady state φ_{zipper} does not depend on time and the integral over p_{origin} is by definition equal to 1. This, in combination with the results (3.17), (3.20) and (3.23), yields the identity with Φ_{zipper}. We therefore need an independent argument to fix the densities of the inactive segments. To obtain this we use the steady state rule that population size = nucleation rate × average lifetime. Consider a newly 'born' growing segment, created either by a nucleation or a zippering event. Its average life time is by definition the average time until it shrinks back to zero length, i.e. the average return time. Clearly this time only depends on its orientation θ, the steady state microtubule length density $k(\theta')$ and the dynamical instability parameters, but not on the segment number. We therefore denote it by $\tau(\theta)$. The steady state density of inactive segments with length l_i, orientation θ and segment number i is then given by

$$m_i^0(l_i, \theta) = \int d\theta'\, \varphi_{\text{zipper}}(\theta \to \theta', l_i)\tau(\theta') \qquad (3.24)$$

$$= v^+ m_i^+(l_i, \theta)\int d\theta'\, z(\theta - \theta')k(\theta')\tau(\theta'), \qquad (3.25)$$

where φ_{zipper} is defined by equation (3.13), as inactive segments are created by a zippering event. Because the only length-dependent term on the right-hand side is $m^+(l_i, \theta)$, it follows that the length-dependence of the inactive segment distributions is proportional to those of the active segments, i.e.

$$m_i^0(l_i, \theta) = m_i^0(\theta) e^{-\frac{l_i}{l(\theta)}} \tag{3.26}$$

At the same time, the total integrated length density of segments, both active and inactive, with segment number $i+1$ in the direction θ' is given by

$$N_{i+1}^{\text{total}}(\theta') = \int dl_{i+1} \left[m_{i+1}^0(l_{i+1}, \theta') + m_{i+1}^+(l_{i+1}, \theta') + m_{i+1}^-(l_{i+1}, \theta') \right] \tag{3.27}$$

$$= \int d\theta'' \int dl_i \, \varphi_{\text{zipper}}(\theta'' \to \theta', l_i) \, \tau(\theta'), \tag{3.28}$$

where the last equality follows from the fact that every segment with index $i+1$ has been created by a zippering event of a segment with index i. We solve this for $\tau(\theta')$ and insert the result in (3.25), which, after expanding φ_{zipper} (3.13), produces the following expression for $m_i^0(\theta)$:

$$m_i^0(\theta) = m_i^+(\theta) \int d\theta' \, z(\theta - \theta') l(\theta') \frac{\{m_{i+1}^0(\theta') + m_{i+1}^+(\theta') + m_{i+1}^-(\theta')\}}{\int d\theta'' z(\theta' - \theta'') l(\theta'') m_i^+(\theta'')}. \tag{3.29}$$

We use the nucleation equation (3.23) to replace the integral in the denominator of the integrand on the right hand side of this expression. In addition, we define the quantity $Q_i(\theta)$ through

$$m_i^0(\theta) = Q_i(\theta) \left[m_i^+(\theta) + m_i^-(\theta) \right]$$

$$= \left(1 + \frac{v^+}{v^-} \right) Q_i(\theta) m_i^+(\theta)$$

$$\equiv u Q_i(\theta) m_i^+(\theta) \tag{3.30}$$

and equation (3.29) leads to the following recursion relation for $Q_i(\theta)$

$$Q_i(\theta) = \int d\theta' \, z(\theta - \theta') \, k(\theta') \, l(\theta') \left(1 + Q_{i+1}(\theta') \right). \tag{3.31}$$

We now argue that the ratio $Q_i(\theta)$ is in fact *in*dependent of the segment number. Using the fact that the growing, shrinking and inactive segments have an identical exponential profile, it follows from (3.30) that $Q_i(\theta)$ is equal to the ratio between inactive and active segments

$$Q_i(\theta) = \frac{m_i^0(\theta)}{u m_i^+(\theta)} = \frac{N_i^0(\theta)}{N_i^+(\theta) + N_i^-(\theta)}. \tag{3.32}$$

After a new microtubule segment has been created it will generally spend some time in an active state and some time in an inactive state. The expected lifetime

$\tau(\theta)$ can also be separated into the expected active and inactive lifetimes for any newly created segment: $\tau(\theta) = \tau_{\text{active}}(\theta) + \tau_{\text{inactive}}(\theta)$. These lifetimes are necessarily proportional to the total number of active and inactive segments, so that $Q_i(\theta) = \tau_{\text{inactive}}(\theta) / \tau_{\text{active}}(\theta)$. As we have argued before, these lifetimes do not depend on the segment number, and, hence, neither does $Q_i(\theta)$. An alternative route to the same conclusion follows from expanding out the forward recursion in (3.31) to show that $Q_i(\theta)$ can for every i formally be written as the same infinite series of multiple integrals involving $z(\theta - \theta')$, $k(\theta)$ and $l(\theta)$. We therefore write the self-consistency relationship

$$Q(\theta) = \int d\theta' \, z(\theta - \theta') \, k(\theta') \, l(\theta') \left(1 + Q(\theta')\right). \tag{3.33}$$

The final closure of this set of equations is provided by the definition of the length density (3.8) applied to the steady state

$$k(\theta) = \sum_i \int dl_i \, l_i \left[m_i^+(l_i, \theta) + m_i^-(l_i, \theta) + m_i^0(l_i, \theta) \right]$$

$$= u l(\theta)^2 (1 + Q(\theta)) \sum_i m_i^+(\theta). \tag{3.34}$$

3.1.4   Dimensional analysis

In order to simplify our equations for further analysis and to identify the relevant control parameter we perform a dimensional analysis. We therefore introduce a common length scale and rescale all lengths with respect to this length scale. For example, our primary variables $m_i^+(\theta)$ have dimension $[\text{length}]^{-3} [\text{radian}]^{-1}$. Taking our cue from (3.22) and (3.34) we adopt the length scale

$$l_0 = \left(\frac{1}{\pi} \frac{v^+}{u \frac{r_n}{2\pi}} \right)^{\frac{1}{3}}, \tag{3.35}$$

where the additional factor of π^{-1} within the parentheses is added to suppress explicit factors involving π in the final equations. This definition allows us to define the dimensionless variables

$$L(\theta) = l(\theta) / l_0 \tag{3.36a}$$

$$K(\theta) = \pi k(\theta) l_0 \tag{3.36b}$$

$$M_i^+(\theta) = \pi m_i^+(\theta) l_0^3 \tag{3.36c}$$

$$G = g l_0. \tag{3.36d}$$

In the absence of interactions, (3.21) shows that the average length l of the microtubule is given by $l = -1/g$. This implies $G = -l_0/l$, meaning that, for $G < 0$, G can be interpreted as a measure for the non-interacting microtubule length.

In addition, we adopt the dimensionless operator notation

$$\mathbf{F}[h](\theta) = \frac{1}{\pi} \int_0^{2\pi} d\theta'\, f\left(\theta - \theta'\right) h\left(\theta'\right), \tag{3.36e}$$

where $F \in \{C, Z\}$.

We are now in a position to express the equations in terms of the dimensionless quantities. Applying (3.36c) to the nucleation equations (3.22) and (3.23) yields

$$M_{i+1}^+(\theta) = K(\theta)\mathbf{Z}\left[LM_i^+\right](\theta) \tag{3.37}$$

$$M_1^+(\theta) = \frac{1}{u} \tag{3.38}$$

Furthermore, the $M_i^+(\theta)$ for the different segment labels can be absorbed into a single microtubule plus end density (density of active segments), given by

$$T(\theta) = uL(\theta) \sum_{i=1}^{\infty} M_i^+(\theta). \tag{3.39}$$

Performing all substitutions, the final set of dimensionless equations reads

$$\frac{1}{L(\theta)} = -G + \mathbf{C}[K](\theta) + \mathbf{Z}[K](\theta) \qquad \text{Segment length} \tag{3.40a}$$

$$K(\theta) = L(\theta)(1 + Q(\theta))T(\theta) \qquad \text{Density} \tag{3.40b}$$

$$Q(\theta) = \mathbf{Z}[LK(1 + Q)](\theta) \qquad \text{Inactive-active ratio} \tag{3.40c}$$

$$T(\theta) = L(\theta) + L(\theta)K(\theta)\mathbf{Z}[T](\theta) \qquad \text{Plus end density} \tag{3.40d}$$

with

$$G = \left(\frac{2v^+ v^-}{r_n(v^+ + v^-)}\right)^{\frac{1}{3}}\left(\frac{r_r}{v^-} - \frac{r_c}{v^+}\right) \tag{3.40e}$$

Looking at the resulting equations, we see that the segment length L is determined by the intrinsic growth dynamics (G) and the interactions leading to induced catastrophes and zippering. The segment length density K is the product of the plus end density, the ratio of all segments to active segments ($1 + Q$) and the average segment length. The ratio Q of inactive to active segments is modulated by the zippering operator, and the plus end density T consists of contributions from direct nucleation and zippered segments. We only consider parameter regions with physically realizable solutions that have real and positive values for L, K, Q and T.

Finally, we note that the interaction operators defined by (3.36e) are convolutions of the operand with the interaction functions $c(\theta)$ and $z(\theta)$. Both interaction functions are symmetric and π-periodic, and can therefore be written in terms of their

Fourier coefficients as

$$f(\theta) = \frac{\hat{f}_0}{2} + \sum_{n=1}^{\infty} \hat{f}_{2n} \cos(2n\theta) \qquad \hat{f}_{2n} = \frac{1}{\pi} \int_0^{2\pi} f(\theta) \cos(2n\theta) \, d\theta \qquad (3.41)$$

Using the identity $\cos(\theta - \theta') = \cos(\theta)\cos(\theta') + \sin(\theta)\sin(\theta')$ we find that the functions $\cos(2n\theta)$ and $\sin(2n\theta)$ are eigenfunction of the operators $\mathbf{C}$ and $\mathbf{Z}$, with the Fourier coefficients $\hat{c}_{2n}$ and $\hat{z}_{2n}$, respectively, as eigenvalues:

$$\mathbf{F}[\cos(2n\theta)] = \hat{f}_{2n} \cos(2n\theta) \qquad (3.42)$$

This convenient property will often be used in later sections.

MODIFYING THE INTERACTION STRENGTH

We note that two different systems, where the zippering and interaction function only differ by a constant scaling factor can be mapped onto the same dimensionless system. Suppose we have

$$\tilde{c}(\theta) = \alpha c(\theta) \qquad (3.43a)$$

$$\tilde{z}(\theta) = \alpha z(\theta) \qquad (3.43b)$$

Biologically speaking, for $\alpha < 1$, this corresponds to a system that has a uniformly increased probability for crossovers to occur, at the expense of zippering and induced catastrophe events. We will now see that this does not qualitatively affect the results. This can be understood by realizing that the set of equations (3.40) is invariant under the substitutions

$$\mathbf{C} \to \alpha \mathbf{C} \qquad\qquad\qquad L \to \alpha^{-1/3} L$$

$$\mathbf{Z} \to \alpha \mathbf{Z} \qquad\qquad\qquad K \to \alpha^{-2/3} K$$

$$G \to \alpha^{1/3} G \qquad\qquad\qquad T \to \alpha^{-1/3} T$$

where the first substitution reflects the presence of α in the rescaling (3.43). The existence of this scaling relation implies that all functional dependencies between any of these parameters and variables remain unchanged when subjected to the *inverse* scaling. Specifically, the relevant parameters become $\mathbf{C}/\alpha$, $\mathbf{Z}/\alpha$ and $\alpha^{-1/3} G$ and the variables $\alpha^{1/3} L$, $\alpha^{2/3} K$ and $\alpha^{1/3} T$.

   Because the qualitative aspects of the system are invariant under parameter changes that leave $\alpha^{-1/3} G$ constant, we see that a uniform change in the interaction functions can be compensated for by an appropriate scaling of the nucleation rate, the dynamic instability rates or the velocities. This relation will be exploited in chapter 4 to investigate the validity of the mean field approximation that forms the basis of our model.

   In the remainder of this chapter, we will generally omit the explicit mention of this scaling relation, effectively choosing $\alpha = 1$. However, the appropriate scaling relation is explicitly indicated on the axes of the figures with results.

3.2 Results

3.2.1 Isotropic solution

In the isotropic phase all angular dependence drops out. Because $\mathbf{C}[1](\theta) = \hat{c}_0$ and $\mathbf{Z}[1](\theta) = \hat{z}_0$ we are left with the equations

$$\frac{1}{\bar{L}} = -G + (\hat{c}_0 + \hat{z}_0) \bar{K} \tag{3.44a}$$

$$\bar{K} = \bar{L}(1 + \bar{Q})\bar{T} \tag{3.44b}$$

$$\bar{Q} = \hat{z}_0 \bar{L}\bar{K}(1 + \bar{Q}) \tag{3.44c}$$

$$\bar{T} = \bar{L} + \hat{z}_0 \bar{L}\bar{K}\bar{T} \tag{3.44d}$$

where the overbar denotes quantities evaluated in the isotropic phase. Solving for $\bar{Q}$ and $\bar{T}$ and inserting this into equation (3.44b) readily gives

$$\bar{K} = \frac{\bar{L}^2}{(1 - \hat{z}_0 \bar{L}\bar{K})^2}, \tag{3.45}$$

and it follows from equation (3.44a) that

$$\hat{c}_0 \bar{K} - G = \frac{1 - \hat{z}_0 \bar{L}\bar{K}}{\bar{L}} = \frac{1}{\sqrt{\bar{K}}}. \tag{3.46}$$

This can be combined to yield the following relation between G and the density

$$\bar{K}\left(\hat{c}_0 \bar{K} - G\right)^2 = 1 \tag{3.47}$$

We see that the isotropic density is an increasing function of the microtubule dynamics parameter G and does not depend on the amount of zippering. This can be understood by the fact that zippering only serves to reorient the microtubules, which has no net effect in the isotropic state. In the absence of induced catastrophes ($\hat{c}_0 = 0$), the density $\bar{K}$ diverges as $G \uparrow 0$, consistent with the result by Dogterom and Leibler (1993). In the presence of induced catastrophes a stationary isotropic solution exists for all values of G, although this solution need not actually be stable.

3.2.2 Bifurcation analysis

We now search for a bifurcation point by considering the existence of steady state solutions that are small perturbations away from the isotropic solution. These solutions are parameterized as follows

$$L = \bar{L}(1 + \lambda) \tag{3.48a}$$

$$K = \bar{K}(1 + \kappa) \tag{3.48b}$$

$$Q = \bar{Q}(1 + \chi) \tag{3.48c}$$

$$T = \bar{T}(1 + \tau) \tag{3.48d}$$

Inserting these expressions into (3.40), subtracting the isotropic solutions and expanding to first order in the perturbations gives

$$\lambda = -\bar{N}\left(\mathbf{C}[\kappa] + \mathbf{Z}[\kappa]\right) \tag{3.49a}$$

$$\kappa = \lambda + \tau + \hat{z}_0\bar{N}\chi \tag{3.49b}$$

$$\chi = \frac{1}{\hat{z}_0}\mathbf{Z}\left[\lambda + \kappa + \hat{z}_0\bar{N}\chi\right] \tag{3.49c}$$

$$\tau = \lambda + \bar{N}(\hat{z}_0\kappa + \mathbf{Z}[\tau]) \tag{3.49d}$$

where $\bar{N} = \bar{L}\bar{K}$. Note that in these equations, $\bar{N}$ has become the control parameter instead of G. Using equation (3.49b) and exploiting the linearity of $\mathbf{Z}$, we expand

$$\mathbf{Z}[\kappa] = \mathbf{Z}[\tau] + \mathbf{Z}\left[\lambda + \kappa + \hat{z}_0\bar{N}\chi\right] - \mathbf{Z}[\kappa] \tag{3.50}$$

$$= \frac{1}{\bar{N}}(\tau - \lambda) - \hat{z}_0\kappa + \hat{z}_0\chi - \mathbf{Z}[\kappa] \tag{3.51}$$

Solving this for $\mathbf{Z}[\kappa]$ and inserting the result into equation (3.49a), combined with (3.49b), yields the relation

$$(1 - \hat{z}_0\bar{N})\kappa = -2\bar{N}\mathbf{C}[\kappa] \tag{3.52}$$

For this equation to hold, $\kappa(\theta)$ must be an eigenfunction of $\mathbf{C}$. We know that the family of functions $\cos(2n\theta)$, $n \geq 1$, are eigenfunctions of $\mathbf{C}$ with eigenvalues $\hat{c}_{2n}$. We therefore get a set of bifurcation values of $\bar{N}$, one for each eigenvalue:

$$N_{2n}^* = (-2\hat{c}_{2n} + \hat{z}_0)^{-1}. \tag{3.53}$$

In addition, we know that the isotropic solution must be stable as $G \to -\infty$, because in this limit the microtubules have a vanishing length and do not interact. Therefore, the relevant bifurcation point is that for the lowest value of G, corresponding with the most negative eigenvalue of $\mathbf{C}$ (see also appendix 3.A). Assuming that the induced catastrophe probability increases monotonically with the collision angle, $\hat{c}_2$ is always the most negative eigenvalue, so

$$N^* = \frac{1}{-2\hat{c}_2 + \hat{z}_0}. \tag{3.54}$$

We now derive the location of this bifurcation point in terms of the control parameter G. Denoting $\bar{N} = \bar{L}\bar{K}$, equation (3.45) can be transformed to $\bar{N}(1 - \hat{z}_0\bar{N})^2 = \bar{L}^3$, into which we can substitute $G\bar{L} = (\hat{c}_0 + \hat{z}_0)\bar{N} - 1$ from equation (3.44a) and solve for G giving

$$G^3\bar{N}(1 - \hat{z}_0\bar{N})^2 = \left[(\hat{c}_0 + \hat{z}_0)\bar{N} - 1\right]^3 \tag{3.55}$$

Combining this with the result (3.54) yields

$$G^* = (-2\hat{c}_2)^{1/3}\left(\frac{\hat{c}_0}{-2\hat{c}_2} - 1\right). \tag{3.56}$$

The implication is that the location of the bifurcation point as a function of the control parameter G is determined entirely by the eigenvalues of the induced catastrophe function $c(\theta)$. Like the density in the isotropic phase, the location of the bifurcation point, this time perhaps more surprisingly, does not depend on the presence or amount of zippering.
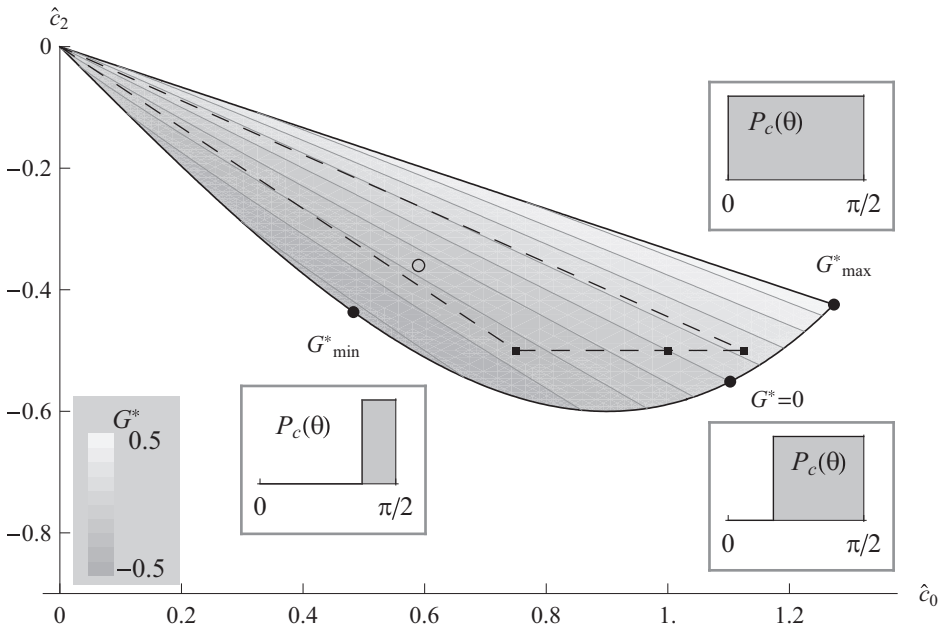

Figure 3.3: Graphical representation of the range of possible values of the Fourier coefficients $\hat{c}_0$ and $\hat{c}_2$ of the induced catastrophe function $c(\theta)$ (derived in section 3.B). The gray scale indicates the corresponding value of the bifurcation point G^*. The points for which the minimum and maximum values of G^* are attained, as well as the most extreme point for which $G^* = 0$, are indicated by solid circles. The insets depict the corresponding profiles of the induced catastrophe probability $P_c(\theta)$. The dashed triangle depicts the range of the simplified interaction functions (section 3.2.4) for $0 \leq \alpha \leq 1$. The squares indicate the parameters for which full numerical solutions are obtained (assuming $\alpha = 1$). Finally, the location of the open circle stands for the Fourier coefficients that follow from the measurements of Dixit and Cyr (2004) (see also figure 3.2). Note that it corresponds to a bifurcation for $G^* < 0$.

Figure 3.3 indicates the possible combinations of $\hat{c}_0$ and $\hat{c}_2$ (derived in section 3.B) and the corresponding values of G^*. Using the constraints on $\hat{c}_0$ and $\hat{c}_2$ we can

also calculate the extreme values of the bifurcation point G^*:

$$G^*_{min} = -\left(\frac{1119744}{(9331351 + 947399\sqrt{97})\pi^2}\right)^{\frac{1}{6}} \approx -0.43, \tag{3.57}$$

$$\text{for } P_C(\theta) = H\left(\cos^{-1}\left(\sqrt{\frac{3}{11+\sqrt{97}}}\right)\right) \approx H(68°)$$

$$G^*_{max} = \left(\frac{1}{3\pi}\right)^{1/3} \approx 0.47, \qquad \text{for } P_C(\theta) = 1, \tag{3.58}$$

where $H(\theta)$ is the Heaviside step function.

3.2.3   Segment length and mesh size

An attractive interpretation of the microtubule length density $K(\theta)$ is that it represents the density of 'obstacles' that are pointing in the direction θ as seen by a microtubule growing in the perpendicular direction. From the obstacle density we can define a mesh size $\xi(\theta)$ – the average distance between obstacles. Taking into account the geometrical factor $\sin(\theta)$, we obtain

$$\xi(\theta) = \left(\frac{1}{\pi l_0}\int_0^{2\pi}\left|\sin\left(\theta - \theta'\right)\right|K(\theta')\mathrm{d}\theta'\right)^{-1}. \tag{3.59}$$

In the case of the isotropic solution, this simplifies to $\bar{\xi} = \pi l_0/(4\bar{K})$. Using this equality we can derive an expression for the average microtubule length $\bar{\Lambda}$ in the isotropic phase, expressed in units of the mesh size. The length of each segment is given by $\bar{L}$ and the number of segments per microtubule is given by $(1+\bar{Q})$, so using (3.45) we find

$$\bar{\Lambda} = \frac{l_0\bar{L}(1+\bar{Q})}{\bar{\xi}} = \frac{4\bar{K}^{3/2}}{\pi} \tag{3.60}$$

Inserting this result into (3.47) provides the relationship between $\bar{\Lambda}$ and G

$$G = \left(\frac{4}{\pi\bar{\Lambda}}\right)^{\frac{1}{3}}\left(\frac{\pi\hat{c}_0\bar{\Lambda}}{4} - 1\right) \tag{3.61}$$

As was the case for the density (equation (3.47)), we see that the microtubule length as a function of mesh size does not depend on the amount of zippering. However, it should be noted that the mesh size is defined through the average distance between single microtubules. In real systems, zippering would naturally lead to bundling, which in turn produces a system that has a larger mesh size between bundles (see also the discussion).

Combining equations (3.60) and (3.54), the expression for $\bar{\Lambda}$ at the bifurcation point becomes

$$\bar{\Lambda}^* = -\frac{2}{\pi\hat{c}_2} \tag{3.62}$$

Assuming a monotonically increasing induced catastrophe probability $P_c(\theta)$, we know that the minimum value for $\hat{c}_2$ is reached when every collision at an angle larger than 45° leads to a catastrophe. From (3.62), we see that this implies $\Lambda^* \geq 3/(2\sqrt{2})$, meaning that for a bifurcation to occur, the microtubules need to be longer (sometimes much longer) than the mesh size, as is to be expected.

Equation (3.61) can also provide an interpretation of the length scale l_0. In the absence of catastrophic collisions, we find

$$\bar{\Lambda}|_{\hat{c}_0=0} = \frac{4}{\pi}(-G^{-3}) = \frac{4}{\pi}\left(\frac{l}{l_0}\right)^3, \tag{3.63}$$

where $l = -1/g$ is the average length of the microtubules. l_0 is therefore a measure of the microtubule length that is required to enable a significant number of interactions ($\bar{\Lambda} = 4/\pi$ for $l = l_0$). If the free microtubule length l is (much) shorter than l_0, the system is dominated by the (isotropic) nucleations, keeping the system in an isotropic state. On the other hand, when $l \gg l_0$, the interactions dominate and, depending on the interaction functions, the system has the potential to align.

3.2.4   Numerical solutions away from the bifurcation point

To find solutions beyond the immediate vicinity of the bifurcation point, we are hampered by the fact that these solutions are part of an infinite-dimensional solution space. In this section, we will show that it is possible to restrict the solutions to a finite-dimensional space by imposing constraints on the interaction operators **C** and **Z**. We start by reformulating the equations (3.40) by replacing $L(\theta)$ and $T(\theta)$ through the definitions

$$S(\theta) = \frac{1}{L(\theta)}, \qquad\qquad U(\theta) = \frac{1}{K(\theta)}\left(\frac{T(\theta)}{L(\theta)} - 1\right). \tag{3.64}$$

Following these substitutions, the interaction operators are all applied at the outermost level of the equations, enabling us to make use of their properties in Fourier space. Explicitly, we obtain

$$S(\theta) = -G + \mathbf{C}[K](\theta) + \mathbf{Z}[K](\theta) \tag{3.65a}$$

$$Q(\theta) = \mathbf{Z}[K(1+Q)/S](\theta) \tag{3.65b}$$

$$U(\theta) = \mathbf{Z}[(1+KU)/S](\theta) \tag{3.65c}$$

and

$$K(\theta) = \frac{1+Q(\theta)}{S^2(\theta) - U(\theta)(1+Q(\theta))}. \tag{3.65d}$$

Denoting the Fourier components of $S(\theta)$, $Q(\theta)$ and $U(\theta)$, by $\hat{s}_n$, $\hat{q}_n$ and $\hat{u}_n$, respectively, the interacting microtubule equations reduce to a (potentially infinite) set of

scalar integral equations.

$$\hat{s}_{2n} = -2\delta_{n,0}G + \frac{\hat{c}_{2n} + \hat{z}_{2n}}{\pi} \int_0^{2\pi} \cos(2n\theta) K(\theta) \mathrm{d}\theta \tag{3.66a}$$

$$\hat{q}_{2n} = \frac{\hat{z}_{2n}}{\pi} \int_0^{2\pi} \frac{\cos(2n\theta) K(\theta) (1 + Q(\theta))}{S(\theta)} \mathrm{d}\theta \tag{3.66b}$$

$$\hat{u}_{2n} = \frac{\hat{z}_{2n}}{\pi} \int_0^{2\pi} \frac{\cos(2n\theta) (1 + K(\theta) U(\theta))}{S(\theta)} \mathrm{d}\theta \tag{3.66c}$$

SIMPLIFIED INTERACTION FUNCTIONS

From the form of these equations, we immediately see that we can greatly reduce the dimensionality of the problem by setting a number of Fourier coefficients $\hat{c}_{2n}$ and $\hat{z}_{2n}$ to zero. In other words, by restricting our space of interaction functions $c(\theta)$ and $z(\theta)$, the problem can be reduced to a finite number of scalar equations. In this section, we will define a set of simplified interaction functions by restricting ourselves to Fourier modes up to and including $\cos(4\theta)$. These modes provide us with just enough freedom for the model to exhibit rich behavior, whilst reducing the model to a set of only 7 scalar equations.

Using the fact that $c(0) = z(0) = z(\pi/2) = 0$, we find that $\hat{z}_2 = 0$ and that both $\hat{z}_4$ and $\hat{c}_4$ are determined by the remaining parameters. Furthermore, we introduce an overall factor of α in both equations (per equation (3.43)), allowing us to set $\hat{c}_2 = -1/2$, so that $c(\pi/2) = \alpha$. We thus obtain a system that is fully specified by $\hat{c}_0$, $\hat{z}_0$ and α.

$$c(\theta) = \alpha \left[\frac{\hat{c}_0}{2} - \frac{1}{2}\cos(2\theta) + \frac{1}{2}(1 - \hat{c}_0)\cos(4\theta) \right] \tag{3.67a}$$

$$z(\theta) = \alpha \left[\frac{\hat{z}_0}{2}(1 - \cos(4\theta)) \right] \tag{3.67b}$$

For $\alpha = 1$, $\hat{c}_0$ and $\hat{z}_0$ are the actual Fourier coefficients of the interaction functions. Requiring that $P_c(\theta) = c(\theta)/\sin(\theta)$ is monotonically increasing on the interval $[0, \pi/2]$ leads to the constraint

$$\frac{3}{4} \leq \hat{c}_0 \leq \frac{9}{8} \tag{3.68}$$

and $\hat{z}_0$ is a positive real number. Of course, the total probability of zippering and catastrophe induction may not exceed 1, placing an upper bound on α. In the absence of zippering, we have $\alpha \leq 1$. As discussed in section 3.1.4, the value of α does not qualitatively affect the bifurcation diagram. Equation (3.56) indicates that – for the *simplified interaction functions* – the bifurcation point is located in the range

$$-\frac{1}{4} \leq G^* \leq \frac{1}{8} \tag{3.69}$$

and from (3.47) and (3.62) we find that $K^* = \alpha^{-2/3}$ and $\Lambda^* = 4/(\alpha\pi)$.
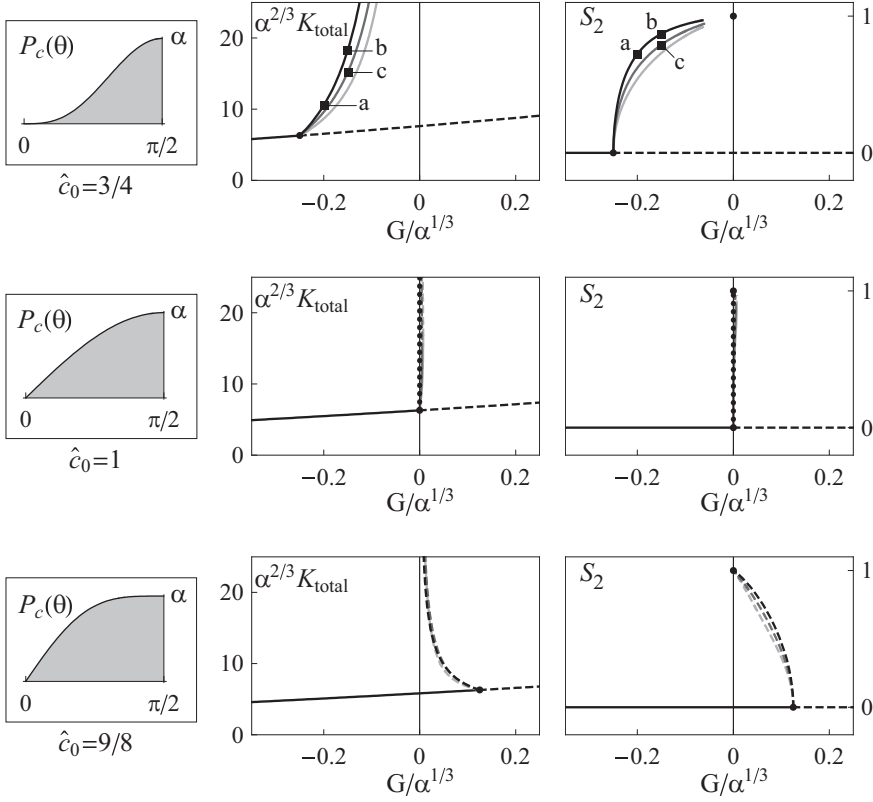
Figure 3.4: Bifurcation diagrams for the simplified interaction model using three different induced catastrophe parameters. The figures on the left depict the probability $P_c(\theta)$ to induce a catastrophe upon collision, along with the corresponding values of $\hat{c}_0$. The center and right columns depict the corresponding bifurcation diagrams as a function of G, expressed in terms of the total density K_{total} and the 2D nematic order parameter S_2, respectively, where $K_{\text{total}} = \int K(\theta) \mathrm{d}\theta$. The isotropic solutions are by definition disordered, so $S_2 = 0$, and their density is computed from (3.47). The bifurcation point is determined using (3.56), with $\hat{c}_2 = -1/2$. For each diagram, ordered solutions have been computed for $\hat{z}_0 = 0$ (black), $\hat{z}_0 = 1$ (slightly lighter) and $\hat{z}_0 = 10$ (lightest). The solutions have been computed using the method discussed in appendix 3.2.4. Solid lines indicate stable solutions and dashed lines indicate unstable solutions (see also section 3.A). Note that the case of $\hat{c}_0 = 1$ in the absence of zippering is a singular case where the stability cannot be determined, because non-isotropic solutions only exist for $G = 0$. This has been indicated by a dotted line. The S_2-diagrams include the asymptotic limit point at $G = 0$ with absolute ordering (at infinite density). The labels *a*, *b* and *c* indicate the parameter values of the results depicted in figures 3.5 and 3.6. The fact that the solutions for S_2 in the case $\hat{c}_0 = \frac{3}{4}$ do not reach the asymptotic point $S_2 = 1$ is a consequence of the slowdown in convergence of the path-following method with respect to the G-coordinate as $G \uparrow 0$.

a) $G/\alpha^{1/3} = -0.2$ $\hat{z}_0 = 0$ b) $G/\alpha^{1/3} = -0.15$ $\hat{z}_0 = 0$ c) $G/\alpha^{1/3} = -0.15$ $\hat{z}_0 = 1$
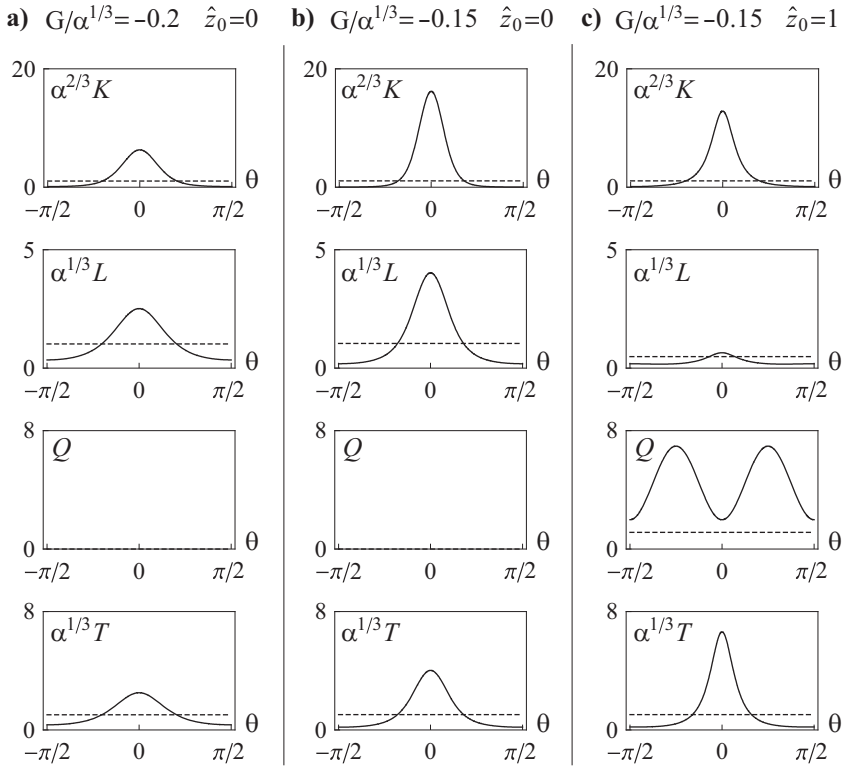
Figure 3.5: Three stable ordered solutions, the positions of which are indicated by the labels (a), (b) and (c) in figure 3.4. The (unstable) isotropic solutions for the same parameter values are indicated with a dashed line. The parameter values for (a) and (b) differ only in the value of G, whereas the parameter values for (b) and (c) differ only in the value of $\hat{z}_0$. All results have been calculated using the method described in section 3.2.4.

NUMERICAL SOLUTIONS

We will now determine the non-isotropic stationary solutions of the model using the simplified interaction functions introduced above. Directly solving equations (3.66) numerically to find the stationary solutions does not yield satisfactory results, hence we perform a more targeted search for solutions. We know that the sets of stationary solutions form lines in the 8-dimensional phase space Φ spanned by the variables $\{\hat{s}_0, \hat{s}_2, \hat{s}_4, \hat{q}_0, \hat{q}_4, \hat{u}_0, \hat{u}_4\}$ and the parameter G. At least two of such solution lines exist, one corresponding to the isotropic solution and the other to the ordered solution, and these lines intersect at the bifurcation point.

a) G=−0.16
$\hat{z}_0$=0
$\hat{c}_0$=3/4
α =1/2

b) G=−0.12
$\hat{z}_0$=0
$\hat{c}_0$=3/4
α =1/2
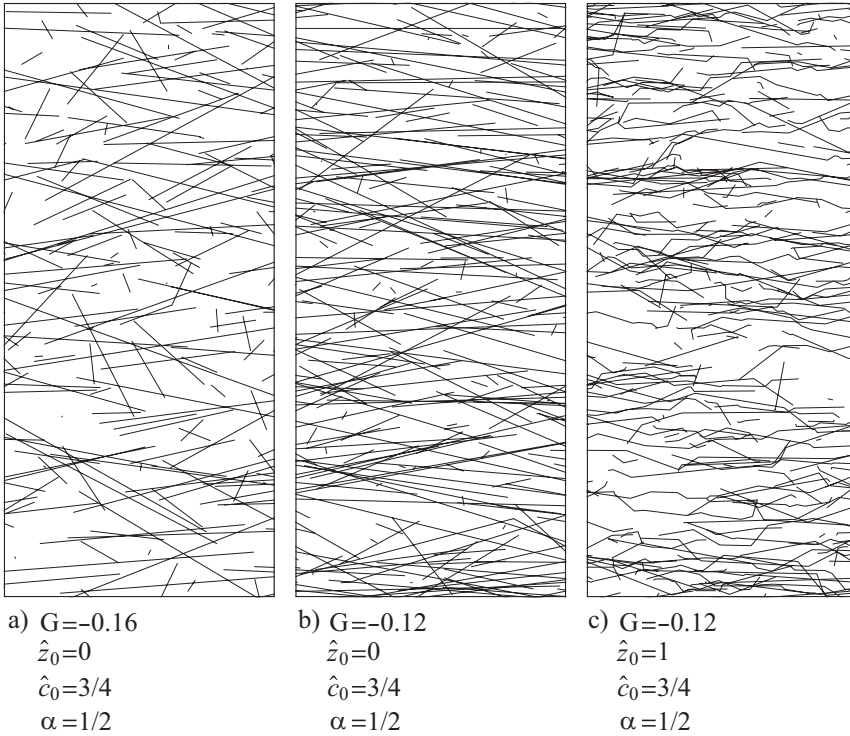
c) G=−0.12
$\hat{z}_0$=1
$\hat{c}_0$=3/4
α =1/2

Figure 3.6: Real space representation of the three solutions depicted in figure 3.5. For the conversion to real coordinates, a value of $\alpha = 1/2$ has been used, to ensure that $P_c(\theta) + P_z(\theta) \leq 1$ in all cases. Each plot covers an area of $5l_0 \times 11l_0$. Note that our use of a coarse-grained homogeneous model technically precludes the explicit use of a spatial representation, so these image should be taken as an intuitive visualization tool only.

Within this 8-dimensional space, we have used a numerical path-following method (Allgower and Georg, 2003; Deuflhard et al., 1987) that follows the ordered solution branch by searching for a local minimum in the root mean error of the constituent equations (3.66). We have implemented the algorithm as follows.

1. Define a definite positive error function $X(\mathbf{p}) : \Phi \to \mathbb{R}$ that is zero for all stationary solutions

2. Select an initial point $\mathbf{p}_0 : \{\mathbf{p}_0 \in \Phi; X(\mathbf{p}_0) = 0\}$ and an initial direction $\mathbf{d}$.

3. Select a step size δ

4. Starting with $i = 1$, do...

(a) Generate trial point $\tilde{\mathbf{p}} = \mathbf{p}_{i-1} + \delta \frac{\mathbf{d}}{||\mathbf{d}||}$

(b) Construct a plane P through $\tilde{\mathbf{p}}$ that is perpendicular to $\mathbf{d}$

(c) Calculate $\mathbf{p}_i$ as the local minimum of $X(\mathbf{p})$, constrained to P

(d) Set $\mathbf{d} = \mathbf{p}_i - \mathbf{p}_{i-1}$

(e) Increase i and go to (a) as long as more points are needed

5. Interpolate the set $\{\mathbf{p}_i\}$ to approximate the solution branch

Applying this algorithm to the problem at hand, the error function X is defined as the root mean square error of the constituent equations (3.66). The initial value of $\mathbf{p}_0$ should be chosen to coincide with the bifurcation point, with coordinates

$$ S^* = \frac{\hat{z}_0 - 2\hat{c}_2}{(-2\hat{c}_2)^{2/3}}, \qquad Q^* = -\frac{\hat{z}_0}{2\hat{c}_2}, \qquad U^* = \frac{\hat{z}_0}{(-2\hat{c}_2)^{1/3}}. \tag{3.70} $$

so that in the case of our simplified interaction model

$$ \{G, \hat{s}_0, \hat{s}_2, \hat{s}_4, \hat{q}_0, \hat{q}_4, \hat{u}_0, \hat{u}_4\} = \{c_0 - 1, 2(\hat{z}_0 + 1), 0, 0, 2\hat{z}_0, 0, 2\hat{z}_0, 0\} \tag{3.71} $$

The initial instability affects only the $\cos(2\theta)$ mode. This mode only appears in the equation for $\hat{s}_2$ and the other parameters are only affected by higher order corrections. For this reason we choose the initial direction $\mathbf{d}$ of the path to be the unit vector in the $\hat{s}_2$-direction and trace it from there.

We have used the numerical procedure described above to determine the ordered solutions of (3.40), starting from the bifurcation point. This has been done for nine different parameter values. For the values of $\hat{c}_0$ we used the extreme values $3/4$ and $9/8$, as well as 1, the latter corresponding to $G^* = 0$. For each of these three cases, we have varied the zippering parameter $\hat{z}_0$, choosing values of 0, 1 and 10. Figure 3.4 shows the results, depicting both the total density of the system and the degree of ordering as a function of G. The degree of ordering is measured by the 2D nematic order parameter S_2, defined as

$$ S_2 = \frac{|\int_0^{2\pi} e^{i2\theta} K(\theta)\mathrm{d}\theta|}{\int_0^{2\pi} K(\theta)\mathrm{d}\theta}, \tag{3.72} $$

which yields a value of 0 for a completely disordered system and a value of 1 for a fully oriented system. Note that this order parameter is insensitive to the polarity of the segments. Furthermore, figures 3.5 and 3.6 illustrate the properties of three specific solutions, indicated by the labels a, b and c in figure 3.4.

3.2.5   A finite tubulin pool

So far, the expressions in this chapter have been stated under the implicit assumption of constant values for the parameters governing the microtubule dynamics. Specifically, we have seen that some combinations of parameters can lead to diverging

microtubule densities. Of course, this is at odds with biological reality, due to restricted availability of tubulin dimers inside the cell. To determine the effect this has on the ordering of microtubules, we can assume that there is a tubulin pool of a fixed size, and the depletion of free tubulin dimers affects the microtubule polymerization rate (growth speed). This is sufficient to place an upper bound on the total density of a system. Assuming a given amount of tubulin to be present in the system, corresponding to a microtubule density k_{max}, we take the growth speed to be proportional to the amount of free tubulin (cf. Mitchison and Kirschner, 1984)

$$v^+(k_{tot}) = v_0^+ \left(1 - \frac{k_{tot}}{k_{max}}\right) \tag{3.73}$$

This dependency will lead to a decrease in the effective value for G (defined in (3.40e)) as the density of polymerized microtubules increases. Specifically, the effective value of G at a finite density must always be smaller than its initial value in the absence of polymerized microtubules: $G_{\text{eff}} < G_0$. Accordingly, because the density increases along the branch of ordered solutions, these solutions correspond to increasingly large initial values of G_0. This is illustrated in figure 3.7 where the ordered solution curves cross the left-leaning contour lines depicting constant G_0-values. The asymptotic solution for the initial value $G_0 \to \infty$ is that solution for which $K = K_{max}$.

We thus find that the biologically motivated inclusion of a finite tubulin pool provides a mechanism by which a stable solution is created for *any* value of G_0. Specifically, figure 3.7 shows that also the hitherto singular case of $\hat{c}_0 = 1$ now gives rise to stable solutions for any value of the initial parameters, summarized in G_0. In a similar vein, the unstable (in terms of G) solution branch associated with $\hat{c}_0 = 9/8$ now turns around to produce stable ordered solutions for values of G_0 that are sufficiently large.

THE LINE $G_{\text{EFF}} = 0$

Both the asymptotic solutions derived in section 3.D and the solutions for the simplified interaction functions with $\hat{c}_0 = 1$ and $\hat{z}_0 = 0$ are degenerate sets of solutions with the property $G_{\text{eff}} = 0$, and therefore $g_{\text{eff}} = 0$. Combining this with equation (3.73) we can deduce the steady state microtubule density of the peaked solution and the length scale l_0 (3.35) from the model parameters, assuming the presence of a tubulin pool.

$$k_{tot} = k_{max} \left(1 - \frac{r_c v^-}{r_r v_0^+}\right), \tag{3.74}$$

$$l_0 = \left[\frac{1}{2} r_n \left(\frac{1}{v^-} + \frac{1}{v_0^+ - (r_c/r_r)v^-}\right)\right]^{-1/3}. \tag{3.75}$$

The pool thus offers a mechanism through which a solution with a particular density is selected.
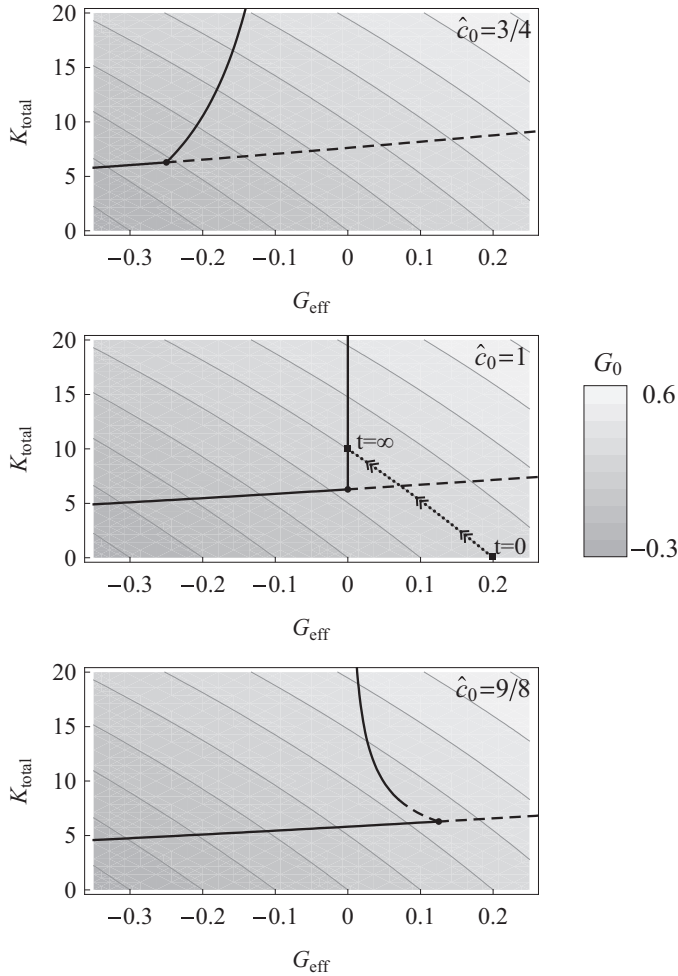
Figure 3.7: Bifurcation diagrams for the simplified interaction functions with $\hat{z}_0 = 0$ (no zippering) and $\hat{c}_0 = 4/3; 1; 9/8$. Contour lines have been added that indicate the corresponding initial values G_0, assuming a finite tubulin pool size. Systems outside of the steady state will evolve along lines of constant G_0. The dotted arrow in the center panel indicates an example of such an evolution, starting with an empty system and $G_0 = 0.2$ at $t = 0$. Parameters used to calculate the relation between G_{eff} and G_0 were: $v^+ = 0.078\,\mu m\,s^{-1}$, $v^- = 0.164\,\mu m\,s^{-1}$, $r_r = 0.068\,s^{-1}$ (Vos et al., 2004). For demonstration purposes, we have used $k_{max} = 21\,\mu m^{-1}$ and $r_n = 0.001\,\mu m^{-1}$. The catastrophe rate r_c was varied between $0.028\,s^{-1}$ and $0.038\,s^{-1}$ to obtain the different values of G_0. Note that for $K_{total} = 0$, $G_0 = G$.

3.3   Discussion

Based on biological observations, we have constructed a model for the alignment of cortical microtubules. The model has a number of prominent features. First of all, it allows us to identify a single dimensionless control parameter G, which is fully determined by the nucleation rate and intrinsic dynamics of individual microtubules. This control parameter determines the steady state degree of order of the system, when the probabilities for zippering ($P_z(\theta)$) and catastrophe induction ($P_c(\theta)$) upon collision are specified. This result by itself may turn out to be very useful in comparing different *in vivo* systems. For increasing values of G, the isotropic stationary solutions to the model show an increase both in density and in abundance of interactions, as measured by the ratio of microtubule length over the mesh-size. Secondly, the bifurcation point, i.e. the critical value of G^* of the control parameter at which the system develops ordered stationary solutions from the isotropic state is determined solely by the probability of collisions between microtubules that lead to an induced catastrophe.

Indeed, from the numerical solutions of the minimal model introduced in section 3.2.4 it appears, perhaps surprisingly, that the co-alignment of microtubules due to zippering events, if anything, *diminishes* the degree of order. Together, these results identify the "weeding out" of misaligned microtubules — by marking them for early removal by the induced switch to the shrinking state — as the driving force for the ordering process.

Finally, in spite of not being able to directly assess the stability of the solutions in the time-domain, we have provided arguments that stable ordered solutions are possible for the regime $G < 0$, i.e. where the length of individual microtubules is intrinsically bounded. For $G > 0$, stable ordered solutions do not seem to exist, with the exception of a very small region around $G = 0$ (see, for example, the solution for $\hat{c}_0 = 1$ and $\hat{z}_0 = 1$). However, the *isotropic* state may still be locally stable for $G > 1$, but only if it is not perturbed too much, as the aligned state is diverging.

The divergence of the ordered solution as $G \to 0$ and the boundless growth of this state for $G \geq 0$ is a consequence of the fact that our model implicitly assumes that there is an infinite supply of tubulin dimers available for incorporation into microtubules. In section 3.2.5, we have argued that it is reasonable to assume that *in vivo* there is a limit to the size of the free tubulin pool. This pool-size limit feeds back into the system through the growth speed of the microtubules, ensuring that the total length of the system remains bounded. Therefore, the system will always settle into a steady state – even when the initial value of G is larger than 0.

How realistic is the model presented? To that end we need to address several known factors that have not been included. First of all, microtubules typically can de-attach from their nucleation sites and then perform so called treadmilling motion, whereby the minus-end shrinks at a more or less steady pace, which is small compared to both the growth- and the shrinking speed of the more active plus end. In the special case that no zippering occurs at all it is relatively easy to show that the effect of treadmilling simply entails a renormalization of the parameter G and the

interaction functions $c(\theta)$ and $z(\theta)$, but leaving the qualitative behavior of the model identical to the one discussed here (see appendix 3.E).

When zippering does occur in combination with treadmilling, one expects the treadmilling to enhance the degree ordering in an ordered state, as it serves to over time "eat-up" the, by definition, less ordered initial segments of each microtubule. This effect is also consistent with the observation in Figure 3.5c that in the case with zippering the active tips are on average more strongly aligned than the average segment. In fact, the comparison between figures 3.5b and 3.5c also shows that, all else being equal, zippering sharpens the orientational distribution of the active tips as compared to the case with no zippering. It is therefore conceivable that the combination of zippering and treadmilling could lead to more strongly ordered systems for the same value of the control parameter, and possibly the existence of an ordered state for lower values of G.

Next it is known that in vivo severing proteins, such as katanin are active in, and crucial to, the formation of the cortical array (Roll-Mecak and Vale, 2006). However, including the effect of severing proteins explicitly in the model would present formidable problems in the analysis, and would introduce additional parameters into the model for which precise data is lacking. In chapter 4 we use simulations to investigate the effect of severing.

Another effect that has not been taken into account explicitly is microtubule bundling. Whenever a microtubule zippers alongside another segment, they form a parallel bundle. However, the coarse-grained homogeneous nature of our model precludes the formation of bundles and only allows for alignment of the two. This means that a microtubule that is growing in a different direction encounters both microtubules separately instead of as a single bundle. It is to be expected that the catastrophe and zippering rates stemming from N individual collisions will be higher than those from a single collision with a bundle of N microtubules. Hence, in realistic systems the event rate is likely to be lower than that predicted by the model. To a first approximation, this effect can be accounted for by a decrease of the zippering and induced catastrophe probabilities $P_z(\theta)$ and $P_c(\theta)$ (at least for the isotropic state). Bundles are also thought to be more than simply adjacent co-aligned microtubules, because they may be stabilized through association with bundling proteins that e.g. decrease the catastrophe rate of individual microtubules within a bundle (see e.g. Gaillard et al., 2008). This is a non-trivial effect that should be considered separately and is likely to lead to an increased tendency to form an ordered structure.

To see whether our model, in spite of its approximate nature, makes sense in the light of the available data we first use the collision event probabilities obtained by Dixit and Cyr (2004) (see figure 3.2) to obtain an estimate for the bifurcation value of the control parameter of $G^* = -0.15$ for the case of Tobacco BY-2 cells. An ordered phase of cortical microtubules should therefore be possible provided $G > G^*$. Given the available data on the microtubule instability parameters in this same system taken from Dhonukshe and Gadella (2003) and Vos et al. (2004) we would predict using the definition (3.40e) that this requires the nucleation rate of new microtubules to be larger than $0.05 \, \mathrm{min}^{-1} \mu\mathrm{m}^{-2}$ (Dhonukshe) and $0.01 \, \mathrm{min}^{-1} \mu \, \mathrm{m}^{-2}$ (Vos) respectively.

Both these estimates for a lower bound on the nucleation rate are reasonable as they imply the nucleation of order 10^3 microtubules in the whole cortex over the course of the build-up towards full transversal order, comparable to the number that is observed. Furthermore, because both studies make no distinction between spontaneous and collision-induced catastrophes, the spontaneous catastrophe rate can be significantly lower (approximately half the reported number, see also appendix 3.F). This further decreases the minimum nucleation rate that is required to be in the ordered state.

Finally, we should point out that our model so far only addresses the question of what causes cortical microtubules to align with respect to each other. Given that in growing plant cells the cortical array is invariably oriented transverse to the growth direction, the question of what determines the direction of the alignment axis with respect to the cell axes is as, if not more, important from a biological perspective. With the help of computer simulations, we take some first steps in this direction in chapter 5.

3.A   Symmetries and the stability of solutions

The symmetry structure of the evolution equations (3.1) contains important clues to the symmetry of its solutions and their stability (Golubitsky et al., 1988; Golubitsky and Stewart, 2003). We note that the equations are symmetric (by construction) under arbitrary rotations and reflections. The equations are thus equivariant under the symmetry group $\mathbf{S}^1 \times \mathbf{Z}_2 \cong \mathbf{O}(2)$. Clearly, the isotropic solution reflects the full symmetry of the equations.

The bifurcation equation (3.52) has shown that the space of bifurcating functions κ_n is spanned by the functions $\cos(2n\theta)$ and $\sin(2n\theta)$ for a given value of $n \geq 1$. The symmetry group $\mathbf{O}(2)$ acts irreducibly on the two-dimensional coefficient space of each pair of functions, so the equivariant branching lemma (Golubitsky et al., 1988, chap. XIII) predicts that any bifurcating branch will be symmetric with respect to the maximum isotropy subgroup $\mathbf{Z}_2$. In other words, the solutions that branch off from the isotropic solution are symmetric with respect to an arbitrary axis, which we will place at $\theta = 0$.

Note that even after the restriction to the symmetry axis there are still two solution branches emanating from the bifurcation point, differing in the sign of the coefficient of the perturbation. These branches correspond to solutions peaked around $\theta = 0$ and $\theta = \pi/(2n)$, respectively, that are otherwise identical. The symmetry of these solutions indicates that the bifurcation is of the pitchfork type.

The presence of a pitchfork bifurcation implies a loss of stability of the originating branch (Golubitsky and Schaeffer, 1984). In our system, we know that the isotropic solution must be stable in the limit $G \to -\infty$. Therefore, the local stability of the isotropic solution is lost at the first bifurcation point (for the lowest value of G), corresponding to the eigenfunction $\cos(2\theta)$. Because this eigenfunction is orthogonal to the eigenfunctions related to the subsequent bifurcation points ($\cos(2n\theta)$, $n > 1$),

the stability of the unstable mode cannot be regained at any point along the isotropic solution and the isotropic solution itself remains unstable. This also means that the solution branches originating at further pitchfork bifurcations will be unstable near the isotropic solution. In this chapter we restrict ourselves to the analysis of the first bifurcation point and the corresponding ordered solution branch. Because the solutions on this branch already have the lowest symmetry permitted by the interaction functions, there are no further bifurcation points along this branch.

Typically (Golubitsky and Schaeffer, 1984, chap. IV), the branches of the initial pitchfork bifurcation are stable for a *supercritical* bifurcation (branches bending towards higher values of G) and unstable for a *subcritical* bifurcation (branches bending towards lower values of G). In addition, turning points in the bifurcating branches generally correspond to an exchange of stability (Iooss and Joseph, 1980, page 22). This analysis allows us to assign stability indicators to the bifurcation diagrams in figure 3.4, even in the absence of a detailed study of the time-dependent equations (3.1).

3.B   The coefficients of $c(\theta)$

The Fourier coefficients of the induced catastrophe function $c(\theta)$ play an important role in determining the type and shape of the non-isotropic solutions. In this section, we investigate the range of possible values of these Fourier coefficients, starting from the physically motivated assumption that the probability $P_c(\theta)$ of inducing a catastrophe is a monotonically increasing function of the angle $\theta \in [0, \pi/2]$. Naturally, this implies that $c(\theta) = |\sin(\theta)| P_c(\theta)$ is also increasing monotonically. The coefficients $\hat{c}_n$ are defined by

$$\hat{c}_n = \frac{4}{\pi} \int_0^{\pi/2} c(\theta) \cos(n\theta) \, d\theta, \quad \text{for even } n \tag{3.76}$$

Using the fact that $c(\theta)$ is differentiable and $c(0) = 0$, we can rewrite this as follows

$$\hat{c}_n = \frac{4}{\pi} \int_0^{\pi/2} \cos(n\theta) \int_0^\theta \frac{dc(\theta')}{d\theta'} d\theta' d\theta \tag{3.77}$$

$$= \frac{4}{\pi} \int_0^{\pi/2} \frac{dc(\theta')}{d\theta'} \int_{\theta'}^{\pi/2} \cos(n\theta) \, d\theta d\theta' \tag{3.78}$$

$$= -\int_0^{\pi/2} \frac{dc(\theta')}{d\theta'} \frac{4}{\pi n} \sin(n\theta') \, d\theta' \tag{3.79}$$

Because $dc(\theta)/d\theta \geq 0$ it follows that

$$\hat{c}_2 \leq 0, \quad \hat{c}_0 \geq 0 \quad \text{and} \quad \hat{c}_2 \leq \hat{c}_n \leq \hat{c}_0 \quad \text{for even } n \geq 2 \tag{3.80}$$

This result indicates that all Fourier coefficients of the interaction function $c(\theta)$ are bounded by $\hat{c}_2$ from below and $\hat{c}_0$ from above. In addition, we can determine the bounds of $\hat{c}_0$ and $\hat{c}_2$ themselves. To do so, we formally write the interaction function

on the interval $[0, \pi/2]$ as a weighted integral over an infinite set of Heaviside step functions $H(\theta - \theta')$

$$c(\theta) = \sin(\theta) \int_0^{\pi/2} \frac{\mathrm{d}P_c(\theta')}{\mathrm{d}\theta'} H(\theta - \theta') \mathrm{d}\theta'. \tag{3.81}$$

Therefore, we can view $c(\theta)$ as a linear combination of the infinite set of basis functions

$$f_\phi(\theta) = \sin(\theta) \, H(\theta - \phi) \quad \phi \in [0, \pi/2] \tag{3.82}$$

Since the calculation of $\hat{c}_0$ and $\hat{c}_2$ is linear, their values are also linear combinations (with only positive weights) of the Fourier coefficients corresponding to the basis functions $f_\phi(\theta)$. Because the total integrated weight cannot exceed 1, $\hat{c}_0$ and $\hat{c}_2$ are restricted to the area defined by

$$\{\hat{c}_0, \hat{c}_2\} = \alpha \{\hat{f}_{\phi,0}, \hat{f}_{\phi,2}\}, \quad \alpha \in [0, 1], \quad \phi \in [0, 2\pi] \tag{3.83}$$

The thus permitted values for $\hat{c}_0$ and $\hat{c}_2$ are indicated by the enclosed area in figure 3.3.

3.C   Discrete angles

The spectral method discussed in section 3.2.4 transforms the infinite-dimensional model equations to a finite set of equations for a limited class of models in which the interaction functions have a finite Fourier representation. Even in the case where these limitations are met, the integrals in equations (3.66) need to be evaluated numerically, which can be costly. Hence we introduce a second, *approximate*, method to reduce the dimensionality of the model equations: discretization of the angular coordinate θ. Discretizing the angular coordinate into $2N$ distinct values and making use of the π-periodicity, the integrals are replaced by sums according to the substitution

$$\int_0^{2\pi} f(\theta) \mathrm{d}\theta \rightarrow \frac{2\pi}{N} \sum_{n=0}^{N-1} f\left(\frac{n\pi}{N}\right). \tag{3.84}$$

Physically, this reduction corresponds to a system in which nucleation only occurs in specific directions $\theta_k = \frac{k\pi}{N}$, with $k = 1, ..., 2N$. For simplicity, we will assume N to be even, but this restriction is not strictly necessary.

PROPERTIES OF THE INTERACTION OPERATORS

In the discretized problem, the functions $L(\theta)$, $Q(\theta)$, $T(\theta)$ and $K(\theta)$ are replaced by N-dimensional vectors and the operators $\mathbf{C}$ and $\mathbf{Z}$ are sampled at discrete intervals to form the matrix operators $\tilde{\mathbf{C}}$ and $\tilde{\mathbf{Z}}$. The operator matrices are real, symmetric matrices that are invariant under rotations (cyclic permutation of the indices). They are thus guaranteed to have an orthonormal basis of eigenvectors. We will now

investigate the properties of the interaction matrices and indicate the parallels and differences between the discretized and continuous models.

Let us define a generic π-periodic function $g(\theta)$ with a generic Fourier series representation

$$g(\theta) = \frac{a_0}{2} + \sum_{n=1}^{\infty} a_{2n}\cos(2n\theta) + \sum_{n=1}^{\infty} b_{2n}\sin(2n\theta) \tag{3.85}$$

that is sampled at the set of points

$$\{\theta_k\} = \left\{ \frac{k\pi}{N} \right\}, \qquad k = 0, 1, ..., N-1. \tag{3.86}$$

We now define a function $\tilde{g}(\theta)$ that interpolates $g(\theta)$ at $\{\theta_k\}$. This function has the Fourier expansion

$$\tilde{g}(\theta) = \frac{\alpha_0}{2} + \sum_{n=1}^{N/2-1} \alpha_{2n}\cos(2n\theta) + \sum_{n=1}^{N/2-1} \beta_{2n}\sin(2n\theta) + \frac{\alpha_N}{2}\cos(N\theta) \tag{3.87}$$

Similarly, the discretized interaction function $f(\theta)$ – an even function – has the expansion

$$\tilde{f}(\theta) = \frac{\gamma_0}{2} + \sum_{n=1}^{N/2-1} \gamma_{2n}\cos(2n\theta) + \frac{\gamma_N}{2}\cos(N\theta) \tag{3.88}$$

The Fourier coefficients of the discretized and original functions are related as follows (Boyd, 2001, page 93), clearly illustrating the aliasing of high-frequency information.

$$\alpha_{2n} = a_{2n} + \sum_{j=1}^{\infty} (a_{2n+2jN} + a_{-2n+2jN}) \qquad n = 0, 1, ..., \frac{N}{2}, \tag{3.89a}$$

$$\beta_{2n} = b_{2n} + \sum_{j=1}^{\infty} (b_{2n+2jN} + b_{-2n+2jN}) \qquad n = 1, 2, ..., \frac{N}{2} - 1, \tag{3.89b}$$

$$\gamma_{2n} = \hat{f}_{2n} + \sum_{j=1}^{\infty} (\hat{f}_{2n+2jN} + \hat{f}_{-2n+2jN}) \qquad n = 0, 1, ..., \frac{N}{2}, \tag{3.89c}$$

where $\hat{f}_{2n}$ are the Fourier coefficients of the interaction function $f(\theta)$.

The function of the discretized operator $\hat{\mathbf{F}}$ can now be rewritten using the identities from Boyd (2001, eqn. (4.43))

$$\tilde{\mathbf{F}}[g](\theta_k) = \frac{2}{N} \sum_{j=0}^{N-1} f(\theta_k - \theta_j)g(\theta_j) \tag{3.90}$$

$$= \frac{2}{N} \sum_{j=0}^{N-1} \left[\frac{\gamma_0}{2} + \sum_{n=1}^{N/2-1} \gamma_{2n}\left(\cos(2n\theta_k)\cos(2n\theta_j) + \sin(2n\theta_k)\sin(2n\theta_j)\right) \right.$$

$$\left. + \frac{\gamma_N}{2}\cos(N\theta_k)\cos(N\theta_j) \right] g(\theta_j) \tag{3.91}$$

$$= \frac{\gamma_0\alpha_0}{2} + \sum_{n=1}^{N/2-1} \gamma_{2n}\alpha_{2n}\cos(2n\theta_k) + \sum_{n=1}^{N/2-1} \gamma_{2n}\beta_{2n}\sin(2n\theta_k) + \frac{\gamma_N\alpha_N}{2}\cos(N\theta_i)$$

$$\tag{3.92}$$

Comparing this with equation (3.87) we conclude that the eigenfunctions of the discretized operators are given by the set $\cos(2n\theta_k)$, with $n = 0,\dots,N/2$ and $\sin(2n\theta_k)$, with $n = 1,\dots,N/2-1$. The corresponding eigenvalues are γ_{2n}.

Specifically, when the interaction functions $c(\theta)$ and $z(\theta)$ can be represented *exactly* by a cosine series up to degree N, we see that the eigenvalues γ_{2n} of the matrix operators $\tilde{\mathbf{C}}$ and $\tilde{\mathbf{Z}}$ are simply

$$\gamma_{2n} = \hat{f}_{2n} \qquad\qquad n = 0, 1, \dots, \frac{N}{2} - 1 \qquad\qquad (3.93)$$

$$\gamma_N = 2\hat{f}_N \qquad\qquad (3.94)$$

The simplified interaction functions introduced in section 3.2.4 contains modes up to $\cos(4\theta)$, so it can be represented by a discretized model with $N = 4$, leaving all eigenmodes intact with the exception of a factor 2 for the highest mode. The corresponding interaction matrices are

$$\tilde{\mathbf{C}}_4 = \frac{1}{2}\begin{pmatrix} 0 & \hat{c}_0 - \frac{1}{2} & 1 & \hat{c}_0 - \frac{1}{2} \\ \hat{c}_0 - \frac{1}{2} & 0 & \hat{c}_0 - \frac{1}{2} & 1 \\ 1 & \hat{c}_0 - \frac{1}{2} & 0 & \hat{c}_0 - \frac{1}{2} \\ \hat{c}_0 - \frac{1}{2} & 1 & \hat{c}_0 - \frac{1}{2} & 0 \end{pmatrix} \qquad \tilde{\mathbf{Z}}_4 = \frac{\hat{z}_0}{2}\begin{pmatrix} 0 & 1 & 0 & 1 \\ 1 & 0 & 1 & 0 \\ 0 & 1 & 0 & 1 \\ 1 & 0 & 1 & 0 \end{pmatrix} \qquad (3.95)$$

It should be stressed that even though the operators correctly reproduce the mapping of all low-frequency modes, the operand functions themselves can *not* generally be represented exactly using a finite number of modes. This results in aliasing through equations (3.89). Fundamentally, this problem goes back to the $1/L(\theta)$ term in the collision equation (3.40a) and can be reduced, but not fully avoided, by increasing N.

BIFURCATION RESULTS

Accepting that the results will not be exact, but realizing that they will improve with increasing N, we may calculate the bifurcation diagrams for the simplified interaction functions introduced in section 3.2.4. We do so for increasing values of N and compare the solutions with the computationally intensive exact results from section 3.2.4. First of all, because the interaction functions for the minimal model only have a limited number of Fourier modes, the first two eigenvalues are conserved for $N = 4$ or higher, resulting in the location of the bifurcation point G^* being identical to the continuous case.

However, in the discretized case there are *two* branches of solutions. Both classes of solutions have mirror symmetry, but one of them contains solutions that are symmetric around values θ_k and the other contains solutions that are symmetric around the midpoints of two values. Mathematically, the existence of two separate solution branches is caused by the fact that the $\mathbf{D}_n$ symmetry group has two distinct isotropy subgroups with $\mathbf{Z}_2$ symmetry (see also Golubitsky et al., 1988, sec. XIII.5b). At most one of these branches is stable.

Once again, we employ the numerical methods developed in section 3.2.4 to trace the solution curves, starting from the bifurcation point. This time, the solutions can
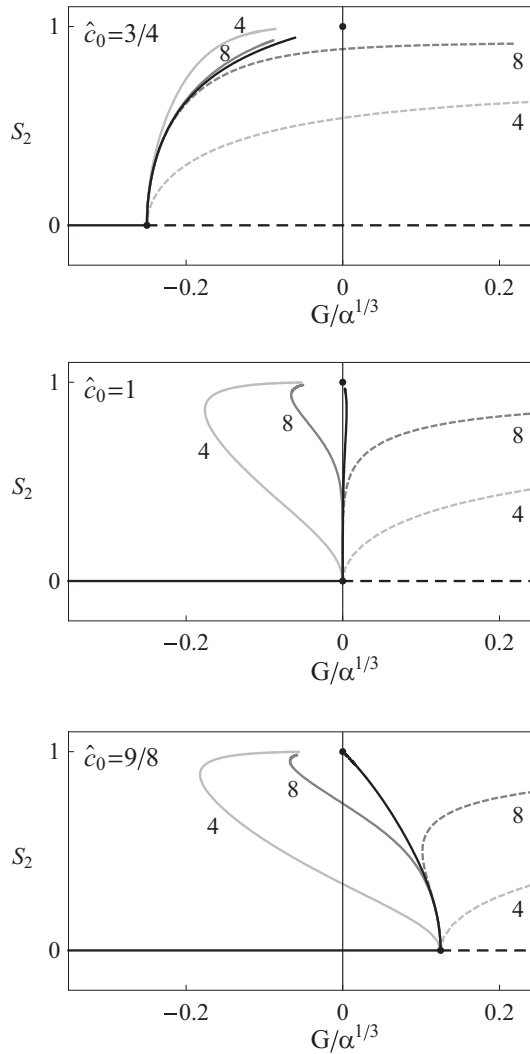
Figure 3.8: Bifurcation diagrams of the 2D nematic order parameter S_2 for solutions of the discretized system. Solutions have been calculated for the discretized simplified interaction functions with $\hat{z}_0 = 1$ and $\hat{c}_0 = 3/4; 1; 9/8$. Solutions for $N = 4$ have been indicated in light grey, solutions for $N = 8$ in dark grey. For reference, the numerically computed solutions for the continuous model have been added in black. The solid lines correspond to the 'dominant solutions', symmetric around $\theta = 0$ (one of the discrete directions). The dashed lines correspond to the solutions that are symmetric around $\theta = \pi/(2N)$ (the midpoint of two adjacent directions).

be traced directly in the space of the discretized functions $L(\theta_k)$, $Q(\theta_k)$, $T(\theta_k)$ and the parameter G. The density $K(\theta)$ is calculated implicitly through (3.40b). The initial values at the bifurcation point are

$$G^* = -1 + \hat{c}_0 \qquad L^*(\theta_k) = \frac{1}{1 + \hat{z}_0} \qquad Q^*(\theta_k) = \hat{z}_0 \qquad T^*(\theta_k) = 1 \qquad (3.96)$$

The initial perturbation away from the bifurcation corresponds to the one of the eigenfunctions $e(\theta_k) = \cos(\theta_k)$ or $e(\theta_k) = \cos\left(\theta_k - \frac{\pi}{2N}\right)$. Solving (3.40) for these perturbations gives the following expressions for the initial changes of the parameters:

$$\partial G = 0 \qquad \partial L(\theta_k) = \frac{e(\theta_k)}{1 + \hat{z}_0} \qquad \partial Q(\theta_k) = 0 \qquad \partial T(\theta_k) = (1 + 2\hat{z}_0) e(\theta_k) \qquad (3.97)$$

As the error function X we select the sum of the absolute differences of the dimensionless equations (3.40). The resulting solutions are depicted in figure 3.8, for $N = 4$ and $N = 8$. Note that the solutions rapidly converge to the (numerically computed) exact solution.

The dominant – and potentially stable – solution branch, we will assume, is the one that corresponds to the highest density. This branch of solutions has a diverging density and approaches perfect ordering, analogous to the result obtained in the continuous case. Not surprisingly, the most peaked solutions (solid lines in figure 3.8) are symmetric around a *single* preferred direction θ_k, avoiding the induced catastrophes within the peak that are a property of the alternate solutions. It is interesting to note that these solutions appear to show hysteresis, although the size of the hysteresis loop decreases rapidly as N increases. The appearance of hysteresis is probably caused by the absence of induced catastrophes at very shallow angles due to discretization.

The alternate solution branch (dashed lines in 3.8) does not diverge near $G = 0$, but continues to exist for arbitrarily large values of G. The reason for this behavior is that the symmetry of the solutions imposes that a peak should consist of at least two neighboring directions with equal density. The microtubules in those directions will have catastrophic collisions with one another, keeping the total density in check. However, this situation is almost certainly not stable.

3.D No zippering: asymptotic solutions for $G = 0$

In section 3.2.4, where we traced the ordered branches of solutions for a simplified model, we observed that these branches always converge to a solution with $S_2 \to 1$ and a diverging density. In this appendix we derive the asymptotic form of the ordered solutions to equations (3.40) in the *absence* of zippering and assuming that $c(\theta)$ is quadratic around the origin. The equations then reduce to

$$\frac{1}{L(\theta)} = -G + \frac{1}{\pi} \int_0^{2\pi} c(\theta - \theta') K(\theta') \mathrm{d}\theta' \qquad (3.98)$$

$$K(\theta) = L(\theta)^2 \qquad (3.99)$$

Because we are searching for peaked (nearly-diverging) solutions, we will assume that the result of the convolution in equation (3.98) is essentially determined by the shape of $K(\theta)$ (hence of $L(\theta)$) in a small region around the peak. Fixing the arbitrary location of the peak at $\theta = 0$ we start with the *Ansatz*

$$\frac{1}{L(\varepsilon)} = a_0 + a_2\varepsilon^2 + O(\varepsilon^4), \tag{3.100}$$

$$c(\varepsilon) = c\varepsilon^2 + O(\varepsilon^4) \tag{3.101}$$

where $a_0 \ll 1$. We expect the higher order terms to become irrelevant as a_0 approaches 0, and the distribution becomes increasingly localized. Note that $a_0 \geq -G$, because the microtubules in the interacting system cannot become longer than those in the non-interacting system.

Assuming that the distribution of $L(\theta)$ is sufficiently localized, we can extend the limits of the integral to infinity (assuming that $L(\theta)/L(0)$ decays fast enough). Finally, we need to add a factor of two to the integral to account for the peaks at both $\theta = 0$ and $\theta = \pi$. Using these assumptions, we can use equation (3.98) as a self-consistency equation relating a_0, a_2 and G. Solving

$$\frac{1}{L(\theta)} = -G + \frac{2}{\pi}\int_{-\infty}^{\infty}\frac{c(\theta - \theta')^2}{(a_0 + a_2\theta'^2)^2}\mathrm{d}\theta' \tag{3.102}$$

$$= -G + \frac{c}{a_2\sqrt{a_0 a_2}} + \frac{c}{a_0\sqrt{a_0 a_2}}\theta^2 \tag{3.103}$$

yields a family of solutions satisfying

$$a_0 a_2 = c^{2/3}, \tag{3.104}$$

$$G = 0. \tag{3.105}$$

Taking a_0 and c as parameters, these solutions have the following properties, with diverging density and perfect alignment as $a_0 \to 0$.

$$L_{\text{peak}} = \frac{1}{a_0} \tag{3.106}$$

$$K_{\text{total}} = \int_0^{2\pi} K(\theta)\mathrm{d}\theta = \frac{c^{2/3}}{a_0} = c^{2/3}L_{\text{peak}} \tag{3.107}$$

$$S_2 = 1 - \frac{2a_0^2}{c^{2/3}} = 1 - \frac{2}{c^{2/3}L_{\text{peak}}^2} \tag{3.108}$$

Which particular value of a_0 corresponds to the real solution will in biological systems be determined by the concentration of tubulin dimers (see section 3.2.5).

APPLIED TO THE SIMPLIFIED INTERACTION FUNCTIONS

Applying this to the simplified interaction functions introduced in section 3.2.4, we see that

$$c = 4\hat{c}_0 - 3 \tag{3.109}$$

and obtain the results

$$K_{\text{total}} = (4\hat{c}_0 - 3)^{2/3} L_{\text{peak}} \tag{3.110}$$

$$S_2 = 1 - \frac{2a_0^2}{c^{2/3}} = 1 - \frac{2}{(4\hat{c}_0 - 3)^{2/3} L_{\text{peak}}^2} \tag{3.111}$$

IN THE PRESENCE OF A FINITE TUBULIN POOL

Finally, we investigate the asymptotic solutions in the presence of a finite supply of tubulin (section 3.2.5). As $G = 0$ for the asymptotic solutions, we can use (3.107), and (3.74) and (3.75) for the density and length scale, to derive

$$S_2 = 1 - \frac{2c^{2/3}}{K_{max}^2 \left(1 - \frac{r_c v^-}{r_r v_0^+}\right)^2} \tag{3.112}$$

$$= 1 - \frac{2c^{2/3}}{\pi^2 k_{max}^2 l_0^2 \left(1 - \frac{r_c v^-}{r_r v_0^+}\right)^2} \tag{3.113}$$

Naturally, it is assumed that the amount of tubulin present in the cell (k_{max}) is large enough so that the solution is sufficiently peaked for the asymptotic approximation to be valid.

3.E No zippering: the effect of treadmilling

As indicated in the introduction, treadmilling of microtubules is also thought to play an important role in the cell and could be an important factor in the establishment of the cortical array. The integration of treadmilling into equations (3.1) is not straightforward, so we aim to obtain a qualitative understanding of the effect of treadmilling by considering the equations in the absence of zippering.

Considering the master equations (3.1), the inclusion of the treadmilling velocity v^{tm} is reflected in the growth and shrinkage terms

$$\Phi_{growth} = -(v^+ - v^{tm})\partial_l m_i^+(l, \theta, t) \tag{3.114}$$

$$\Phi_{shrinkage} = (v^- + v^{tm})\partial_l m_i^-(l, \theta, t) \tag{3.115}$$

and the boundary condition

$$m_1^+(l_1 = 0, \theta, t) = \frac{r_n}{2\pi(v^+ - v^{tm})} \tag{3.116}$$

Retracing the steps leading up to the dimensionless equations (3.40) we see that

these are reproduced exactly, with the substitutions

$$v^+ \to v^+ - v^{tm} \tag{3.117}$$

$$v^- \to v^- + v^{tm} \tag{3.118}$$

$$\mathbf{C}[f] \to \frac{v^+}{v^+ - v^{tm}} \mathbf{C}[f] \tag{3.119}$$

and we get the control parameter

$$G^{tm} = \left(\frac{2(v^+ - v^{tm})(v^- + v^{tm})}{r_n \, (v^+ + v^-)} \right)^{\frac{1}{3}} \left(\frac{r_r}{v^- + v^{tm}} - \frac{r_c}{v^+ - v^{tm}} \right) \tag{3.120}$$

and the length scale

$$l_0 = \left(\frac{2(v^+ - v^{tm})(v^- + v^{tm})}{r_n \, (v^+ + v^-)} \right)^{\frac{1}{3}} \tag{3.121}$$

We observe that the results map onto those without treadmilling, with the growth and shrinkage velocities defined relative to the treadmilling velocity and a higher induced catastrophe rate. Furthermore, using the scaling relations (3.43), we can map the increased induced catastrophe and zippering rates back to their non-treadmilling values, using $\alpha = v^+ / (v^+ - v^{tm}) \geq 1$.

The existence of this one-to-one correspondence between treadmilling and non-treadmilling systems with the same relative velocities ($v^+ - v^{tm} =$ constant; $v^- + v^{tm} =$ constant) has a few interesting consequences. Although the systems are qualitatively the same, the treadmilling system shows nontrivial behavior over a larger range of values of G^{tm}. Furthermore, the density of the equivalent treadmilling system is *lower* than that of the non-treadmilling system. In fact, the average number of intersections per microtubule $\bar{\Lambda}^*$ at the bifurcation point (3.62) becomes

$$\bar{\Lambda}^* = -\frac{2(v^+ - v^{tm})}{\pi v^+ \hat{c}_2}, \tag{3.122}$$

the value of which can be made arbitrarily small by increasing the treadmilling velocity. The presence of a bifurcation at low densities can readily be understood because of the fact that treadmilling microtubules have a higher collision rate for a given density than non-treadmilling microtubules.

Finally, we may take into account the fact that only a limited amount of tubulin is present through the modified polymerization velocity expression (3.73). For the special case of solutions for which $G^{tm} = 0$, the equivalent of the steady state density equation (3.74) in the presence of treadmilling becomes

$$k_{total}^{tm} = \frac{k_{max}}{r_r \, v_0^+} \left(r_r (v_0^+ - v^{tm}) - r_c (v^- + v^{tm}) \right) \leq k_{total}. \tag{3.123}$$

The combination of treadmilling and finite availability of tubulin dimers thus leads to a lower overall density of microtubules compared to a non-treadmilling system with the same relative velocities.

APPLICATION TO THE COLLISION INDUCED ORGANIZATION MODEL BY BAULIN ET AL.

The results obtained in the presence of treadmilling allow us to apply the theory that has been developed in this chapter to the model described by Baulin et al. (2007). That model specifies microtubules that grow with a constant velocity v^+ at their plus ends and shrink with a constant velocity v^{tm} at their minus ends. When a microtubules collides with another one, its plus end remains stationary until the other microtubule has moved on, freeing the way for continued polymerization. Nucleation takes place with a constant rate in a random direction and zippering is not considered.

In this problem, we have $P_c(\theta) = 1$ and $P_z(\theta) = 0$. The stalling of microtubules can be represented by induced catastrophes to a shrinking state with $v^- = 0$. Note that spontaneous catastrophes do not occur ($r_c = 0$). Within this model, rescues are no longer a process that is intrinsic to the microtubules, but their occurrence depends on the environment. When a microtubule is stalled due to a collision with another microtubule of length l, the average stalling time will be $\tau_l = l/(2v^{tm})$. Denoting the probability distribution of a microtubule in direction θ to collide with a microtubule in direction θ' by $p(\theta \to \theta')$, and realizing that the steady state density is proportional to $l^2(\theta)$, we obtain the following angle-dependent expression for the rescue rate.

$$r_r(\theta) = \int \frac{2v^{tm} p(\theta \to \theta')}{l(\theta')} \mathrm{d}\theta' \tag{3.124}$$

$$= 2v^{tm} \frac{\int \sin\left(|\theta - \theta'|\right) l^2(\theta')/l(\theta')\mathrm{d}\theta'}{\int \sin\left(|\theta - \theta''|\right) l^2(\theta'')\mathrm{d}\theta''} \tag{3.125}$$

$$= 2v^{tm} \frac{\mathbf{C}[l](\theta)}{\mathbf{C}[l^2](\theta)}. \tag{3.126}$$

Using this expression and the parameter values fixed above, the full set of model equations (3.40) reduces to

$$\frac{1}{L(\theta)} = -2\frac{\mathbf{C}[L](\theta)}{\mathbf{C}[L^2](\theta)} + \alpha\mathbf{C}[L^2](\theta) \tag{3.127}$$

with the only parameter

$$\alpha = \frac{v^+}{v^+ - v^{tm}}. \tag{3.128}$$

It follows that the isotropic average length is given by

$$\bar{L} = \left(\frac{3}{\alpha \hat{c}_0}\right)^{1/3} = \left(\frac{3\pi}{4\alpha}\right)^{1/3}, \tag{3.129}$$

or, in dimensional units, by

$$\bar{l} = \left[\frac{3\pi v^{tm}(v^+ - v^{tm})^2}{2r_n(v^+)^2}\right]^{1/3}, \tag{3.130}$$

conform equation (C.5) from Baulin et al. (2007).

Applying the bifurcation analysis from section 3.2.2 to equation (3.127) yields the bifurcation condition

$$L^* = \left[\frac{1}{\alpha} \left(-\frac{1}{2\hat{c}_2} - \frac{1}{\hat{c}_0} \right) \right]^{1/3} = \left(\frac{\pi}{8\alpha} \right)^{1/3} \tag{3.131}$$

for the lowest mode. Comparing this with the isotropic length $\bar{L}$ shows us that $\bar{L} > L^*$, for any value of α. Because the steady state length is *always* longer than the critical length, the isotropic state cannot be stable. Also, although no firm conclusions can be drawn without a detailed study of equation (3.127), it is well possible that no bounded ordered solution exists, given the structure of the bifurcation diagrams in figure 3.4. Both conclusions are in agreement with the observations from simulations that were reported by Baulin et al. Naturally, restricting the available amount of tubulin through the introduction of a tubulin pool would suffice to stabilize the diverging ordered solutions to this model.

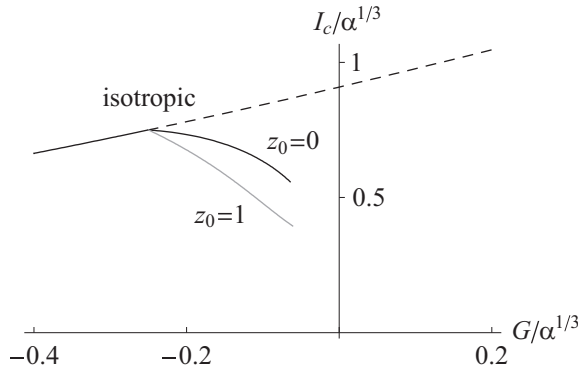## 3.F   Comparing spontaneous and induced catastrophes

Figure 3.9: Plot of the ratio of the effective induced catastrophe rate per microtubule and the spontaneous catastrophe rate. The results have been calculated for the minimal model with $\hat{c}_0 = 3/4$ and both $\hat{z}_0 = 0$ and $\hat{z}_0 = 1$.

There are two processes that cause a microtubule to switch from a growing to a shrinking state. The first is the occurrence of a spontaneous catastrophe, which we have modelled by a constant catastrophe rate r_c. The second is the induction of a catastrophe, triggered by a collision with another microtubule. Whereas the spontaneous catastrophe rate r_c is a model parameter, the induced catastrophes are

an emergent property of the system. This discrepancy causes some difficulties in the comparison of the theory (and simulations in later chapters) with experiments.

In experimental measurements of the catastrophe rate (for example in Vos et al., 2004), the distinction between spontaneous and induced catastrophes is usually not made. The measured value is therefore effectively an upper bound for the spontaneous catastrophe rate, the input parameter in our model. In this section, we will determine the ratio between induced and spontaneous catastrophes within the context of our model. The results can be used to make an educated guess of the spontaneous catastrophe rates from measured data of the total catastrophe rate.

The spontaneous catastrophe rate density is given by

$$\mathbb{C}_s = r_c \sum_i \int d\theta \int dl \, m_i^+(\theta, l) \tag{3.132}$$

$$= \frac{r_c}{u\pi l_0^2} \int d\theta \, T(\theta) \tag{3.133}$$

and the induced catastrophe rate density by

$$\mathbb{C}_i = v^+ \sum_i \int d\theta \int dl \, m_i^+(\theta, l) \int d\theta' c(\theta - \theta') k(\theta') \tag{3.134}$$

$$= \frac{v^+}{r_c \pi l_0^3} \int d\theta \, T(\theta) \mathbf{C}[K](\theta). \tag{3.135}$$

Hence the ratio of induced to spontaneous catastrophes is given by

$$\frac{\mathbb{C}_i}{\mathbb{C}_s} = \left(\frac{v^+}{r_c l_0}\right) \frac{\int d\theta \, T(\theta) \mathbf{C}[K](\theta)}{\int d\theta \, T(\theta)} \equiv \left(\frac{v^+}{r_c l_0}\right) I_c. \tag{3.136}$$

We note that the scale is set by the ratio of the free run length v^+/r_c to the length scale l_0. In the isotropic case, this expression simplifies to

$$\frac{\bar{\mathbb{C}}_i}{\bar{\mathbb{C}}_s} = \frac{v^+ \hat{c}_0 \bar{K}}{r_c l_0}. \tag{3.137}$$

In order to get a sense for the scale of the resulting number, we evaluate $\bar{K}$ at $G = 0$, yielding $\hat{c}_0^{-2/3}$, which is a reasonable assumption for $G \approx 0$. Using this assumption, we get the following expression for the relation between the spontaneous catastrophe rate r_c and the total measured catastrophe rate r_c^{total}:

$$r_c = r_c^{total} - \frac{v^+ \hat{c}_0^{1/3}}{l_0}. \tag{3.138}$$

Of course, this estimate is only approximately valid for measurements done in the isotropic state. For ordered solutions, we must evaluate I_c in (3.136) explicitly. Figure 3.9 shows the value of I_c for the simplified model with $\hat{c}_0 = 3/4$, for both the

isotropic and the ordered solutions with $\hat{z}_0 = 0$ and $\hat{z}_0 = 1$. We note that ordered solutions generally correspond to a value of $I_c \approx \alpha^{1/3}/2$. This can be combined with the generic expression

$$r_c = r_c^{total} - \frac{v^+}{l_0} I_c, \qquad (3.139)$$

to estimate the true value of r_c from experimental data. Using the data summarized in Vos et al. (2004), we see that $r_c^{total} = 0.6 \pm 0.1 \text{ min}^{-1}$ and $v^+/l_0 = 2.3 \pm 0.2 (\mu m/s)^{2/3} r_n^{1/3}$ (interphase; raw data across studies). Assuming a nucleation rate of $r_n = 10^{-2} \text{min}^{-1} \mu m^{-2}$ and $I_c = 0.4$ we obtain $r_c = 0.4 \pm 0.1 \text{min}^- 1$, approximately two-thirds of the measured catastrophe rate.

Simulating the cortical array: alignment

4

In chapters 2 and 3 we have used analytical methods for the analysis of microtubule dynamics and the formation of the cortical array. When possible, this is the preferred approach because it allows one to make generic statements about a system's behavior and discover connections that may otherwise have remained hidden. An example of the latter is the extraction of the parameter G in the previous chapter.

However, there are limits to the applicability of the theoretical model, due to two intrinsic difficulties. Firstly, the translation of the conceptual model for interacting microtubules to an analytical model involves an inevitable coarse-graining step that should be justified *a posteriori*. Secondly, many (combinations of) additional relevant mechanisms cannot be included without resulting in a practically unsolvable model.

For these reasons, this and the following chapter focus on explicit simulations of the cortical array model consisting of individual microtubules. The simulation results are first compared to the theoretical predictions from the previous chapter. Furthermore, we investigate the effect of combinations of processes that have been studied in isolation in the previous chapters, namely the combination of microtubule zippering and treadmilling and the effect of microtubule severing on interacting microtubules.

Simulations of the microtubule cytoskeleton have traditionally focused on the more common case of animal cells, in which the microtubules are relatively free to move in three dimensions, controlled by the actions of motor proteins (Karsenti et al., 2006). In plant cells, however, the microtubules are mostly confined to the two-dimensional inner surface of the cell membrane, thought to be held in place by protein complexes (Barton et al., 2008; Sainsbury et al., 2008). The result of this plant-specific constraint is that microtubule locomotion is controlled only by polymerization and depolymerization. Baulin et al. (2007) have presented a two-dimensional simulation model for treadmilling rods that displays a collision-induced ordered phase, but this model does not incorporate the intrinsic dynamic instability of the

microtubules, and microtubule collisions only lead to pausing. These mechanisms *have* been included in the simulations by Dixit and Cyr (2004), but unfortunately those simulations were hampered by biased initial conditions, small microtubule numbers and short run times. In this chapter we present a simulation method that is specific to the plant cell cortical microtubules and has the speed and accuracy that is required to make substantiated statistical statements about the ability of the microtubules to form an ordered array for a given set of parameters.

4.1   Simulation model

The model that is used for the simulations is similar to that introduced in chapter 3. Microtubules are confined to a two-dimensional surface that, in the context of this chapter, is a flat square surface with periodic boundary conditions. The microtubules themselves are modelled as rigid rods, or, in the presence of zippering, series of connected rigid rods. New microtubules of infinitesimal length are nucleated at random locations with random directions at a fixed rate r_n per unit of area.
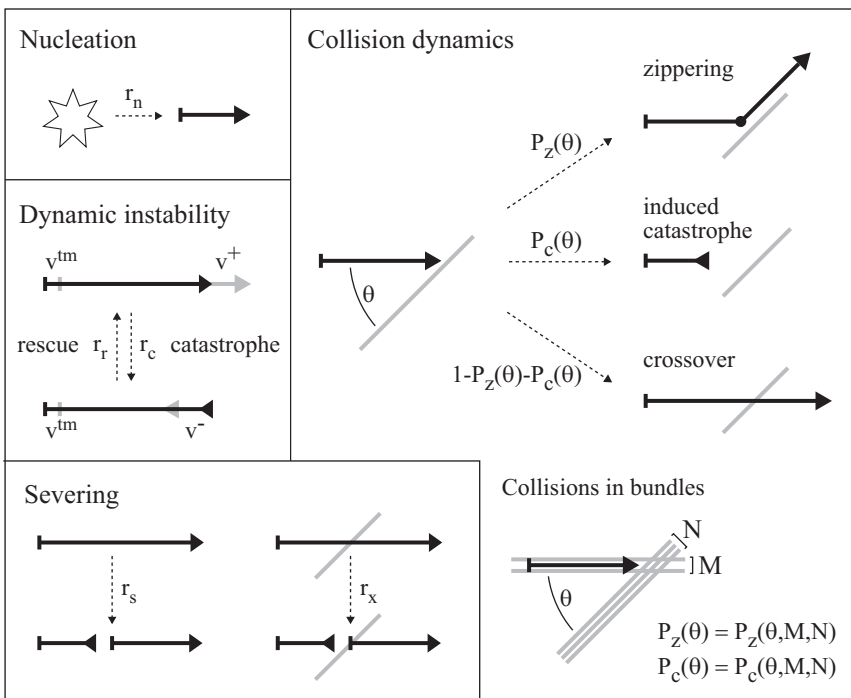

Figure 4.1: Schematic representation of the elements of the model. See also the description of the parameters in table 4.1.

Each microtubule has two distinct ends. The so-called plus end exhibits dynamic instability, alternating between growing and shrinking states. In the growing state, it extends with a speed v^+ and in the shrinking state it shrinks with a speed v^-. The spontaneous switch from the growing to the shrinking state is called a *catastrophe* and occurs with a fixed rate r_c; the switch back to the growing state, the *rescue*, occurs with a rescue rate r_r. The other end of the microtubule depolymerizes steadily with a fixed speed v^{tm}. For an overview of the parameter values that are used in the simulations, see table 4.1.

In cells, there is a limited supply of the tubulin dimers that can be used to construct microtubules. The depletion of free tubulin will primarily affect the rate at which tubulin dimers polymerize on growing microtubule tips, and is linear to a first approximation (Mitchison and Kirschner, 1984). To model the effect of a finite tubulin pool we include the option to use a length-dependent growth rate, defined by

$$v^+(t) = v_0^+ \left(1 - \frac{L(t)}{L_{\max}} \right), \tag{4.1}$$

where L is the total length of the microtubules in the system, and $L_{\max}$ is the length-equivalent of the total amount of tubulin in the system[1]. This way, the total microtubule length is bounded by $L_{\max}$.

MICROTUBULE INTERACTIONS

The adherence of the cortical microtubules to the cell membrane ensures that there are frequent collisions of growing (polymerizing) microtubule ends with other microtubules, something that would be a rare occurrence for microtubules that are free to move in three dimensions. Such collisions have been found to result in one of three possible outcomes: (i) *zippering*, a reorientation of the growing tip alongside the other microtubule; (ii) *induced catastrophe*, a collision-induced switch to the shrinking state; (iii) *cross-over*, leading to a continuation of the growth in the original direction. Which of these outcomes is selected is a stochastic process that depends on the angle between the two microtubules involved. Figure 4.8 depicts experimental data on the relative occurrence of these outcomes, along with the approximation that is used for many of the simulations in this and the following chapter.

The possibility for microtubules to zipper alongside each other naturally leads to the formation of microtubule bundles. *In vivo*, bundling is speculated to involve microtubule-associated proteins, that could possibly influence the microtubule dynamics (Gaillard et al., 2008). For the sake of simplicity, we assume that the

---

[1]Something to watch out for in the case of a finite tubulin pool is that in the absence of shrinking microtubules the plus end growth speed will asymptotically approach the treadmilling velocity. In this case, the depolymerization rate at the minus end eventually equals the polymerization rate at the plus end. If additional microtubules are nucleated in this limit, it will lead to the unrealistic situation where the system becomes populated with treadmilling microtubules of vanishing length. Currently, this exception is explicitly handled by the simulation code, but a more extensive treatment of the tubulin pool would have to address the effects of tubulin availability on the nucleation rate.

formation of a bundle does not influence the dynamic instability parameters of the microtubules within the bundle. However, we should nevertheless address the question of how single-microtubule collision probabilities translate to the situation where one or both of the microtubules involved are part of a bundle. For instance, does a microtubule that collides with a bundle of three microtubules have the same probability to undergo a catastrophe as one that collides with a single microtubule at the same angle of incidence? We will consider four different scenarios, described in more detail below.

single collision In this case, microtubules ignore the presence of other microtubules in the same bundle, and collisions with another bundle are treated as a *single* collision with a solitary microtubule.

sticky bundles This scenario assumes that microtubules have a strong affinity for other microtubules in the same bundle, resulting in microtubules *always* crossing over another (bundle of) microtubule(s) if a microtubule from the same bundle has already crossed it. In other situations, the 'single collision' scheme is used.

no zippering from bundles In a variation of the *sticky bundle* scheme, microtubules that are part of a bundle will not zipper alongside other microtubules, but they can still undergo an induced catastrophe. Every encountered bundle is treated as a single collision.

bundle multi-collisions In an attempt to approximate the coarse-grained dynamics of the analytical model presented in chapter 3 we introduce a final interaction mode that aims to nullify the effect of bundles. Collisions between bundles are treated as a dense series of collisions between one of M parallel incoming microtubules with N oblique microtubules (see figure 4.1). Appendix 4.B describes this method in more detail, along with a method to compute the resulting probabilities for zippering $P_z(\theta, M, N)$ and catastrophe induction $P_c(\theta, M, N)$.

MICROTUBULE SEVERING

Microtubule severing by the enzyme katanin has been observed to occur in the cortical array, and is thought to play a significant role in the ability of the microtubules to align successfully (Burk et al., 2007). Generally, the severing of microtubules can be divided into three types. The first type is when katanin acts to detach a microtubule from its nucleation site, thereby enabling treadmilling. This severing process is not simulated explicitly, but the effect of treadmilling is investigated in section 4.4.2. The second type of severing occurs at random positions along the length of a microtubule, a process that has been discussed in detail in chapter 2. In our theoretical and simulation models, this type of severing has been implemented as a constant severing rate r_s per unit length. After a microtubule has been severed, the newly created plus

Parameter	Description	Value
v_0^+	growth speed	$0.078\ \mu\text{m s}^{-1}$
v^-	shrinkage speed	$0.164\ \mu\text{m s}^{-1}$
v^{tm}	treadmilling speed	$0.02\ \mu\text{m s}^{-1}$
r_r	rescue rate	$6.8 \times 10^{-3}\ \text{s}^{-1}$
r_c	catastrophe rate	variable: $3 \times 10^{-3} - 1.2 \times 10^{-2}\ \text{s}^{-1}$
r_n	nucleation rate	$0.002\ \text{s}^{-1}\mu\text{m}^{-2}$
r_s	severing rate	$0\ \text{(default)} - 2 \times 10^{-4}\ \mu\text{m}^{-1}\text{s}^{-1}$
r_x	intersection severing rate	$0\ \text{(default)} - 0.05\ \text{s}^{-1}$
$L_{\max}$	total tubulin pool (length equiv.)	$5\ \mu\text{m}, \infty\ \text{(default)}$
$W \times H$	system size (periodic)	$80 \times 80\ \mu\text{m}$

Table 4.1: Overview of all parameters and variables with their default values (when applicable). The dynamic instability parameters are taken from Vos et al. (2004) and the value for v^{tm} has been approximated from the data by Shaw et al. (2003). The nucleation rate has been selected to give rise to an ordered state in combination with the chosen dynamic instability parameters and the interaction functions measured by Dixit and Cyr (2004) (see also section 3.3). Because biological observations have made no distinction between spontaneous and collision-induced catastrophes, the reported value for r_c ($4.7 \times 10^{-3}\text{s}^{-1}$) is likely to be too high, by an unknown factor (see section 3.F). Because of this uncertainty and the fact that G is a linear function of r_c, we use the spontaneous catastrophe rate r_c as our primary means to change the value of the control parameter G. The system size corresponds to a reasonable measure for the surface area of a young Tobacco BY-2 cell (Jan Vos, personal communication; see also chapter 5) and strikes a good balance between simulation speed and suppression of finite size effects. For the interaction functions, see figure 4.8.

end immediately undergoes a catastrophe, placing it in the shrinking state. There is some controversy about the importance of this mode of severing in plant cells (Burk et al., 2007). The final type severing was reported by Wightman and Turner (2007), who observed that, in *Arabidopsis* cotyledons, severing takes place almost exclusively at locations where one microtubule crosses over another microtubule. In our simulation model, this is represented by a separate severing mechanism that severs each intersection with a rate r_x. The microtubule that is severed is always a microtubule that has crossed over a pre-existing microtubule. The microtubule that is severed is the one on the cytoplasmic side, i.e. 'on top' if we view the membrane as the surface on which the microtubules move. Similarly, in the case of overlapping bundles, a microtubule is selected at random from the second bundle to arrive at the intersection.

4.2   Simulation method

The model described above leads to dense systems with many interactions and spontaneous events such as nucleations or catastrophes. Between these events, microtubules are steadily growing and shrinking. To simulate the cortical array model in a way that is both accurate and fast, we have opted for an event-driven simulation method. Whenever an event has taken place, the time of the next event is computed, the microtubule lengths are updated to reflect that time and the next event is executed. This cycle is repeated until a stop event is encountered, indicating that the end of the simulation has been reached. For the implementation, we make a distinction between deterministic and stochastic events. Deterministic events are those events for which the event time is fully determined by the state of the system, whereas stochastic events are the result of a random process. Table 4.2 lists the relevant events of both classes for our model. The simulation scheme for the queuing and evaluation of stochastic and deterministic events is explained in more detail below and summarized in figure 4.2.

stochastic events	deterministic events
nucleations	collisions
catastrophes	shrinking past previously crossed intersections
rescues	disappearance of segments
severing	simulation control (measurement, stop)

Table 4.2: Division of the simulation events into two classes: deterministic and stochastic events.

STOCHASTIC EVENTS

Because all stochastic events are independent and memoryless, we use a kinetic Monte Carlo algorithm (Fichthorn and Weinberg, 1991) to determine the next stochastic event, with two twists: (1) the event rates are typically time-dependent and (2) before a stochastic event is executed, its time is compared with the first deterministic event. If the deterministic event should occur at an earlier time, it is executed first and a new stochastic time is computed, because the result of the deterministic event will typically affect the stochastic event rates.

Each stochastic event that can occur is associated with an event rate $r_i(t)$. Most event rates are constant between events, with the exception of the severing rate, which is dependent on the total length of growing and shrinking microtubules. The total event rate is given by

$$R(t) = \sum_i r_i(t) \tag{4.2}$$

The value – and time-dependence – of $R(t)$ will depend on the state of the system. For a given rate, the time interval Δt_s to the next stochastic event can be computed
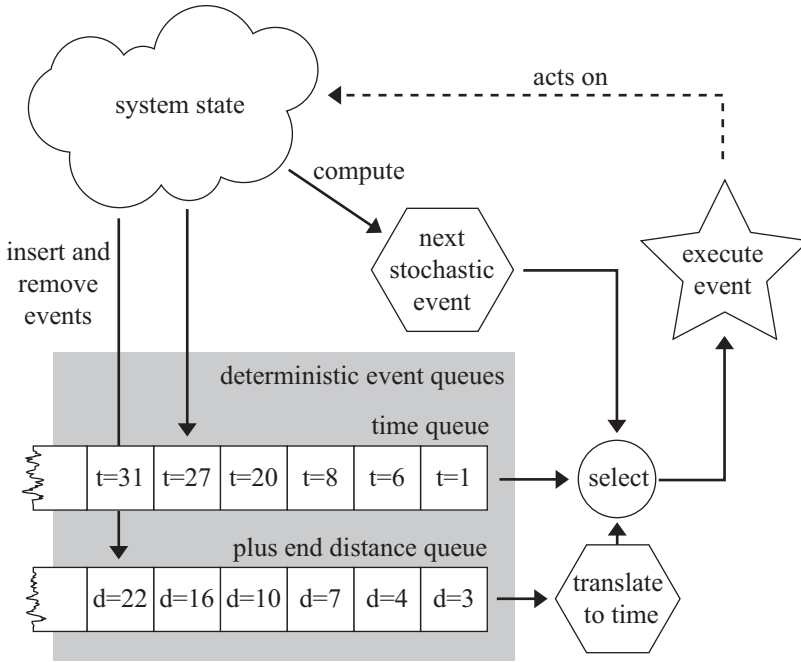
Figure 4.2: Schematic depiction of the event-driven simulation scheme. Two queues of deterministic events are maintained, and updated according to the state of the system. The system state also determines the timing of the next stochastic event. The nearest event is selected and executed, which usually changes the state of the system. The cycle is repeated until a stop event is encountered.

from the expression

$$\int_{t}^{t+\Delta t_s} R(t')\mathrm{d}t' = -\log(u),\qquad(4.3)$$

where u is a uniform number in $(0,1]$. An explicit expression for Δt_s is derived in appendix 4.C. Because the stochastic events have no memory, we may recalculate Δt_s whenever it is (potentially) invalidated, such as after the execution of any deterministic event.

The interval Δt_s indicates the occurrence of the first stochastic event of any type. The specific type of stochastic event that takes place is determined by selecting an event at random proportionally to the corresponding rates $r_i(t+\Delta t_s)$, evaluated at time $t+\Delta t_s$.

For a given state of the system, deterministic events – such as collisions – occur at a known time in the future. This allows us to pre-compute the times at which deterministic events will take place and store them in a queue. At any given time, the front of the queue indicates the time interval Δt_d to the first deterministic event. This interval is compared with the interval Δt_s for the first stochastic event and the one with the shortest interval is executed. The resulting change in the state of the system will typically cause new deterministic events to be added to the queue, or obsolete events to be invalidated.

The process of handling deterministic events is more complicated when a finite tubulin pool is used. In that case, the speed of the growing plus ends is dependent on the total length of all microtubules in the system (see equation (4.1)). As a consequence, the time it takes a plus end to travel a certain distance to the next collision depends on the dynamics of all microtubules in the meantime. In particular, these dynamics are potentially affected by intermediate deterministic and stochastic events. It is therefore no longer possible to calculate collision times *a priori*.

This problem is resolved by the creation of a second deterministic event queue, specifically for the plus end collisions. This queue does not store (and sort) events by their time of occurrence, but rather by the distance that has to be covered by a growing plus end to reach to the collision position. Because all plus ends are affected equally by the limited tubulin pool, their relative positions in the queue are conserved by the dynamics of the system. To determine from which queue the next deterministic event should be taken, the plus end distance of the first event is converted to an event time that can be compared to the event time from the other queue. Functions to convert from plus end distance to time and back are derived in appendix 4.D.

4.3   Analysis

ORDER PARAMETERS

To measure the degree of ordering in the system, we introduce the microscopic (i.e. derived from the individual particles) order parameter S_2

$$S_2 = \left| \langle e^{i2\theta} \rangle_l \right| = \frac{|\sum_n l_n e^{i2\theta_n}|}{\sum_n l_n} = \frac{\sqrt{\left(\sum_n l_n \cos(2\theta_n)\right)^2 + \left(\sum_n l_n \sin(2\theta_n)\right)^2}}{\sum_n l_n}, \qquad (4.4)$$

where the index n runs over the segments in the system, with length l_n and angle θ_n. The S_2 order parameter has a value of 0 for an isotropic system and a value of 1 for a fully oriented system. Note that this order parameter is insensitive to the polarity of the segments. In the coarse-grained limit, this definition is equal to definition (3.72) from chapter 3. Whereas the S_2 value gives an indication of the amount of order, the

dominant direction of this order is given by the angle

$$\Phi_2 = \arctan\left(\frac{\sum_n l_n \cos(2\theta_n)}{\sum_n l_n \sin(2\theta_n)}\right). \tag{4.5}$$

A problem particular to most experimental studies is that the spatial resolution of optical microscopy is too low to observe individual microtubules within a bundle. Although the relative brightness of the observed (bundles of) microtubules can give some guidance, this is generally inaccurate (Barton et al., 2008). To account for this effect, we may also compute worst case 'optical' measures for the density and the S_2 order parameters. These measures are determined by counting the bundled sections of microtubules as a single microtubule. The optical density will therefore necessarily be lower than the actual density, and the difference between the two provides insight into the degree of bundling. The optical S_2 value will generally also be lower than the real value, because bundles (which contribute more to S_2) tend to be oriented more towards the direction of global alignment than the average microtubule.

CONTROL PARAMETERS

The work in chapter 3 has allowed us to identify two control parameters that can assist in the understanding of the simulation results, and clarify their dependence on the system parameters. These compound parameters are the natural length scale l_0 and the control parameter G, that, for a given set of angular interaction probabilities, determines the steady state properties of the system. Higher values for G generally correspond to more ordered systems.

The expressions for l_0 and G were initially derived in the context of a model that includes microtubule zippering but not the treadmilling motion of the minus end. In section 3.E, these definitions were extended to include treadmilling, at the expense of zippering. Because the definitions for the treadmilling-only case reduce to those for the zippering-only case when $v^{tm} = 0$ (no treadmilling), we use the treadmilling parameters to interpret all simulation results in this chapter. Note that we also use these parameters for the simulations with *both* zippering and treadmilling, for which the theory gives no guidance.

In the absence of treadmilling, the natural length scale l_0 is given by (3.35), which translates into (3.121) when treadmilling is enabled:

$$l_0^{tm} = \left(\frac{2(v^+ - v^{tm})(v^- + v^{tm})}{r_n(v^+ + v^-)}\right)^{\frac{1}{3}}. \tag{4.6}$$

The control parameter G is defined by equation (3.40e), and its treadmilling equivalent is given by (3.120). The change in control parameter for a treadmilling system is accompanied by a scaling of the interaction functions with a factor $v^+/(v^+ - v^{tm})$, which reduces to 1 as the treadmilling velocity vanishes. Using the scaling properties of the system (see section 3.1.4) we find that the system is ultimately controlled by

the value of the combined control parameter $G' = G^{tm}((v^+ - v^{tm})/v^+)^{1/3}$. Explicitly, G' is given by

$$G' = \left(\frac{2(v^+ - v^{tm})^2(v^- + v^{tm})}{r_n v^+ (v^+ + v^-)} \right)^{\frac{1}{3}} \left(\frac{r_r}{v^- + v^{tm}} - \frac{r_c}{v^+ - v^{tm}} \right). \qquad (4.7)$$

4.4   Results

The simulation model presented above has many independent parameters and there is a large variety of questions that can be addressed using the simulations. In this chapter we will focus on three aspects. We start by comparing the steady state simulation results with the theoretical predictions derived in chapter 3. Next, we look at a number of biologically observed processes and see how they affect the propensity for the system to align. As a final step we take a single set of parameters that closely matches experimental results and track the process of alignment as a function of time.

4.4.1   Comparison with the coarse-grained model

For the comparison with the theoretical results from chapter 3, we use the simplified interaction functions that were introduced in section 3.2.4, with $\hat{c}_0 = 3/4$ (to get an ordered phase at negative values of G') and $\hat{z}_0 = 0$ or 1 (to control zippering). The remaining parameter α is used to scale both the probabilities for zippering and induced catastrophes, at the expense of cross-over events. Figure 4.3 shows the resulting interaction probabilities, with zippering enabled and $\alpha = 1/2$.

To start, simulations were performed without zippering and treadmilling, and $\alpha = 1$, so that every perpendicular collision leads to a catastrophe. Figure 4.4a shows the resulting S_2-values as a function of G, both with and without rescue events. To adjust for the difference in rescue rates, the catastrophe rates for both systems were chosen to obtain an identical range of G values. The agreement between the two curves suggests that G is indeed the relevant control parameter, also for the simulations.

Furthermore, we note that there is substantial agreement between the measured S_2-values and the theoretical prediction (the solid line). The remaining differences are probably caused by a mixture of three factors: finite-size effects, finite-number effects and the existence of spatial correlations that are ignored in the coarse-grained model. Temporal correlations do not appear to be of great importance, because if this were the case, disabling the rescue events would have had a significant impact. To further probe the limit of large numbers and weak interactions in which the theory should provide exact results, we decreased value of α so that more collisions result in cross-over events. This should both decrease the spatial correlations and increase the number density. At the same time, we increased the nucleation rate by the same factor, to keep the value of $G/\alpha^{1/3}$ constant. The increased nucleation rate leads
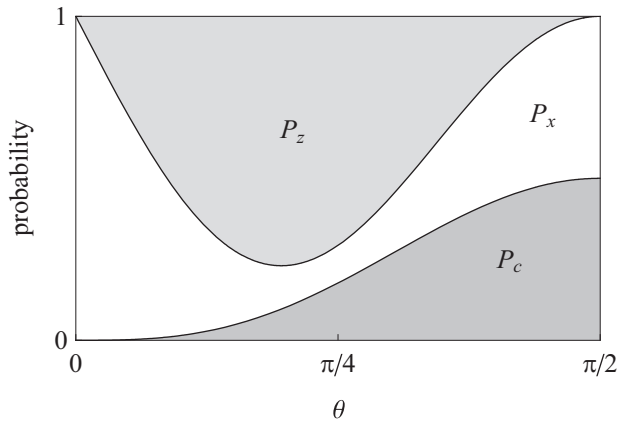
Figure 4.3: Overview of the collision outcome probabilities $P_c(\theta)$ (induced catastrophe), $P_z(\theta)$ (zippering) and $P_x(\theta)$ (crossover) for the simplified interaction functions defined in section 3.2.4, with $\alpha = 1/2$, $\hat{c}_0 = 3/4$ and $\hat{z}_0 = 1$. The predicted bifurcation value for G' is located at $G'/\alpha^{1/3} = -0.25$.

both to an increased number density and to a decrease of the natural length scale l_0, which should suppress the finite-size effects (for a given system size). Figure 4.4b shows that the results do indeed converge to the theoretical prediction in this limit.

The situation changes when we enable zippering ($\hat{z}_0 = 1$), which by its very nature introduces strong spatial correlations in the form of microtubule bundles. Figures 4.6 and 4.7 show the S_2 values as a function of $G/\alpha^{1/3}$, for all four bundle interaction modes under consideration. This time, we observe large differences in the onset of alignment, and correspondingly large deviations from the theoretical prediction. Furthermore, the results do not appear to converge to each other nor to the theoretical curve when α is decreased. The exception to this pattern is the multi-collision interaction mode, which has been constructed specifically to approximate the coarse-grained model (see appendix 4.B). Using this interaction mode, there still are large deviations from the theoretical solutions for moderate interaction strengths, but in the limit of very weak interactions ($\alpha = 0.01$) the simulation results do indeed converge to the predicted bifurcation point between the ordered and disordered states. Nevertheless, even with the multi-collision significant deviations from the theoretical curve remain visible for highly ordered systems. Most likely, this is caused by the fact that only microtubules that have previously crossed over the intersection are taken into account in the multi-collision computation. Microtubules that have previously zippered along the other bundle are ignored. This can have a marked effect on the validity of the multi-collision approximation if the strength of the interactions or the thickness of the bundles causes a significant fraction of the microtubules to
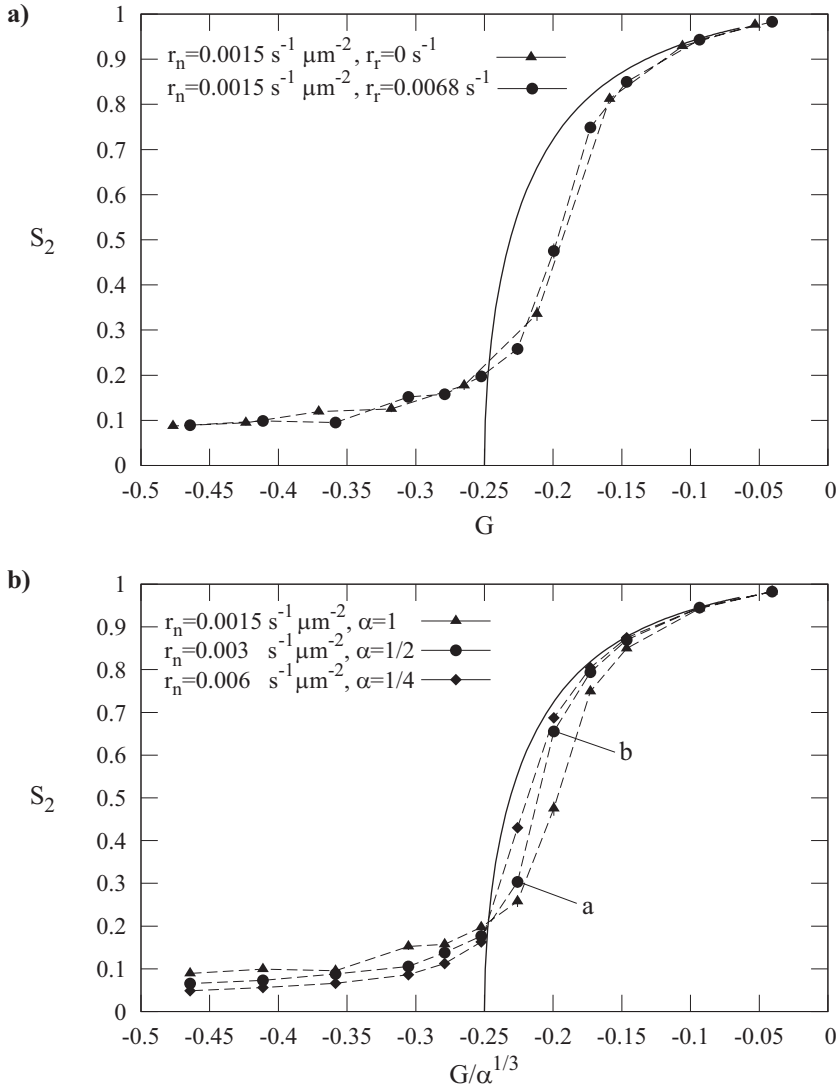
Figure 4.4: Steady state alignment as a function of $G/\alpha^{1/3}$, using interaction functions derived from those in figure 4.3 without zippering ($\hat{z}_0 = 0$) and with varying values of α. **(a)** Comparison of systems with and without rescue events; $\alpha = 1$ **(b)** Comparison of systems with different collision cross sections (α) and nucleation rates (r_n). In both graphs, the solid line represents the theoretical solution shown in figure 3.4. The point indicated by 'a' and 'b' corresponds to the panels in figure 4.5. All systems were initialized at the highest catastrophe rate (lowest G) and equilibrated for $50,000$ seconds before the alignment was measured. After that, the catastrophe rate was decreased and the procedure was repeated. Results were averaged over 80 runs and the standard error of the mean is indicated by vertical bars (not always visible). $r_c \in [10^{-3}, 9 \times 10^{-3}]$ s^{-1} (rescues disabled) or $r_c \in [4 \times 10^{-3}, 1.2 \times 10^{-2}]$ s^{-1} (rescues enabled). Non-default parameters are specified in the legends.
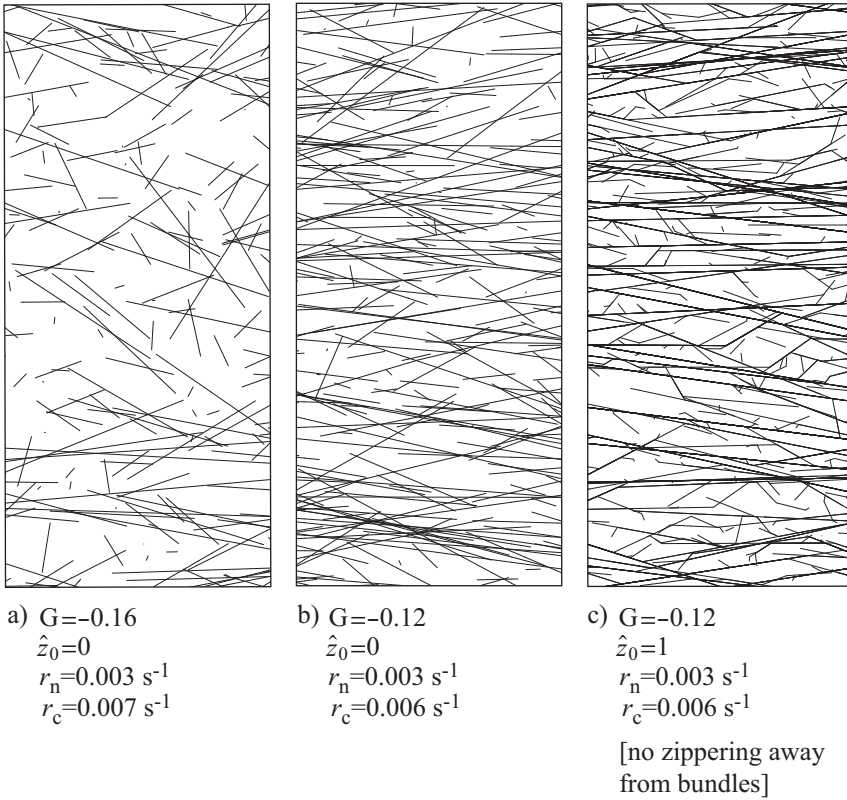
a) G=−0.16
   $\hat{z}_0$=0
   r_n=0.003 s^{-1}
   r_c=0.007 s^{-1}

b) G=−0.12
   $\hat{z}_0$=0
   r_n=0.003 s^{-1}
   r_c=0.006 s^{-1}

c) G=−0.12
   $\hat{z}_0$=1
   r_n=0.003 s^{-1}
   r_c=0.006 s^{-1}

   [no zippering away
   from bundles]

Figure 4.5: Snapshots of steady state systems at various parameter set-
tings. For all panels $\alpha = 1/2$, and panel (c) has been created using the
bundle interaction mode in which zippering away from a bundle is
not permitted. Each panel has been rotated for horizontal alignment
and covers an area of $5l_0 \times 11l_0$, where $l_0 = 3.3\,\mu$m for these parameter
settings.

zipper at a given intersection.

Summarizing, we see that the four bundle interaction modes lead to very different
results, even in the limit of weak interactions. The theoretical prediction is only
matched by the multi-collision interaction mode when combined with very weak
interactions. For the other cases, it only offers qualitative guidance: for the interaction
probabilities defined in figure 4.3, we see a sharp transition from disorder to order at
negative values of G. It follows that the details of the interactions between bundles
are of vital importance for the quantitative understanding of cortical array formation
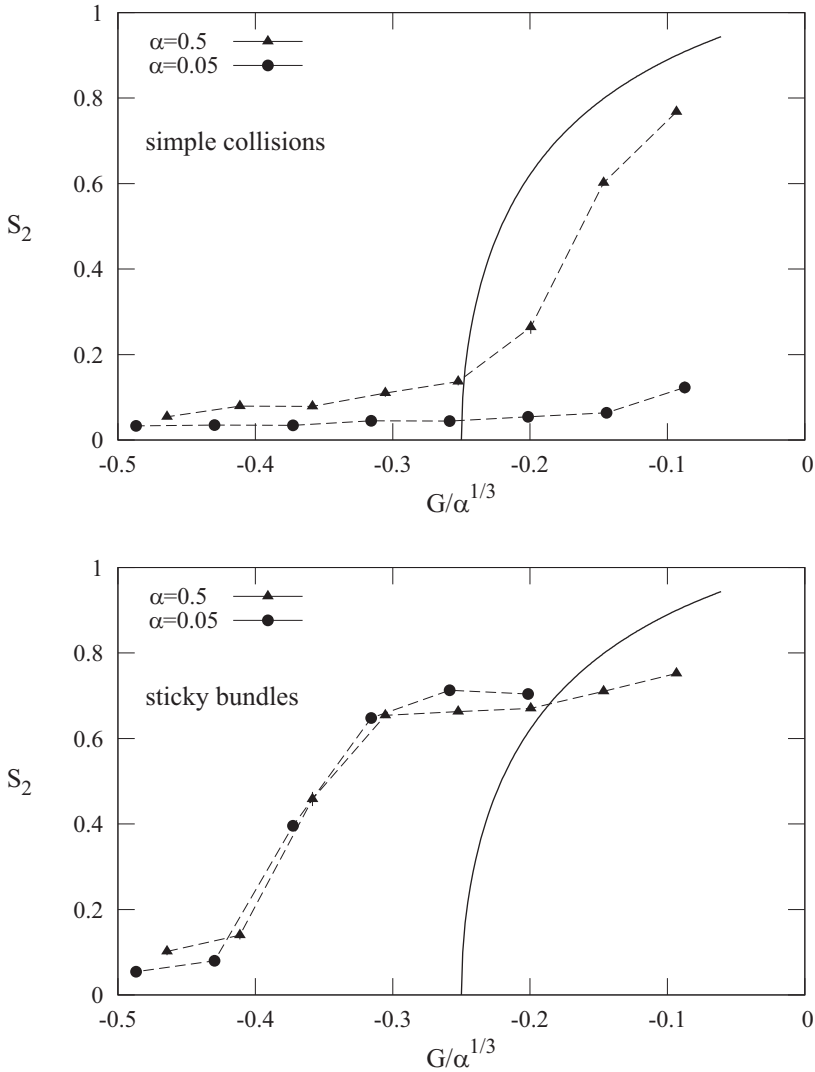in plant cells. In the absence of experimental leads, we apply Occam's razor and will

Figure 4.6: Steady state alignment as a function of $G/\alpha^{1/3}$ using the simplified interaction functions and zippering enabled ($\hat{z}_0 = 1$). Results are shown for simple bundle collisions and for 'sticky' bundles, each with two different collision cross sections α. The solid line represents the theoretical solution shown in figure 3.4. All systems were initialized at the highest catastrophe rate (lowest G) and equilibrated for 250,000 seconds before the alignment was measured. After that, the catastrophe rate was decreased and the procedure was repeated. Results were averaged over 40 runs ($\alpha = 0.5$) or 20 runs ($\alpha = 0.05$) and the standard error of the mean is indicated by vertical bars. $r_n = 3 \times 10^{-3}$ s^{-1}. For $\alpha = 0.5$: $r_c \in [5 \times 10^{-3}, 1.2 \times 10^{-2}]$ s^{-1}; for $\alpha = 0.05$: $r_c \in [4 \times 10^{-3}, 7.5 \times 10^{-3}]$ s^{-1}.
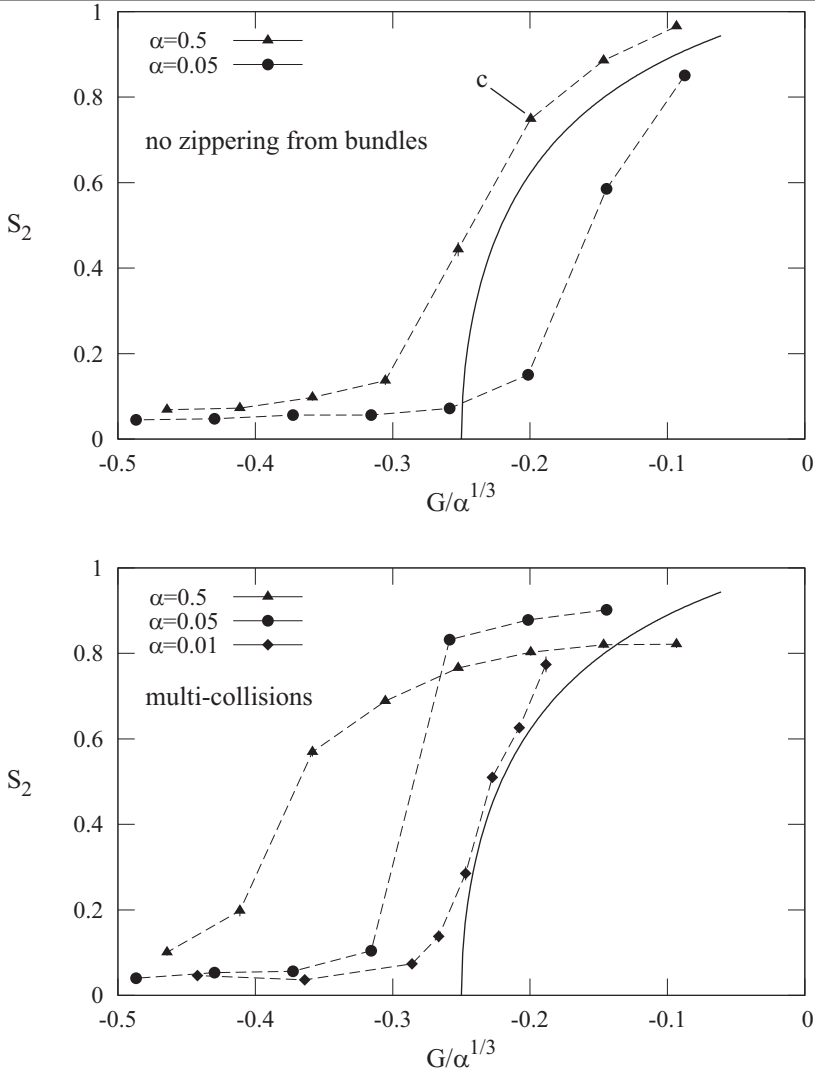
Figure 4.7: Steady state alignment as a function of $G/\alpha^{1/3}$ using the simplified interaction functions and zippering enabled ($\hat{z}_0 = 1$). Results are shown for the repression of zippering away from bundles and for multi-collisions, each with varying collision cross sections α. The solid line represents the theoretical solution shown in figure 3.4. The point indicated by 'c' corresponds to panel c in figure 4.5. All systems were initialized at the highest catastrophe rate (lowest G) and equilibrated for 250,000 seconds before the alignment was measured. After that, the catastrophe rate was decreased and the procedure was repeated. Results were averaged over 40 runs ($\alpha = 0.5$) or 20 runs ($\alpha = 0.05$, $\alpha = 0.01$) and the standard error of the mean is indicated by vertical bars. $r_n = 3 \times 10^{-3} \text{ s}^{-1}$. For $\alpha = 0.5$: $r_c \in [5 \times 10^{-3}, 1.2 \times 10^{-2}] \text{ s}^{-1}$; for $\alpha = 0.05$: $r_c \in [4 \times 10^{-3}, 7.5 \times 10^{-3}] \text{ s}^{-1}$; for $\alpha = 0.01$: $r_c \in [4.2 \times 10^{-3}, 5.5 \times 10^{-3}] \text{ s}^{-1}$.

use the simple single-collision interaction mode for the simulations in the remainder of this and the following chapter.

Figure 4.5 shows partial snapshots of three systems in the steady state. The first two are taken from non-zippering systems with different values of G, indicated by (a) and (b) in figure 4.4. The last one is taken from a system with zippering enabled (no zippering away from bundles), indicated by (c) in figure 4.7. The results can be compared with the theoretical equivalent presented in figure 3.6. The visible density differences between the figures are directly related to the corresponding deviations of the S_2 values from the theoretical results.

4.4.2   Realistic interactions and other control mechanisms

Having established the link with the theoretical results from the previous chapter, we continue by investigating the influence of various factors that have been reported to affect microtubule alignment. For the remainder of the simulations in this and the following chapter, we will use the experimentally motivated interaction probabilities that are shown in figure 4.8.

ZIPPERING AND TREADMILLING

In figure 4.9 we show the effects of treadmilling and zippering on the alignment of the cortical microtubules. In panel (a), the S_2 values are plotted as a function of G' (equation (4.7)). To start, we note that the parameter G' absorbs the effect of treadmilling, evidenced by the overlapping results for systems with and without treadmilling (in the absence of zippering). In addition, both results closely match the predicted transition between the ordered and disordered states, indicated by the short thick line. Switching on zippering (using the single collision interaction mode) leads to an increase of the order, in apparent contradiction to the result in figure 4.6 for the simplified interaction functions. This means that the qualitative effect of zippering not only depends on the bundle interaction mode, but also on the specific probabilities of the various collision outcomes. The fact that the S_2 values of the zippering systems reach a plateau below 1 is caused by persistent areas with slightly differing orientations. Because of the high zippering probability for shallow angles, the microtubules can move from one area to another without being penalized by an induced catastrophe. Finally, we note that switching on zippering for the treadmilling system leads to an even larger increase in alignment.

It is important to note that the results in 4.9a are plotted as a function of G', which allows us to link the results for a treadmilling system to theoretical predictions. However, because the definition of G' (4.7) involves the treadmilling velocity, figure 4.9a cannot be used to visually answer the question whether or not switching on treadmilling and/or zippering leads to an enhancement of alignment. For that purpose, figure 4.9b shows the same data as a function of G (the same as G' with $v^{tm} = 0$). In this figure we see that enabling treadmilling leads to a significant reduction in the level of alignment. This reduction does, however, go hand in hand with
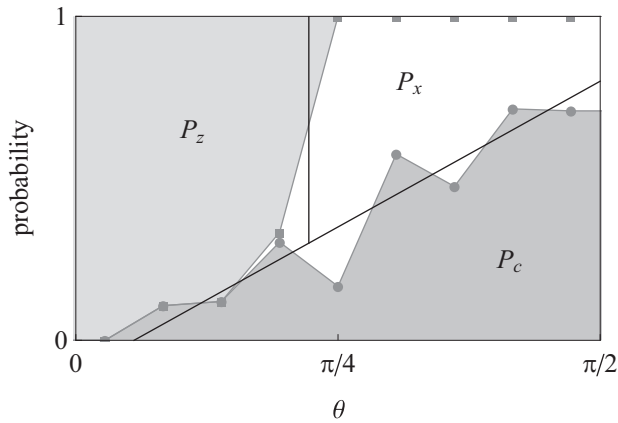
Figure 4.8: *In vivo* microtubule collision data from Dixit and Cyr (2004, combined data from MBD-DsRed and YFP-TUA6 labelling), where the collision outcome probabilities $P_c(\theta)$ (induced catastrophe), $P_z(\theta)$ (zippering) and $P_x(\theta)$ (crossover) are plotted on a cumulative scale. Every data point is plotted at the center of the corresponding bin (10° bin width), and the shaded regions have been extended to the boundaries using horizontal lines. Superimposed in black lines is the approximation that is used in simulations. In this approximation, the probability of an induced catastrophe increases linearly from 0 at 10° to 0.8 at 90°. When a collision does not lead to an induced catastrophe, it results in zippering for angles below 40° and a cross-over above 40°. The coarse-grained theory from chapter 3 predicts a bifurcation at $G' = -0.15$ for this interaction function.

decreased density and could therefore be (partially) offset by an increased growth velocity in the presence of a finite tubulin pool. When treadmilling is combined with zippering and plotted as a function of G there is a small net enhancement of the ordering ability, although it is not quite as large as the effect caused by zippering in the absence of treadmilling motion. Notably results for treadmilling and zippering in conjunction with the simplified interaction functions from the previous section (data not shown) also indicate a small beneficial effect from the combination of zippering and treadmilling, even though zippering alone is detrimental in that case.

MICROTUBULE SEVERING

As a next step we focus on the effects of microtubule severing. Generally, micro-tubule severing events fall into three categories. The first is severing at their base, releasing the microtubules from their nucleation site. This type of severing enables
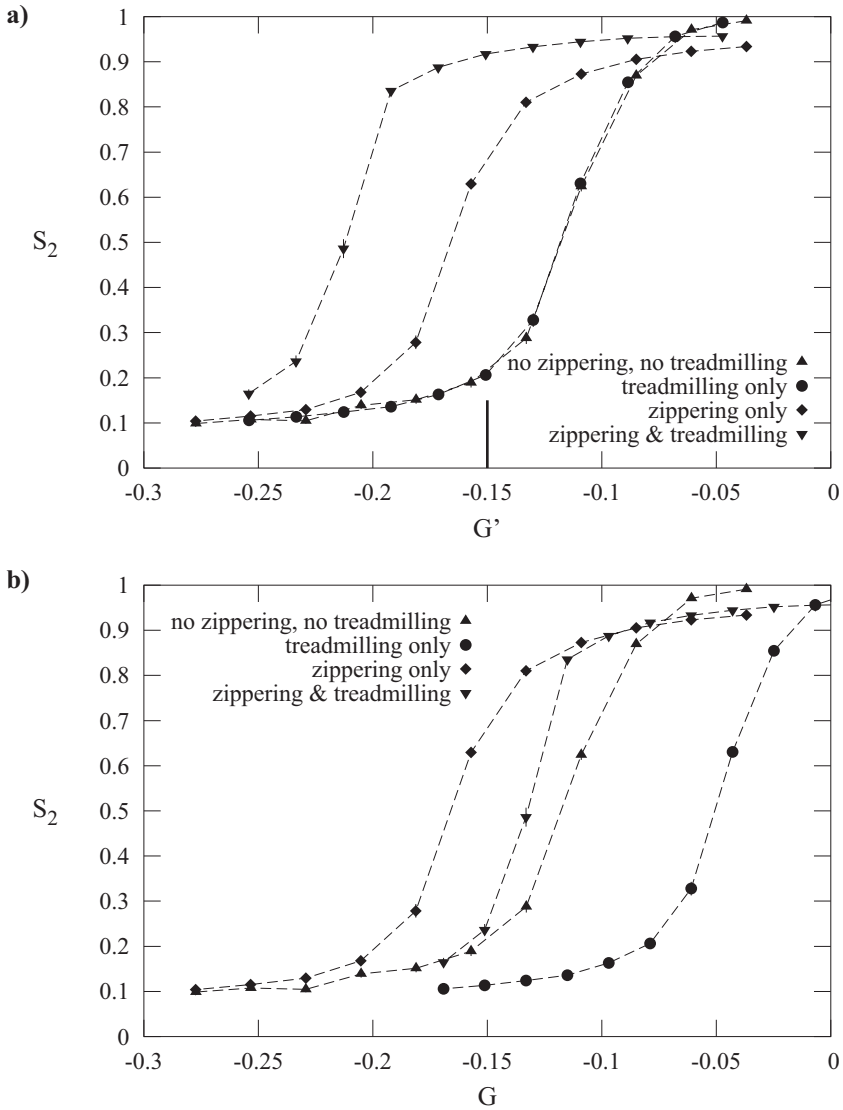
Figure 4.9: The influence of zippering and treadmilling on alignment using the Dixit
& Cyr interaction parameters. **a)** Alignment as a function of G'. The location of
the predicted bifurcation value is indicated by the thick vertical line. **b)** The same
data, plotted as a function of the non-treadmilling G parameter that is defined by
(3.40e). All systems were initialized at the highest catastrophe rate (lowest G') and
equilibrated for 50,000 seconds before the alignment was measured. After that,
the catastrophe rate was decreased and the procedure was repeated. Results were
averaged over 80 runs and the standard error of the mean is indicated by vertical bars.
For non-treadmilling systems $r_c \in [3 \times 10^{-3}, 6.75 \times 10^{-3}]$ s^{-1}; for treadmilling systems
$r_c \in [4 \times 10^{-3}, 9 \times 10^{-2}]$ s^{-1}.

treadmilling motion, the effect of which has been discussed in the previous section. In this section we subsequently focus on the two remaining severing mechanisms: uniform severing along the length of a microtubule and severing at microtubule intersections. Both types of severing will be applied to systems with neither treadmilling nor zippering and systems with both treadmilling and zippering.

Figure 4.10 shows the result of a uniform severing rate along the microtubule's length, for various severing rates. We note that in all cases, an increase in the severing rate leads to a decreased level of alignment. This is not unexpected, because we have seen in chapter 2 that, at a constant nucleation rate, severing leads to a decrease in the average microtubule length and a decreasing microtubule density. This results in a lower frequency of collision events that mediate the 'alignment negotiations' between microtubules.

In the upper graph of figure 4.11 we find a similar effect for severing at intersections, in the absence of zippering and treadmilling. However, the situation is dramatically reversed when both zippering and treadmilling are enabled. In that case, microtubule severing at intersections leads to a marked increase of the system's ability to align. The most likely explanation for this observation is related to the fact that for our implementation of severing at intersections, the microtubule that is severed is always part of the bundle (or single microtubule) that was last to arrive at that particular intersection (i.e., the one that is 'on top'). The microtubule bundles that are formed through zippering events are inherently more stable over time than individual microtubules, and are therefore more likely to be shielded from severing. This effective stabilization of bundles compared to individual microtubules is probably what enhances the ability to align.

4.4.3 Time-dependent properties

Up to this point we have only considered the steady state properties of the simulated systems. In this section we briefly investigate the time-dependent properties of systems for a single set of parameters. To best approximate the experimental observations, we enable both treadmilling and zippering (single collisions). Furthermore, we introduce a finite tubulin pool with a length density equivalent of $L_{\max} = 5\,\mu\text{m}/\mu\text{m}^2$, corresponding to a reasonable tubulin concentration in the cell[2]. It is further justified *a posteriori* because – for the selected parameters – it leads to approximately half of the available tubulin being incorporated into microtubules, in line with generic observations on tubulin distributions (Boal, 2002). As a result of the inclusion of a finite tubulin pool, the microtubule plus end velocity will become a time-dependent variable. Knowing that the density in the system will eventually stabilize at approximately half the value of $L_{\max}$ (see below), we have opted to *double*

---

[2]For a cylindrical cell with a length and diameter of $40\,\mu\text{m}$ where half of the space is taken up by the vacuole, and using the fact that a tubulin dimer has a length of 8 nm and there are 13 protofilaments in a microtubule, this corresponds to a tubulin concentration of 2.7 μM, not taking account the tubulin that is used outside of the cortex. This concentration is lower than the 20 μM that is commonly quoted (Boal, 2002), but not unreasonable given the substantial differences between plant and animal cells.
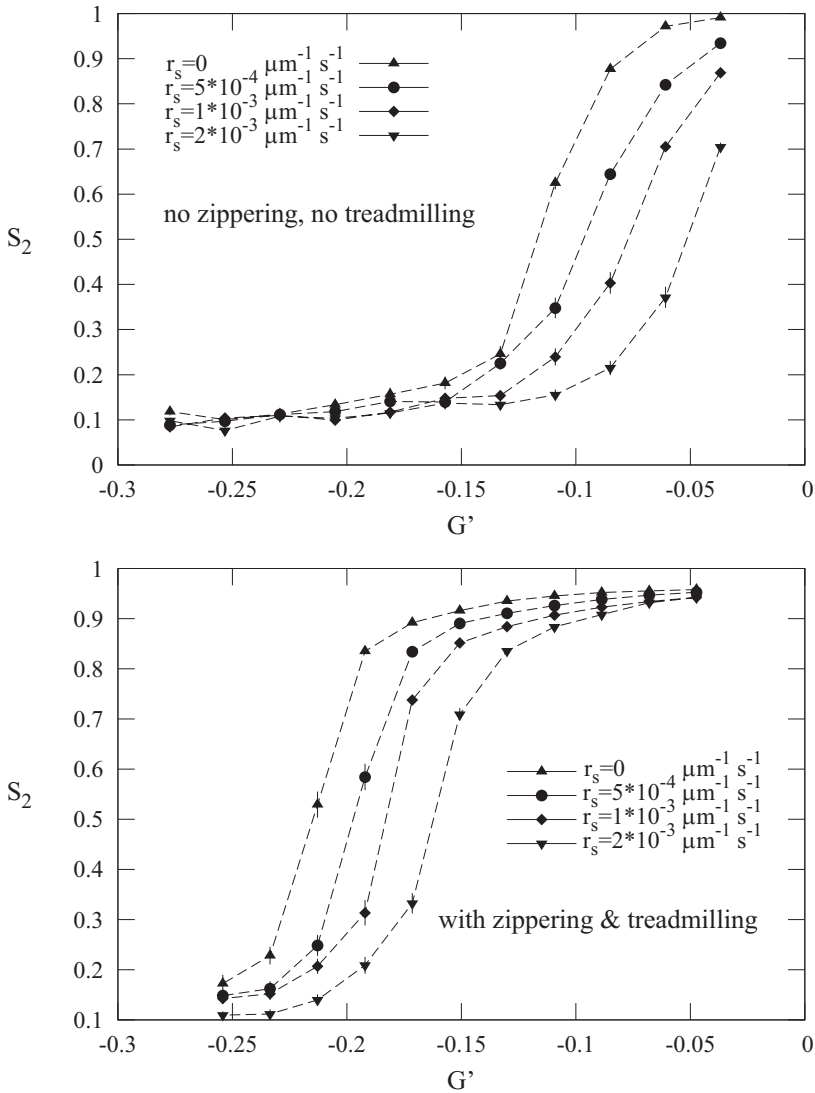
Figure 4.10: The effect of random microtubule severing on alignment. The Dixit & Cyr interaction model was used for all simulations, first without zippering and in the absence of treadmilling (top figure) and then with both zippering and treadmilling enabled (bottom figure). All systems were initialized at the highest catastrophe rate (lowest G') and equilibrated for $50,000$ seconds before the alignment was measured, the catastrophe rate was decreased and the procedure was repeated. Results were averaged over 40 runs and the standard error of the mean is indicated by vertical bars. For non-treadmilling systems $r_c \in [3 \times 10^{-3}, 6.75 \times 10^{-3}]$ s^{-1}; for treadmilling systems $r_c \in [4 \times 10^{-3}, 9 \times 10^{-2}]$ s^{-1}.
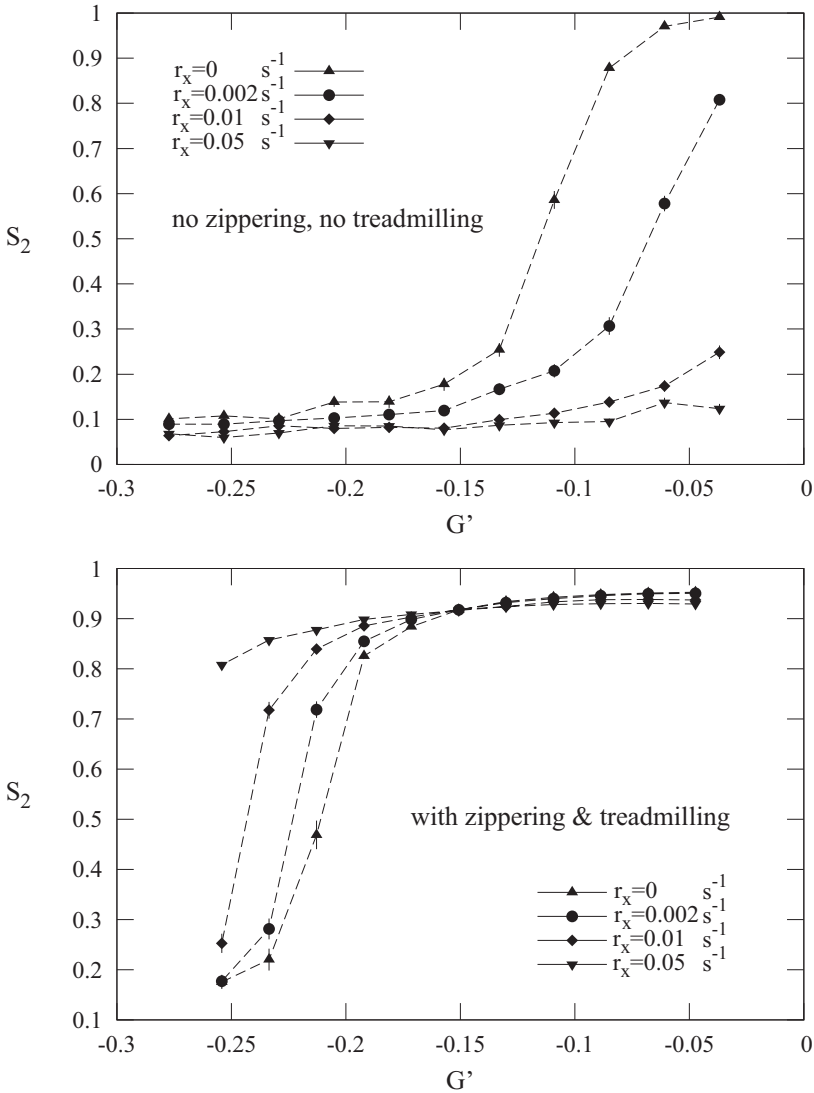
Figure 4.11: The effect of severing at microtubule intersections on the system's ability to align. The Dixit & Cyr interaction model was used for all simulations, first without zippering and in the absence of treadmilling (top figure) and then with both zippering and treadmilling enabled (bottom figure). All systems were initialized at the highest catastrophe rate (lowest G') and equilibrated for $50,000$ seconds before the alignment was measured, the catastrophe rate was decreased and the procedure was repeated. Results were averaged over 40 runs and the standard error of the mean is indicated by vertical bars. For non-treadmilling systems $r_c \in [3 \times 10^{-3}, 6.75 \times 10^{-3}]$ s^{-1}; for treadmilling systems $r_c \in [4 \times 10^{-3}, 9 \times 10^{-2}]$ s^{-1}.

the value v_0^+ to $0.156\,\mu$m s^{-1} from the value used earlier in this chapter. This way, the steady state growth speed remains approximately the same. Finally, the catastrophe rate is chosen as $r_c = 4.7 \times 10^{-3}$ s^{-1} (Vos et al., 2004). This value does not account for the experimental overestimation of the spontaneous catastrophe rate due to the occurrence of induced catastrophes (see section 3.F), but we use it regardless because (a) there is no reliable estimate for the fraction of induced catastrophes and (b) the reported value is already the lowest of those referenced by Vos et al. (2004).

Figure 4.12 shows a series of snapshots of the evolution of a single system, ranging from 500 seconds to 24,000 seconds. We see that after an initial phase of local alignment in various orientation, the global alignment is firmly established after approximately 5000 seconds. Next, figure 4.13 shows the average of the S_2 order parameter for an ensemble of 1000 systems. We observe that the average system attains a significant level of alignment ($S_2 > 0.5$) after approximately one hour, whereas after two hours virtually all systems have passed that point. Looking at the density graphs, we see that the real density follows a profile similar to that of the S_2 order parameter. The optical density, on the other hand, rapidly approaches a plateau value and its sample variation remains fairly small at all times. Due to the limitations of optical microscopy, it is the optical density that should be compared to experiments. However, very detailed comparisons of the time-dependent properties will likely be affected by our linear approximation of the effect of tubulin availability on the plus end growth speed and our use of a constant nucleation rate. In the examples given in this section, the initial growth speed is twice as high as its steady state value.

Observable	Value
S_2	0.8751(10)
optical S_2	0.7948(10)
density	2.656(3) μm^{-1}
optical density	0.9229(13) μm^{-1}
average microtubule length	10.106(6) μm
segments per microtubule	1.5721(10)
v^+	0.07313(9)μm s^{-1}

Table 4.3: Averaged properties measured from 1,000 runs after 50,000 simulation seconds. Indicated margins represent the standard error of the mean.

Table 4.3 provides an overview of various ensemble properties of the system at the end of the 50,000 second run. We note that the resulting values correspond favorably with those reported in the literature. Specifically, the plus end growth speed is close to the value reported by Vos et al. (2004) (because of our choice for v_0^+), the optical density (the inverse length between microtubules for an aligned array) is comparable to the 1 μm^{-1} number reported by Ambrose et al. (2007), the microtubule length is also within a reasonable range (Barton et al., 2008) and the optical S_2 value lies in the range 0.5-0.8 (Tanase, 2004). In addition, the simulation

Figure 4.12: Snapshots showing the gradual alignment of the cortical microtubules. The system size is $80 \times 80 \, \mu$m (periodic boundary conditions). $L_{\max} = 5 \, \mu$m, $v_0^+ = 0.156 \, \mu$m s^{-1}, $r_c = 4.7 \times 10^{-3}$ s^{-1}.
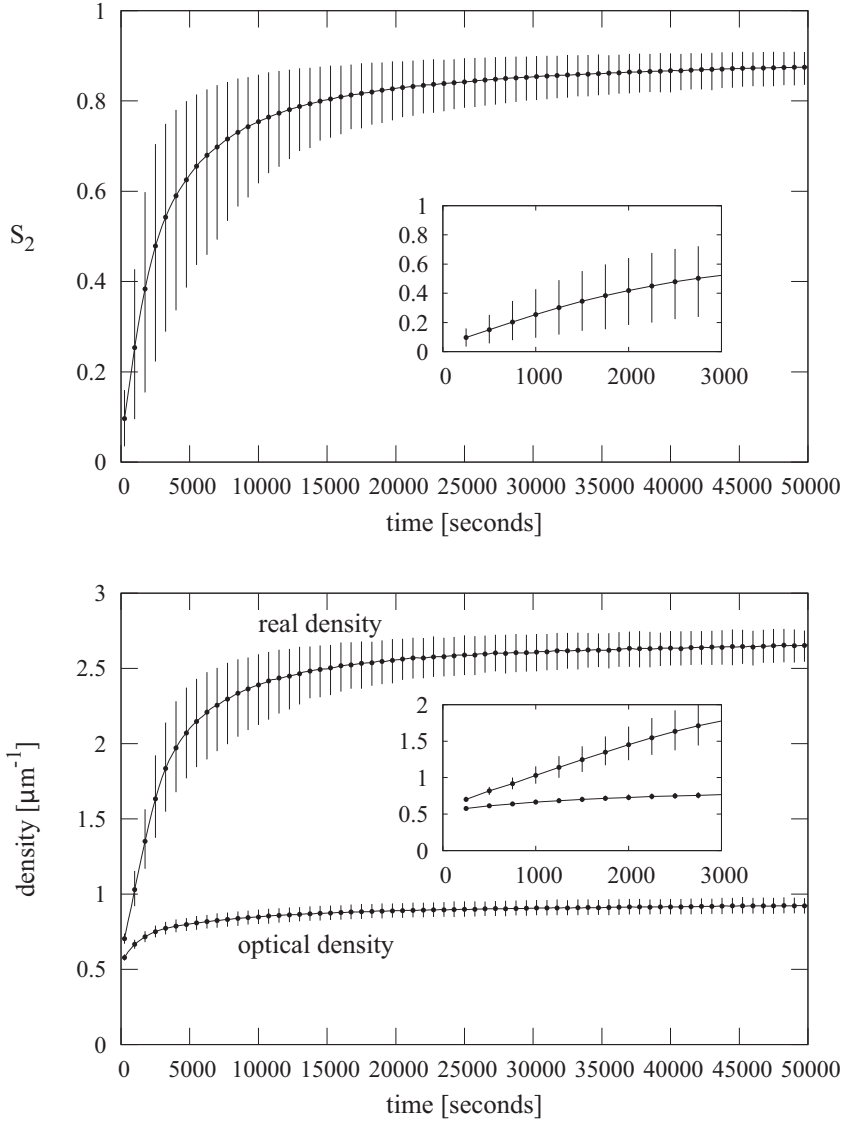
Figure 4.13: Evolution of the S_2 order parameter and the regular and optical densities as a function of time. The dots are the average values of 10,000 runs and the lines indicate the range from the 10th to the 90th percentile. $L_{\max} = 5\,\mu\text{m}$, $v_0^+ = 0.156\,\mu\text{m}$ s^{-1}, $r_c = 4.7 \times 10^{-3}\,\text{s}^{-1}$.
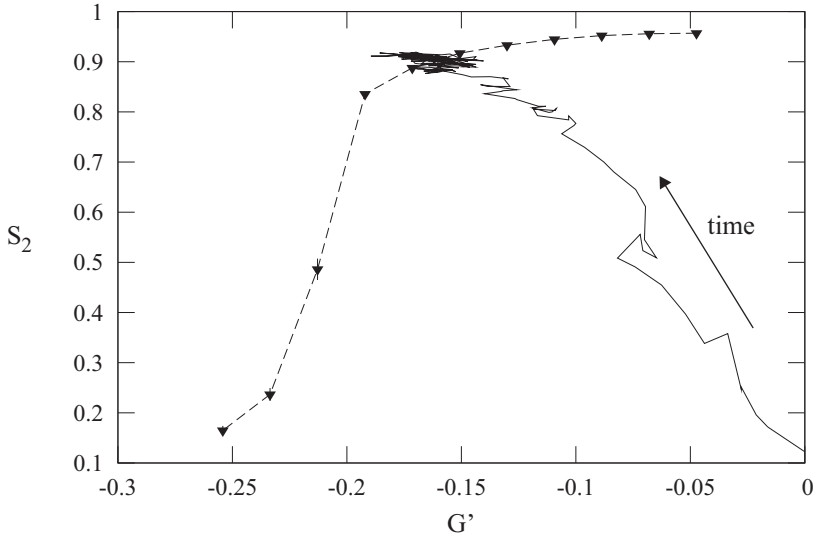
Figure 4.14: Trace of a single system as it evolves in the G'-S_2 plane (solid line). Because of the finite tubulin pool, the value of G' decreases, until it finally stabilizes on the steady state curve already shown in figure 4.9 (dashed line). Run time=50,000 s, $L_{\max} = 5\,\mu$m, $v_0^+ = 0.156\,\mu$m s^{-1}, $r_c = 4.7 \times 10^{-3}$ s^{-1}.

predicts that every microtubule consists of approximately 1.5 segments on average. From the ratio between the real and optical density we deduce that the average degree of bundling is 2.9: every visible stretch of microtubule is, on average, a bundle with 2.9 microtubules.

Finally, figure 4.14 shows the trajectory of a single system in the G'-S_2 plane. Initially, in the absence of microtubules, the plus end growth speed is at its highest ($v^+ = v_0^+$) and the initial value of G' is positive ($G' = 9.8 \times 10^{-3}$). As the density (and S_2) increases, G' decreases and finally settles at an ensemble averaged value of $G' = -0.1602(3)$. The same effect was demonstrated in a theoretical context in figure 3.7.

4.5   Discussion

In this chapter we have introduced a simulation model for the microtubules in the cortical array that builds upon the theoretical model introduced in chapter 3 and extends it by adding a number of processes that have been shown to be relevant in the biological context. In conjunction with the model, an efficient event-driven simulation scheme has been presented that is tailored to the specific needs imposed by the model. The use of an efficient simulation algorithm allows us to address a wide range of questions regarding the self-organized alignment of cortical microtubules.

The simulations have shown that the theoretical framework from chapter 3 provides an accurate description for systems without zippering and severing, as evidenced by figures 4.4 and 4.9a. The extent of the agreement between the theory and simulations was perhaps unexpected, given the approximations that were involved in the construction of the theory. For systems in which zippering was enabled, the theoretical results reached a similar level of accuracy only in the limit of very weakly interacting microtubules, in conjunction with the multi-collision interaction mode between bundles. This interaction mode has been constructed specifically to improve the match with the theoretical predictions (see appendix 4.B), but has little biological relevance. For other bundle interaction modes, the ability for the system to spontaneously align is very sensitive to the specific interaction mode (figures 4.6 and 4.7), as well as the choice of collision outcome probabilities (figure 4.9). Practically, because cortical microtubules in plant cells are not in the weakly-interacting limit and not much is known about the interactions between microtubules in bundles, very few generic statements can be made regarding the qualitative effect of zippering in cells. The results are so sensitive to the model parameters that the analysis should be done on a case by case basis, using the specific parameters for the cell type under investigation. A necessary first step would be the experimental characterization of the collision interactions between microtubules in intersecting bundles.

The effect of treadmilling motion in the absence of zippering is well-described by the theoretical framework of chapter 3, and enabling treadmilling for a given system leads to a decrease of the degree of alignment (figure 4.9). The results are less clear for the case where both treadmilling and zippering are enabled. For the two examples discussed in this chapter, the combination of zippering and treadmilling leads to a slight enhancement of the ordered phase, compared to the baseline without zippering and treadmilling. However, due to the sensitive dependence on the underlying zippering mechanism, it should not be expected that this result can be generalized to all systems.

The final mechanism under consideration is that of microtubule severing. As was expected, uniform severing along the length of the microtubule leads to a decrease in the ability of the system to align (figure 4.10), due to the shorter microtubules and corresponding decrease in density. The effect of severing at intersections is more subtle. Whereas it also leads to decreased alignment in the absence of both treadmilling and zippering, switching on both effects causes the severing events to have a *beneficial* effect on alignment (figure 4.11). This observation is consistent with

the results by Wightman and Turner (2007), who found that severing in *Arabidopsis* cotyledons primarily occurred at intersections and appeared to enhance the microtubule alignment. The sudden reversal of the effect of severing at intersections is likely to be caused by the asymmetry of the severing mechanism in our model: the microtubule that is cut is always the one that is on the cytoplasmic side, i.e. part of the bundle that was last to arrive at that particular intersection. This leads to an effective stabilization of microtubule bundles due to their longer lifetimes. Further investigations should verify whether this is indeed the case in the case of our model, and whether this asymmetry is also present in experiments.

The time-dependent results in section 4.4.3 show that the simulation model is able to reproduce a number of the observables reported in the literature (table 4.3), starting from literature values for the parameters, augmented with educated guesses for the remaining parameters. As more experimental data becomes available and more parameters can be pinned down, the simulations can be expected to yield more accurate quantitative insights into the self-organized alignment of microtubules.

4.A   Simulation: program structure

The simulation code (`corticalSim`, written in C++) is constructed around a hierarchy of objects. The objects that are implemented as separate C++ objects are indicated in italic type. The simulation *system* contains a number of growing and shrinking *microtubules*, each of which has a plus and a minus *tip*, connected by a series of *segments*.

Microtubule positions and interactions are encoded in a single system *geometry* object. The geometry consists of a series of connected *regions* (in our case, rectangles or discs), along with prescriptions for their connections and how to combine region-specific measurements into system-wide properties. Whenever a microtubule is nucleated on a particular region, or enters it at the boundary, a straight-line *trajectory* is created that spans the region. The trajectories serve as 'rails' for the microtubules segments and tips. The positions of the tips and segment ends are measured along the length of their associated trajectories. Bundled microtubules are characterized by the fact that they share the same trajectory.

Upon creation of a new trajectory, the intersections with all other trajectories in the region are computed and stored in a sorted *intersection list*. Within a region, any two trajectories either intersect once or not at all, so this procedure leads to a well-defined ordered list for all possible collision events between microtubules on the trajectories. This list is used to efficiently locate the next collision event and its distance from the current tip location. It should be noted that the computation of all intersections upon creation of a trajectory is a significant overhead that is only worth the computational expense if the microtubule(s) on the trajectory will reach a fair number of these intersections. Trial runs have indicated that the optimal efficiency is obtained when the region size is approximately equal to the length scale l_0 ($\approx 3.5\mu m$ for the parameters used in this chapter). This is achieved by dividing the geometry (a

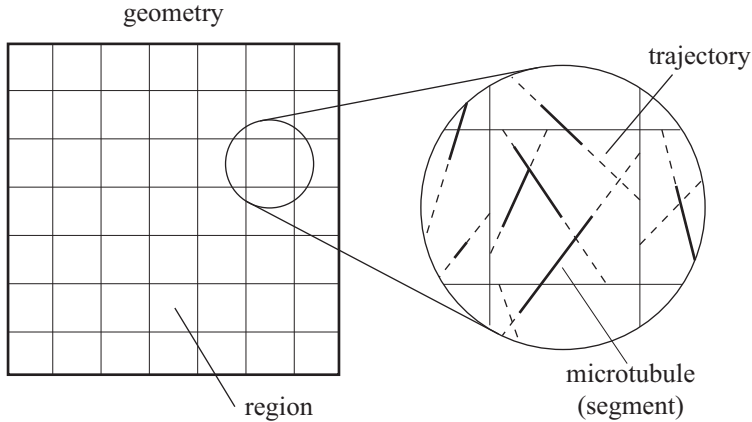square, in this chapter) into a number of smaller connected regions. See also figure 4.15.

Figure 4.15: Schematic representation of the relation between the geometry, regions, trajectories and microtubule segments.

For speed and efficiency reasons, the simulation code relies heavily on the caching of information, both implicitly (through the queues) and explicitly (through the caching of length information, so that not every segment needs to be updated at each event). It is important to realize that numerical errors can accumulate over the course of the simulation, to the point where they potentially affect the ordering of events. This potential problem is countered in two ways. Firstly, the intersection list position information is used as a 'master' list to correct positional information on the fly and when the ordering of two events is unclear, the sort order is used. Secondly, after the execution of every one million events, all queues and caches are cleared and the deterministic events are recalculated. After clearing, the new event times are stored with respect to the current simulation time, to avoid the repeated comparison of large numbers (times) with very small differences, a notorious source of relatively large numerical errors.

4.B   Multi-collision events

The *multi-collision* interaction mode is one of the four bundle collision recipes mentioned in section 4.1. This interaction mode attempts to approximate the dynamics of the coarse-grained model introduced in chapter 3, in which bundles are absent by definition. Therefore, the collision of a microtubule that is part of an ongoing bundle of M other microtubules with another bundle that has N microtubules is described as a dense series of collisions. Microtubules that have previously zippered at the intersection, and are therefore part of both microtubules, are ignored.

The multiple collision process can be imagined as a microtubule working its way through an $(M+1) \times N$ lattice, as shown in figure 4.1. Every individual collision inside the grid is governed by the single-microtubule interaction probabilities $P_c(\theta)$ (induced catastrophe, $P_z(\theta)$ (zippering) and $P_x(\theta)$ (crossover). If the microtubule exits on the opposite side of the grid, it results in a cross-over event and if it exits on the side it results in a zippering event. When one of the collisions induces a catastrophe, the microtubule retreats. It should be noted that we do not explicitly track the position of the incoming microtubule with respect to the other microtubules in the bundle, i.e. whether it's on the left, the right or somewhere in the middle. We therefore average the resulting probabilities uniformly over all possible positions in the incoming bundle.

In this section we compute the total multi-collision probabilities $P_x(\theta, M, N)$ (crossover) and $P_z(\theta, M, N)$ (zippering). The probability $P_c(\theta, M, N)$ for an induced catastrophe follows from

$$P_c(\theta, M, N) = 1 - P_z(\theta, M, N) - P_x(\theta, M, N). \tag{4.8}$$

To simplify the expressions, we introduce the following shorthand notation for the individual collision probabilities:

$$z \equiv P_z(\theta, 0, 1), \tag{4.9}$$

$$x \equiv P_x(\theta, 0, 1). \tag{4.10}$$

4.B.1   Crossover events

First, we analyze the collision process that results in crossovers. As an initial step, we compute the probability to traverse an $i \times N$ grid of intersections, starting at one corner and exiting at the opposite corner in the same direction (see figure 4.16). A path from entry to exit consists of a series of zippering and crossover events that cause the path to move sideways and up through the lattice, so every possible path consists of $i + N - 1$ individual collision events. The probability $P_x^{i,N}$ for a crossover event with the given entry and exit points is given by the sum over the probabilities of all possible paths

$$P_x^{i,N} = \sum_{p \in \mathrm{paths}(i,N)} P_x(p). \tag{4.11}$$

Arbitrarily designating the direction of the incoming microtubule as 'vertical' (V) and that of the other bundle as 'diagonal' (D), every path p corresponds to a series of $N-1$ vertical and $i-1$ diagonal steps between lattice sites, with additional vertical steps at the beginning and end of the path. For example, a path on a 3×5 lattice could be described by the string V-DDVVDV-V. In this string, a DV pair corresponds to a zippering event, whereas DD and VV pairs indicate crossover events. The probability for a specific path to be followed is given by the product of the probabilities of each pair in its string.
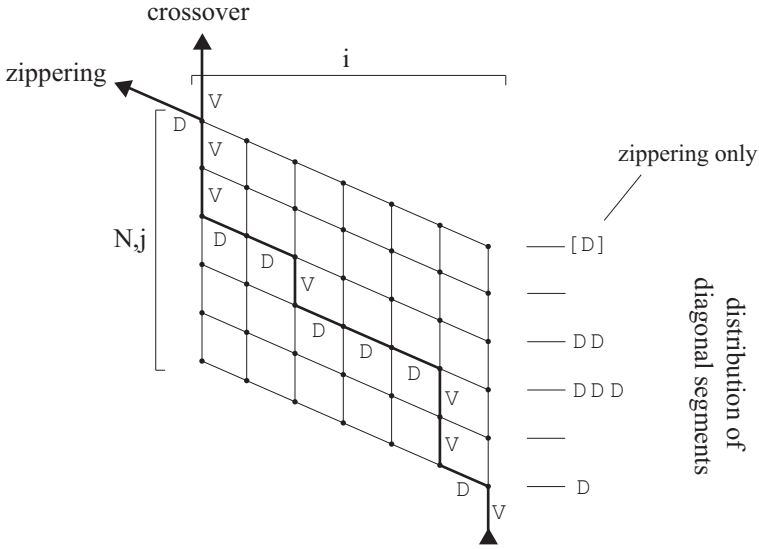
Figure 4.16: An example of a microtubule collision path traversing an $i \times N$ (or $i \times j$) lattice of intersections, eventually resulting in either zippering or crossing over. Also indicated are the translation into a string of D's and V's, and the mapping of the D's onto the traversed microtubules. The indicated path contains three DD-pairs, so $q = 3$.

Initially, let us assume that all $i-1$ D-characters are disconnected. This leads to the following base probability with $2i-2$ zippering events and $N-i+1$ crossovers:

$$P_{x,\text{base}}^{i,N} = x^{N-i+1} z^{2i-2}. \tag{4.12}$$

An actual path p will typically have a number of consecutive diagonal steps, corresponding to fewer zippering events and more crossover events. For all paths with q DD-pairs, the probability is given by

$$P_x^{i,N}(p|q) = x^{2q} z^{-2q} P_{x,\text{base}}^{i,N}. \tag{4.13}$$

To determine the number of paths with a particular value of q, we introduce a 1-to-1 mapping of the paths onto a series of counts by noting how many diagonal segments are located along each of the N microtubules that is crossed (see figure 4.16). We thus get a distribution of $i-1$ diagonal moves over N nodes, with the number of occupied nodes being $i-1-q$. The value of q is therefore in the range

$$q \in [\max(i-1-N,0), \max(i-2,0)] \equiv [q_{\min}, q_{\max}] \tag{4.14}$$

The total probability for crossing over is symbolically given by

$$P_x^{i,N} = \sum_{q=q_{\min}}^{q_{\max}} [\text{ways to pick } i-1-q \text{ out of } N \text{ nodes}] \times$$

$$[\text{ways to distribute } q \text{ items over } i-q-1 \text{ nodes}] P_x^{i,N}(p|q). \tag{4.15}$$

The number of ways to distribute q items over $i-q-1$ nodes is equal to the number of ways to arrange q items and $i-q-2$ 'node divisions', so that we may write

$$P_x^{i,N} = \sum_{q=q_{\min}}^{q_{\max}} \binom{N}{i-q-1} \binom{\max(i-2,0)}{q} x^{N-(i-1)+2q} z^{2(i-1)-2q}. \tag{4.16}$$

Finally, the total crossover probability is obtained by summing the probabilities of all possible paths through the $(M+1) \times N$ grid of intersections, with a uniform distribution of the initial position, producing the final result

$$P_x(\theta, M, N) = \frac{1}{M+1} \sum_{i=1}^{M+1} (M-i+2) P_x^{i,N} \tag{4.17}$$

$$= \sum_{i=1}^{M+1} \sum_{q=q_{\min}}^{q_{\max}} \frac{(M-i+2)}{M+1} \binom{N}{i-q-1} \binom{i-2}{q} x^{N-(i-1)+2q} z^{2(i-1)-2q}. \tag{4.18}$$

4.B.2 Zippering events

The total probability for a multi-collision zippering event can be computed in a similar way. This time, we start with the probability to traverse an $i \times j$ grid ($j \le N$) of intersections, entering vertically on one corner and exiting diagonally on the opposite corner (see figure 4.16). Each path across the lattice consists of $i+j-1$ events, with an odd number of zippering events. The probability $P_z^{i,j}$ for a zippering event with the given entry and exit points is given by the sum over all paths

$$P_z^{i,j} = \sum_{p \in \text{paths}(i,j)} P_z(p) \tag{4.19}$$

Analogous to the crossover events, each zippering path p corresponds to a series of $j-1$ vertical and $i-1$ diagonal steps between lattice sites, with an additional vertical step at the beginning and an additional diagonal step at the end. This can be expressed as a string of the form `V−VDVVD−D` in which every `DV` pair corresponds to a zippering event, and `DD` and `VV` pairs indicate crossover events.

For a path in which all i diagonal steps are disconnected, we obtain the following base probability with $2i-1$ zippering events and $j-i$ crossovers:

$$P_{z,\text{base}}^{i,j} = x^{j-i} z^{2i-1}. \tag{4.20}$$

An actual path p will generally have a number of neighboring diagonal steps. For all paths with q DD-pairs the probability for that path to be taken is given by

$$P_z^{i,j}(p|q) = x^{2q} z^{-2q} P_{x,\text{base}}^{i,j}.\tag{4.21}$$

To determine the number of paths with a particular value of q, we introduce a 1-to-1 mapping of the paths onto a series of counts by noting how many diagonal segments are located along each of the j microtubules that is crossed (see figure 4.16). We thus get a distribution of i diagonal moves over j nodes, where the number of occupied nodes is $i - q$ and the j-th node is always occupied. The value of q is in the range

$$q \in [\max(i-j,0), i-1] \equiv [q_{\min}, q_{\max}]\tag{4.22}$$

The total probability for zippering is therefore symbolically given by

$$P_z^{i,j} = \sum_{q=q_{\min}}^{q_{\max}} [\text{ways to pick } i - q - 1 \text{ (free) nodes out of } j - 1 \text{ nodes}] \times$$

$$[\text{ways to distribute } q \text{ items over } i - q \text{ nodes}] P_z^{i,j}(p|q)\tag{4.23}$$

which equates to

$$P_z^{i,j} = \sum_{q=q_{\min}}^{q_{\max}} \binom{j-1}{i-q-1}\binom{i-1}{q} x^{j-i+2q} z^{2i-1-2q}.\tag{4.24}$$

Finally, the total zippering probability is obtained by summing the probabilities of all possible paths through the $(M+1) \times N$ grid of intersections that enter on the bottom and exit on the side. The entry points are weighted uniformly, because of the unknown position of the incoming microtubule. The expression for the total zippering probability is given by

$$P_z(\theta, M, N) = \frac{1}{M+1} \sum_{i=1}^{M+1} \sum_{j=1}^{N} P_z^{i,j}\tag{4.25}$$

$$= \frac{1}{M+1} \sum_{i=1}^{M+1} \sum_{j=1}^{N} \sum_{q=\max(0,i-j)}^{i-1} \binom{j-1}{i-q-1}\binom{i-1}{q} x^{j-i+2q} z^{2i-1-2q}.\tag{4.26}$$

4.C   Determining length-dependent event times

To determine the timing of the next stochastic event, we should explicitly solve equation (4.3) for Δt_s, starting from the expression for the stochastic event rate $R(t)$ that is given by

$$R(t) = r_n A + r_c N^+ + r_r N^- + r_x X + r_s L(t).\tag{4.27}$$

Here, N^+ (N^-) is the total number of growing (shrinking) microtubules, A is the total area of the system and X is the total number of intersections. Between events, these

numbers are all constant, and only the total microtubule length $L(t)$ varies. In the presence of a finite tubulin pool (4.1), the rate of change of the total microtubule length $L(t)$ in the system is given by

$$\frac{\mathrm{d}L(t)}{\mathrm{d}t} = N^+ v^+(t) - N^- v^- - (N^+ + N^-)v^{tm} \tag{4.28}$$

$$= \left(N^+ v_0^+ - N^- v^- - (N^+ + N^-)v^{tm}\right) - \left(\frac{N^+ v_0^+}{L_{\max}}\right)L(t) \tag{4.29}$$

$$\equiv \gamma - \beta L(t), \tag{4.30}$$

where $L_{\max}$ is the length-equivalent of the total amount of tubulin in the system. Solving this for $L(t)$ yields

$$L(t) = \left(L(0) - \frac{\gamma}{\beta}\right)\mathrm{e}^{-\beta t} + \frac{\gamma}{\beta} \tag{4.31}$$

with

$$\beta = \frac{N^+ v_0^+}{L_{\max}} \tag{4.32}$$

$$\gamma = N^+ v_0^+ - N^- v^- - (N^+ + N^-)v^{tm} \tag{4.33}$$

We note that the total length asymptotically approaches $L^\infty = \gamma/\beta$.

   Having obtained an explicit expression for the total event rate $R(t)$, we are in a position to compute the interval to the next event by evaluating (4.3). Arbitrarily setting $t = 0$, we get

$$-\log(u) = \int_0^{\Delta t_s} R(t')\mathrm{d}t' \tag{4.34}$$

$$= \left(r_n A + r_c N^+ + r_r N^- + r_x X + r_s \frac{\gamma}{\beta}\right)\Delta t_s + \frac{r_s}{\beta}\left(L(0) - \frac{\gamma}{\beta}\right)\left(1 - \mathrm{e}^{-\beta\Delta t_s}\right) \tag{4.35}$$

$$\equiv w\Delta t_s + v\left(1 - \mathrm{e}^{-\beta\Delta t_s}\right), \tag{4.36}$$

where

$$v = \frac{r_s}{\beta}\left(L(0) - \frac{\gamma}{\beta}\right), \qquad w = r_n A + r_c N^+ + r_r N^- + r_x X + r_s \frac{\gamma}{\beta}. \tag{4.37}$$

Multiplying (4.36) by $\beta\mathrm{e}^{\beta\Delta t_s}/w$ and reordering the terms gives

$$\frac{v\beta}{w} = \beta\left(\Delta t_s + \frac{\log(u)}{w} + \frac{v}{w}\right)\mathrm{e}^{\beta\Delta t_s} \tag{4.38}$$

$$= \beta\left(\Delta t_s + \frac{\log(u)}{w} + \frac{v}{w}\right)\mathrm{e}^{\beta\left(\Delta t_s + \frac{\log(u)}{w} + \frac{v}{w}\right)}\mathrm{e}^{-\beta\left(\frac{\log(u)}{w} + \frac{v}{w}\right)}. \tag{4.39}$$

Defining

$$x = \frac{\beta v}{w}, \qquad\qquad y = -\frac{\beta}{w}\log(u) \qquad\qquad (4.40)$$

we can write

$$\left(\beta\Delta t_s + x - y\right)e^{\beta\Delta t_s + x - y} = xe^{x-y}. \qquad\qquad (4.41)$$

Finally, we solve this equation for Δt_s and obtain

$$\Delta t_s = \frac{1}{\beta}\left[-x + y + W(xe^{x+y})\right], \qquad\qquad (4.42)$$

where W is the Lambert W function, the inverse of ze^z. In the simulations, its value is computed using the numerical procedure described by Barry et al. (1995), with a single conversion pass.

THE CASE $\beta = 0$

Special attention should be given to the case $\beta = 0$. This corresponds to both the situation with an unlimited supply of tubulin (constant $v^+ = v_0^+$) and to a system without growing microtubules ($N^+ = 0$). In this case, the length evolves as

$$L(t) = L(0) + \gamma t \qquad\qquad (4.43)$$

and expression (4.3) evaluates to

$$-\log(u) = \left(r_n A + r_c N^+ + r_r N^- + r_x X + r_s L(0)\right)\Delta t_s + \frac{1}{2}r_s\gamma\Delta t_s^2. \qquad (4.44)$$

Defining the constant

$$c = r_n A + r_c N^+ + r_r N^- + r_x X + r_s L(0) \qquad\qquad (4.45)$$

the solution is given by

$$\Delta t_s = \frac{-c + \sqrt{c^2 + 2r_s\gamma(-\log(u))}}{r_s\gamma}. \qquad\qquad (4.46)$$

Note that a solution only exists if $2r_s\gamma\log(u) < c^2$. The case where no (real) solution can be found correspond to cases where an event would occur after the system has reached a *negative* total length. Naturally, one or more deterministic events will take place before this ever happens, decreasing the number of shrinking microtubule until it reaches 0. Each of these events will trigger the recalculation of the stochastic event interval Δt_s so that a real value for Δt_s is eventually generated.

4.D   Converting between plus end growth and time

The variable speed of growing plus ends that results from the limited availability of tubulin necessitates the creation of a separate deterministic event queue, as described in section 4.2. To maintain this queue, we need to convert the distance that needs to be traversed by a plus end to reach the first collision position in the queue to a time interval. Conversely, for the bookkeeping of the segment lengths, the traversed plus end distance as a function of time should be known. In this section, we derive the relationship between the plus end distance d and a time interval t.

Arbitrarily setting the initial time to zero, the distance d travelled by a growing tip is given by

$$d(t) = \int_0^t v^+(t')\mathrm{d}t' \tag{4.47}$$

In the case of an infinite tubulin supply, this immediately gives the simple relation $d = v_0^+ t$. For the remainder of this section, we assume that the tubulin supply is limited ($L_{\max}$ is finite). This leads to the relation

$$d(t) = v_0^+ \int_0^t \left(1 - \frac{L(t')}{L_{\max}}\right)\mathrm{d}t'. \tag{4.48}$$

4.D.1   In the presence of growing segments

Typically, some of the microtubules in the system will be in the growing state. This means we may use equation (4.31) for the time evolution of the total length $L(t)$. Inserting it into (4.48) we obtain

$$d(t) = v_0^+ t - \frac{v_0^+}{L_{\max}} \int_0^t \left[\left(L(0) - \frac{\gamma}{\beta}\right)e^{-\beta t'} + \frac{\gamma}{\beta}\right]\mathrm{d}t' \tag{4.49}$$

$$= \frac{v_0^+}{L_{\max}}\left[\left(L_{\max} - \frac{\gamma}{\beta}\right)t - \frac{1}{\beta}\left(L(0) - \frac{\gamma}{\beta}\right)\left(1 - e^{-\beta t}\right)\right] \tag{4.50}$$

In the special case where $N^- = 0$ and $v^{tm} = 0$ (i.e. only growing, non-treadmilling microtubules are present), $\gamma/\beta = L_{\max}$ and this expression simplifies to

$$d(t) = \frac{v_0^+}{\beta L_{\max}}(L_{\max} - L(0))\left(1 - e^{-\beta t}\right), \tag{4.51}$$

which can be inverted when $N^+ d < (L_{\max} - L(0))$, yielding

$$t = -\frac{1}{\beta}\log\left(1 - \frac{N^+ d}{L_{\max} - L(0)}\right). \tag{4.52}$$

In other cases, equation (4.50) can be rewritten as

$$p e^{p-q} = (\beta t + p - q)e^{\beta t + p - q}, \tag{4.53}$$

with

$$p = -\frac{L(0) - \gamma/\beta}{L_{max} - \gamma/\beta}, \qquad\qquad q = \frac{N^+ d}{L_{max} - \gamma/\beta}. \qquad (4.54)$$

Its solution is given by

$$t = \frac{1}{\beta}\left[q - p + W\left(p\,e^{p-q}\right)\right], \qquad (4.55)$$

where W is the Lambert W function, defined as the inverse of $z\,e^z$. In the simulations, its value is usually computed using the numerical method described by Barry et al. (1995), with a single conversion pass. However, when the value of $p - q$ is sufficiently large, the exponentiation causes a numerical overflow, even though the resulting time interval will be of order 1. Therefore, when $p - q > 250$, we use the asymptotic series expansion by Corless et al. (1996):

$$W(z) = L_1 - L_2 + \frac{L_2}{L_1} + \frac{L_2(-2 + L_2)}{2{L_1}^2} + \frac{L_2(6 - 9L_2 + 2{L_2}^2)}{6{L_1}^3}$$
$$+ \frac{L_2(-12 + 36L_2 - 22{L_2}^2 + 3{L_2}^3)}{12{L_1}^4} + O\left(\left[\frac{L_2}{L_1}\right]^5\right), \quad (4.56)$$

where $L_1 = \log(z)$ and $L_2 = \log\big(\log(z)\big)$. Specifically, for the calculation of $W(p\,e^{p-q})$, this becomes

$$L_1 = p - q + \log(p), \qquad\qquad L_2 = \log\big(p - q + \log(p)\big). \qquad (4.57)$$

4.D.2   In the absence of growing segments

In case there are no growing microtubules in the system ($N^+ = 0$), the length as a function of time is given by the linear relation (4.43), so that (4.48) evaluates to

$$d(t) = v_0^+\left[\left(1 - \frac{L(0)}{L_{max}}\right)t - \frac{\gamma}{2L_{max}}t^2\right] \qquad (4.58)$$

Inverting this equation, we need to be aware of the special case in which no microtubules are present in the system at all. In this case $\gamma = 0$ and the inverted expression becomes

$$t(d) = \frac{d}{v_0^+\,(1 - L(0)/L_{max})} \qquad (4.59)$$

In the more general case where $\gamma \neq 0$, the time as a function of distance is given by

$$t(d) = \frac{(L_{max} - L(0)) - \sqrt{(L_{max} - L(0))^2 - 2\gamma L_{max}d/v_0^+}}{\gamma} \qquad (4.60)$$

Simulating the cortical array: orientation

In the previous chapter, we have investigated the potential for cortical microtubules to align and found a robust ability to form an ordered phase. Absent from our investigations up to this point was the issue of the absolute orientation of this alignment. Plant cells need a reliable method for orienting the cortical array, because its orientation determines the direction of cell growth and subsequent cell division. Generally, subsequent divisions occur in the same direction, so that the orientation of the cortical array is preserved between cell generations. However, the are situations in which organisms are shown to exert precise control over the orientation of individual cell divisions, for example in the formation of stomatal complexes in maize (Cartwright et al., 2009). In this chapter we build upon the simulation scheme presented in chapter 4 and investigate the influence of the cell geometry and possible biochemical cues on the orientation of the cortical array.

The simulations in the previous chapter were all run on a square canvas with periodic boundary conditions. This geometry should not impose any directional bias to the system, as evidenced by figure 5.4, although a preference for the horizontal and vertical directions may occur for smaller systems due to finite-size effects[1]. An additional problem with the periodic square system is that it is topologically equivalent to a torus (genus 1), whereas the cell (genus 0) does not have a penetrating hole. This is an important distinction, because whereas it is possible to create a uniformly ordered vector field (or a field of microtubules) on the torus, such a field on the cell surface must contain at least two singularities. It is reasonable to expect that the location of these singularities will be sensitive to the cell geometry. For the remainder of this chapter, we represent the cell geometry by a cylinder of length L and radius R.

Making the switch from a flat two-dimensional system to the surface of a three-dimensional object necessitates the re-thinking of two basic assumptions that were

---

[1] MSc thesis Eva Deinum, AMOLF 2009

made in the previous chapters. First, we need to determine the path that a growing microtubule will follow on the curved surface. Second, it means we need to replace the strictly two-dimensional order parameter S_2 by one that explicitly takes into account the embedding of the surface in three dimensions. These issues will be addressed in more detail on the following pages.

In addition to the cell geometry we also touch on the potential for local chemical cues to influence the orientation of the cortical array. It is well-established, for example, that auxin gradients are in place that can provide information about the growth axis of the cell (Lucas and Shaw, 2008). Also, localized cell wall stress has been found to influence cortical array orientation (Hamant et al., 2008). As a first step towards understanding the effect of local cues, we have chosen to selectively increase the spontaneous catastrophe rate on the end caps of the cylinder by an arbitrary factor c. The possibility for localized changes in the catastrophe rate was also mentioned by Ehrhardt and Shaw (2006) and doing so on the end caps is in agreement the lower density of microtubules observed near the ends of tobacco BY-2 cells (Jan Vos, personal communication). For $c = 1$ we recover the regular capped cylindrical geometry, and for $c \to \infty$ we obtain a finite cylinder without end caps (i.e. the end caps are effectively inaccessible to microtubules).

5.1   Microtubule trajectories on the cylinder

Microtubules have a persistence length that is large on the scale of the cell (Van den Heuvel et al., 2008), so they can be treated as stiff rods that resist bending. However, their confinement to the cell's volume and their adherence to the cell membrane means that the microtubules will generally be curved. The question that needs to be addressed is which path the microtubule will follow after it has nucleated at a given location and in a certain direction.

Depending on the specific constraints, there are two solutions to this problem. When the microtubule is only confined by the cell membrane, but still free to move laterally, the solution is given by a *global* minimization of the curvature along the microtubule. This solution has been determined for an infinite cylinder – and, by extension, for spherocylinders – by Lagomarsino et al. (2007) and is shown in figure 5.1. As the filament becomes longer, its free end will tend to align more with the axis of the cylinder. However, the cortical microtubules in plant cells are linked to the cell membrane and are therefore restricted in their lateral movement (Shaw et al., 2003; Vos et al., 2004; Sainsbury et al., 2008). This means that a microtubule cannot make use of lateral relaxation to decrease its energy as it gets longer. Instead, the polymerizing microtubule end can only *locally* minimize the bending energy before the curvature is 'frozen in' by binding to membrane linkers. The trajectory of growing microtubules is therefore given by a minimal curvature path on the cell membrane, starting from a given initial position and direction.

The curvature κ of any regular curve on a surface can be decomposed into two components, the normal curvature κ_n in the normal plane and the lateral curvature

global curvature
minimization
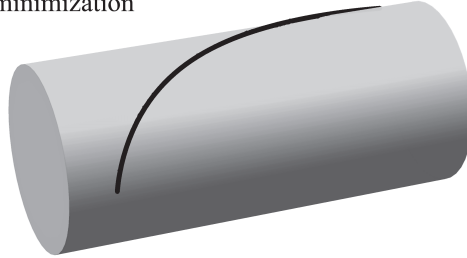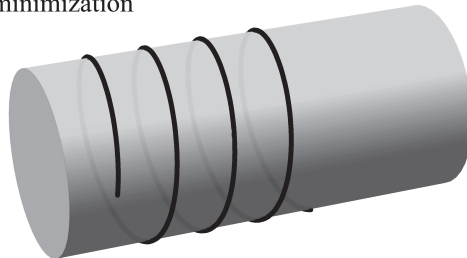
local curvature
minimization

Figure 5.1: Comparison of the curves resulting from global and local
curvature minimization, starting from the same initial conditions. Both
solutions have an initial opening angle of 5.7° and the curve for the
global energy minimization has a total length of 4.5 times the cylinder
radius (the length is not relevant for the local energy minimization).

κ_l in the tangent plane (see figure 5.2). These curvatures are related by

$$\kappa^2 = \kappa_n^2 + \kappa_l^2. \tag{5.1}$$

The Meusnier theorem states that for a given surface S, all possible curves through a
certain point with a given tangent vector have the same normal curvature (Do Carmo,
1976), so that any differences in curvature must be attributed to the lateral curvature
κ_l. It follows from equation (5.1) that the total curvature is always minimized by
setting $\kappa_l = 0$. The solutions on the surface of a cylindrical body are therefore helices,
defined by their starting position and angle. In figure 5.1, the local and global curva-
ture minimization solutions on the body of a cylinder are compared. The transition
from the cylinder body to the end caps can also be treated as the limiting case of
a smooth transition: a 90° turn on a cylinder with a vanishing radius. The implica-
tion is that the crossing of the rim of the cylinder conserves the angle between the

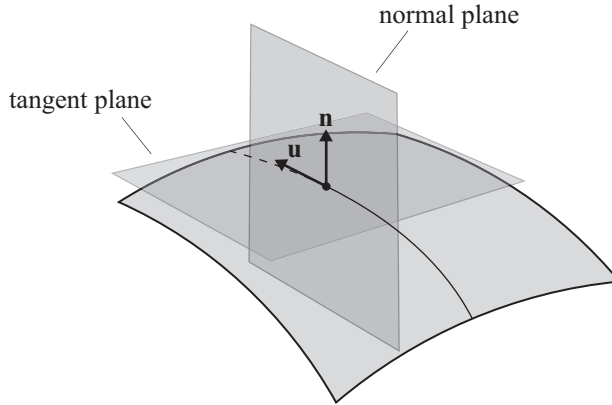Figure 5.2: A curve on a two-dimensional curved surface. Indicated are the tangent vector **u** and the surface normal **n**. The normal plane contains both vectors and the tangent plane contains only the tangent vector and is perpendicular to the normal vector.

microtubule and the edge.

Of course, cortical microtubules are not actually attached to the cell membrane at all points along their length, but rather at intervals of a finite size (Gardiner et al., 2001; Kirik et al., 2007; Barton et al., 2008), so there is some room for non-local curvature minimization. However, as long as the attachment interval is much smaller than the radius of the cylinder, the helical solution is a good approximation.

5.2   Measuring order in three dimensions

Having developed the tools to simulate the cortical microtubules on the surface of a cylinder, we construct an order parameter to assist in the interpretation of the results, analogous to the definition of S_2 in (3.72) (for fields) and (4.4) (for line elements). The formation of the cortical array is thought to serve the purpose of aligning the cellulose microfibrils in the cell wall, which, in turn, allows the cell wall to expand in the perpendicular direction (Lucas and Shaw, 2008). The order parameter should be an indicator of the ability for the cell to undergo directional expansion, so it should measure the *underrepresentation* of microtubules pointing in a certain direction.

We start by defining a nematic order parameter that is a generalization of the one used for liquid crystals in three dimensions (for the derivation, see appendix 5.A). We define the second order tensor **Q** with the elements

$$Q_{\alpha\beta} = \frac{\sum_i \int_0^{l_i} u_\alpha^{(i)}(l') u_\beta^{(i)}(l') \mathrm{d}l'}{\sum_i l_i} - T_{\alpha\beta}, \tag{5.2}$$

where l_i is the length of the i-th microtubule segment and $\mathbf{u}^{(i)}(l)$ is the tangent vector at position l along the segment i (see figure 5.2). The isotropic tensor $\mathbf{T}$ is used to ensure that $\mathbf{Q}$ is zero in the isotropic homogeneous phase and accounts for the potential anisotropy of the simulation geometry. In the case of a cylinder of length L and radius R that is oriented along the x-axis, $\mathbf{T}$ is given by the matrix

$$\mathbf{T} = \frac{1}{2(L+R)} \begin{pmatrix} L & 0 & 0 \\ 0 & \frac{1}{2}L+R & 0 \\ 0 & 0 & \frac{1}{2}L+R \end{pmatrix} \tag{5.3}$$

From the tensors $\mathbf{Q}$ and $\mathbf{T}$ we derive the scalar order parameter R_2, defined as

$$R_2 = -\frac{\lambda_{\min}(\mathbf{Q})}{\lambda_{\max}(\mathbf{T})}. \tag{5.4}$$

Here, $\lambda_{\min}(\mathbf{Q})$ is the lowest eigenvalue of $\mathbf{Q}$ (interpreted as a matrix), expressing our wish to identify the *absence* of microtubules in a certain direction. The division by the highest eigenvalue of $\mathbf{T}$ guarantees that R_2 is in the range $[0,1]$ (see appendix 5.A for details). The lowest eigenvalue of $\mathbf{Q}$ is associated with an eigenvector $\mathbf{v}_{\min}$ that indicates the preferential direction of cell expansion. To remove the redundancy caused by the rotational symmetry of the cylinder, we reduce this vector to the angle Θ_2 between $\mathbf{v}_{\min}$ and the cylinder axis ($\mathbf{e}_x$) (see figure 5.3).

$$\Theta_2 = \arccos(|\mathbf{v}_{\min} \cdot \mathbf{e}_x|) \tag{5.5}$$
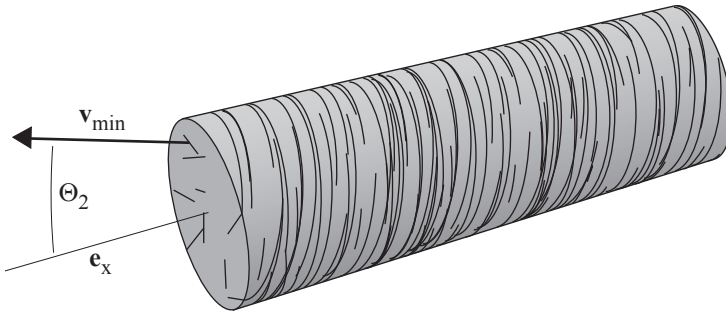

Figure 5.3: Example of a microtubule configuration on a cylindrical geometry, showing the corresponding direction of the director $\mathbf{v}_{\min}$ and the angle Θ_2 that indicates the deviation from the transverse orientation.

Summarizing, the value of $R_2 \in [0,1]$ measures the degree in which there is a preferred expansion direction and Θ_2 indicates its deviation from the transverse orientation. Note that the highest attainable value of R_2 depends on the orientation of $\mathbf{v}_{\min}$. For the case of a finite cylinder with $L \geq 2R$, the range of possible values for R_2 decreases from $[0,1]$ when $\Theta_2 = 0$ to $[0, 1/2 + R/L]$ for $\Theta_2 = \pi/2$.

5.3   Results

For the results in this chapter we make use of the biologically motivated parameters that have been introduced in section 4.4.3 of the previous chapter. There, we have seen that these parameters invariably lead to a highly ordered system ($R_2 > 0.8$) on a periodic geometry[2]. Figure 5.4 shows the degree of alignment R_2 and the angle Θ_2 (measured from the y-axis) for an ensemble of 1000 systems, evaluated at 50,000 seconds, clearly indicating the isotropic distribution of the orientations in the ensemble.
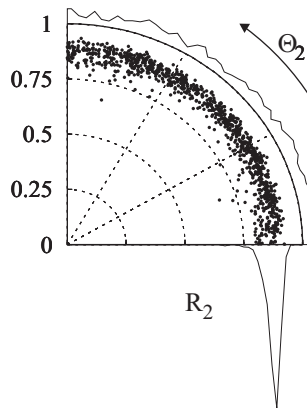

Figure 5.4: Scatter plot of 1000 R_2-Θ_2 pairs for the periodic $80 \times 80\,\mu$m system discussed in section 4.4.3, evaluated at 50,000s. The R_2 and Θ_2 distributions are obtained by projecting the data onto the respective axes into 50 bins.

For the cylindrical geometry we have opted to use a cell length of $40\,\mu$m and a radius of $20\,\mu$m, which is reasonable estimate for a tobacco BY-2 cell at the beginning of interphase, when the transverse cortical array is first established (Jan Vos, personal communication). On the end caps of the cylinder we have subsequently imposed an induced catastrophe multiplication factor c with values of 1 (no effect), 2 and 4. This makes the end caps of the cylinder increasingly inhospitable to microtubules.

Figures 5.6 and 5.7 show the resulting 3D order parameters of an ensemble of 1000 systems as a function of time. The results show that for $c = 1$, within a period of a few hours the population begins to separate into two distinct subpopulations with transversal and longitudinal orientations. The switch to a cylindrical geometry thus breaks the orientational symmetry of the solution space. For judging the distributions along the orientation angle Θ_2, it should be kept in mind that this angle is computed through a projection onto one of three coordinate axes. This implies that a truly isotropic distribution of orientation angles would result in an angle distribution that

---
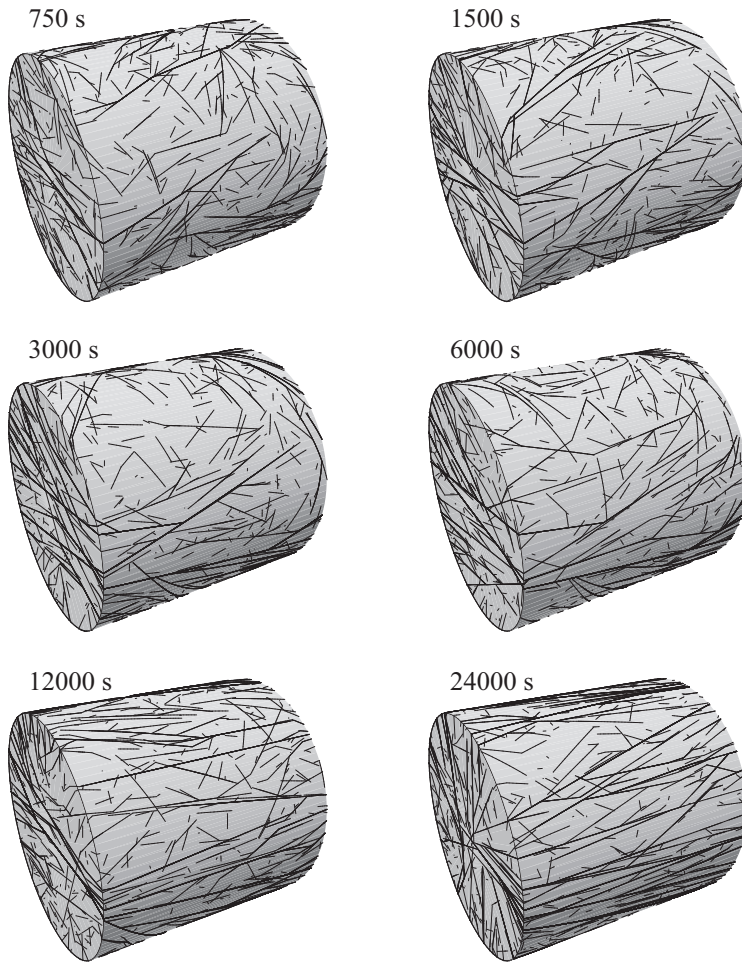
[2]Note that for a two-dimensional surface $R_2 = S_2$.

Figure 5.5: Time series of snapshots of a longitudinally ordered system with $c = 1$.
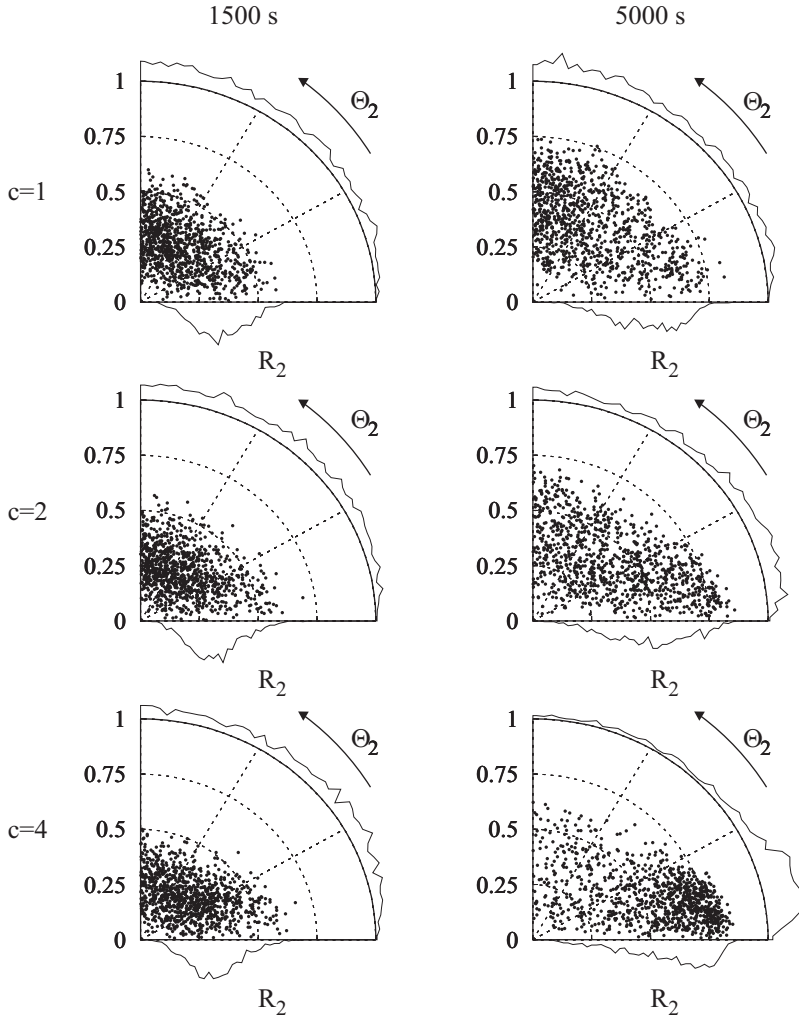
Figure 5.6: Scatter plots showing the evolution of 1000 R_2-Θ_2 pairs for cylindrical systems with a length of $40\,\mu m$ and a radius of $20\,\mu m$, for three different values of the spontaneous catastrophe multiplier c. The R_2 and Θ_2 distributions are obtained by projecting the data onto the respective axes into 50 bins.
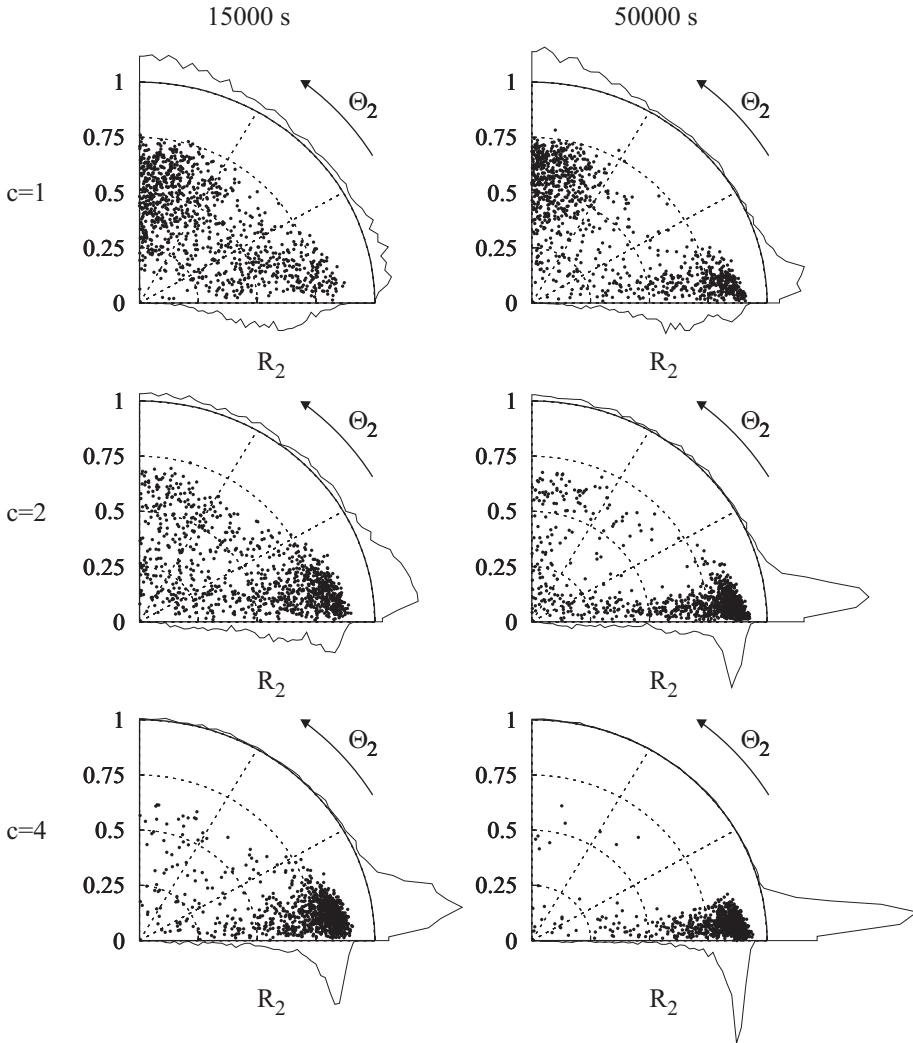
Figure 5.7: Scatter plots showing the evolution of 1000 R_2-Θ_2 pairs for cylindrical systems with a length of 40 μm and a radius of 20 μm, for three different values of the spontaneous catastrophe multiplier c. The R_2 and Θ_2 distributions are obtained by projecting the data onto the respective axes into 50 bins.

is not uniform, but proportional to $\sin(\Theta_2)$. Looking again at figures 5.6 and 5.7, we conclude that even for $c = 1$, the final orientation distribution is not just the result of systems settling down in the nearest stable orientation, but there is already a distinct bias in the direction of the cylinder axis. However, this bias is not strong enough to force all systems to orient their microtubules transversally. An example of a stable longitudinally ordered system is given in figure 5.5.

Increasing the spontaneous catastrophe multiplier to $c = 2$, an initial tendency to form two subpopulations is visible at 15,000 seconds, but by 50,000 seconds most of the systems have oriented their microtubules in the transverse direction ($\Theta_2 \approx 0$). We see the same effect occur, albeit more rapidly for $c = 4$. To understand why all systems eventually orient transversally, we look at the value of the control parameter G'. In the steady state, its definition (4.7) can be written as $G' = C_1 r_r - C_2 r_c$, clearly exposing the role of the catastrophe rate r_c. In the cases under consideration, G' is always negative, implying that $C_2 r_c > C_1 r_r$. This means that a local multiplication of the catastrophe rate by a factor c leads to an effect on G' that is *larger* than that obtained by a multiplication by c. So, for a system that is well into the ordered phase on the cylinder body, a factor c that is slightly larger than 1 can push the caps back into the isotropic phase. As long as the caps are large enough, so that they cannot easily be traversed by ordered microtubules from the cylinder body, the caps will effectively repel microtubules, forcing them to align in the transverse orientation. An example is shown in figure 5.8, where the final value of G' on the cylinder body is -0.13, firmly in the ordered range, whereas its value on the cylinder caps is -0.89, in the isotropic range (compare with figure 4.14).

Looking closer at the final distributions for $c = 2$ and $c = 4$ in figure 5.7, we see that although the values of the orientation angle Θ_2 are tightly focused around 0, the values of R_2 are more widely distributed, with an obvious tail towards lower values. Visual inspection of the systems with low R_2-values shows that many of these systems have a subtly helical arrangement of microtubules. In these systems, the microtubules on the cylinder body are well-aligned, but they are not lined up with the end caps, leading to an angle-dependent penalty at the boundary. Assuming the system is oriented more or less in the transverse direction ($\Theta_2 \approx 0$), the existence of a helical distribution can also be deduced by comparing the R_2 order parameter with the $S_2^{(\text{body})}$ order parameter that is computed on the unrolled cylinder body alone and its corresponding angle $\Phi_2^{(\text{body})}$. If $S_2^{(\text{body})}$ is significantly larger than R_2, some degree of helical order is present in the system, and its pitch is given by the orientation angle $\Phi_2^{(\text{body})}$. An example of the formation of a helical pattern is given in figure 5.9. In the final configuration, it has the order parameters $R_2 = 0.73$, $S_2^{(\text{body})} = 0.90$, $\Theta_2 = 4°$, $\Phi_2^{(\text{body})} = 13°$. For comparison, the transverse pattern shown in the final configuration of figure 5.8 has the order parameters $R_2 = 0.87$, $S_2^{(\text{body})} = 0.89$, $\Theta_2 = 9°$, $\Phi_2^{(\text{body})} = 2.5°$.
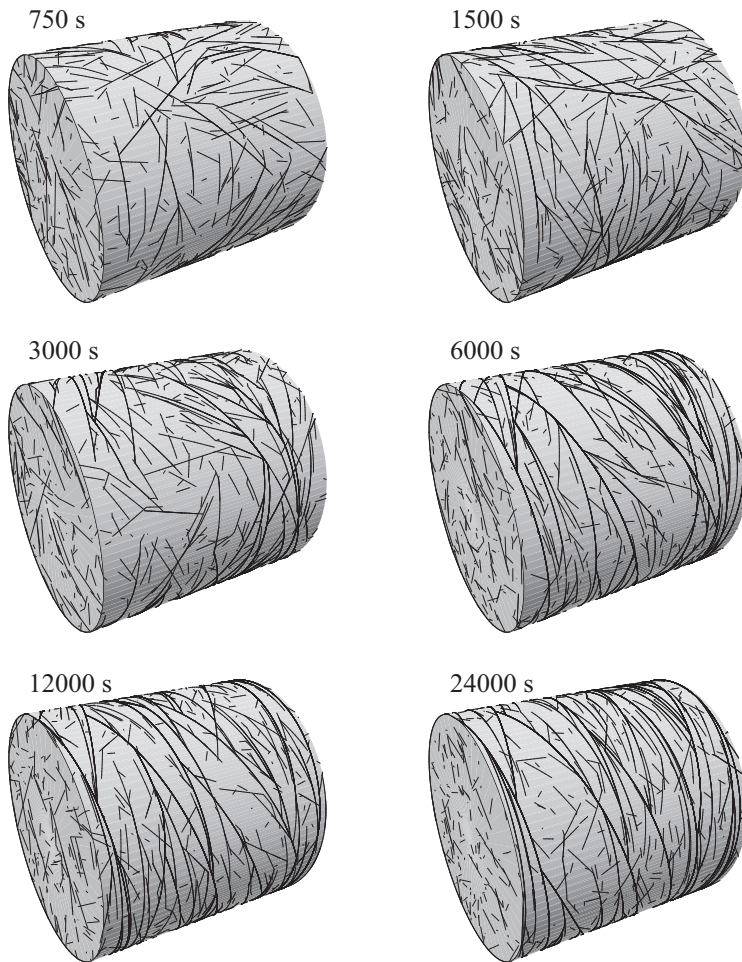
Figure 5.8: Time series of snapshots of a transversely ordered system with $c = 4$. In the final configuration, $R_2 = 0.87$, $\Theta_2 = 9°$.
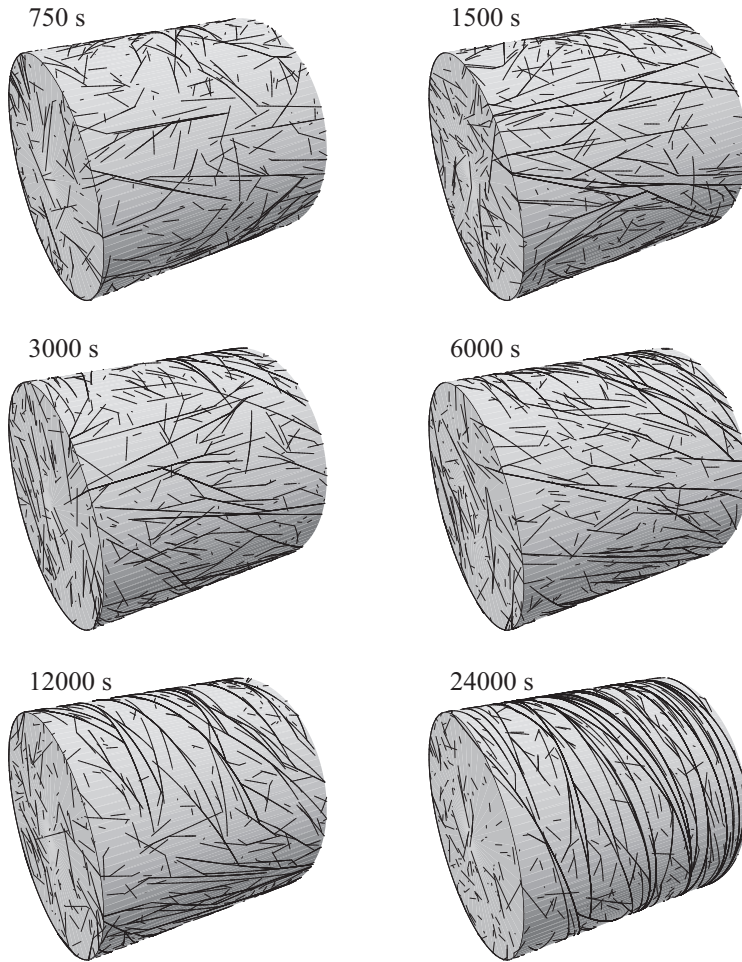
750 s

1500 s

3000 s

6000 s

12000 s

24000 s

Figure 5.9: Time series of snapshots of a helically ordered system with $c = 4$. In the final configuration, $R_2 = 0.73$, $\Theta_2 = 4°$.

5.4 Discussion

In this chapter we have extended the two-dimensional cortical array simulations from chapter 4 to the surface of a cylinder in three dimensions. This step necessitated the determination of minimum-curvature microtubule trajectories on curved surfaces and the creation of the R_2 order parameter that describes the degree in which microtubules on a surface exhibit collective alignment perpendicular to an emergent cell expansion axis. Although both concepts have only been used for the cylinder surface, they are applicable to generic curved surfaces in three spatial dimensions. Extensions to other basic cell shapes, such as boxes or spherocylinders, can therefore be implemented in a straightforward manner.

The simulation results in figures 5.6 and 5.7 indicate that the use of a cylindrical cell geometry restricts the possible orientations of the cortical array, and the observed orientations (along the cylinder axis and perpendicular to it) correspond to the symmetries of the underlying geometry. In addition, the cylindrical geometry imposes a slight bias to the orientation of the array in the direction of the cell axis (i.e. with the microtubules perpendicular to the cell axis), but this is not strong enough to reliably determine the orientation of alignment. In addition, we varied the spontaneous catastrophe rate on the end caps of the cylindrical cell by multiplying it by a factor c. Comparing the result for $c = 1, 2$ and 4, we see that a local cue in the form of in increased spontaneous catastrophe rate at the cylinder end caps *is* sufficient to ensure that (nearly) all systems eventually orient their microtubules perpendicular to the cell axis.

The suggestion that local cues at the cell ends exist and may play a role in cortical array orientation has popped up repeatedly in the literature. It is known, for example, that the PIN family of proteins, related to auxin transport, localize to these faces (Lucas and Shaw, 2008), making them a potential candidate for (indirect) modification of microtubule activity. Also, the ROP2/RIC1 proteins are thought to modify microtubule activity in specific regions of the cortex (Ehrhardt and Shaw, 2006). Furthermore, recent experiments by Hamant et al. (2008) have demonstrated the existence of a connection between stresses applied to the cell wall and cortical array orientation. The model that was introduced by the authors relied on a macroscopic description in which the average microtubule direction on the outward-facing cell surface co-aligns with the direction of maximal stress on the surrounding cell walls. The simulation results from this chapter could provide a microscopic understanding of this connection: If we assume that tension on the cell wall activates a stress response that locally increases the catastrophe rate, the two sides of the cell that are under maximum tension will act as the 'cell poles'. The cortical array will then be established along the axis between these poles, with the microtubule pointing in the perpendicular direction – parallel to the direction of maximum wall stress, as observed in the experiments.

We conclude that there is plenty of circumstantial evidence for location-specific modulation of microtubule dynamics. However, experiments will have to indicate whether the dynamics of the cortical microtubules are indeed different at the cell

poles, and, if so, which parameters are most affected.

5.A   Derivation of the 3D order parameter

5.A.1   The tensorial order parameter

To measure the degree of order of the collective set of microtubules in the cell cortex, we must specify an order parameter. We start from the definition of the nematic order parameter Q that is commonly used for liquid crystals (Gramsbergen et al., 1986). It is an second order tensor (equivalent to a matrix) that can be defined as

$$\mathbf{Q} = <\mathbf{u} \otimes \mathbf{u}> -\frac{1}{3}\mathbf{I}^{(3)}. \tag{5.6}$$

In the case of particles, $\mathbf{u}$ is the director of the individual particles in the system and the angled brackets denote an averaging over all particles. In the case of orientational density fields, $\mathbf{u}$ is the orientation and the brackets indicate a density-weighted average over all angles and space. The definition of $\mathbf{Q}$ is easily adjusted for a two-dimensional system, by reducing the dimensionality and replacing the fractions by 1/2. However, it is important to realize that in both of these cases the particles are free to orient themselves in all dimensions.

This is clearly not the case in the cortical array, where we have particles that are located on a two-dimensional surface S that is embedded in $\mathbb{R}^3$, restricting the admissible orientations to the tangent plane at each location. This means that the geometry has a large, possibly non-isotropic, influence on the possible realizations of $\mathbf{Q}$, resulting in the problematic outcome that locally isotropic configurations can lead to non-zero elements in $\mathbf{Q}$. To rectify this, we note that the identity matrix in (5.6) ensures that the isotropic configuration corresponds to $\mathbf{Q} = 0$. Therefore, we may generalize (5.6) by replacing the correction term with a geometry-dependent correction term.

The definitions below will be given in terms of an orientational density field $\rho(\mathbf{r},\theta)$, where $\mathbf{r} \in S$ and θ is a coordinate indicating the orientation in the local tangent plane. The translation to a particle-based definition is straightforward, and will be given below. In terms of the orientational density field ρ, we define

$$\mathbf{Q} = <\mathbf{u} \otimes \mathbf{u}>_{\rho(\mathbf{r},\theta)} - <\mathbf{u} \otimes \mathbf{u}>_{\text{iso,homo}} \tag{5.7}$$

$$= <\mathbf{u} \otimes \mathbf{u}>_{\rho(\mathbf{r},\theta)} -\mathbf{T}. \tag{5.8}$$

Here, the first term is an average that is weighted by the actual orientation density field and the second is the isotropic correction term, where the averaging is done with respect to an isotropic and homogenous distribution. This correction is represented by the geometry-dependent tensor $\mathbf{T}$.

THE ISOTROPIC CORRECTION

The isotropic homogeneous distribution tensor $\mathbf{T}$ is defined as the result of two subsequent averaging procedures: first a local averaging over all directions in the tangent plane (isotropic) and then an averaging over $\mathbf{r} \in S$ (homogeneous). Defining a local orthogonal frame by the surface normal $\mathbf{n}$ and two orthogonal unit vectors $\mathbf{v}$ and $\mathbf{w}$, the local averaging yields

$$< \mathbf{u} \otimes \mathbf{u} >_{\text{iso}} = \mathbf{v} \otimes \mathbf{v} + \mathbf{w} \otimes \mathbf{w} \tag{5.9}$$

$$= \mathbf{I}^{(3)} - \mathbf{n} \otimes \mathbf{n}. \tag{5.10}$$

The tensor $\mathbf{T}$ can now be computed as

$$\mathbf{T} = \frac{1}{A} \int_S \left(\mathbf{I}^{(3)} - \mathbf{n} \otimes \mathbf{n} \right) \mathrm{d}A', \tag{5.11}$$

where A is the total area of the surface S. Its values for a few common shapes are

$$\mathbf{T}_{\text{plane(x,y)}} = \begin{pmatrix} \frac{1}{2} & 0 & 0 \\ 0 & \frac{1}{2} & 0 \\ 0 & 0 & 0 \end{pmatrix} \qquad \mathbf{T}_{\text{cylinder(x)}} = \begin{pmatrix} \frac{1}{2} & 0 & 0 \\ 0 & \frac{1}{4} & 0 \\ 0 & 0 & \frac{1}{4} \end{pmatrix} \tag{5.12}$$

and

$$\mathbf{T}_{\text{sphere}} = \mathbf{T}_{\text{cube}} = \begin{pmatrix} \frac{1}{3} & 0 & 0 \\ 0 & \frac{1}{3} & 0 \\ 0 & 0 & \frac{1}{3} \end{pmatrix}. \tag{5.13}$$

We note that the generalized definition (5.8) reduces to the regular definition (5.6) on isotropic surfaces such as the sphere, and to its two-dimensional form on a plane.

A PARTICLE BASED DEFINITION

Definition (5.8) is based on the existence of a directional density field ρ, but as the microtubules in the cortical array are individual extended particles, we need to modify our definition accordingly, by integrating the direct product $\mathbf{u} \otimes \mathbf{u}$ along the length of each microtubule segment. Summing over all microtubule segments i with lengths l_i, we get

$$\mathbf{Q} = \frac{\sum_i \int_0^{l_i} \mathbf{u}^{(i)}(l') \otimes \mathbf{u}^{(i)}(l') \mathrm{d}l'}{\sum_i l_i} - \mathbf{T} \tag{5.14}$$

$$= \frac{\sum_i \tilde{\mathbf{U}}^{(i)}}{\sum_i l_i} - \mathbf{T} \tag{5.15}$$

To determine $\mathbf{Q}$ for the cortical array on a finite-sized cylinder, the components of $\tilde{\mathbf{U}}^{(i)}$ must be computed for segments on the cylinder body and the end caps. For these calculations, we will assume that the cylinder is pointing along the x-axis. On

the end caps, each segment has a direction that can be parameterized by the angle α it makes with the z-axis in the direction of increasing y. This gives

$$\mathbf{u}^{(i)}(l) = \begin{pmatrix} 0 \\ \sin{(\alpha_i)} \\ \cos{(\alpha_i)} \end{pmatrix} \qquad (5.16)$$

Noting that $\tilde{\mathbf{U}}_{mn}^{(i)}$ is symmetric, only six components need to be computed, which are

$$\tilde{U}_{xx}^{(i)} = \tilde{U}_{xy}^{(i)} = \tilde{U}_{xz}^{(i)} = 0, \qquad (5.17)$$

$$\tilde{U}_{yy}^{(i)} = l_i \sin{(\alpha_i)}^2, \qquad (5.18)$$

$$\tilde{U}_{yz}^{(i)} = l_i \sin{(\alpha_i)}\cos{(\alpha_i)}, \qquad (5.19)$$

$$\tilde{U}_{zz}^{(i)} = l_i \cos{(\alpha_i)}^2. \qquad (5.20)$$

On the body of the cylinder, every microtubule segment can be characterized by the position of its base, its length and the direction of growth. The x-coordinate of the base is not relevant, and the y- and z-coordinates are encoded in the angle β with the z-axis, in the direction of increasing y. The growth direction of the microtubules is oriented at an angle α to the x-axis. Denoting the radius of the cylinder by R, the local director $\mathbf{u}^{(i)}$ is given by

$$\mathbf{u}^{(i)}(l) = \begin{pmatrix} \cos{(\alpha_i)} \\ \sin{(\alpha_i)}\cos{\left(\beta_i + \frac{l\sin(\alpha_i)}{R}\right)} \\ -\sin{(\alpha_i)}\sin{\left(\beta_i + \frac{l\sin(\alpha_i)}{R}\right)} \end{pmatrix}. \qquad (5.21)$$

The components of $\tilde{\mathbf{U}}_{mn}^{(i)}$ are

$$\tilde{U}_{xx}^{(i)} = l_i \cos{(\alpha_i)}^2 \qquad (5.22)$$

$$\tilde{U}_{xy}^{(i)} = R\cos{(\alpha_i)}\left[-\sin{(\beta_i)} + \sin{\left(\beta_i + \frac{l_i \sin{(\alpha_i)}}{R}\right)}\right] \qquad (5.23)$$

$$\tilde{U}_{xz}^{(i)} = R\cos{(\alpha_i)}\left[-\cos{(\beta_i)} + \cos{\left(\beta_i + \frac{l_i \sin{(\alpha_i)}}{R}\right)}\right] \qquad (5.24)$$

$$\tilde{U}_{yy}^{(i)} = \frac{1}{4}\sin{(\alpha_i)}\left[2l_i\sin{(\alpha_i)} + R\left[-\sin{(2\beta_i)} + \sin{\left(2\beta_i + \frac{2l_i\sin{(\alpha_i)}}{R}\right)}\right]\right] \qquad (5.25)$$

$$\tilde{U}_{yz}^{(i)} = \frac{1}{2}R\sin{(\alpha_i)}\left[-\cos{(\beta_i)}^2 + \cos{\left(\beta_i + \frac{l_i\sin{(\alpha_i)}}{R}\right)}^2\right] \qquad (5.26)$$

$$\tilde{U}_{zz}^{(i)} = \frac{1}{4}\sin{(\alpha_i)}\left[2l_i\sin{(\alpha_i)} + R\left[\sin{(2\beta_i)} - \sin{\left(2\beta_i + \frac{2l_i\sin{(\alpha_i)}}{R}\right)}\right]\right]. \qquad (5.27)$$

5.A.2   A scalar order parameter

The order parameter $\mathbf{Q}$ as defined in (5.8) is a second order tensor. In this section we extract from $\mathbf{Q}$ a single scalar order parameter R_2 that indicates the extent to

which a particular direction is avoided by the microtubules. We note that $\mathbf{Q}$ is a symmetric real matrix and as such it has an orthogonal basis of eigenvectors. By choosing a reference frame that coincides with the eigenvectors, it is easily seen that the larger eigenvalues correspond to preferred directions of the microtubules. The direction that is avoided by the microtubules (and thus the preferred direction of cell expansion) is indicated by the eigenvector corresponding to the *lowest* eigenvalue $\lambda_{\min}(\mathbf{Q})$.

Furthermore, since $\mathbf{Q}$ is traceless, the sum of all three eigenvalues equals zero, implying that $\lambda_{\min}(\mathbf{Q})$ is negative. We can determine a lower bound for $\lambda_{\min}(\mathbf{Q})$ by evaluating the terms in equation (5.8). Suppose we have a director $\mathbf{v}_{\min}$ corresponding to the lowest eigenvalue. In every point on S, it is possible to choose the particle/field director $\mathbf{u}$ perpendicular to this vector, so that the first term of (5.8) does not contribute to the eigenvalue. The second term is $-\mathbf{T}$, which in itself is a symmetric matrix with eigenvalues in the range [0,1/2]. The maximum (negative) contribution it can give in the direction of $\mathbf{v}_{\min}$ is equal to its maximum eigenvalue $\lambda_{\max}(\mathbf{T})$. Using this information we define the order parameter $R_2 \in [0,1]$ that measures the expansion asymmetry in plant cells as

$$R_2 = -\frac{\lambda_{\min}(\mathbf{Q})}{\lambda_{\max}(\mathbf{T})}. \tag{5.28}$$

For the special case of a distribution of microtubules on a 2D plane, it can be shown that R_2 is identical to S_2, defined by (3.72) (for density fields) and (4.4) (for a set of line segments).

Designing ground state patterns for DNA-coated colloids

6

In the previous chapters we have investigated in detail the processes that lead to the self-organization of cortical microtubules in plant cells. These processes have evolved over the course of millions of years through natural selection. In this chapter, we focus on the possibility to design a complex self-organizing system from scratch. Biomolecules are natural candidates for the design of materials with custom interactions, due to their large variety and the specificity of their interactions. Our subject of study is a prominent model system for self-assembly through biomolecular interactions: DNA-coated colloids.

In this system, first proposed by Mirkin et al. (1996), DNA is grafted onto micrometer-sized beads. The two strands forming the DNA are of slightly differing lengths, so that a short stretch of single stranded DNA is exposed at the far end of the strand. This creates what is called a 'sticky' end, to which another single DNA strand can bind through hybridization. The range of possible binding sequences provided by DNA's four-letter alphabet combined with the specificity of base pair binding means that the binding affinity can be precisely manipulated, and this can not only be done for a single pair of DNA strands, but orthogonal interactions can be defined simultaneously for a large number of sticky ends. In principle, it is possible to create a system with many different types of beads, each of which has tunable interactions with every other type of bead. The sticky ends of two different beads can either bind directly (see figure 6.1), or mediated by a piece of linker DNA that has preferential affinities for both types of beads. The latter provides more flexibility to control the interactions in the system, especially when many beads with different sticky ends are involved. The holy grail of the research on DNA-coated colloids is to design materials that will, in the proper circumstances, self-assemble from their constituents (the DNA-coated beads).

The range of possibilities offered by DNA-mediated interactions is fundamentally different from the use of, for example, electrostatic interactions, for which the
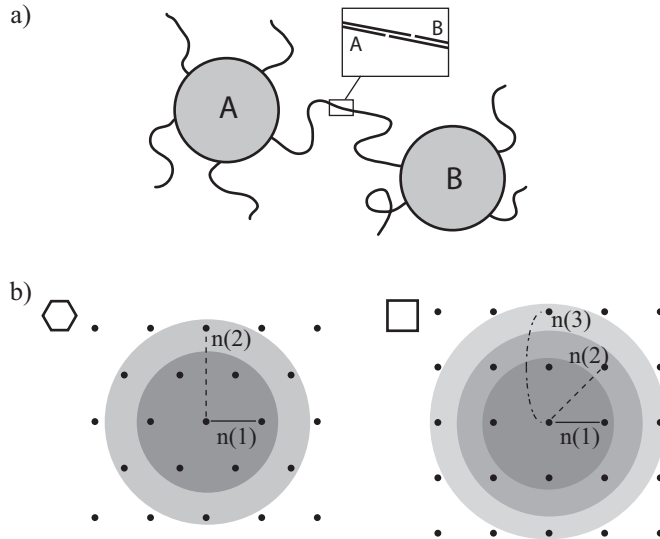
Figure 6.1: a) Schematic overview of bead-bead binding through DNA interactions. b) Overview of the nearest neighbor ($n(1)$), next-nearest neighbor ($n(2)$) and next-next-nearest neighbor ($n(3)$) interactions on hexagonal and square lattices.

control is limited to the sign, strength and range of the interactions, without further possibilities for discrimination. Patterns of colloids are therefore generally limited to two colloidal species (see, for example, Leunissen et al., 2005). However, it must be said that the full potential of DNA-mediated interactions has so far not been utilized, as experiments have only been done on systems with a single bead species (Biancaniello et al., 2005; Hill et al., 2008) or two species of beads (Nykypanchuk et al., 2008; Park et al., 2008; Geerts et al., 2008). Also, theoretical work (Tkachenko, 2002) and simulations (Lukatsky and Frenkel, 2004; Bozorgui and Frenkel, 2008) have predominantly focused on systems with two types of beads. Notable exceptions are the work by Licata and Tkachenko (2006), which was however limited to a single particle per bead type and the lattice model by Lukatsky et al. (2006) that used four species of beads, and provided the basis for the work in this chapter.

In order for a collection of DNA-coated colloids to self-assemble into a complex pattern, every bead – through its interactions – should contain enough information to 'find' its target position. A complication is that the distribution of the sticky DNA ends that mediate the interactions is to a first approximation isotropic (Crocker, 2008) so that the interactions can only be a function of the distance between beads. Furthermore, for practical purposes, this distance is constrained by the length of the DNA (Geerts et al., 2008). Therefore we may ask ourselves whether it is at all possible

to design large patterns using only short-ranged isotropic interactions, and, if so, whether there is a lower limit to this interaction range. We will address this question in the context of a two-dimensional lattice model with isotropic interactions and we investigate whether the interactions between the beads on this lattice can be designed in such a way that the beads self-assemble into a complex crystal structure. A necessary requirement for self-assembly is that the target structure represents the unique minimum energy ground state of the system, so that it will be the preferred state for $T \rightarrow 0$. For the basic theoretical work in presented in this chapter we therefore restrict ourselves to the design of a unique ground state for non-trivial crystal structures, using only isotropic interactions.

After introducing the model, we will derive a requirement for the minimum interaction range between beads, depending on the symmetry of the underlying lattice and the size of the desired pattern. Subsequently, we present a minimal recipe for the interactions that allows for the design of arbitrarily large periodic patterns. Besides periodic patterns, this recipe can also be used to construct patterns with glide reflections and two-fold rotations. Finally, these results are illustrated by means of Monte Carlo simulations that demonstrate the self-assembly of the designed patterns from random initial conditions.

6.1 Model definition

We define a simple geometrical lattice model for the interactions in a system of DNA-coated colloids, as a generalization of the model by Lukatsky et al. (2006). Let us consider a lattice on which every site may be occupied by at most one bead. Each bead is of a particular type that is characterized by its sticky end and labelled by an alphabetical index (A, B, etc.). Formally, every lattice site i is in a state

$$s(i) \in \{\text{A}, \text{B}, ..., \text{Z}\}, \tag{6.1}$$

in which Z is the final element of the set of distinguishable beads (not necessarily containing 26 elements). Empty sites can be included in the model as an additional non-interacting bead 'species'. We can trivially assign a unit vector in a $Z + 1$ dimensional vector space to each of the possible states through the identification

$$\text{A} = \begin{pmatrix} 1 \\ 0 \\ \vdots \\ 0 \end{pmatrix}, \quad ..., \quad \text{Z} = \begin{pmatrix} 0 \\ \vdots \\ 0 \\ 1 \end{pmatrix}; \quad 0 = \begin{pmatrix} 0 \\ \vdots \\ 0 \end{pmatrix} \tag{6.2}$$

The beads on the lattice interact with each other in two distinct ways. First, they obey the rule that no two beads can occupy the same lattice site, corresponding to an excluded volume effect with the size of a lattice unit cell. Second, the interaction between the DNA strands of different beads gives rise to an effective two-body interaction energy that is both isotropic and short-ranged. This interaction will therefore be a function of the distance on the lattice.

It is convenient to introduce the shorthand notation $n(r)$, $r \in \mathbf{N}$, for the set of particles with identical site-to-site distances on the lattice, ordered by increasing distance for increasing r. $n(1)$ thus contains all nearest-neighbor pairs, $n(2)$ all next-nearest-neighbor pairs, etc. In the context of this chapter, we restrict ourselves to two-dimensional lattices, but the language used to describe the interactions is also applicable to various lattices in higher dimensions. See figure 6.1 for the interaction ranges for the square and hexagonal lattices used in this chapter.

The Hamiltonian for the system is defined as

$$H = \sum_{r=1}^{R} \sum_{(i,j) \in n(r)} \frac{1}{2} J_{mn}^{(r)} s_m(i) s_n(j).$$ (6.3)

Here, R indicates the maximum range of the particle interactions, as measured along the lattice links, and we introduce a symmetric interaction matrix $J^{(r)}$ for every lattice distance r. The aim is therefore to design the interaction matrices $J^{(r)}$ in such a way that the Hamiltonian is uniquely minimized for a predetermined crystal lattice – up to global transformations corresponding to the symmetries of the underlying lattice (rotations, translations and reflections).

At this point, it will be clear that the above model can easily be used to describe *any* multi-state lattice model with pairwise interactions that are both short-ranged and isotropic. However, for conceptual clarity, we will only refer to the DNA-coated colloid system and leave further applications up to imagination of the reader.

6.2   Lower limits to the interaction range

So far, the maximum interaction range $n(R)$ has not been specified. For reasons of conceptual clarity and experimental tractability, we'd like the interaction range to be as short as possible. However, it is reasonable to expect that a very short interaction range can impose limitations on size or complexity of the patterns that can be designed. This is certainly true in the limiting case of vanishing interactions. In this section we determine lower limits for the interaction range, depending on the underlying lattice type (square, hexagonal) and the desired complexity of the designed pattern.

The square and hexagonal lattices have a large number of intrinsic symmetries: translations, rotations, reflections and glide reflections (reflections accompanied by a translation along the reflection axis). The collection of these symmetries is summarized by the corresponding wallpaper group: *p4m* for the square lattice, *p6m* for the hexagonal lattice (Grünbaum and Shephard, 1987). Applying any of these symmetry operations to a configuration of beads *on* the lattice produces another valid (on-lattice) configuration. Furthermore, for any given configuration and symmetry operation, a number of *symmetrized configurations* can be constructed that are invariant under the given symmetry operation. For example, a pair of reflection-symmetrized configurations is created by copying the pattern one side of a reflection axis over to the other side, and vice-versa.
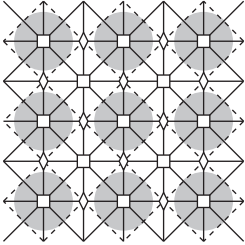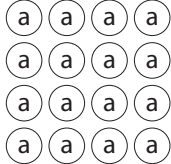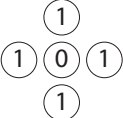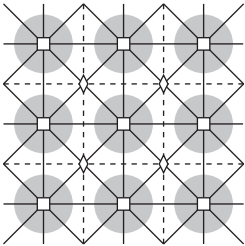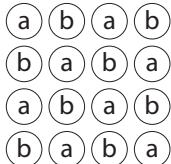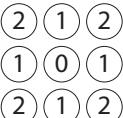
The goal of this chapter is to design the interaction matrices in such a way that the system has a unique ground state for a configuration of beads that is equal to an *a priori* specified pattern. Naturally, this means the energy of this distribution should be lower than that of every other possible distribution, including all possible symmetrized forms. We conclude that the ground state can only possibly be unique if each of the possible symmetrized distributions either (a) increases the energy or (b) is equal to the original distribution (i.e. it was already symmetric).
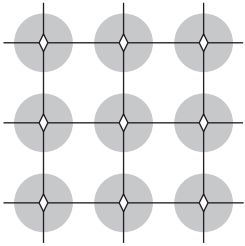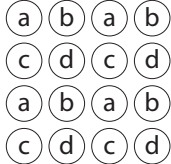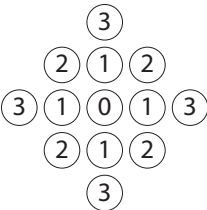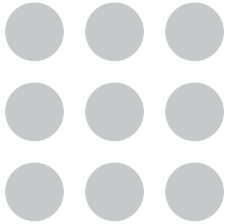
This observation gives us a handle on the relation between ground state design and interaction range. Figure 6.2 gives a graphical overview of this relation on a square lattice. Starting on top, for an interaction range of $n(0)$ (no interactions) the interaction energy is always zero. Obviously, any symmetrized solution will have the same energy, so a solution can only be a unique ground state if it itself is symmetric under all symmetry operations on the lattice (*p4m*). This is shown as the maximum complexity pattern on the top right, consisting of only A-type beads.

Increasing the interaction range to $n(1)$, the nearest-neighbor interactions along lattice links can be used to distinguish a bead from its neighbors, as shown in the interaction patch by the different labels 0 and 1. The presence of these interactions can cause a symmetrized state to have a higher energy than the original state. Graphically speaking, this happens when, for a given symmetry operation, the interaction patch can be placed on a position such that either (a) the 0 is mapped onto a 1 or vice-versa, or (b) the patch is split by a glide reflection. A large fraction of the intrinsic lattice symmetries can be suppressed this way, such as the reflection symmetry between columns and rows of beads. The remaining symmetries are shown in the second row of figure 6.2 (the glide symmetries are a resultant of the remaining symmetries). Again, the symmetry group is *p4m*, but this time with a unit cell of two beads. Every ground state should by symmetric under this group, so that the most complex ground state pattern is given by the checkerboard pattern of A and B type beads.

Increasing the range yet again to $n(2)$ further reduces the symmetries that cannot be suppressed to the *p2m* wallpaper group, corresponding to a 2 × 2 repeated pattern of beads. This class of interactions and the corresponding solutions have been used by Lukatsky et al. (2006). When the interactions reach up to $n(3)$, all lattice symmetries can be suppressed and this method does not indicate any remaining symmetry-derived limitations. An interaction range of $n(3)$ or longer is therefore a necessary condition for the design of patterns that are larger than 2 × 2. In the next section, we will show that this interaction range is also sufficient.

Figure 6.3 shows a similar derivation on the hexagonal lattice. Starting from the full symmetry of the lattice (*p6m*), symmetries are suppressed by increasing the interaction range. For $n(1)$ interactions, the remaining lattice symmetries are of group *p3m*, corresponding with a triangular 3-bead pattern. In contrast to the square lattice, $n(2)$ interactions are already sufficient to suppress all lattice symmetries on the hexagonal lattice. The design recipe that is presented in the following section will prove that the $n(2)$ interaction range is not only necessary, but also sufficient for designing unique ground states with arbitrarily large numbers of beads.

range	interaction patch	unsuppressible lattice symmetries	group	maximum complexity pattern
n(0)	⓪		p4m	a a a a a a a a a a a a a a a a
n(1)	① ① ⓪ ① ①		p4m (larger)	a b a b b a b a a b a b b a b a
n(2)	② ① ② ① ⓪ ① ② ① ②		p2m	a b a b c d c d a b a b c d c d
n(3)	③ ② ① ② ③ ① ⓪ ① ③ ② ① ② ③		0	∞

———	reflection
- - - -	glide reflection
◊	2-fold rotation
□	4-fold rotation

Figure 6.2: Table relating the interaction range, the unsuppressible lattice symmetries and the corresponding maximum complexity patterns on a square lattice.

range	interaction patch	unsuppressible lattice symmetries	group	maximum complexity pattern

Figure 6.3: Table relating the interaction range, the unsuppressible lattice symmetries and the corresponding maximum complexity patterns on a hexagonal lattice.

6.3   Proof of designability

The previous section has demonstrated that non-trivial patterns can only be reliably designed if interaction range is at least $n(2)$ (on a hexagonal lattice) or $n(3)$ (on a square lattice). Building on this generic result we now introduce a simple recipe for interactions between the beads that is both minimal in terms of the interaction range and guaranteed to produce a unique ground state for a large class of patterns.

   The prescription for the interactions consists of a mixture of positive and negative design elements. First, each pair of beads that should form a nearest-neighbor pair in the final pattern is assigned a negative interaction energy $-\alpha < 0$ in the nearest-neighbor matrix $J^{(1)}$ (positive design). In addition, at longer distances there is a self-repulsion, represented by a contribution $\varepsilon > 0$ for all diagonal elements in the next-nearest neighbor matrix $J^{(2)}$ and, for a square lattice, the next-next-nearest neighbor matrix $J^{(3)}$. The remaining interactions are set to zero. This choice of the interaction matrices is far from unique, but it is simple, leading to sparse matrices, and it is sufficient to guarantee a unique ground state with an energy of $-\alpha N/2$ per particle, where N is the coordination number (the number of nearest-neighbors per site) of the lattice. A motivation and proof for this design strategy is given below, for both lattice types under consideration.

ONE DIMENSION

It is instructive to start our analysis with a one-dimensional system. The symmetry argument from the previous section suggests that the interactions should range up to $n(2)$ in order to suppress the reflection symmetry through the center of each bead. Suppose we wish to design a linear pattern containing the sequence `...KLMN....` Using only nearest-neighbor interactions, this requires a preferential binding of `L` to both `K` and `M`. However, when `L` is bound to `K` on one side, there is nothing to stop another `K` from binding on the other side of `L`, producing the sequence `LKL`. Hence, as expected, the only sequence that can reliably be designed is an alternating sequence.

   This restriction can be circumvented by extending the range of interactions to $n(2)$. This allows us to include a *self-repulsion* at range $n(2)$ for both `K` and `M`. Suppose `K` binds to `L` first, forming the complex `KL`. The long-range self-repulsion of `K` will prevent it from also binding to the other side of `L`, or it can only do so with a reduced affinity. In both cases, if `M` has approximately the same nearest-neighbor affinity for `L` as `K` does, the ground state will contain the sequence `...KLM...`, or its reverse, which is allowed by a global symmetry operation. The same argument can be applied iteratively to each position in the sequence, from which we conclude that a sequence of infinite length can indeed be designed. Using the interaction recipe defined in the beginning of this section, every link in the lattice has an energy $-\alpha$, which corresponds to the lowest possible energy state of the lattice, making it the ground state.

   This argument shows that it is theoretically possible to design arbitrarily long

unique strings of letters, but in practice it is more desirable to form a string of a limited length, say AB...YZ, and to create a repeated 'tiling' based on this fragment. Implementing this periodic boundary condition is straightforward, as we can simply design A and Z to become nearest neighbors (positive design).
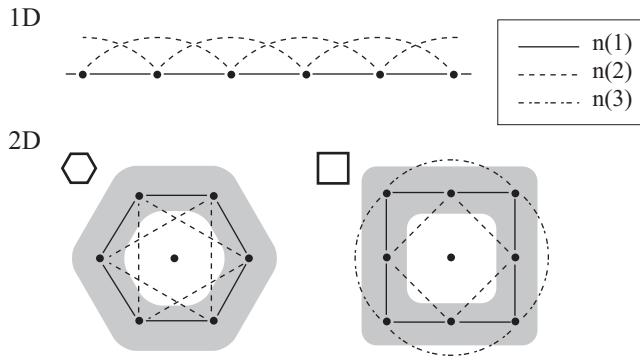

Figure 6.4: Top: overview of the $n(1)$ and $n(2)$ interactions on a one-dimensional lattice. Bottom: the mapping of local neighborhoods of a central particle onto a one-dimensional periodic structure with $n(2)$ (hexagonal) or $n(3)$ (square) range.

TRIANGULAR LATTICE IN TWO DIMENSIONS

We now move on to the more interesting case of two-dimensional designs, starting with the hexagonal lattice. As in the one-dimensional case, a minimum interaction range extending to the next-nearest neighbors ($n(2)$) is required to design crystals with more than three beads (see section 6.2). That the design recipe with this interaction range is also sufficient can be seen as follows. Consider a single particle A, having six nearest-neighbors, and suppose we wish to design a ring of particles BCDEFG around A (see also figure 6.5). The attractive nearest-neighbor interactions between bead A and the other particles cause the ring of particles around A to be made up of the correct beads in the ground state, but does not specify their order.

However, let us now consider this ring of particles as a periodic line of six particles around A. Figure 6.4 shows that the $n(2)$-interactions on this ring on the hexagonal lattice also correspond to the next-nearest neighbor interactions along the ring. The implication is that the one-dimensional argument for designability carries over directly to this situation, meaning that the sequence BCDEFG will reliably form around bead A, up to a global rotation or reflection. By iterative application of this argument to the points in the outer ring of the hexagon (B, C, etc.), the proof scales to arbitrarily large systems. Note that the orientation of the subsequent hexagons is completely fixed with respect to the initial patch. There is only a *global* freedom to orient the pattern.

On the square lattice the self-repulsion energy ε of the design recipe should be extended to the $n(3)$ range (the $J^{(3)}$ matrix). The proof then follows along the same lines as that for the triangular lattice. We pick any lattice location and consider the 8-vertex square around it. This square can be represented as a line with periodic boundary conditions and next-nearest neighbor interactions (see figure 6.4), proving the local uniqueness of the ground state. This process can be repeated iteratively for points on the edge of the square to extend the proof to arbitrarily large systems.

6.4   Crystal structures

The derivations above prove that the design recipe produces a unique ground state locally, and, by extension, on larger patches consisting of unique beads. Ideally, one would like to limit the number of unique beads that need to be designed, and therefore the maximum size of such an ordered patch. Retaining the ability to make complex patterns, these patches can be treated as tiles that can be programmed to attach to one another and form a crystal structure. The 17 crystallographic *wallpaper groups* provide an exhaustive set of all possible symmetry groups on the two-dimensional plane that contain two independent translations (periodic patterns) (Grünbaum and Shephard, 1987).

It should be noted that a crystal structure can only exist on our lattice model if its symmetry group is compatible with that of the lattice itself. Specifically, the 5 wallpaper groups containing a 3-fold rotation are not compatible with a square lattice and the 3 groups with a 4-fold rotation are not compatible with the hexagonal lattice. Formally, the symmetry group of the crystal should be a subgroup of that of the lattice (*p4m* or *p6m*), and at least contain two independent translations on the lattice (*p1*). For a pattern with symmetry group g, we have $p1 \subseteq g \subseteq p4m$ (square) or $p1 \subseteq g \subseteq p6m$ (hexagonal).

In this section we show how the interaction recipe outlined above can be successfully applied to generate patterns representing 4 out of the 17 wallpaper groups by selectively enabling symmetries. The simplest wallpaper group, p1, represents a periodic crystal structure with only translation symmetries. The ground state for such a pattern can be reliably designed simply by instructing the beads on one side of a patch to connect to those on the opposite side. There is, however, a lower limit to the translation distances that can be used. The proof for the existence of a unique ground state in section 6.3 assumes that the beads that form a ring around any bead A (see figure 6.5a) only have attractive interactions with the neighboring beads. However, if one of the two translation vectors becomes so short that the ring of beads around bead A has nearest-neighbor interactions with another copy of itself, the design recipe leads to spurious attractions that can cause a degeneracy of the ground state. An example of a regular periodic pattern on a hexagonal lattice is given in figure 6.6. Note that this pattern has the shortest repeat length that is possible without creating
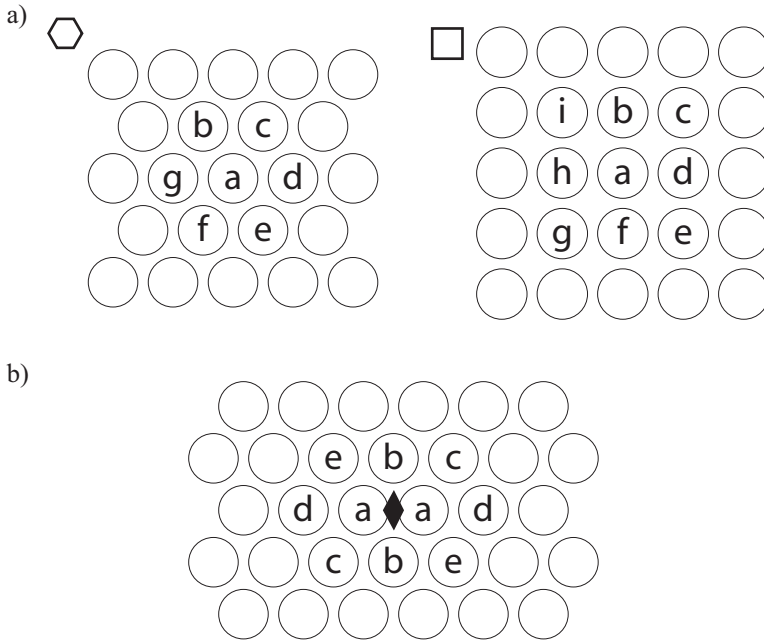
Figure 6.5: a) Locally ordered neighborhoods on the hexagonal and square lattices. b) Locally ordered neighborhood of a two-fold rotation center on a hexagonal lattice.

interactions between a single bead's local neighborhoods.

Another symmetry that can be implemented in a straightforward fashion is the glide reflection: a reflection followed by a translation along the reflection axis. Again, if the translation is large enough so that the local neighborhoods of identical beads do not touch one another, the glide reflection is simply achieved by applying the interaction recipe to the desired pattern. Producing a periodic pattern based on the glide reflection generates the *pg* wallpaper group, an example of which is shown in figure 6.8. For this symmetry group, the unit cell is twice the size of the fundamental domain, the patch of uniquely designed beads.

As a final step we implement a non-trivial symmetry operation that forces us to revisit the uniqueness proof of section 6.3. This symmetry operation is the two-fold rotation around the center point of two beads on the hexagonal lattice. An example of the local target pattern for this symmetry is given in figure 6.5b. For all the beads outside this region, the local neighborhood is unaffected, so the (local) ground state remains unique. For each of the beads *inside* the region, we have enumerated the possible local neighborhoods and verified that the target configuration is the only one that leads to attractive interactions on all lattice links. There is, however, an energy
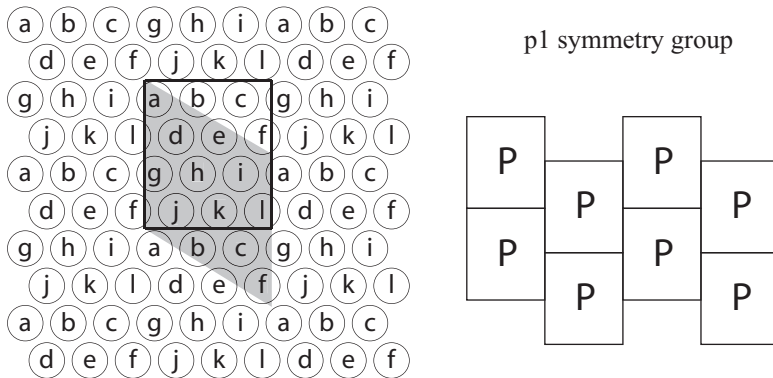
Figure 6.6: Example of a simple periodic crystal on a hexagonal lattice. The basic tile of beads is delineated by the black rectangle, and the unit cell is indicated by the gray parallelogram. The image on the right shows how the tiles are connected to produce the pattern, where the P indicates the intrinsic orientation of each tile.

penalty associated with the presence of two B beads at a next-nearest neighbor distance from each other. As long as this energy penalty is similar in magnitude to the attractive interactions – and it's likely to be much smaller – this penalty will be overcome by the attractive interactions and the target pattern represents the unique ground state. Obviously, a very large repulsive energy between the B-beads will disrupt the target pattern, but the exact threshold value will generally depend on non-local interactions involving the rest of the design. The use of a two-fold rotation allows us to generate patterns from two other wallpaper groups: the group *p2* with only two-fold rotation symmetries (and resulting translations) and the group *pgg* that combines two-fold rotations with glide reflections. An example of the latter is given in figure 6.10. For the group *pgg*, the unit cell is four times the size of the fundamental domain.

6.5 Simulation results

To illustrate and support our findings, we have applied the interaction recipe to the target patterns shown in figures 6.6, 6.8 and 6.10 and we have run Monte Carlo simulations starting from random initial conditions. The resulting configurations are shown for comparison on the opposing pages, in figures 6.7, 6.9 and 6.11. The results clearly indicate a strong tendency to assemble into the designed target patterns. In addition, in figures 6.7 and 6.11 distinct grain boundaries are visible between locally ordered patches with incompatible macroscopic orientations.

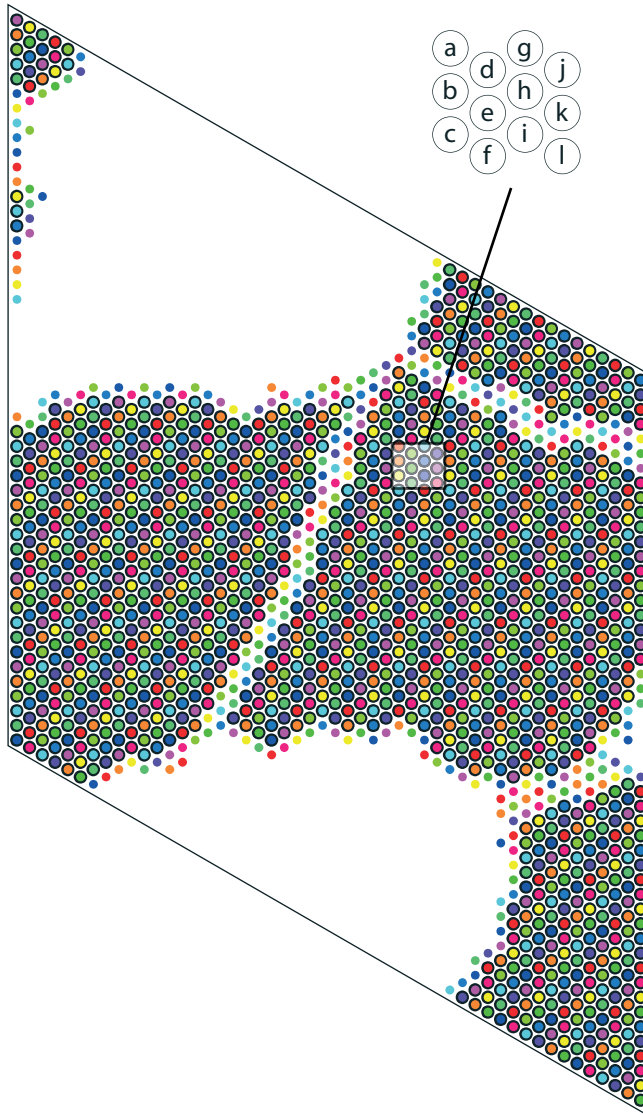For the simulations, the interaction energies were chosen as $\alpha = 3k_B T$, $\varepsilon = 3k_B T$.

Figure 6.7: Simulation result for the pattern shown in figure 6.6. Beads with locally ordered nearest-neighbors are indicated with a dark ring.
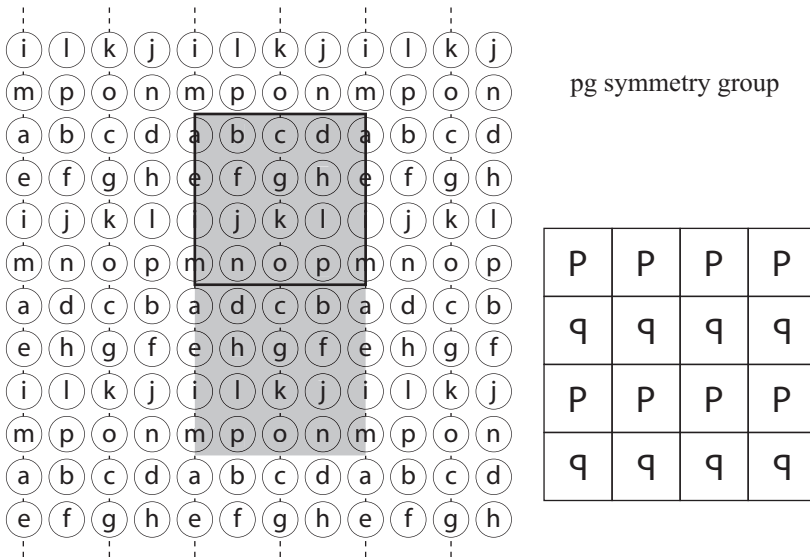
Figure 6.8: Example of a periodic crystal (group *pg*) with glide symmetries (dashed lines) on a square lattice. The basic tile of beads is delineated by the black rectangle, and the unit cell is indicated by the gray rectangle. The image on the right shows how the tiles are connected to produce the pattern, where the P indicates the intrinsic orientation of each tile.

The system dimensions were 50 × 50, forming a square for a square lattice and a parallelogram for a hexagonal lattice, both with periodic boundary conditions. The systems were initialized with 2/3 of the sites occupied by beads of all types in equal proportions, and at random positions. For the evolution of the system a Metropolis algorithm was used with 10^9 steps in which a swap of two random beads was attempted. In all cases, this led to sufficient equilibration of the system, with the possible exception of grain boundaries. Local ordering is determined by detecting whether a bead has all the correct nearest neighbors in the correct order. Beads with locally ordered neighborhoods are indicated by a black ring around them. Connected regions of these beads therefore indicate macroscopic crystal structures of the correct type.

6.6   Discussion

In this chapter we have introduced a two-dimensional lattice model for the interactions between DNA-coated colloids. The model allows for a multitude of bead types that interact according to pair-specific interaction energies that are isotropic and of

Figure 6.9: Simulation result for the pattern shown in figure 6.8. Beads with locally ordered nearest-neighbors are indicated with a dark ring.

pgg symmetry group

Figure 6.10: Example of a periodic crystal (group *pgg*) with 2-fold rotational (diamonds) and glide symmetries (dashed lines) on a hexagonal lattice. The basic tile of beads is delineated by the black parallelogram, and the unit cell is indicated by the gray rectangle. The image on the bottom shows how the tiles are connected to produce the pattern, where the P indicates the intrinsic orientation of each tile.
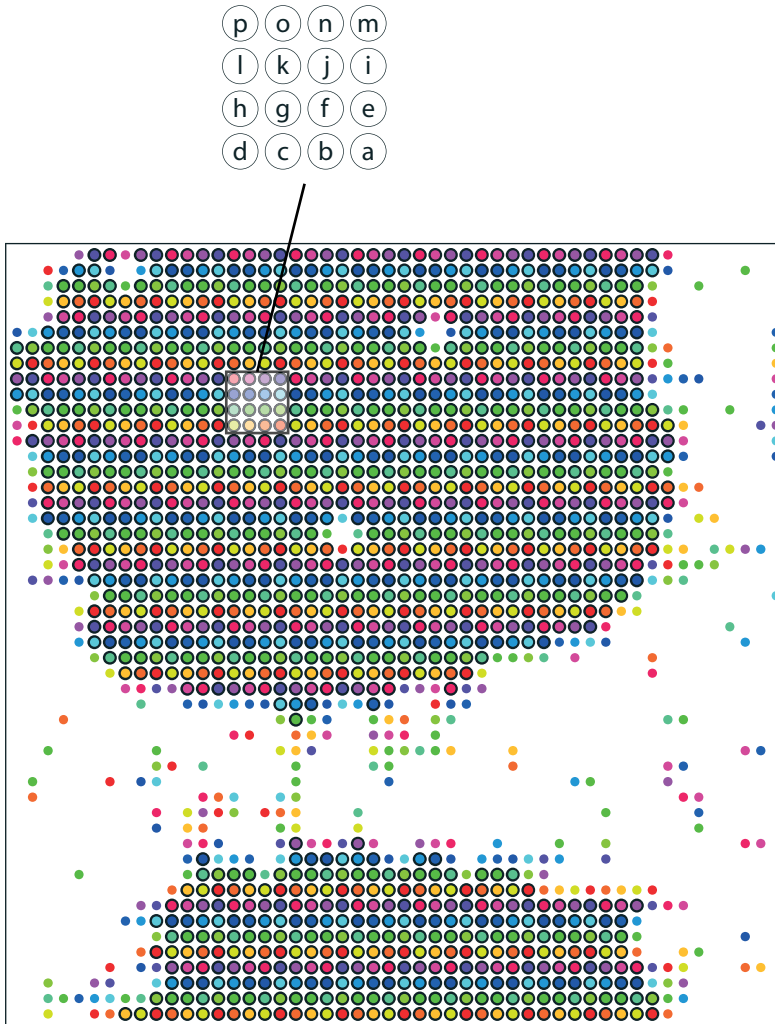
Figure 6.11: Simulation result for the pattern shown in figure 6.10. Beads with locally ordered nearest-neighbors are indicated with a dark ring.
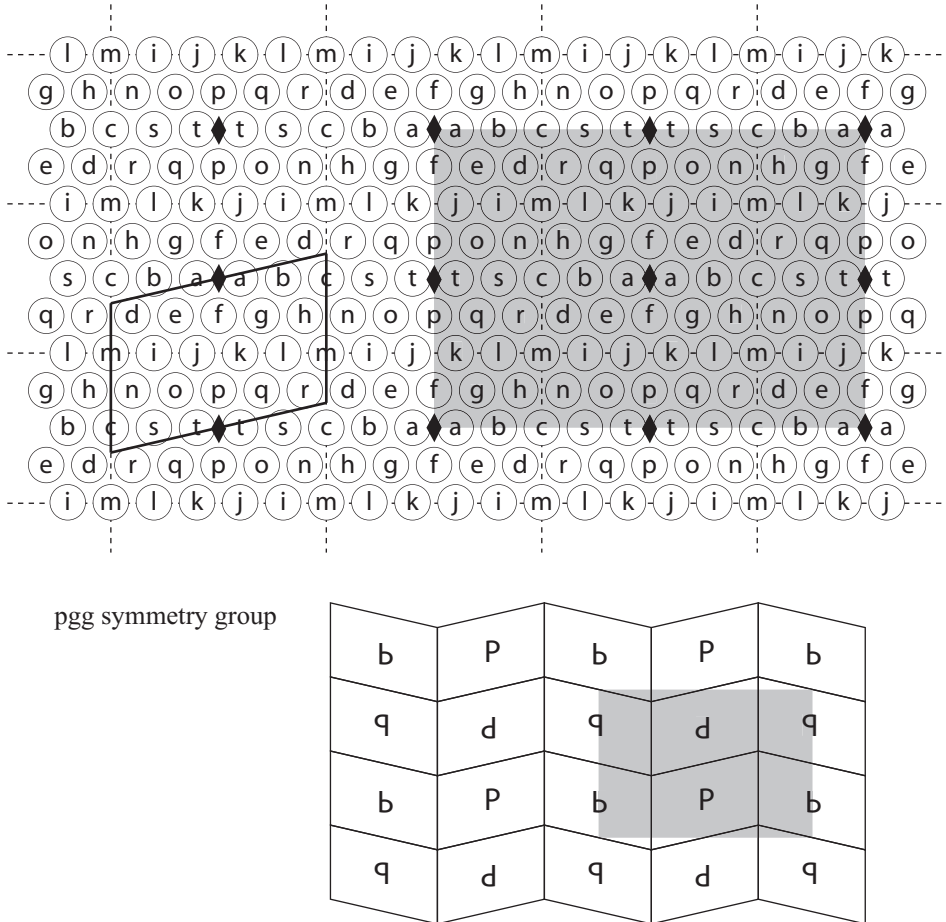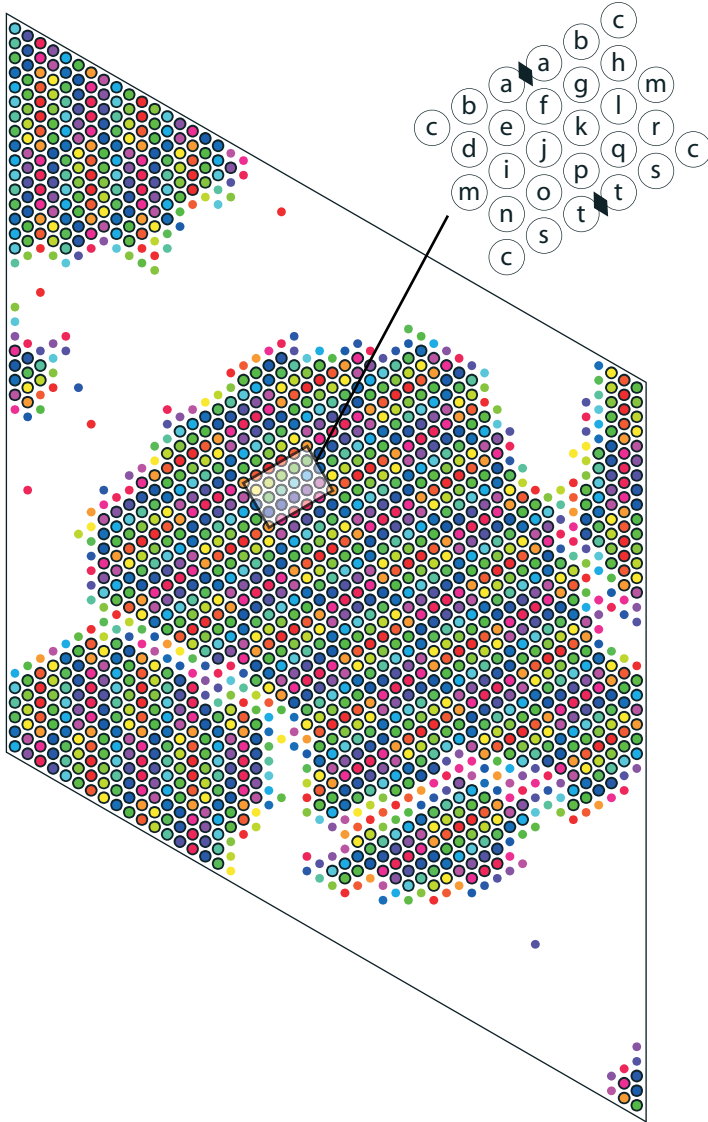
finite range. For this system we have investigated whether it is possible to choose the interaction energies in such a way that a predetermined periodic pattern is the unique ground state of the system.

Essential to the establishment of a non-trivial pattern as a unique ground state is the ability for the interactions between beads to suppress the symmetries of the underlying lattice. This has lead to the derivation in section 6.2 of a minimum interaction range that depends on the lattice type. On a square lattice, interactions need to extend to the next-next-nearest neighbors, whereas on a hexagonal lattice, interactions up to and including the next-nearest neighbors are sufficient.

Building on this result, we have introduced a simple recipe for the interactions between bead species that is minimal in terms of the interaction range between particles and guarantees the local uniqueness of the ground state. The prescription consists of an attractive nearest-neighbor potential for particles that should become nearest neighbors in the final pattern and a self-repulsion at larger distances (up to the required interaction range) between particles of the same type . This recipe has been shown to work for simple periodic patterns, patterns with glide reflections and patterns with two-fold rotations on a hexagonal lattice.

The choice of interactions energies that has been made for the simple recipe is meant as a proof of concept and is certainly not unique. This is especially true for the choice for the long-range self-repulsion that does not contribute to the energy of the ground state, but merely prevents lattice symmetries from disrupting the pattern. Another valid choice would be to add an offset to all long-range interaction energies, whilst maintaining a slightly more repulsive interaction for beads of the same type. A similar assumption of long-range repulsions has been necessary to stabilize bead configurations in off-lattice models (Tkachenko, 2002; Licata and Tkachenko, 2006). The authors did not arrive at the requirement for this repulsion to be pair-specific, but that is likely because they did not address the situation with many copies of each bead type, which is the reason for the existence of the self-repulsion in our recipe.

Any further adjustments to the interaction recipe will need to be made in the light of the temporal aspects of self-assembly, which have been ignored in the context of this chapter. For example, the ground state of a system, however well designed, may be kinetically inaccessible. On the other hand, well-chosen interactions could speed up the formation of the ground state pattern, for example through a 'staged' ordering process (Lukatsky et al., 2006).

In section 6.4 crystal structures have been created by enabling specific symmetries: translations, glide reflections and two-fold rotations. These crystals have fundamental domains that consist of beads that are all unique in terms of their interactions. One of the distinct advantages of more complex crystal structures over the simple periodic crystals is that the fundamental domain, the basic unit of the tiling, is smaller than the unit cell, limiting the number of uniquely designed beads that is required to make a pattern of a given periodicity. For example, the unit cell of the *pgg* symmetry group is four times larger than its fundamental domain (see figure 6.10).

In addition, it is important to stress that the requirement for all beads in a tile to be unique only refers to their DNA-mediated interactions. The other properties
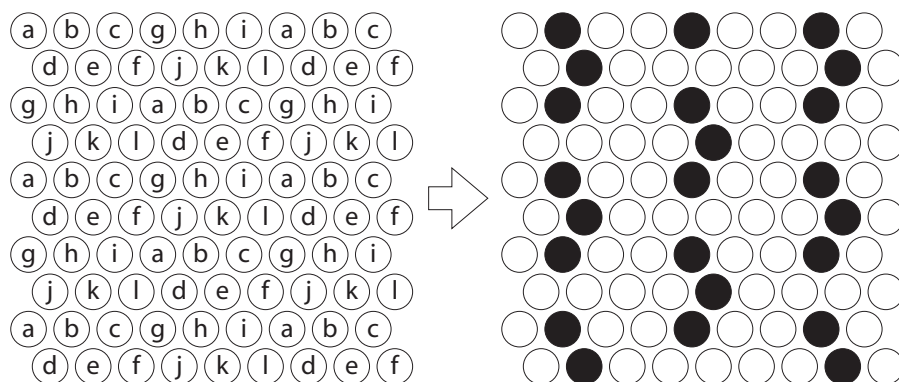
Figure 6.12: Demonstration of the use of a periodic pattern of unique beads as a template. Beads `b`, `e` and `h` are colored black, the others are white.

of the beads can be chosen independently and can be used to create a higher level pattern on top of the periodic crystal that now serves as a template. For example, some beads could have additional chemical binding sites, or fluorescent or electrical properties. The ability to use the underlying crystal as a template is visualized in figure 6.12 for the simple periodic pattern shown in figure 6.6.

In future work, the interaction recipe presented in this chapter could be extended to allow for additional symmetries, enabling even more complex crystals to be designed. Furthermore, the techniques that have been introduced in this chapter could be applied to the three-dimensional case, which has many more symmetry operations, but otherwise is not fundamentally different from the two-dimensional situation discussed here.

6.A Classification of possible tilings

In this chapter we have created and classified various patterns according to their symmetries. The collection of possible symmetries is given by the crystallographic wallpaper groups. However, an alternative approach to the design of patterns is worth mentioning, especially if the interactions energies are chosen differently for the various beads. Then, it may be more fruitful to consider the self-assembly as a two-step process, in which a number of beads first assemble into tiles (due to strongly attractive interactions) and these tiles assemble into a crystal structure on longer time scales.

In this context, the symmetry groups can be used to classify the *result* of a tiling process, but the starting point should be the shape and connectivity properties of the tiles themselves. For simplicity, we restrict ourselves to marked isohedral tilings.

A tiling is isohedral if every tile belongs to one equivalence class under the symmetry group of the tiling, i.e. the pattern consists of a single 'type' of tile. Furthermore, the DNA-coated colloid tiles are marked (oriented) because they have an internal structure of unique beads. In this section we present a classification of all possible ways in which a marked isohedral tiling can be constructed, for both triangular and square underlying lattices. This information is presented as a resource for potential future work.

6.A.1　Tiling topologies

The following analysis is based on the classification of marked isohedral tilings by Grünbaum and Shephard (1987). They have constructed an exhaustive list of 93 topologically distinct marked isohedral tilings of the 2D plane. However, 47 of these are based on prototiles (the equivalence class of tiles with all possible rotations) that have non-trivial internal symmetries, implying that they can be decomposed into other, more basic tiles. It is therefore sufficient to consider only the remaining 46 tilings.

In figures 6.13 and 6.14 we show all possible tilings by their respective adjacency diagrams. All tilings are edge-to-edge and isohedral, so the tiling is fully determined when we specify which edges of the prototile connect to each other and the orientation with which they do so. The connectivity is indicated by the dots in the center of the tile edges in the adjacency diagram. If two dots are connected by a line, the corresponding edges will be connected to each other in the resulting tiling. The absence of a connecting line indicates that an edge connects to itself. Every connection dot or pair of connection dots also has a sign associated with it. A plus sign indicates that the orientation of the attached tile can be obtained from the presented tile using only a rotation, whereas a minus sign indicates that a reflection is required. The IHxx classification below the diagrams is the name assigned by Grünbaum and Shephard (1987). The diagrams are ordered according to their symmetry groups, and their compatibility with the square and hexagonal lattices is indicated.

6.A.2　Topologically equivalent tilings

The 46 different tilings thus created are only representatives of their respective topological classes. These archetypical examples can be modified to form an infinitely large family of different prototile shapes by a continuous transformation, under the constraint that the resulting prototile still defines a valid tiling. This transformation, and the constraints imposed on it, can be decomposed into two steps.

First, we may change the positions of the vertices of the tiling. This generally involves changing the length of the edges and the opening angles between adjacent edges. In this process, care must be taken to scale edges that are connected by an adjacency line by the same amount. Another restriction applies to the angles at which the edges meet. Since the number of tiles that meet at a particular lattice vertex is conserved by any continuous transformation, the decrease of one angle implies the

Figure 6.13: Adjacency diagrams of all marked isohedral tilings, sorted by symmetry group. Compatibility with the square and hexagonal lattices is indicated by a small square or triangle, respectively.
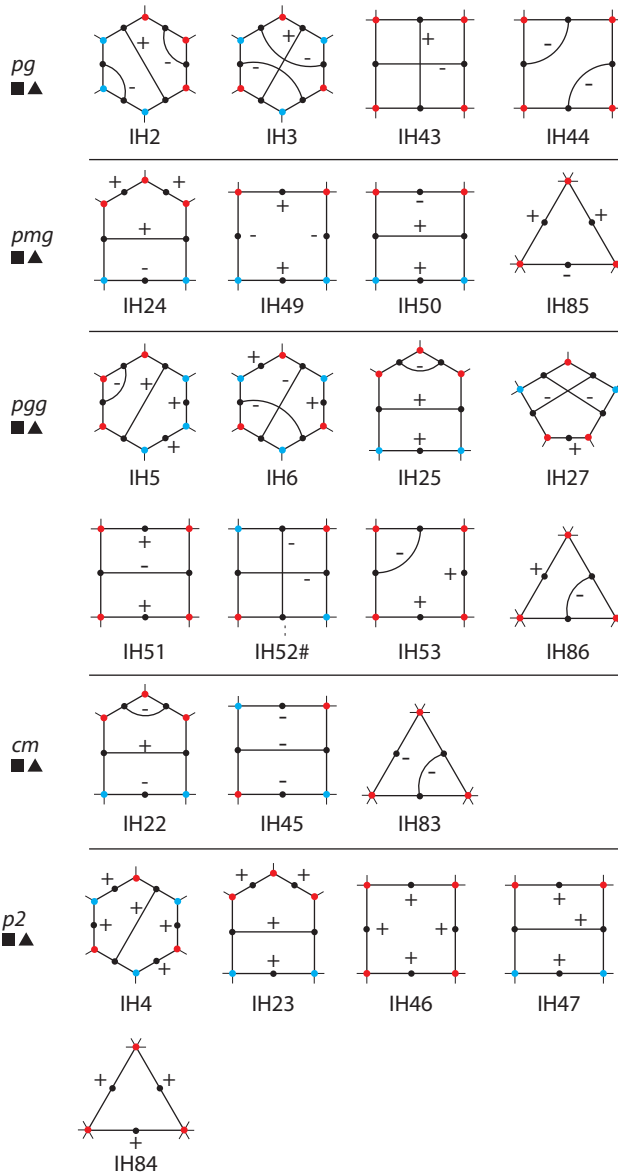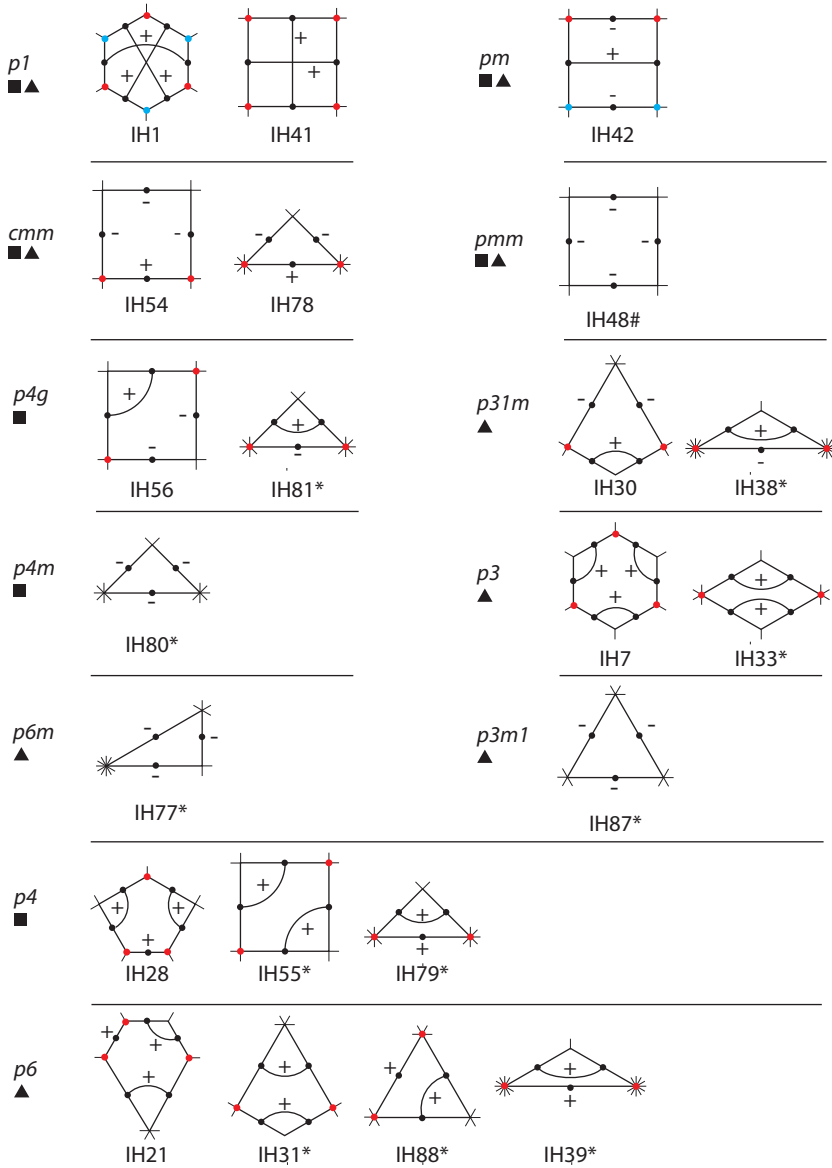
Figure 6.14: Adjacency diagrams of all marked isohedral tilings, sorted by symmetry group. Compatibility with the square and hexagonal lattices is indicated by a small square or triangle, respectively.

increase of another one. This imposes a strong restriction when combined with the isohedral assumption. It is possible to divide the corners of the prototile into equivalence classes, with corners sharing the same vertex locations belonging to the same equivalence class. This means that any change in angle of one corner needs to be compensated for by an opposite change in the angle of (an)other corner(s) belonging to the same equivalence class. Furthermore, it implies that any corners that form an equivalence class of their own necessarily have a fixed angle. In the adjacency diagrams in figures 6.13 and 6.14, corners belonging to equivalence classes that have more than one element are indicated by a colored dot, specific for that class. To see these transformations in action, we note that our definition of the fundamental domain in figure 6.6 corresponds to the tiling labelled IH1, the one in figure 6.8 corresponds to IH43 and the one in figure 6.10 corresponds to IH51.

Note that the dependencies between the changes in vertex angles and edge lengths may prevent changes in the positions of the vertices. The diagrams in figures 6.13 and 6.14 that are indicated with an asterisk (*) have fixed vertex positions for this reason. The prototiles IH48 and IH52 indicated by a hash (#) sign can only change their aspect ratios, whereas the vertex angles are fixed.

Finally, although we have not done so, the shapes of the edges of the prototiles can be modified, in accordance with the adjacency diagram: adjacent edges must transform in similar ways.

7

Discussion and outlook

In this final chapter we summarize the main findings from the earlier chapters and, where applicable, relate them to each other. In addition, suggestions are made for continued theoretical work and experiments are indicated that would help in giving direction to that work. To elucidate the connections between the work presented in different chapters, the results will be discussed in their biological context. This necessarily leads to a reduced exposure for results that are interesting mainly from a theoretical or methodological perspective. For these, we refer the reader to the discussion sections of the individual chapters.

The chapter is divided into three sections. The first section discusses the processes causing cortical microtubules to align (chapters 2, 3 and 4); the second section delves into the possible mechanisms underlying the orientation of this alignment (chapter 5), and the final section addresses the design of unique ground states for DNA-coated colloids (chapter 6).

7.1 Alignment of cortical microtubules

There is a large number of factors that influence the ability of the cortical array in plant cells to align. We have investigated these mechanisms using a mixture of theoretical and simulations tools. We start this section by discussing these tools, before summarizing the results for each of the mechanisms the cell has at its disposal to control the cortical array formation.

7.1.1 Methods

In chapter 3 we have constructed a model for the alignment of cortical microtubules, based on biological observations. An important aspect of this model is that it allows us to identify a single dimensionless control parameter G, which is fully determined

by the nucleation rate and intrinsic dynamics of individual microtubules. This control parameter determines the steady state degree of order of the system, when the probabilities for zippering ($P_z(\theta)$) and catastrophe induction ($P_c(\theta)$) upon collision are specified. For increasing values of G, the isotropic stationary solutions to the model show an increase both in density and in abundance of interactions, as measured by the ratio of microtubule length over the mesh-size. The control parameter G has been used throughout the research in this thesis and may also turn out to be very useful in comparing different *in vivo* systems.

In chapter 4 we have introduced a simulation model for the microtubules in the cortical array that builds upon the theoretical model and extends it by adding a number of additional processes that have been shown to be relevant in a biological context. In conjunction with the model, an efficient event-driven simulation scheme has been presented that is tailored to the specific needs imposed by the cortical array model. The simulations make it possible to directly probe the dynamics of discrete microtubules, instead of the coarse-grained averages described by the theory. This also allows us to verify the applicability of the theory to real-life (non-coarse-grained) situations.

7.1.2   Induced catastrophes

One of the most striking results from the theory of interacting microtubules is that the collision-induced catastrophes are the primary driver of alignment. The bifurcation point of the isotropic solution, i.e. the critical value of G^* of the control parameter at which the system develops ordered stationary solutions from the isotropic state, is determined solely by the angle-dependent probability for collisions to induce a catastrophe (equation (3.56)).

For a limited class of models for which the geometrically corrected induced catastrophe probability consists of a small number of Fourier modes, the ordered solution to the theoretical model can be determined numerically as a function of G (section 3.2.4). In spite of the coarse-grained approximation in the derivation of the theory, simulation results match these predictions very closely, as evidenced by figure 4.4. From this we conclude that the theory can be used to make quantitative predictions for systems of microtubules that interact only through a combination of crossing over and induced catastrophes. It would be worthwhile to compare these results to *in vitro* experiments on microtubules that are bound to a surface.

7.1.3   Zippering

A surprising corollary of the result that the onset of ordering only depends on the induced catastrophe function is that it does *not* depend on zippering in any way – at least insofar as the theory is concerned. Also, the numerical solutions of the minimal interaction model (section 3.2.4) with zippering enabled, show only a minimal dependence on the amount of zippering, resulting in a slightly less ordered system. However, whereas the simulations yielded a good match with the theory

in the absence of zippering, this was no longer the case when zippering was enabled. The reason for the discrepancy is that zippering, by its very nature introduces strong spatial correlations in the form of microtubule bundles – something that is not accounted for in the theory.

Furthermore, when bundles are present it is necessary to specify how the probabilities for microtubules to undergo a collision-induced catastrophe or to zipper depend on whether they are colliding with a single microtubule or with a bundle, or whether they themselves are part of a bundle. Several of these *bundle interaction modes* were introduced in section 4.1. Simulations comparing all four modes revealed large differences in the onset of alignment as a function of G, and correspondingly large deviations from the theoretical prediction – both towards higher and lower values of G (figures 4.6 and 4.7). Furthermore, as the fraction of crossover events was increased, i.e. in the weak-interaction limit, the results did not seem to converge to the theoretical prediction, nor to each other. The one exception to this pattern is the multi-collision interaction mode that has been constructed specifically to approximate the coarse-grained model (see appendix 4.B), at the expense of biological accuracy. In the limit of very weak interactions, this interaction mode did reproduce the predicted bifurcation point, but significant deviations from the theoretical curve remain visible for highly ordered systems.

Finally, it should be noted that the qualitative impact of zippering depends not only on the bundle interaction mode, but also on the features of the probability functions: enabling zippering for the simple bundle collision mode led to a *decrease* in order with the minimal interaction probabilities (figure 4.6), but it led to an *increase* in combination with the interaction probabilities described in figure 4.8 (see figure 4.9).

The conclusion to be drawn from these observations is that the details of the interactions between bundles are of vital importance for the quantitative understanding of microtubule alignment in the presence of zippering. The large fluctuations of the results depending on the choice of interaction mode show that this is an area in which experimental guidance is extremely valuable. Once a biologically motivated model for bundle interactions has been created, it can be used for simulations, and it may be possible to incorporate it in the theoretical model from chapter 3.

7.1.4   Treadmilling

In a treadmilling microtubule the minus end of a microtubule undergoes a steady depolymerization. In the absence of zippering , the effect of treadmilling can be described through a renormalization of the control parameter G and a rescaling of the collision and zippering probabilities, leading to the definition of an effective control parameter G', defined in (4.7). This scaling behavior works very well in the absence of zippering, as evidenced by the comparison in figure 4.9 (top).

The same figure (bottom) shows that for biologically relevant parameters, enabling treadmilling in the absence of zippering generally leads to a decreased alignment of the system. However, there is some evidence (see the discussion in section

4.4.2) that the combination of zippering and treadmilling leads to a robust increase in the alignment of the system, accompanied by a decrease of its density. This combination may therefore be used by cells to create an ordered system with a smaller tubulin footprint.

7.1.5   Severing

CONSERVATION OF MICROTUBULE NUMBER

One of the surprising theoretical results from chapter 2 is that severing events do not affect the total number of microtubules in the system, provided that the newly created microtubule plus end immediately undergoes a catastrophe (section 2.3). This is true for any number of severing events and regardless of where on the microtubule they occur. This result is a consequence of the fact that the expected lifetime of a shrinking microtubule is proportional to its length, and that a growing microtubule of the same length has a fixed additional lifetime.

The conservation of microtubule number in the presence of severing is in apparent contradiction with the experimentally reported increase in microtubule numbers (Roll-Mecak and Vale, 2006). However, this is readily explained by the fact that our result is based on constant parameter values. In a living cell, the decrease in average microtubule length that is the result of severing will lead to an increased availability of free tubulin dimers. In turn, this is likely to increase the polymerization rate (growth speed) and nucleation rate, either of which indeed causes an increase in the number of microtubules.

RANDOM SEVERING

In chapter 2 we have constructed a model for the length distribution of microtubules that are being severed at random locations on the microtubule lattice with a fixed rate per unit of length. The resulting steady state length distributions have been determined analytically for the special cases of small severing rates and the case without rescues. The generic case has been addressed using a numerical method and the results have been verified by a comparison with the outcome of a direct simulation of an ensemble of microtubules.

As was to be expected, an increase in the severing rate always leads to a decrease in the average length of the microtubules. In addition, we have found that the distributions became more compact, meaning that the microtubules become more similar in length. This can be appreciated from the fact that the rate of severing is proportional to the length of each microtubule, so the number of long microtubules is strongly suppressed. Furthermore, in contrast to the dynamic instability model without severing, the length distributions are no longer always monotonically decreasing with increasing length. A 'bump' can sometimes be created in the distribution when the steady supply of short growing microtubules that are created by severing events is not balanced by a sufficiently high spontaneous catastrophe rate. Unfortunately, we

are not aware of *in vitro* experiments in which the microtubule length distribution has been measured in the presence of severing, so we cannot compare our results with experimental findings.

When microtubule severing at random locations was enabled in simulations of interacting microtubules, this predictably led to a decreased ability of the system to align (figure 4.10), due to the shorter microtubules and corresponding decrease in density. However, there seems to be no clear quantitative link between the decrease in order and the decrease in average length of the non-interacting system with the same parameters.

SEVERING AT INTERSECTIONS

Wightman and Turner (2007) have found evidence in *Arabidopsis* for severing of microtubules at locations where two microtubules cross. Their experiments suggest that this type of severing is required for the formation of the cortical array. In our simulations, the inclusion of this effect led to a rather subtle effect. In the absence of treadmilling and zippering, severing at intersections caused a decrease in the tendency to align, just as for severing at random locations. However, when treadmilling and zippering were enabled, severing at intersections suddenly had a *beneficial* effect on alignment (figure 4.11). The sudden reversal of the effect of severing at intersections is probably caused by the asymmetry of the severing mechanism in our model: the microtubule that is cut is always the one that is on the cytoplasmic side, i.e. part of the bundle that was last to arrive at that particular intersection. This leads to an effective stabilization of microtubule bundles due to the fact that they have longer effective lifetimes than single microtubules. Further investigations should indicate whether this is indeed the case in the case of our model, and whether this asymmetry is also present in experiments.

7.1.6   Finite tubulin pool

For the purposes of the theory and simulations it is common to use fixed values for the model parameters. However, when G approaches or exceeds zero, this can lead to a diverging density of the ordered phase. This can be understood, because the use of constant parameter values implicitly assumes that there is an infinite supply of tubulin dimers available for incorporation into microtubules.

To counter these diverging densities that are at odds with biological reality, we have argued in section 3.2.5 that it is reasonable to assume that the cell contains only a limited pool of tubulin dimers. The depletion of this pool feeds back into the system through a decreased growth speed of the microtubules, ensuring that the total length of the system remains bounded. Through this mechanism, the system will always settle into a steady state – even when the initial value of G is larger than 0. As the density increases, the decreasing growth speed of the microtubule plus end will eventually cause the effective value of G to settle at a value smaller than zero. Examples of this mechanism are shown in figures 3.7 and 4.14.

We have found that the limitation on the amount of available tubulin has a stabilizing effect on the system, making it less sensitive to changes in individual parameters. It should be noted that we have thus far used a linear relation between the available tubulin pool and the plus end growth speed (cf. Mitchison and Kirschner, 1984). For further research, especially into the time-dependent process of alignment, this relationship should be verified experimentally, and adjusted if necessary. Furthermore, in the simulations we have estimated the size of the tubulin pool on an *a posteriori* argument, whereas it is preferable to be able to set it as an independent parameter that is based on experimental findings.

7.1.7   Time-dependent properties

The time-dependent simulation results in section 4.4.3 show that the simulation model is able to reproduce a number of the observables reported in the literature (table 4.3), starting from literature values for the parameters, augmented with educated guesses for the remaining parameters. As more experimental data becomes available and more parameters can be pinned down, the simulations can be expected to yield more quantitative insights into the self-organized alignment of microtubules and the process of its establishment. Specifically, the nucleation rate, and its dependence on the cell cycle and tubulin concentration, remains an important parameter that is largely unknown. Also, although there are measured values for the catastrophe rate, these can only be treated as an upper limit for the actual spontaneous catastrophe rate, because the collision-induced catastrophes are not accounted for. The analysis in section 3.F suggests that the reported values may be too high by a factor of two or more.

7.2   Cortical array orientation

To investigate the origins of the orientation of the cortical array, in chapter 5 we have extended the hitherto two-dimensional cortical array simulations to the surface of a cylinder in three dimensions. This step necessitated the determination of minimum-curvature microtubule trajectories on curved surfaces and the creation of the R_2 order parameter that describes the extent to which microtubules on a surface exhibit collective alignment perpendicular to an emergent cell expansion axis. Although both concepts have only been applied to the cylinder surface, they are applicable to generic curved surfaces in three spatial dimensions. Extensions to other basic cell shapes, such as boxes or spherocylinders, can therefore be implemented in a straightforward manner.

The simulation results in figures 5.6 and 5.7 indicate that the use of a cylindrical cell geometry restricts the possible orientations of the cortical array, and the observed orientations (along the cylinder axis and perpendicular to it) correspond to the symmetries of the underlying geometry. In addition, the cylindrical geometry imposes a slight bias to the orientation of the array in the direction of the cell axis, but this is

not strong enough to reliably determine the orientation of alignment. In addition, we varied the spontaneous catastrophe rate on the end caps of the cylindrical cell by multiplying it by a factor c. Comparing the results for $c = 1, 2$ and 4, we see that a local cue in the form of in increased spontaneous catastrophe rate at the cylinder end caps *is* sufficient to ensure that (nearly) all systems eventually orient their microtubules perpendicular to the cell axis.

The suggestion that local cues at the cell ends exist and may play a role in cortical array orientation has popped up repeatedly in the literature. It is known, for example, that the PIN family of proteins, related to auxin transport, localize to these faces (Lucas and Shaw, 2008), making them a potential candidate for (indirect) modification of microtubule activity. Also, the ROP2/RIC1 proteins are thought to modify microtubule activity in specific regions of the cortex (Ehrhardt and Shaw, 2006). Furthermore, recent experiments by Hamant et al. (2008) have demonstrated the existence of a connection between applied cell wall stress and the cortical array orientation. The model that was introduced by the authors relied on a macroscopic description in which the average microtubule direction on the outward-facing cell surface co-aligns with the direction of maximal stress on the surrounding cell walls. The simulation results from this chapter could provide a microscopic understanding of this connection: If we assume that tension on the cell wall activates a stress response that locally increases the catastrophe rate, the two sides of the cell that are under maximum tension will act as the 'cell poles'. The cortical array will then be established along the axis between these poles, with the microtubule pointing in the perpendicular direction – parallel to the direction of maximum wall stress, as observed in the experiments.

We conclude that there is plenty of circumstantial evidence for location-specific modulation of microtubule dynamics. However, experiments will have to indicate whether the dynamics of the cortical microtubules are indeed different at the cell poles, and, if so, which parameters are most affected.

7.3   DNA-coated colloids

In chapter 6 we have discussed the ability for DNA-coated colloids to self-assemble into a designed pattern. For this purpose we have introduced a two-dimensional lattice model for the interaction between the beads. The model allows for a multitude of bead types that interact according to pair-specific interaction energies that are isotropic and of finite range. For this system we have investigated whether it is possible to choose the interaction energies in such a way that a predetermined periodic pattern is the unique ground state of the system.

Essential to the establishment of a non-trivial pattern as a unique ground state is the ability for the interactions between beads to suppress the symmetries of the underlying lattice. This has lead to the derivation in section 6.2 of a minimum interaction range that depends on the lattice type. On a square lattice, interactions need to extend to the next-next-nearest neighbors, whereas on a hexagonal lattice,

interactions up to and including the next-nearest neighbors are sufficient.

Building on this result, we have introduced a simple recipe for the interactions between bead species that is minimal in terms of the interaction range between particles and guarantees the local uniqueness of the ground state. The prescription consists of an attractive nearest-neighbor potential for particles that should become nearest neighbors in the final pattern and a self-repulsion at larger distances (up to the required interaction range) between particles of the same type . This recipe has been shown to work for simple periodic patterns, patterns with glide reflections and patterns with two-fold rotations on a hexagonal lattice.

The choice of interactions energies that has been made for the simple recipe is meant as a proof of concept and is certainly not unique. This is especially true for the choice for the long-range self-repulsion that does not contribute to the energy of the ground state, but merely prevents lattice symmetries from disrupting the pattern. Another valid choice would be to add an offset to all long-range interaction energies, whilst maintaining a slightly more repulsive interaction for beads of the same type. A similar assumption of long-range repulsions has been necessary to stabilize bead configurations in off-lattice models (Tkachenko, 2002; Licata and Tkachenko, 2006). The authors did not arrive at the requirement for this repulsion to be pair-specific, but that is likely because they did not address the situation with many copies of each bead type, which is the reason for the existence of the self-repulsion in our recipe.

Any further adjustments to the interaction recipe will need to be made in the light of the temporal aspects of self-assembly, which have been ignored in the context of this chapter. For example, the ground state of a system, however well designed, may be kinetically inaccessible. On the other hand, well-chosen interactions could speed up the formation of the ground state pattern, for example through a 'staged' ordering process (Lukatsky et al., 2006).

In section 6.4 crystal structures have been created by enabling specific symmetries: translations, glide reflections and two-fold rotations. In future work, the interaction recipe presented in this chapter could be extended to allow for additional symmetries, enabling even more complex crystal structures to be designed. Furthermore, the techniques that have been introduced in this chapter could be applied to the three-dimensional case, which has many more symmetry operations, but otherwise is not fundamentally different from the two-dimensional situation discussed in chapter 6.

Bibliography

B. Alberts, A. Johnson, J. Lewis, M. Raff, K. Roberts, and P. Walter. *Molecular Biology of the cell*. Garland Science, 4th edition, 2002. ISBN 978-0815332183.

E. L. Allgower and K. Georg. *Introduction to Numerical Continuation Methods*, volume 45 of *Classics in Applied Mathematics*. SIAM, 2003. ISBN 978-0898715446.

J. C. Ambrose, T. Shoji, A. M. Kotzer, J. A. Pighin, and G. O. Wasteneys. The Arabidopsis CLASP gene encodes a microtubule-associated protein involved in cell expansion and division. *Plant Cell*, 19:2763–2775, 2007. doi: 10.1105/tpc.107.053777.

T. Antal, P. L. Krapivsky, S. Redner, M. Mailman, and B. Chakraborty. Dynamics of an idealized model of microtubule growth and catastrophe. *Physical Review E (Statistical, Nonlinear, and Soft Matter Physics)*, 76(4):041907, 2007. doi: 10.1103/PhysRevE.76.041907.

I. S. Aranson and L. S. Tsimring. Theory of self-assembly of microtubules and motors. *Physical Review E (Statistical, Nonlinear, and Soft Matter Physics)*, 74(3):031915, 2006. doi: 10.1103/PhysRevE.74.031915.

A. Ashkin. Acceleration and trapping of particles by radiation pressure. *Phys. Rev. Lett.*, 24(4): 156–159, 1970. doi: 10.1103/PhysRevLett.24.156.

D. A. Barry, P. J. Culligan-Hensley, and S. J. Barry. Real values of the W-function. *ACM Transactions on Mathematical Software*, 21(2):161–171, 1995. doi: 10.1145/203082.203084.

F. Bartolini and G. G. Gundersen. Generation of noncentrosomal microtubule arrays. *J Cell Sci*, 119(20):4155–4163, 2006. doi: 10.1242/jcs.03227.

D. A. Barton, M. Vantard, and R. L. Overall. Analysis of Cortical Arrays from Tradescantia virginiana at High Resolution Reveals Discrete Microtubule Subpopulations and Demonstrates That Confocal Images of Arrays Can Be Misleading. *Plant Cell*, 20(4):982–994, 2008. doi: 10.1105/tpc.108.058503.

V. A. Baulin, C. M. Marques, and F. Thalmann. Collision induced spatial organization of microtubules. *Biophys. Chemist.*, 128:231–244, 2007. doi: 10.1016/j.bpc.2007.04.009.

P. L. Biancaniello, A. J. Kim, and J. C. Crocker. Colloidal interactions and self-assembly using dna hybridization. *Physical Review Letters*, 94(5):058302, 2005. doi: 10.1103/PhysRevLett.94.058302.

A. Bichet, T. Desnos, S. Turner, O. Grandjean, and H. Höfte. BOTERO1 is required for normal orientation of cortical microtubules and anisotropic cell expansion in Arabidopsis. *The Plant Journal*, 25:137–148, 2001. doi: 10.1111/j.1365-313X.2001.00946.x.

D. J. Bicout. Green's functions and first passage time distributions for dynamic instability of microtubules. *Phys. Rev. E*, 56(6):6656–6667, 1997. doi: 10.1103/PhysRevE.56.6656.

D. J. Bicout and R. J. Rubin. Classification of microtubule histories. *Phys. Rev. E*, 59(1):913–920, 1999. doi: 10.1103/PhysRevE.59.913.

D. Boal. *Mechanics of the cell*. Cambridge University Press, 2002. ISBN 9780521796811.

J. P. Boyd. *Chebyshev and Fourier Spectral Methods*. Dover, second edition, 2001. ISBN 0-486-41183-4.

B. Bozorgui and D. Frenkel. Liquid-vapor transition driven by bond disorder. *Physical Review Letters*, 101(4):045701, 2008. doi: 10.1103/PhysRevLett.101.045701.

D. Burk, R. Zhong, and Z.-H. Ye. The katanin microtubule severing protein in plants. *Journal of Integrative Plant Biology*, 49(8):1174–1182, 2007. doi: 10.1111/j.1672-9072.2007.00544.x.

D. H. Burk, B. Liu, R. Zhong, W. H. Morrison, and Z.-H. Ye. A Katanin-like Protein Regulates Normal Cell Wall Biosynthesis and Cell Elongation. *Plant Cell*, 13(4):807–828, 2001. doi: 10.1105/tpc.13.4.807.

H. N. Cartwright, J. A. Humphries, and L. G. Smith. PAN1: A Receptor-Like Protein That Promotes Polarization of an Asymmetric Cell Division in Maize. *Science*, 323(5914):649–651, 2009. doi: 10.1126/science.1161686.

J. Chan, G. M. Calder, J. H. Doonan, and C. W. Lloyd. EB1 reveals mobile microtubule nucleation sites in Arabidopsis. *Nat. Cell Biol.*, 5:967–971, 2003. doi: 10.1038/ncb1057.

J. Chan, G. Calder, S. Fox, and C. Lloyd. Cortical microtubule arrays undergo rotary movements in arabidopsis hypocotyl epidermal cells. *Nat Cell Biol*, 9(2):171–175, 2007. doi: 10.1038/ncb1533.

R. Corless, G. Gonnet, D. Hare, D. Jeffrey, and D. Knuth. On the lambert W function. *Advances in Computational Mathematics*, 5(1):329–359, 1996. doi: 10.1007/BF02124750.

J. C. Crocker. Nanomaterials: Golden handshake. *Nature*, 451:528 – 529, 2008. doi: 10.1038/451528a.

L. J. Davis, D. J. Odde, S. M. Block, and S. P. Gross. The importance of lattice defects in katanin-mediated microtubule severing in vitro. *Biophysical Journal*, 82(6):2916 – 2927, 2002. doi: 10.1016/S0006-3495(02)75632-4.

A. Desai and T. J. Mitchison. Microtubule polymerization dynamics. *Annual Review of Cell and Developmental Biology*, 13(1):83–117, 1997. doi: 10.1146/annurev.cellbio.13.1.83.

P. Deuflhard, B. Fiedler, and P. Kunkel. Efficient numerical pathfollowing beyond critical points. *SIAM J. Numer. Anal.*, 24(4):912–927, 1987.

P. Dhonukshe and J. Gadella, Theodorus W. J. Alteration of microtubule dynamic instability during preprophase band formation revealed by yellow fluorescent protein-clip170 microtubule plus-end labeling. *Plant Cell*, 15(3):597–611, 2003. doi: 10.1105/tpc.008961.

R. Dixit and R. Cyr. Encounters between Dynamic Cortical Microtubules Promote Ordering of the Cortical Array through Angle-Dependent Modifications of Microtubule Behavior. *Plant Cell*, 16(12):3274–3284, 2004. doi: 10.1105/tpc.104.026930.

R. Dixit, E. Chang, and R. Cyr. Establishment of polarity during organization of the acentrosomal plant cortical microtubule array. *Mol. Biol. Cell*, 17:1298–1305, 2006. doi: 10.1091/mbc.E05-09-0864.

M. P. Do Carmo. *Differential Geometry of Curves and Surfaces*. Prentice-Hall, 1976. ISBN 0-13-212589-7.

Dogterom and Leibler. Physical aspects of the growth and regulation of microtubule structures. *Phys. Rev. Lett.*, 70(9):1347–1350, 1993. doi: 10.1103/PhysRevLett.70.1347.

L. Edelstein-Keshet and G. B. Ermentrout. Models for the length distributions of actin filaments: I. Simple polymerization and fragmentation. *Bull. Math. Biol.*, 60:449–475, 1998. doi: 10.1006/bulm.1997.0011.

D. W. Ehrhardt. Straighten up and fly right–microtubule dynamics and organization of non-centrosomal arrays in higher plants. *Current Opinion in Cell Biology*, 20(1):107 – 116, 2008. doi: 10.1016/j.ceb.2007.12.004.

D. W. Ehrhardt and S. L. Shaw. Microtubule dynamics and organization in the plant cortical array. *Annu. Rev. Plant Biol.*, 57:859–75, 2006. doi: 10.1146/annurev.arplant.57.032905.105329.

K. A. Fichthorn and W. H. Weinberg. Theoretical foundations of dynamical monte carlo simulations. *The Journal of Chemical Physics*, 95(2):1090–1096, 1991. doi: 10.1063/1.461138.

H. Flyvbjerg, T. E. Holy, and S. Leibler. Stochastic dynamics of microtubules: A model for caps and catastrophes. *Phys. Rev. Lett.*, 73(17):2372–2375, 1994. doi: 10.1103/PhysRevLett.73.2372.

J. Gaillard, E. Neumann, D. V. Damme, V. Stoppin-Mellet, C. Ebel, E. Barbier, D. Geelen, and M. Vantard. Two Microtubule-associated Proteins of Arabidopsis MAP65s Promote Antiparallel Microtubule Bundling. *Mol. Biol. Cell*, 19(10):4534–4544, 2008. doi: 10.1091/mbc.E08-04-0341.

J. C. Gardiner, J. D. I. Harper, N. D. Weerakoon, D. A. Collings, S. Ritchie, S. Gilroy, R. J. Cyr, and J. Marc. A 90-kD Phospholipase D from Tobacco Binds to Microtubules and the Plasma Membrane. *Plant Cell*, 13(9):2143–2158, 2001. doi: 10.1105/tpc.13.9.2143.

N. Geerts, T. Schmatko, and E. Eiser. Clustering versus percolation in the assembly of colloids coated with long dna. *Langmuir*, 24(9):5118–5123, 2008. doi: 10.1021/la7036789.

E. Geigant, K. Ladizhansky, and A. Mogilner. An integrodifferential model for orientational distributions of f-actin in cells. *SIAM Journal on Applied Mathematics*, 59(3):787–809, 1998. doi: 10.1137/S0036139996309539.

M. Golubitsky and D. G. Schaeffer. *Singularities and Groups in Bifurcation Theory*, volume 1. Springer-Verlag, 1984. ISBN 0-387-90999-0.

M. Golubitsky and I. Stewart. *The Symmetry Perspective*. Birkhäuser Verlag, 2003. ISBN 3-7643-2171-7.

M. Golubitsky, I. Stewart, and D. G. Schaeffer. *Singularities and Groups in Bifurcation Theory*, volume 2. Springer-Verlag, 1988. ISBN 0-387-96652-8.

R. P. Goodman, I. A. T. Schaap, C. F. Tardin, C. M. Erben, R. M. Berry, C. F. Schmidt, and A. J. Turberfield. Rapid Chiral Assembly of Rigid DNA Building Blocks for Molecular Nanofabrication. *Science*, 310(5754):1661–1665, 2005. doi: 10.1126/science.1120367.

E. F. Gramsbergen, L. Longa, and W. H. de Jeu. Landau theory of the nematic-isotropic phase transition. *Physics Reports*, 135(4):195 – 257, 1986. doi: 10.1016/0370-1573(86)90007-4.

B. Grünbaum and G. Shephard. *Tilings and patterns*. W.H. Freeman and company, 1987. ISBN 0-7167-1193-1.

T. Hamada. Microtubule-associated proteins in higher plants. *J. Plant Res.*, 120(1):79–98, 2007. doi: 10.1007/s10265-006-0057-9.

O. Hamant, M. G. Heisler, H. Jonsson, P. Krupinski, M. Uyttewaal, P. Bokov, F. Corson, P. Sahlin, A. Boudaoud, E. M. Meyerowitz, Y. Couder, and J. Traas. Developmental Patterning by Mechanical Signals in Arabidopsis. *Science*, 322(5908):1650–1655, 2008. doi: 10.1126/science.1165594.

A. Hardham and B. Gunning. Structure of cortical microtubule arrays in plant cells. *J. Cell Biol.*, 77(1):14–34, 1978. doi: 10.1083/jcb.77.1.14.

J. J. Hartman and R. D. Vale. Microtubule Disassembly by ATP-Dependent Oligomerization of the AAA Enzyme Katanin. *Science*, 286(5440):782–785, 1999. doi: 10.1126/science.286.5440.782.

T. Hashimoto and T. Kato. Cortical control of plant microtubules. *Curr. Opin. Plant Biol.*, 9(1): 5–11, 2006. doi: 10.1016/j.pbi.2005.11.005.

H. D. Hill, R. J. Macfarlane, A. J. Senesi, B. Lee, S. Y. Park, and C. A. Mirkin. Controlling the lattice parameters of gold nanoparticle fcc crystals with duplex dna linkers. *Nano Letters*, 8 (8):2341–2344, 2008. doi: 10.1021/nl8011787.

T. L. Hill. Introductory analysis of the GTP-cap phase-change kinetics at the end of a microtubule. *Proc. Natl. Acad. Sci. U.S.A.*, 81:6728–6732, 1984.

G. Iooss and D. D. Joseph. *Elementary Stability and Bifurcation Theory*. Springer-Verlag, 1980. ISBN 0-387-90526-X.

T. Ishida, Y. Kaneko, M. Iwano, and T. Hashimoto. Helical microtubule arrays in a collection of twisting tubulin mutants of Arabidopsis thaliana. *Proceedings of the National Academy of Sciences*, 104(20):8544–8549, 2007. doi: 10.1073/pnas.0701224104.

M. E. Janson, M. E. de Dood, and M. Dogterom. Dynamic instability of microtubules is regulated by force. *J. Cell Biol.*, 161(6):1029–1034, 2003. doi: 10.1083/jcb.200301147.

I. M. Jánosi, D. Chrétien, and H. Flyvbjerg. Structural microtubule cap: stability, catastrophe, rescue, and third state. *Biophys. J.*, 83:1317–1330, 2002. doi: 10.1016/S0006-3495(02)73902-7.

E. Karsenti, F. Nédélec, and T. Surrey. Modelling microtubule patterns. *Nat. Cell Biol.*, 8: 1204–1211, 2006. doi: 10.1038/ncb1498.

V. Kirik, U. Herrmann, C. Parupalli, J. C. Sedbrook, D. W. Ehrhardt, and M. Hülskamp. Clasp localizes in two discrete patterns on cortical microtubules and is required for cell morphogenesis and cell division in arabidopsis. *J. Cell Sci.*, 120(Pt 24):4416–4425, 2007. doi: 10.1242/jcs.024950.

K. Kruse, J. Joanny, F. Jülicher, J. Prost, and K. Sekimoto. Generic theory of active polar gels: a paradigm for cytoskeletal dynamics. *Eur Phys J E Soft Matter*, 16:5–16, 2005. doi: 10.1140/epje/e2005-00002-5.

F. Kumagai, A. Yoneda, T. Tomida, T. Sano, T. Nagata, and S. Hasezawa. Fate of nascent microtubules organized at the M/G1 interface, as visualized by synchronized tobacco BY-2 cells stably expressing GFP-tubulin: time-sequence observations of the reorganization of cortical microtubules in living plant cells. *Plant Cell Physiol.*, 42(7):723–732, 2001. doi: 10.1093/pcp/pce091.

M. C. Lagomarsino, C. Tanase, J. W. Vos, A. M. C. Emons, B. M. Mulder, and M. Dogterom. Microtubule Organization in Three-Dimensional Confined Geometries: Evaluating the Role of Elasticity Through a Combined In Vitro and Modeling Approach. *Biophys. J.*, 92(3): 1046–1057, 2007. doi: 10.1529/biophysj.105.076893.

M. E. Leunissen, C. G. Christova, A.-P. Hynninen, C. P. Royall, A. I. Campbell, A. Imhof, M. Dijkstra, R. van Roij, and A. van Blaaderen. Ionic colloidal crystals of oppositely charged particles. *Nature*, 437:235 – 240, 2005. doi: 10.1038/nature03946.

N. A. Licata and A. V. Tkachenko. Errorproof programmable self-assembly of dna-nanoparticle clusters. *Physical Review E (Statistical, Nonlinear, and Soft Matter Physics)*, 74(4):041406, 2006. doi: 10.1103/PhysRevE.74.041406.

C. Lloyd and P. Hussey. Microtubule-associated proteins in plants–why we need a MAP. *Nat. Rev. Mol. Cell Biol.*, 2:40–47, 2001. doi: 10.1038/35048005.

J. Lucas and S. L. Shaw. Cortical microtubule arrays in the arabidopsis seedling. *Current Opinion in Plant Biology*, 11(1):94 – 98, 2008. doi: 10.1016/j.pbi.2007.12.001.

D. B. Lukatsky and D. Frenkel. Phase behavior and selectivity of dna-linked nanoparticle assemblies. *Physical Review Letters*, 92(6):068302, 2004. doi: 10.1103/PhysRevLett.92.068302.

D. B. Lukatsky, B. M. Mulder, and D. Frenkel. Designing ordered dna-linked nanoparticle assemblies. *Journal of Physics: Condensed Matter*, 18(18):S567–S580, 2006. doi: 10.1088/0953-8984/18/18/S05.

R. L. Margolis and L. Wilson. Microtubule treadmilling: what goes around comes around. *BioEssays*, 20:830–836, 1998. doi: 10.1002/(SICI)1521-1878(199810)20:10<830::AID-BIES8>3.0.CO;2-N.

F. J. McNally and R. D. Vale. Identification of katanin, an atpase that severs and disassembles stable microtubules. *Cell*, 75(3):419 – 429, 1993. doi: 10.1016/0092-8674(93)90377-3.

K. McNally, A. Audhya, K. Oegema, and F. J. McNally. Katanin controls mitotic and meiotic spindle length. *J. Cell Biol.*, 175(6):881–891, 2006. doi: 10.1083/jcb.200608117.

C. A. Mirkin, R. L. Letsinger, R. C. Mucic, and J. J. Storhoff. A dna-based method for rationally assembling nanoparticles into macroscopic materials. *Nature*, 382:607 – 609, 1996. doi: 10.1038/382607a0.

T. Mitchison and M. Kirschner. Dynamic instability of microtubule growth. *Nature*, 312: 237–242, 1984. doi: 10.1038/312237a0.

T. Murata and M. Hasebe. Microtubule-dependent microtubule nucleation in plant cells. *J. Plant Res.*, 120(1):73–78, 2007. doi: 10.1007/s10265-006-0054-z.

T. Murata, S. Sonobe, T. I. Baskin, S. Hyodo, S. Hasezawa, T. Nagata, T. Horio, and M. Hasebe. Microtubule-dependent microtubule nucleation based on recruitment of gamma-tubulin in higher plants. *Nat. Cell Biol.*, 7(10):961–968, 2005. doi: 10.1038/ncb1306.

D. Nykypanchuk, M. M. Maye, D. van der Lelie, and O. Gang. Dna-guided crystallization of colloidal nanoparticles. *Nature*, 451:549 – 552, 2008. doi: 10.1038/nature06560.

A. Paradez, A. Wright, and D. W. Ehrhardt. Microtubule cortical array organization and plant cell morphogenesis. *Current Opinion in Plant Biology*, 9(6):571 – 578, 2006. doi: 10.1016/j.pbi.2006.09.005.

A. R. Paredez, C. R. Somerville, and D. W. Ehrhardt. Visualization of cellulose synthase demonstrates functional association with microtubules. *Science*, 312(5779):1491–1495, 2006. doi: 10.1126/science.1126551.

A. R. Paredez, S. Persson, D. W. Ehrhardt, and C. R. Somerville. Genetic Evidence That Cellulose Synthase Activity Influences Microtubule Cortical Array Organization. *Plant Physiol.*, 147 (4):1723–1734, 2008. doi: 10.1104/pp.108.120196.

S. Y. Park, A. K. R. Lytton-Jean, B. Lee, S. Weigand, G. C. Schatz, and C. A. Mirkin. Dna-programmable nanoparticle crystallization. *Nature*, 451:553 – 556, 2008. doi: 10.1038/nature06508.

M. Pastuglia and D. Bouchez. Molecular encounters at microtubule ends in the plant cell cortex. *Current Opinion in Plant Biology*, 10(6):557 – 563, 2007. doi: 10.1016/j.pbi.2007.08.001.

L. Quarmby. Cellular Samurai: katanin and the severing of microtubules. *J Cell Sci*, 113(16): 2821–2827, 2000.

V. Rühle, F. Ziebert, R. Peter, and W. Zimmermann. Instabilities in a two-dimensional polar-filament-motor system. *Eur Phys J E Soft Matter*, 27(3):243–251, 2008. doi: 10.1140/epje/i2007-10377-x.

V. I. Rodionov and G. G. Borisy. Microtubule Treadmilling in Vivo. *Science*, 275(5297):215–218, 1997. doi: 10.1126/science.275.5297.215.

J. Roland, J. Berro, A. Michelot, L. Blanchoin, and J.-L. Martiel. Stochastic severing of actin filaments by actin depolymerizing factor/cofilin controls the emergence of a steady dynamical regime. *Biophysical Journal*, 94(6):2082 – 2094, 2008. doi: 10.1529/biophysj.107.121988.

A. Roll-Mecak and R. D. Vale. Structural basis of microtubule severing by the hereditary spastic paraplegia protein spastin. *Nature*, 451:363–367, 2008. doi: 10.1038/nature06482.

A. Roll-Mecak and R. D. Vale. Making more microtubules by severing: a common theme of noncentrosomal microtubule arrays? *J. Cell Biol.*, 175(6):849–851, 2006. doi: 10.1083/jcb.200611149.

P. W. K. Rothemund. Folding dna to create nanoscale shapes and patterns. *Nature*, 440:297 – 302, 2006. doi: 10.1038/nature04586.

F. Sainsbury, D. A. Collings, K. Mackun, J. Gardiner, J. D. Harper, and J. Marc. Developmental reorientation of transverse cortical microtubules to longitudinal directions: a role for actomyosin-based streaming and partial microtubule-membrane detachment. *Plant J.*, 56: 116–131, 2008. doi: 10.1111/j.1365-313X.2008.03574.x.

T. Schmatko, B. Bozorgui, N. Geerts, D. Frenkel, E. Eiser, and W. C. Poon. A finite-cluster phase in [small lambda]-dna-coated colloids. *Soft Matter*, 3(6):703–706, 2007. doi: 10.1039/b618028k.

J. C. Sedbrook and D. Kaloriti. Microtubules, maps and plant directional cell expansion. *Trends in Plant Science*, 13(6):303 – 310, 2008. doi: 10.1016/j.tplants.2008.04.002.

S. L. Shaw, R. Kamyar, and D. W. Ehrhardt. Sustained microtubule treadmilling in Arabidopsis cortical arrays. *Science*, 300(5626):1715–1718, 2003. doi: 10.1126/science.1083529.

M. Srayko, E. T. O'Toole, A. A. Hyman, and T. Müller-Reichert. Katanin disrupts the microtubule lattice and increases polymer number in c.äelegans meiosis. *Current Biology*, 16(19):1944 – 1949, 2006. doi: 10.1016/j.cub.2006.08.029.

V. Stoppin-Mellet, J. Gaillard, and M. Vantard. Katanin's severing activity favors bundling of cortical microtubules in plants. *Plant J.*, 46:1009–1017, 2006. doi: 10.1111/j.1365-313X.2006.02761.x.

C. Tanase. *Physical modeling of microtubule force generation and self-organization.* PhD thesis, Wageningen University, The Netherlands, 2004.

A. V. Tkachenko. Morphological diversity of dna-colloidal self-assembly. *Phys. Rev. Lett.*, 89 (14):148303, 2002. doi: 10.1103/PhysRevLett.89.148303.

R. Y. Tsien. The green fluorescent protein. *Annual Review of Biochemistry*, 67(1):509–544, 1998. doi: 10.1146/annurev.biochem.67.1.509.

R. D. Vale. Severing of stable microtubules by a mitotically activated protein in xenopus egg extracts. *Cell*, 64(4):827 – 839, 1991. doi: 10.1016/0092-8674(91)90511-V.

M. G. L. Van den Heuvel, M. P. de Graaff, and C. Dekker. Microtubule curvatures under perpendicular electric forces reveal a low persistence length. *Proceedings of the National Academy of Sciences*, 105(23):7941–7946, 2008. doi: 10.1073/pnas.0704169105.

V. VanBuren, L. Cassimeris, and D. J. Odde. Mechanochemical model of microtubule structure and self-assembly kinetics. *Biophys. J.*, 89:2911–2926, 2005. doi: 10.1529/biophysj.105.060913.

F. Verde, M. Dogterom, E. Stelzer, E. Karsenti, and S. Leibler. Control of microtubule dynamics and length by cyclin A- and cyclin B- dependent kinases in Xenopus egg extracts. *J. Cell Biol.*, 118(5):1097–1108, 1992. doi: 10.1083/jcb.118.5.1097.

J. W. Vos, B. Sieberer, A. C. J. Timmers, and A. M. C. Emons. Microtubule dynamics during preprophase band formation and the role of endoplasmic microtubules during root hair elongation. *Cell Biol. Int.*, 27(3):295, 2003. doi: 10.1016/S1065-6995(02)00309-8.

J. W. Vos, M. Dogterom, and A. M. C. Emons. Microtubules become more dynamic but not shorter during preprophase band formation: a possible "search-and-capture" mechanism for microtubule translocation. *Cell Motil. Cytoskeleton*, 57(4):246–258, 2004. doi: 10.1002/cm.10169.

G. O. Wasteneys. Microtubule organization in the green kingdom: chaos or self-order? *J. Cell Sci.*, 115(Pt 7):1345–1354, 2002.

G. O. Wasteneys and R. E. Williamson. Reassembly of microtubules in nitella tasmanica - quantitative-analysis of assembly and orientation. *Eur. J. Cell Biol.*, 50(1):76–83, 1989.

R. Wightman and S. R. Turner. Severing at sites of microtubule crossover contributes to microtubule alignment in cortical arrays. *Plant J.*, 52:742–751, 2007. doi: 10.1111/j.1365-313X.2007.03271.x.

J. Zheng, P. E. Constantinou, C. Micheel, A. P. Alivisatos, R. A. Kiehl, and N. C. Seeman. Two-dimensional nanoparticle arrays show the organizational power of robust dna motifs. *Nano Letters*, 6(7):1502–1504, 2006. doi: 10.1021/nl060994c.

Y. Zheng, M. L. Wong, B. Alberts, and T. Mitchison. Nucleation of microtubule assembly by a gamma-tubulin-containing ring complex. *Nature*, 378:578–583, 1995. doi: 10.1038/378578a0.

A. Zumdieck, M. C. Lagomarsino, C. Tanase, K. Kruse, B. Mulder, M. Dogterom, and F. Jülicher. Continuum description of the cytoskeleton: ring formation in the cell cortex. *Phys. Rev. Lett.*, 95(25):258103, 2005. doi: 10.1103/PhysRevLett.95.258103.

Samenvatting

Biomoleculaire ontwerpbouwstenen:
corticale microtubuli en met DNA gedecoreerde colloïden

Het onderzoek dat is beschreven in dit proefschrift gaat over de zelforganiserende eigenschappen van biomoleculen. Gezamenlijk kunnen deze moleculen geordende systemen vormen die veel groter zijn dan de individuele moleculen, door hun posities en/of bewegingen te coördineren door middel van hun onderlinge interacties. Biomoleculen zijn hiervoor uitermate geschikt, omdat ze een grote structurele diversiteit en zeer specifieke interactie-eigenschappen hebben. Daarmee vormen zij ideale bouwstenen die door de natuur – en de mens – gebruikt kunnen worden om interacties naar keuze te construeren en op deze wijze materialen met specifieke eigenschappen te ontwerpen. In dit proefschrift komen twee zelforganiserende systemen op basis van biomoleculen aan bod.

Het eerste systeem is er een dat in de loop van honderden miljoenen jaren door de natuur is geëvolueerd: het cytoskelet van plantencellen. Het cytoskelet in een cel dankt zijn naam aan het feit dat het een grote bijdrage levert aan de mechanische eigenschappen van de cel, maar het cytoskelet is veel meer. Het dient ook als het cellulaire 'wegennet' waarlangs materialen worden getransporteerd, en het grootste verschil met ons eigen skelet is wellicht dat het cytoskelet een *dynamisch* geheel is. De filamenten waaruit het is opgebouwd veranderen voortdurend van lengte en positie, nieuwe filamenten ontstaan en andere verdwijnen. Daardoor is het cytoskelet in staat om te veranderen van vorm en functie, al naar gelang dit tijdens de verschillende levensfasen van een cel nodig is.

Het cytoskelet bestaat uit een lange dunne filamenten en bijbehorende eiwitten. Het onderzoek in dit proefschrift richt zich op de stijfste van de verschillende typen filamenten: microtubuli. Dit zijn zeer dunne (25 nanometer) holle eiwitstaafjes die vele micrometers lang kunnen worden. Door hun constructie zijn ze erg stijf op de schaal van een cel en ze vervullen daarom vaak de functie van cellulaire draagbalk. In tegenstelling tot wat deze analogie suggereert zijn microtubuli zeer dynamisch door de voortdurende toevoeging en verwijdering van eiwitten aan de uiteinden. Het zijn bovendien polaire structuren, waarvan de twee onderscheidbare uiteinden worden aangeduid als het plus-einde en het min-einde. Het plus-einde schakelt tussen periodes van groei en krimp met ieder een (in eerste benadering) constante snelheid. Het min-einde is minder dynamisch en zit vast aan de plaats waar de

microtubule is ontstaan of krimpt met een vrij constante (lage) snelheid.

In hoofdstuk 2 is beschreven hoe deze dynamica, samen met het willekeurig in tweeën 'knippen' van microtubuli, leidt tot een lengteverdeling van de filamenten in de cel. Zoals verwacht veroorzaakt het knippen een afname van de gemiddelde lengte en een lengteverdeling met minder variatie: heel lange microtubuli kunnen niet lang overleven, omdat ze snel in tweeën worden gedeeld. Een verrassend resultaat is dat het verwachte totale aantal filamenten gelijk blijft: de creatie van een nieuwe microtubule door het knippen wordt precies gecompenseerd door het feit dat de kortere filamenten sneller geheel verdwijnen.

De hoofdstukken 3-5 gaan over het microtubule-cytoskelet in de context van de plantencel. Plantencellen hebben de interessante eigenschap dat ze omringd zijn door een harde celwand en onder een grote inwendige druk staan. Tegelijkertijd zijn ze in staat om in een zeer specifieke richting te groeien, zodat een gecontroleerde expansie van de celwand vereist is. De microtubuli spelen hierin een belangrijke rol. Ze bevinden zich in de cortex van de cel en zijn aan de binnenkant verbonden met het celmembraan. Kort na de celdeling oriënteren de corticale microtubuli zich loodrecht op de groei-as. De zo ontstane *corticale array* dient als 'rails' voor de aanleg van de richtingsgevoelige celwand.

Er is een aantal factoren dat bijdraagt aan het ontstaan van een gezamenlijke richting, maar in welke mate ze dat doen en wat hun wisselwerking is, is nog grotendeels onbekend. Om hier meer licht op te werpen hebben wij de experimentele observaties samengevat in een model voor interacterende microtubuli. De microtubuli zitten vast aan het celmembraan en kunnen slechts bewegen door groei en krimp aan hun uiteindes. Door de tweedimensionale geometrie is het mogelijk dat een groeiend uiteinde botst met een andere microtubule. Experimenten hebben aangetoond dat zo'n botsing leidt tot één van drie mogelijke uitkomsten: (i) ritsen, waarbij het groeiende uiteinde parallel aan de andere microtubule verder groeit, (ii) een 'catastrofe', waarbij het groeiende uiteinde begint te krimpen, of (iii) een oversteek, waarbij de twee microtubuli elkaar kruisen.

In hoofdstuk 3 is op basis hiervan een analytisch model geconstrueerd. Hoewel het model vele parameters heeft, blijkt het een enorme reductie in complexiteit toe te staan: de frequentie waarmee nieuwe microtubuli gecreëerd worden en alle microtubule-eigen parameters (groei/krimpsnelheid en de frequentie waarmee hiertussen geschakeld wordt) kunnen worden samengevat in een enkele controleparameter. Bij een bepaalde waarde van deze controleparameter is er een overgang van een wanordelijke toestand naar een toestand waarin de microtubuli ordenen. De precieze waarde waarbij deze overgang optreedt (en of het geordende systeem stabiel is) hangt verrassend genoeg alleen af van de hoekafhankelijke kans dat een botsing een catastrofe tot gevolg heeft. De kans om te ritsen heeft slechts een kleine invloed op de mate waarin het systeem ordent.

Deze analytische aanpak van het model voor interacterende microtubuli wordt in hoofdstuk 4 aangevuld met computersimulaties. Een vergelijking tussen de resultaten die zijn verkregen met de twee methoden toont aan dat de theoretische voorspellingen erg goed zijn voor systemen waarin microtubuli niet ritsen. Als ritsen

wel mogelijk is, lopen de resultaten uiteen, en hangen de simulatieresultaten sterk af van wat er gebeurt bij een botsing met een bundel van parallelle microtubuli, waarover tot op heden geen experimentele gegevens beschikbaar zijn. Deze bundels zijn het directe gevolg van het ritsen van een plus-einde langs een andere microtubule. Ondanks deze onzekerheid is er niettemin een kwalitatieve overeenkomst tussen de simulaties en de theorie.

De simulaties lenen zich bovendien bij uitstek voor onderzoek naar overige processen die een rol kunnen spelen bij de vorming van de corticale array. Zo is uit de simulaties gebleken dat de combinatie van depolymerisatie (krimp) aan het min-einde en ritsen kan leiden tot ordening bij een lagere dichtheid dan zonder deze effecten het geval zou zijn. Ook is het effect van het knippen van microtubuli onderzocht. Het knippen op willekeurige locaties langs de microtubuli leidt tot een reductie van de ordening, zoals te verwachten was op basis van de in hoofdstuk 2 voorspelde afname van de dichtheid. Het knippen op een kruising van twee microtubuli kan daarentegen leiden tot een forse toename van de ordening, in overeenstemming met experimentele waarnemingen. Ten slotte komt ook het tijdsverloop van het ontstaan van de corticale array redelijk overeen met de experimentele waarnemingen.

De microtubuli in de corticale array liggen niet alleen parallel aan elkaar, maar ook loodrecht op de groeirichting van de cel. In een eerste benadering zijn plantencellen cilindervormig en groeien ze in de richting van de as van de cilinder. In hoofdstuk 5 hebben we onderzocht welke invloed deze geometrie heeft op de ordeningsrichting van de corticale array. Hoewel de resulterende oriëntaties niet langer isotroop zijn en de geometrie dus wel wordt 'opgemerkt' door de microtubuli, leidt dit op zichzelf niet tot een betrouwbare oriëntatie. Daarvoor is een additioneel mechanisme nodig, zoals een lokale modulatie van de groeiparameters van de microtubuli. Een specifiek voorbeeld van een dergelijke beïnvloeding is nader onderzocht: een verhoging van de kans dat een microtubule schakelt van de groei- naar de krimptoestand op de uiteindes van de cilinder. Het blijkt dat dit afdoende is om een betrouwbare oriëntatie van de corticale array te garanderen. Deze door ons gebruikte *ad-hoc* hypothese is niet onredelijk, omdat bekend is dat een aantal eiwitten in de cel lokaliseert aan de uiteindes van de cel en omdat de waargenomen dichtheid van microtubuli daar inderdaad lager is.

Het tweede systeem dat in dit proefschrift wordt behandeld, is een door de mens ontworpen modelsysteem voor zelfassemblage. Het bestaat uit colloïden, kleine bolletjes met een doorsnede van ongeveer 1 micrometer, waarop DNA-strengen zijn bevestigd. Een DNA-streng bestaat uit een aaneenschakeling van nucleotiden die meestal worden weergegeven met de letters A, C, T en G. In de natuurlijke toestand vormt DNA de bekende dubbele helix, waarin twee strengen om elkaar heen zijn gewikkeld. Hierin zijn de nucleotiden door middel van waterstofbindingen verbonden met nucleotiden in de andere streng, waarbij een sterke binding alleen wordt gevormd tussen een A-T paar of een C-G paar. Een DNA-streng, met een specifieke code die bestaat uit het ATCG-alfabet, heeft dus een unieke partner waarmee een optimale binding kan worden aangegaan. De combinatie van de grote verscheidenheid

aan mogelijke codes en de specificiteit van de interacties maakt DNA tot een ideale kandidaat voor *designer*-interacties. De DNA-streng die aan een colloïde bevestigd is, kan op deze wijze 'geprogrammeerd' worden om te binden met het DNA van een specifieke andere colloïde.

Het is een aantrekkelijk vooruitzicht dat de met DNA gedecoreerde colloïden zichzelf kunnen organiseren in complexe structuren door middel van onderlinge interacties die gecodeerd zijn in het DNA. Een fundamentele vraag die zich hierbij opdringt is hoeveel ieder deeltje moet 'weten' over zijn omgeving om een unieke eindtoestand te specificeren. Deze vraag is leidend geweest bij het onderzoek in hoofdstuk 6. Daarin is een abstract model geïntroduceerd met een willekeurig aantal verschillende deeltjes, gemarkeerd met de letters van het alfabet. Deze deeltjes bevinden zich op een tweedimensionaal rooster en hebben paarspecifieke interacties die richtingsonafhankelijk zijn en een korte dracht hebben. Voor dit model hebben we ons afgevraagd of het mogelijk is om de interacties zo te kiezen dat een gegeven kristalstructuur de unieke grondtoestand vormt.

Het blijkt dat hiervoor een minimale interactieafstand benodigd is, die afhankelijk is van het onderliggende roostertype. Als aan deze eis voldaan is, kunnen in principe kristallen van onbeperkte grootte en complexiteit ontworpen worden. Bovendien is een specifiek 'recept' voor de keuze van de interacties gepresenteerd waarvoor is bewezen dat deze keuze leidt tot een unieke grondtoestand voor enkele eenvoudige kristalstructuren. Voorbeelden hiervan zijn geverifieerd door middel van Monte-Carlosimulaties.

Acknowledgments

Many people have contributed, either directly or indirectly, to the work that is presented in this thesis. It's impossible to list them all, but a number deserve a special mention. Let me start with you, the reader. A book is useless without an audience, and I am happy that you are at least reading this page.

The main person behind the scenes has of course been my supervisor, Bela. First of all, thank you for your limitless enthusiasm and optimism. Also, I will look back fondly on our white board sessions in your office – those have resulted in some of the best results in this thesis. Beyond work, it has always been fun to discuss politics, infographics, and the latest obscure software packages with you.

Rhoda has originally constructed the model of interacting microtubules that is described in chapter 3 and started the work on its analysis. I think it's safe to say that neither of us knew how long that particular path was going to be - but we have finally cracked it! Thank you for a great collaboration.

Next, I owe a big thank-you to Jelmer and Eva. During his internship at AMOLF, Jelmer was the first to create a simulation of cortical microtubules based on the experimental observations. This proof of concept has given us the confidence to go ahead and create the speed-optimized version that is described in chapter 4. This new code was put to the test by Eva, who, shortly after commencing her MSc research, started producing large amounts of data. In the process, she uncovered a number of bugs, made some useful extensions to the code and created a bewildering amount of handy scripts. But most of all, the results gave us valuable insight into the behavior of the system for a large range of parameters.

As a physicist with very little previous experience in biology, let alone plants (they tend to die in my presence), I am very grateful to Jan, Jelmer (again) and Anne Mie for answering all the – often trivial – biology questions that I have fired at them over the years, and providing us with references, data and images for talks and papers. The work in chapters 2–5 owes its current form and biological relevance directly to your input. I'd also like to thank the other members of the Plant Cell Biology lab in Wageningen for the warm welcome and the helpful comments I received whenever I came by.

I am glad to have had the opportunity to spend a few months in the group of Frank Jülicher at the MPI-PKS in Dresden, and having received support for my living expenses while I was there. Besides being a good chance to 'taste' a different scientific environment, this stay resulted in most of the work that is presented in chapter 2. In particular, I'd like to thank Frank Jülicher and Benjamin Lindner for their helpful

suggestions, and all the lab members for the good time I have had.

In addition, I'd like to express my gratitude to Kostya, who can always be counted on for sharp questions that trigger you to retrace your steps and be really sure that you know what you're doing. Also, thanks to Rutger for his help in the derivation of the multi-collision probabilities (section 4.B) and interesting discussions on almost any subject, Koos for his assistance in fixing obscure programming problems and getting my last-minute simulations up and running on the cluster, Liedewij and Daan K. for the company during late night thesis writing sessions and Eva, Kostya and Maryam for careful reading of the various chapters.

During my years at AMOLF, I have benefitted from the diverse and dynamic scientific atmosphere, with many (sometimes almost too many) visitors giving talks, group meetings with the groups of Bela, Daan Frenkel and Pieter Rein, bio-meetings with the groups of Marileen, Sander and Gijsje, biophysics meetings at the KNAW and in the earlier years summer schools with the CoSy group at the VU – I especially owe a lot to the latter.

However, even at AMOLF my life has not all been about science. I have learned a lot, whilst generally having a good time, as a member of the PV with Annemieke, Grace, Janne, Marijn, Rimco, Willem and Yves, in the 'Nationale Denktank' team with Harald, Liedewij, Rutger, Ruud and Stefan, driving around the country as 'Boze OIO's' with Eva R, starting up the AMOLF works council with Daan, Duncan, Rutger, Siebe and Sjoerd, and being part of the FOM works council with Joost, Mirjam, Wouter, Leo and many others. Overall, the excellent support you get as a scientist at AMOLF has kept life in the lab easy, and it has been fun because of my great colleagues, especially my fellow overloop-inhabitants and office mates. There have been many of you over the years – in fact, all the (non-permanent) scientists who were at AMOLF when I first arrived have moved on, and new people have come in their place. For this reason, I won't try to list you all by name, because I would have to run on for pages (and still forget names) or draw a boundary that I really don't want to draw. Thank you all!

Outside the lab, I owe a lot to my friends. Specifically, I'd like to mention my paranimfen, Toon and Tobias, who have been around since high school, and the many friends that I have made during the $\beta\gamma$ program and all those that I have met through them. You are a great bunch of people, always up for things that are interesting, different, fun, or just plain weird. Thanks for the support while I was writing (especially Sanne) and keeping me more or less sane.

I'd like to end by thanking my family. My parents have always let me go my own way, but are there for me with helpful advice when I need them. In fact, it's likely I wouldn't have ended up at AMOLF without their help. Arthur, your laid-back and easy approach to life is something I can aspire to. And finally Maryam. What can I say, I'm an incredibly lucky guy. I haven't spent anywhere near enough time with you while I was writing my thesis, and it's about time we change that. With this book out of the way, let's go on our big trip!
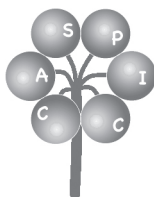
Simon Tindemans, May 2009